CRANFIELD UNIVERSITY

A. J. LAMB

EXPERIMENTAL INVESTIGATION AND NUMERICAL MODELLING OF COMPOSITE-HONEYCOMB MATERIALS USED IN FORMULA 1 CRASH STRUCTURES

SCHOOL OF APPLIED SCIENCES

PhD THESIS

CRANFIELD UNIVERSITY

SCHOOL OF APPLIED SCIENCES

PhD THESIS

Academic Year 2004-2007

A. J. LAMB

Experimental Investigation and Numerical Modelling of Composite-Honeycomb
Materials used in Formula 1 Crash Structures

Supervisor: Professor A. K. PICKETT

January 2007

This thesis is submitted in partial fulfilment of the requirements for the degree of
Doctor of Philosophy.

ABSTRACT

This thesis has investigated composite-honeycomb sandwich materials commonly used in Formula 1 nosecone structures. Experimental work has investigated their failure behaviour under static and dynamic crash loading, from which new constitutive failure laws for implementation in the explicit Finite Element code PAM-CRASH^{TM} have been proposed.

An investigation using an improved Arcan apparatus has been conducted to establish the mixed shear-compression properties of the honeycomb. An investigation has also been performed to establish relationships between in-plane deformation and out-of-plane compression properties. These relationships have been identified and successfully implemented into a honeycomb solid element material model available in PAM-CRASH^{TM}. A further investigation to represent honeycomb using geometrically accurate shell representation of the honeycomb has also been presented. This model was shown to reproduce trends observed during testing.

The composite skin material has also been experimentally investigated and presented. This investigation made use of digital image correlation to examine the onset of intra-laminar shear failure mechanisms, from which a non-linear damage progression law was identified. This law was successfully implemented into the Ladevéze damage model in PAM-CRASH^{TM} for composite material modelling and has been shown to improve the representation of in-plane shear damage progression and failure.

A series of experimental investigations to examine the energy absorbing properties of the sandwich have been conducted and presented. These investigations include three point bend flexural testing and edgewise impact loading. Failure mechanisms in the skin and core have been identified for each loading case. Experimental findings were used to assess the capability of PAM-CRASH^{TM} for sandwich material modelling. This investigation has highlighted deficiencies in the material models when representing the sandwich, specifically with the existing composite skin and honeycomb models. Improvements introduced to the core and skin material models have shown some improvement when representing sandwich structures.

ACKNOWLEDGEMENTS

TABLE OF CONTENTS

TABLE OF FIGURES

LIST OF TABLES

ABBREVIATIONS AND SYMBOLS

Abbreviation	**Description**
BAR	British American Racing, currently known as Honda Racing F1
CC	Compliance Calibration (DCB analysis method)
CSB	Cracked Sandwich Beam test
DCB	Double Cantilever Beam test
DIC	Digital Image Correlation
FE	Finite Element Analysis
FIA	Federation Internationale de l'Automobile
MBT	Modified Beam Theory (DCB analysis method)
MCC	Modified Compliance Calibration (DCB analysis method)
MMB	Mixed-Mode Beam test
SEA	Specific Energy Absorption
UD	Unidirectional composite material
3PB	Three-Point Bend test.

General Terms

Symbol	**Description**	**Symbol**	**Description**
A	Cross-sectional area	I	Second moment of inertia
a	Crack length	L	Sample width
b	Width of DCB sample	q	Shear flow
C	Compliance	P	Applied force
E	Elastic modulus	t	Sample thickness
G	Shear modulus	δ_I	Load point deflection during Mode-I DCB test
G_{IC}	Mode-I strain energy release rate		
G_{IIC}	Mode-II strain energy release rate	δ_{II}	Load point deflection due to Mode-II loading
h_{DCB}	Thickness of DCB Sample	σ	Stress
h_{cont}	Distance for kinematic computation; used in FE boundary conditions and tied interface modelling	τ	Shear stress
		ε	Strain
		ρ	Density
		υ	Poisson's ratio

Honeycomb Notation

Symbol	Description	Symbol	Description
T, W, L	Honeycomb principal directions	t	Cell wall thickness
TW, TL	Out-of-plane shear directions	l	Cell wall length (single thickness wall)
S	Base material		
σ_{TW}	Out-of-plane shear stress in TW direction	h	Cell wall length (double thickness wall)
σ_{TL}	Out-of-plane shear stress in TL direction	D	Cell minor diameter
		α	Arcan angle during mixed shear-compression loading
σ_{EL}	Elastic yield stress		
σ_P	Plateau crushing stress	λ	'T' direction cell wall fold length
ε_{EL}	Elastic yield strain		
σ_{YS}	Yield stress of base material	F_V	Vertical force
ε_C (ε_d)	Compaction strain	F_H	Horizontal force
θ	Honeycomb wall angle	β	In-plane orientation angle

Composite Notation

Symbol	Description	Symbol	Description
1,2	Fibre and transverse fibre directions respectively	HM	High modulus
		V_f	Fibre volume
δ	Fibre angle relative to loading direction	R_C	Resin content
		$R_{(P)}$	Plastic hardening function
d_{12}	Shear damage	σ_{11}	Stress of the composite in the fibre direction
d_{22}	Transverse matrix dominated damage		
		σ_{22}	Stress of the composite in the transverse fibre direction
P	Plastic Strain		
R	Plastic hardening function	σ_{12}	Shear stress
Y	Damage limitation	ε^e	Elastic strain
IM	Intermediate modulus	ε^P	Inelastic strain

Other notations are stated in the main text of this thesis.

1 Introduction

Motorsport companies rely on engineers to make use of modern materials to produce competitive vehicles to compete in the highly competitive, and lucrative, sport of motor racing; nowhere is this more evident than in Formula 1. In order to assure vehicle crashworthiness, designers must also adhere to the stringent safety regulations of the motorsport governing body, the Federation Internationale de l'Automobile (FIA). The process of developing a new energy absorbing structure is achieved through experimental testing and knowledge gathered from previous developments. This is an expensive and time consuming process as it requires the development of prototype components and full scale testing at a dedicated impact facility. Failure to meet crashworthiness requirements can be costly to a team as it may halt the progression of an improved car [1]. There is interest in the use of Finite Element (FE) analysis programs to determine the crashworthiness of a new component during in the design phase; however, commercial FE codes have yet to be equipped with accurate constitutive models required for composite component crashworthiness.

The introduction of reliable and accurate FE modelling could potentially improve the design process of new crash structures and significantly reduce development costs. An optimisation process can also be applied without the need for prototype development. Knowledge concerning the energy absorbency of new and existing structures could be increased to assess variations in the impact conditions, such as impact direction and barrier properties. Within an office environment, a group of aerodynamicists, structural engineers and material specialists could potentially design and assess a structure is within a matter of hours.

An investigative research study has been conducted to improve the constitutive material models used in each element of the sandwich. This required an experimental investigation of the core, composite skins and sandwich structure under a variety of loading conditions to establish new material laws and improve the representation of the numerical material models.

1.1 Aims and Objectives

This work presents contributions towards the improved modelling of honeycomb core and composite laminate skin materials. These improvements are based on findings from a series of experimental studies to investigate variations in loading conditions on honeycomb materials and improved damage progression in the composite laminate. The suitability of current FE techniques with regard to modelling composite-honeycomb sandwiches is assessed. An experimental research program was conducted to determine the energy absorbing properties of a composite-honeycomb sandwich used in a typical Formula 1 impact absorbing structure.

The aims of this research thesis are to:

- Investigate the energy absorption properties of the materials used in the nosecone structure of the 2004 BAR-Honda Formula 1 race car.

- Develop new testing methods to investigate variations in loading conditions on the principal directions of aluminium honeycomb.

- Identify options available within the FE package PAM-CRASH^{TM} to represent a composite-honeycomb sandwich structure.

- Determine limitations of the FE computational code when representing a composite-honeycomb sandwich and investigate improvements to overcome these limitations.

Thesis Summary

The following summarises the contents of each Chapter in this research thesis.

Chapter 2:   *Literature Review*

A review of safety requirements in motorsport and the impact of composite materials on vehicle crashworthiness are presented. The components used to construct a composite-honeycomb sandwich are described, beginning with the energy absorbing properties of honeycomb materials. Composite materials are then introduced; this covers manufacture of these materials and property prediction techniques. This is then followed by a description of composite-honeycomb structures. This Chapter is concluded with an introduction to FE analysis and methods used in previous research to represent composite, honeycomb and sandwich materials.

Chapter 3:   *FE Modelling of Composite-Honeycomb Materials*

This Chapter introduces the required material properties to develop appropriate numerical models of the materials used in the composite-honeycomb sandwich. These requirements are based on the potential failure mechanisms in the nosecone structure when subjected to a frontal impact and to fulfil the material properties required by the current numerical material models.

Chapter 4:   *Experimental Procedures and Results*

This Chapter presents the results from experimental investigations of the composite-honeycomb sandwich structure. This research includes an investigation of the variation in honeycomb properties when subject to a variety of loading conditions and a damage analysis of the composite skin material. The Chapter concludes with an investigation of the energy absorbing properties of the composite-honeycomb sandwich.

Chapter 5:   *Numerical Modelling Procedures and Results*

This Chapter presents results of the calibrated numerical models to represent the honeycomb core and composite skin materials. New material properties produced from experimental testing are introduced to the constitutive material model to represent honeycomb materials. In addition, an improved damage progression law is introduced to the numerical shell model to represent the woven composite material. A variety of methods to represent the composite-honeycomb sandwich are investigated using options available in PAM-CRASH^{TM}. To conclude, considerations towards modelling the nosecone structure are presented with respect to boundary conditions fulfilling the requirements specified by the FIA.

Chapter 6:   *Discussion*

This Chapter discusses the limitations and validity of the presented experimental results and methods. Numerical modelling of the honeycomb, composite and sandwich are discussed. The benefits and disadvantages of the developed improvements to the constitutive material codes are also discussed.

Chapter 7:   *Conclusions*

This Chapter presents the conclusions of this thesis and summarises the contributions produced by this work.

Chapter 8:   *Future Studies*

To conclude this thesis, future potential areas of research are suggested to address limitations encountered during this work and investigate the properties of these materials further.

2   Literature Review

This Chapter reviews the established knowledge concerning all elements focused upon in this research thesis. This literature review includes:

- A history of Formula 1 crashworthiness and survivability, focusing on the frontal impact case. This Section also comments upon the effect of introducing composite materials to the sport.

- The use and properties of sandwich materials, focusing on the properties of the core, composite skin and applications in Formula 1.

- Computational methods to determine the energy absorption of core materials, composite materials and sandwich structures.

Composite sandwich structures are being introduced to an increasing array of structural applications. The aerospace and motorsport industries, for example, rely on these materials to reduce operational costs and increase performance. The development of predictive tools to determine the energy absorption and crashworthiness of these structures will assist further development and applications.

2.1   Formula 1 Structures and Crash Testing

Formula 1 racing cars are considered to represent the pinnacle of automotive engineering due to the amount of technology and structural development involved in the production of these vehicles. Designed primarily for speed and endurance, a Formula 1 racing car must also protect the driver in the event of an accident. To assist designers, the FIA has taken steps to set requirements for high-energy testing which will ensure vehicle crashworthiness. Meeting these requirements and producing a competitive vehicle presents the designers with difficult challenges.

2.1.1 A Brief History of Motorsport Safety and Materials

Before the FIA began a drive for safety, fatalities and serious injuries were frequent occurrences in Formula 1. This was due mainly to the attitude at the time, where many of the drivers and engineers were prepared to sacrifice safety systems in a bid to gain extra performance [2].

Currently, the FIA dictate stringent safety tests to ensure participating cars are capable of absorbing high-energy loading conditions in such a way that the drivers escape serious injury. The frontal impact crash test is the focus of this thesis; however, there are a further 15 crash tests (including static loading tests) that the vehicle must pass before it can be used for racing [3]. In a bid to increase performance, whilst maintaining safety, engineers have adopted computational software and performed numerous crashworthiness and material examinations in order to maximise the component performance; these methods will be discussed in later sections.

In the early years of Formula 1, the materials used for the chassis were wood and steel as the vehicles of the day were built to a budget using simplistic techniques suitable for 'home build' constructions. Later, Formula 1 cars made use of aluminium tubular frames surrounded by body panels, also made from aluminium, in an effort to reduce mass whilst maintaining strength. These Formula 1 structures displayed plastic collapse and folding mechanisms when subjected to impact loading conditions [4]. Whilst this approach was effective in absorbing crash energy, the vehicle would tend to crumple during an impact and potentially trap the driver.

Prior to the 1980's, composite materials were studied primarily by aerospace engineers who wished to exploit their superior mechanical performance and weight saving advantages. The first Formula 1 car to truly embrace the benefits of composite materials was the McLaren MP4/1 in 1980 [4], as shown in Figure 2-1. The car, designed by John Bernard and built by Hercules Aerospace, brought several wins to the McLaren team over a 3 year period and heralded a new era of composite applications in Formula 1.

Figure 2-1: McLaren MP4/1, the first truly composite F1 car [5]

Many of the other teams doubted the use of such an amount of composite for the chassis as they were well known for their brittle properties [4]. These reservations were put to rest when John Watson crashed an MP4/1 during the 1981 Italian GP. The car was effectively torn to pieces as it slammed heavily into a crash barrier; however, the critical monocoque Section remained intact. Watson was seen walking away from the incident, which a few years earlier could have proven fatal [6].

From the 1980's to the present, Formula 1 racing cars have increasingly adopted composite materials in vital structural areas in a bid to reduce weight and improve performance without compromising safety. As a result, high velocity impact events, such as the one in Figure 2-2, usually occur without serious injury to the driver.

Figure 2-2: High performance yet safety conscious design in action [7]

2.1.2 BAR-Honda 006 Frontal Impact Structure

The frontal nosecone impact structure, hereafter referred to as the nosecone, must adhere to energy absorbing criteria in addition to fulfilling various performance requirements, i.e. aerodynamic and weight considerations. The primary function of the

structure is to hold the front wing and provide protection in the event of a frontal impact. This research thesis focuses on the modelling of the nosecone structure from the BAR-Honda 006 racing car, shown in Figure 2-3, during the frontal crash test.

Figure 2-3: 2004 BAR-Honda Formula 1 race car [8]

The nosecone structure is constructed from a low-mass composite-honeycomb sandwich material to maximise stiffness and energy absorption. The sandwich skin used is a high performance pre-impregnated composite material with IM9 fibres embedded in a 2035 epoxy resin system. The core is constructed from two types of honeycomb material to increase the structural rigidity of the component. The majority of the structure uses HEXCEL-1/8-5052-0.001-4.5[1] ($72kg/m^3$ density) and a small region contains HEXCEL-1/8-5052-0.002-8.1 ($129.7kg/m^3$ density). These materials will be discussed in later sections of this thesis.

The design of a Formula 1 nosecone is very similar to a square frusta. The behaviour of these structures during axial loading conditions is critical to the energy absorption and crushing strength. This has been experimentally investigated by Mamalis et al. [10]. Square frusta structures have been observed to fail in four major modes, depending on structural dimensions and material properties, shown in Figure 2-4.

---

[1] HEXCEL 1/8-5052-0.001-4.5 = Cell minimal diameter 1/8inch, Aluminium grade 5052, minimal wall thickness is 0.001inch and density of material is $4.5lb/ft^3$

Deformation confined at impact wall

Longitudinal crack progression

Centrally confined circumference crack

Large hinge progressive folding
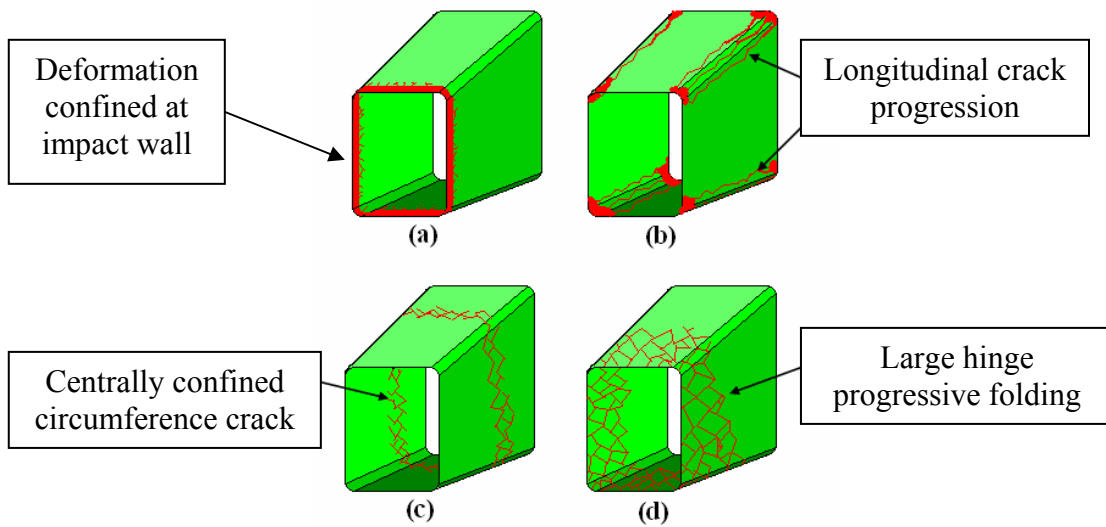
Figure 2-4: Variations in collapse modes of square frusta subjected to a frontal loading (a) Mode-1 (b) Mode-2 (c) Mode-3 and (d) Mode-4 [10]

A Formula 1 nosecone structure is designed to produce a Mode-1 failure mechanism as the structure maintains a constant crushing strength throughout the crushing process and the highest energy absorption. There are two categories for Mode-1 failure;

- Mode-1a is described as a "mushrooming" or fountain failure where the structure begins to fail by micro-cracks at the edges of the frusta and produces a split in the structure, as shown in Figure 2-5a.

- Mode-1b is when the structure folds in one direction due to micro-cracks, Figure 2-5b, and does not display the same mushrooming effect seen in Mode-1a. This effect is commonly seen in dynamic and oblique testing.
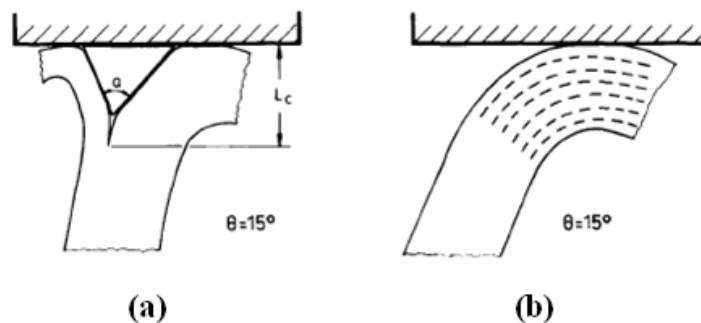
Figure 2-5: Variation in Mode-1 type failure (a) Mode-1a (b) Mode-1b [11]

The failure mechanisms of composite structures during impact loading are extensive. A variety of failure mechanisms have been characterised for differing structural geometries and materials. Sigalas et al [9] and Hull [12] discuss these mechanisms in detail for composite tubes and comment upon geometry and material composition influences on the structural performance. Hull [12] detailed the failure mechanisms occurring in a glass fibre composite tube during axial progressive crushing. The work summarised the forces acting at various locations in the progressive crush wedge and presented in Figure 2-6.
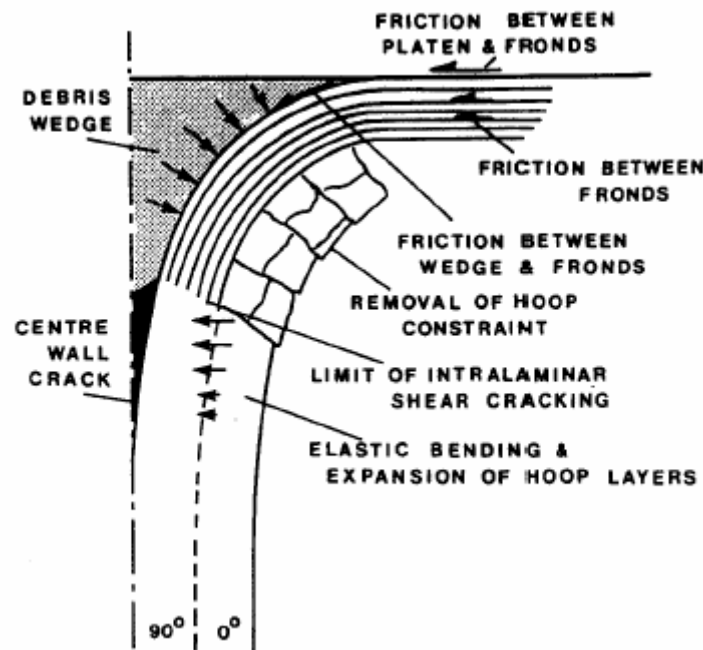
Figure 2-6: Summary of forces and failure mechanisms in the progressive crush zone [12]

By increasing the properties of the composite material to resist these forces, the crushing strength of the tube can be influenced. Warrior et al [110] investigated the influence of increasing the inter-laminar properties of the composite on the crushing strength of the tube. The investigated methods of increasing the inter-laminar properties of the composite included a toughened resin and inter-laminar stitching. The research found that the use of a toughened resin was the best method investigated to increase the crushing strength of the tube. The use of inter-laminar stitching and thermoplastic interleaves actually decrease the crushing strength due to reduction in the in-plane properties and contact frictions.

10

2.1.3 Design of a New Nosecone

The design of any new Formula 1 structure is mainly orientated toward the potential benefit in overall vehicle performance. Focusing on the development of the rear impact structure (RIMP), Savage et al. [7] detailed the concept-to-crashworthiness evaluation approach used by Honda Racing F1. The RIMP structure, like the nosecone structure, must undergo stringent crashworthiness and load bearing tests specified by the FIA before the component can be applied to the car. The nosecone structure is designed using the same process. Article 16 of the FIA Technical Regulations [3] specifies the frontal impact test for the nosecone structure; this test is summarised in Appendix A. Simplifying the design process, as seen in Figure 2-7, a series of dynamic impact tests and component refinements are required to achieve crashworthiness [7].

The use of FE methods has been investigated to improve design process [7]. Implicit FE analysis is used to analyse the quasi-static crushing strength of these components. Although this is a useful tool it is not capable of replicating the energy absorption behaviour during dynamic loading; for this an explicit FE code is necessary. An explicit FE code LS DYNA^{TM} has been used to determine the crashworthiness of composite Formula 1 impact components with accuracy by Bisagni et al. [13].
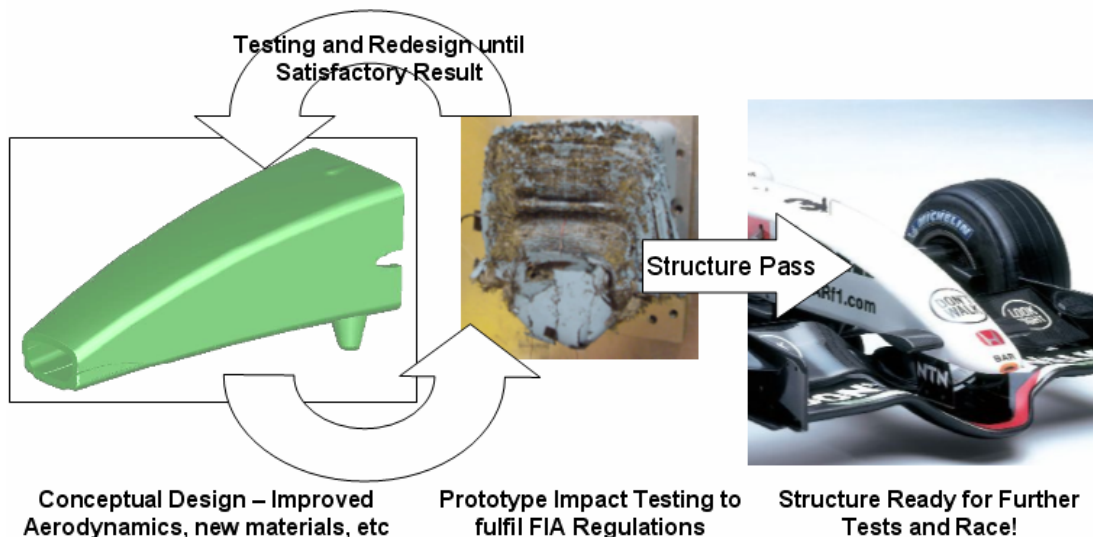
Figure 2-7: Simplified design process for a new frontal impact structure

2.2 Composite-Honeycomb Sandwich Materials

Composite-honeycomb sandwich structures are increasing being used to replace traditional materials in highly loaded applications [14] [15]. A composite sandwich structure is produced by bonding composite laminate skins to a honeycomb or foam core. The result is a stiff light-weight structure which has revolutionised motorsport structures. This Section introduces the properties and characteristics of core materials and composite laminates, focusing specifically on the materials used to construct the nosecone component of the 2004 BAR-Honda Formula 1 car. The manufacturing methods used to produce sandwich structures are presented together with the failure mechanisms and damage effects on structural properties.

2.2.1 Honeycomb Materials

Honeycomb materials are described as cellular solids [17], materials that make use of voids to decrease mass, whilst maintaining qualities of stiffness and energy absorption. As a core material for composite sandwiches, engineers are able to produce low-mass components with high stiffness properties. This improvement, at relatively little expense, in terms of mass, is of great interest in aerospace, automotive and many other applications [16].

Types of Cellular Solids

Cellular solids are divided into two groups, namely honeycombs and foams [17], examples are shown in Figure 2-8. Honeycombs are categorised as 2-dimensional cellular materials since the arrangement of the cells varies only in two directions as shown in Figure 2-8a; variations of 2-dimesional cellular geometries are shown in Figure 2-9. Foam materials, Figure 2-8b and c, are classed as 3-dimensional cellular materials, as the arrangement of the cells varies throughout the solid.
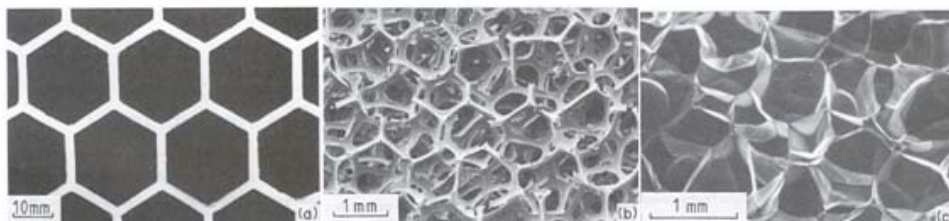
Figure 2-8: Core types (a) honeycomb (b) open-cell foam (c) closed-cell foam [17]
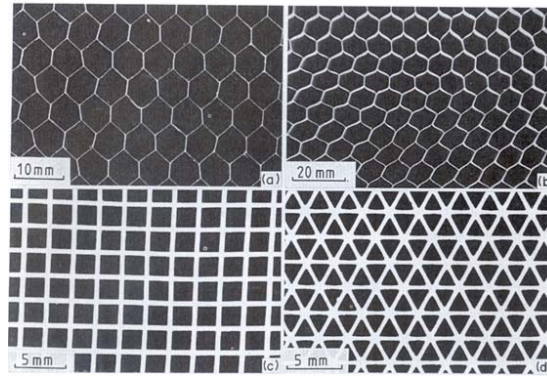
Figure 2-9: Varieties of honeycomb (a) aluminium hexagonal (b) paper-phenolic resin (Nomex) (c) ceramic square (d) ceramic triangular [17]

Macro-Scale Mechanical Properties

From a design or application prospective, the properties of honeycomb can be simplified in such a way as to assume a simple block of homogenous material with orthotropic properties. Hexagonal honeycomb materials have three axes of orthotropy and produce the stress-strain relationship shown in equation 2-1. The three principal directions, shown in Figure 2-10, are described relative to the pattern of the hexagonal geometry.

$$
\begin{Bmatrix} \varepsilon_T \\ \varepsilon_W \\ \varepsilon_L \\ \gamma_{WL} \\ \gamma_{TL} \\ \gamma_{TW} \end{Bmatrix} =
\begin{bmatrix}
1/E_T & -\upsilon_{WT}/E_W & -\upsilon_{LT}/E_L & 0 & 0 & 0 \\
-\upsilon_{TW}/E_T & 1/E_W & -\upsilon_{LW}/E_L & 0 & 0 & 0 \\
-\upsilon_{TL}/E_T & -\upsilon_{WL}/E_W & 1/E_L & 0 & 0 & 0 \\
0 & 0 & 0 & 1/G_{WL} & 0 & 0 \\
0 & 0 & 0 & 0 & 1/G_{TL} & 0 \\
0 & 0 & 0 & 0 & 0 & 1/G_{TW}
\end{bmatrix}
\begin{Bmatrix} \sigma_T \\ \sigma_W \\ \sigma_L \\ \sigma_{WL} \\ \sigma_{TL} \\ \sigma_{TW} \end{Bmatrix}
\qquad [2\text{-}1]
$$
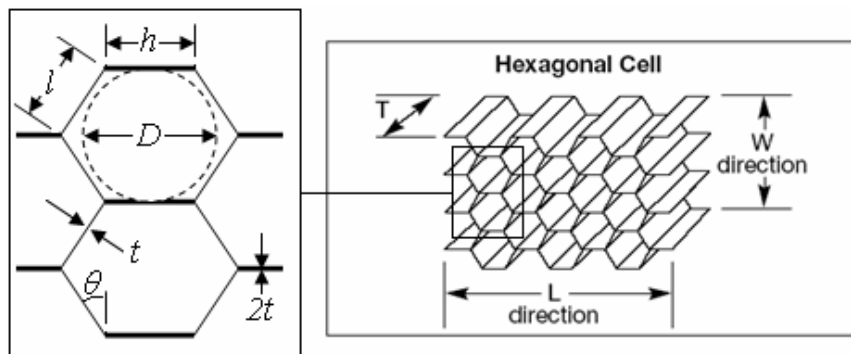
Figure 2-10: Principal directions of honeycomb material [18] and cell geometry

The properties of these materials in published literature, for example the manufacturer's datasheets from HEXCEL[TM] [18], use these directions as a reference frame. The properties in the 'W' and 'L' directions are described as in-plane properties, whilst those in the 'T' direction are out-of-plane. Experimental studies have shown that traditionally the properties in the 'T' direction are higher than those in the 'W' and 'L' directions [17]. The definitions of in-plane and out-of-plane normal and shear loading conditions are presented in Figure 2-11.
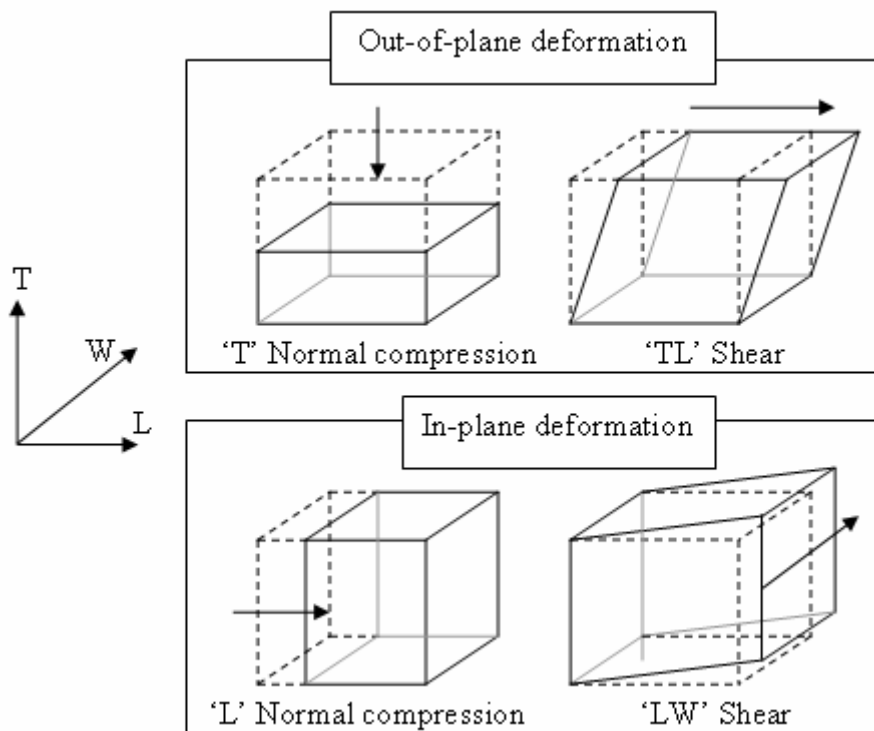
Figure 2-11: Definition of in- and out-of-plane loading

The testing methods to determine out-of-plane normal and shear properties of the honeycomb, with respect to the principal directions, have been standardised. ASTM C365-03 [19] refers to the testing method required to determine 'T' direction crushing properties. The experimental layout, shown in Figure 2-12, compresses a small sample loaded at a constant rate of 0.5mm/min and uses a mechanical displacement measuring device to determine relative displacement of the upper and lower faces. The standard also specifies the size of the test sample depending on the diameter of the hexagonal cell. For cell diameters below 6mm, the minimum sample cross-Sectional area is 2500 mm^2 whilst for diameters above 6mm, the minimum samples cross-Sectional are is 5800

mm^2. This standard does also suggest reinforcing the sample with facings to prevent localised crushing. The test in this configuration is called a stabilized compression test. Without stabilized skins, the test becomes a bare compression test.
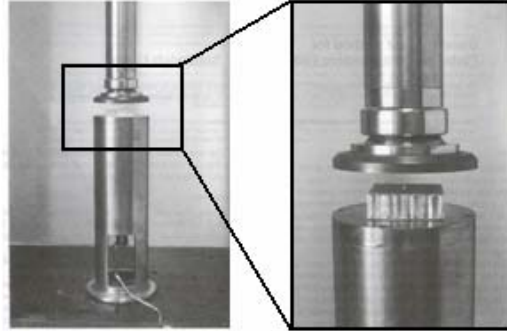
Figure 2-12: ASTM C365-03 compression testing apparatus [19]

The 'T' direction compression strength and strain for the elastic and plastic crushing domains are then established using equation 2-2;

$$\sigma = \frac{P}{A},$$
[2-2]

where σ is the crushing strength, P is the applied force and A is the cross-sectional area. When loaded in the 'T' direction, a general force-displacement trend is followed as shown in Figure 2-13. This curve has an initial linear elastic phase to a peak load at which point buckling of the cell walls is initiated; thereafter, the material crushes at a lower, approximately constant, plateau load, up to a state of full compaction when the load capacity rapidly rises.
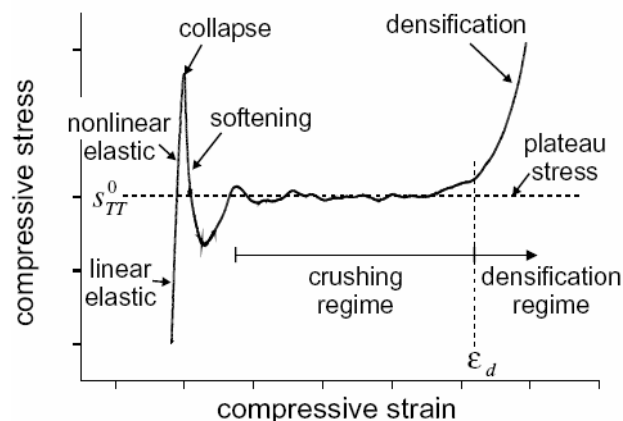
Figure 2-13: 'T' direction compressive load profile [20]

The shear properties of honeycomb are established using ASTM 273-00 [21]. There are two approaches to determine shear properties of honeycomb samples, namely, compression and tension. In each test case, the sample is bonded to the loading blocks which have the ability to move and rotate relative to each other. This creates the condition of pure shear as the thickness of the sample is allowed to change during the test. Kelsey et al. [22] have identified a number of potential difficulties with honeycomb shear testing, such as glue fillet influence on the depth of the specimen, which can influence the shear properties of the sample.

During a mixture of loading conditions, such as out-of-plane shear and compression, the properties in the principal directions have been found to vary. Mohr and Doyoyo [23] [24] [25] have investigated the effects of varying loading direction with respect to the out-of-plane shear and normal properties of honeycomb. The investigation [23] specified design modifications to the standard Arcan apparatus [26] to examine the effects of multi-directional loading on cellular solids. These improvements include:

- The circular sections must be clamped instead of pinned, Figure 2-14. This restricts the rotation of the circular sections of the apparatus, which prevents localised buckling of the honeycomb cells.
- The clamps should be fixed in such a way that they do not move laterally relative to each other.
- A method to measure the vertical and horizontal load components is necessary.
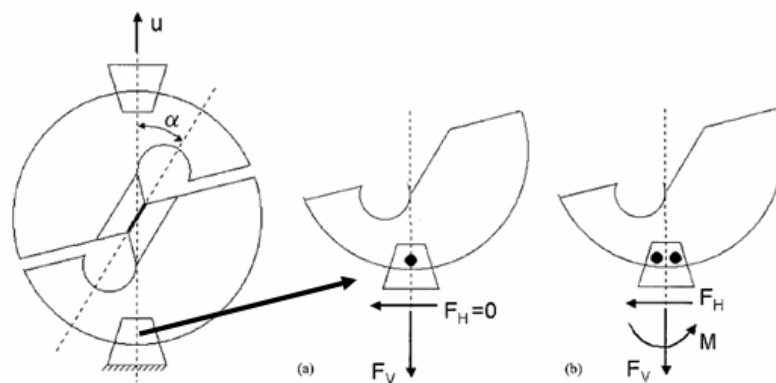
Figure 2-14: Arcan apparatus in (a) pinned and (b) clamped configuration [23]

Using these modifications, Mohr and Doyoyo [24] produced the test apparatus shown in Figure 2-15. This apparatus was used to test a single row of cells from a honeycomb

sample to observe and measure the strength and deformation in the cell walls. The out-of-plane properties in the principal directions were calculated from measured forces using equations 2-3 and 2-4 [27].
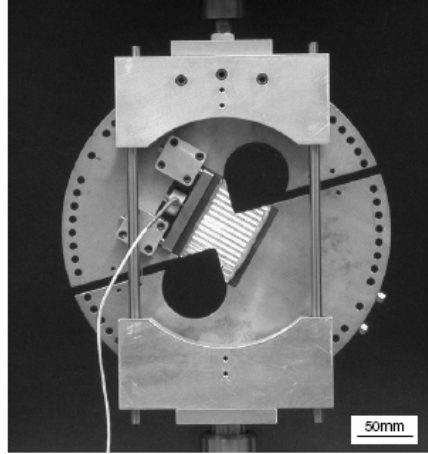
Figure 2-15: Mohr and Doyoyo modified Arcan apparatus [24]

$$\sigma_T = \frac{F_V}{A} \sin \alpha - \frac{F_H}{A} \cos \alpha \,, \qquad \text{[2-3]}$$

$$\sigma_{TW} = \frac{F_V}{A} \cos \alpha + \frac{F_H}{A} \sin \alpha \,, \qquad \text{[2-4]}$$

where, σ_T and σ_{TW} are the normal and shear stresses, F_V and F_H are the vertical and horizontal forces acting on the specimen and α is the loading direction, where pure shear is 0^0. Mohr and Doyoyo [25] also conducted a study on the effect of load direction on larger honeycomb samples; a schematic of the apparatus is shown in Figure 2-16. This apparatus was designed to produce a stiff boundary condition by clamping the sample to restrict movement and incorporated horizontal load-cells to measure horizontal forces. The investigation revealed the relationships shown in Figure 2-17 between normal and shear initial collapse and average crushing loads depending on load direction. The relationship shown in Figure 2-17 is specifically for compression in the 'T' direction with 'TW' shear loading, this configuration is referred to as 'T-TW' in later sections of this thesis.
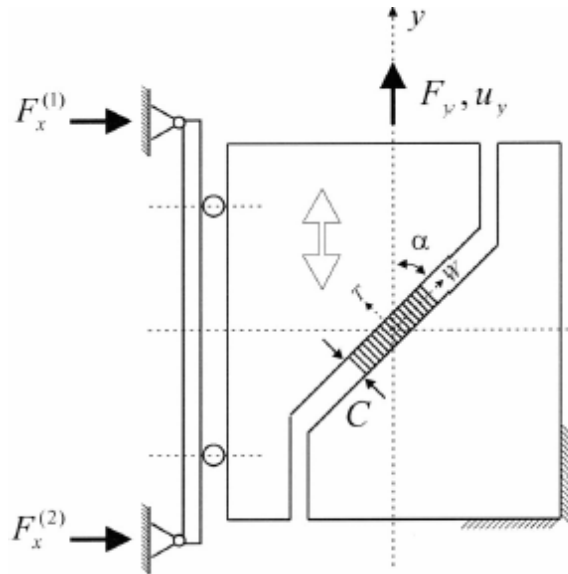
Figure 2-16: Arcan apparatus schematic for large honeycomb samples [25]
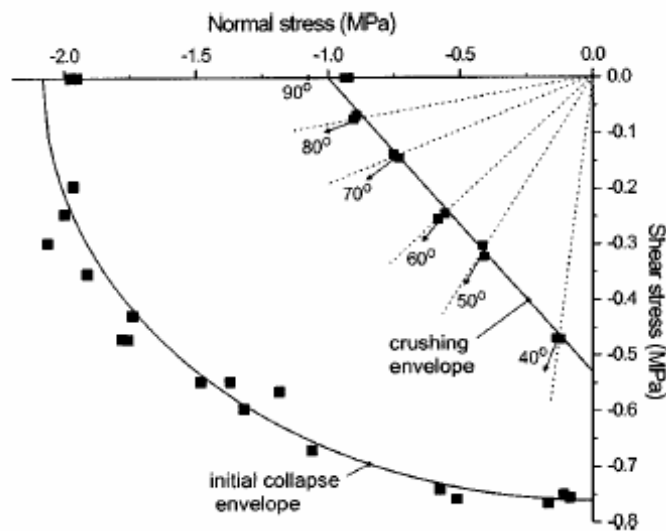
Figure 2-17: Peak and plateau loading profiles of honeycomb dependent on loading direction [25]

An alternative method to investigate combined out-of-plane shear-compression properties of honeycomb materials has been devised by Hong et al. [28]. The apparatus, shown in Figure 2-18, offers increased flexibility compared to the modified Arcan apparatus produced by Mohr and Doyoyo [25] as further non-proportional loading cases can be investigated. The extent of horizontal and vertical displacement can be customised for specific loading cases. As the method did not require an adhesive to hold the sample in place the study revealed, in greater detail, the folding mechanisms which

occur in the cell walls. Previous studies by Mohr and Doyoyo used an adhesive to hold the sample between the Arcan grips which meant the grips could not be removed without damaging the sample. In addition, the in-plane orientation angle, β, as shown in Figure 2-19 can be varied to study further in-plane shear properties. This work demonstrated the differences between out-of-plane mixed shear-compression directions. Both 'T-TW' and 'T-TL' loading configurations were examined and found shear strength in the 'TL' direction to be greater than in the 'TW' direction. The increased shear strength in the 'TL' direction is due to the double thickness walls produced during the manufacturing process.
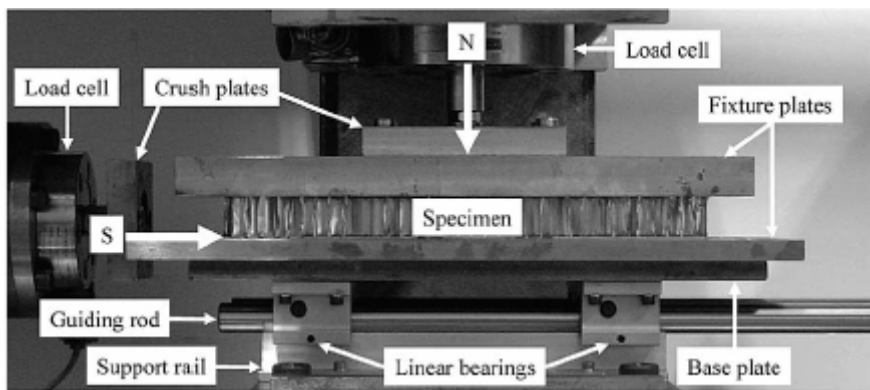
Figure 2-18: Apparatus for combined shear-compression testing by Hong et al. [28]
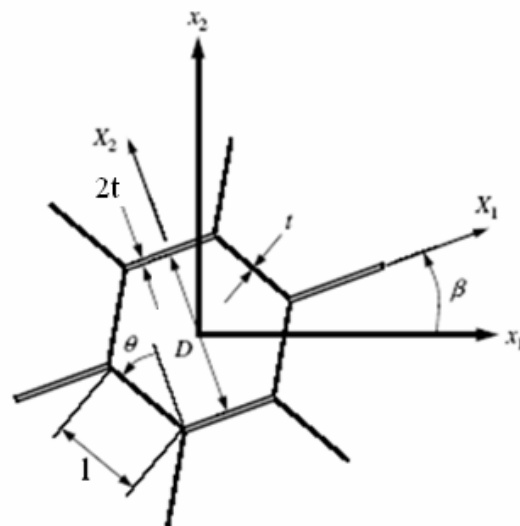
Figure 2-19: Description of in-plane orientation angle [28]

Meso-Scale Mechanical Properties

The properties described in the previous Section are a consequence of folding and collapse processes taking place in the cell walls. Numerous analytical models have been

developed to predict the overall properties of honeycomb based on the geometry of the cells and properties of the base material. In researched studies and literature, the analysis of honeycomb is often separated into two groups, the mechanics of in-plane and out-of-plane deformation.

In-Plane Properties

Ashby and Gibson [17] and Zhang and Gibson [29] have established predictive methods to determine in-plane properties. This work reduced the complexity of the honeycomb cells to a single wall and resolving the forces and moments, Figure 2-20, so that in-plane properties can be predicted.
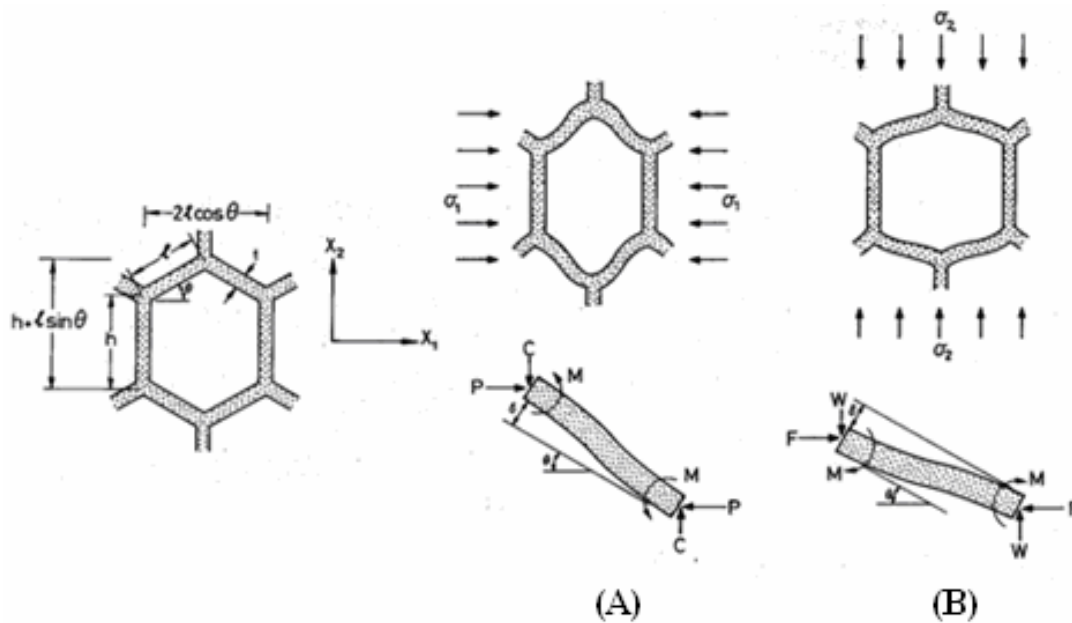
Figure 2-20: Elastic deformation, (A) 'W' compression, (B) 'L' compression [17]

From [17], the in-plane elastic modulus of honeycomb can be determined using equations 2-5 and 2-6;

$$\frac{E_W}{E_S} = \left(\frac{t}{l}\right)^3 \frac{\cos\theta}{(h/l + \sin\theta)\sin^2\theta}, \qquad [2\text{-}5]$$

$$\frac{E_L}{E_S} = \left(\frac{t}{l}\right)^3 \frac{(h/l + \sin\theta)}{\cos^3\theta}, \qquad [2\text{-}6]$$

where θ is the internal angle of the hexagonal, t is the thickness of the cell wall, h and l the lengths of the cell wall and are shown in Figure 2-10 and Figure 2-20. When the

hexagonal shape is regular, when h=l and $\theta=30^0$ shown in Figure 2-10, equations 2-5 and 2-6 become identical and produce equation 2-7;

$$\frac{E_L}{E_S} = \frac{E_W}{E_S} = 2.3\left(\frac{t}{l}\right)^3$$ [2-7]

This equation states that a regular hexagon honeycomb arrangement will produce an identical elastic modulus in both in-plane directions. The in-plane plastic collapse strength, $(\sigma_{PL})_L$ & $(\sigma_{PL})_W$, can also be shown to be identical in both in-plane directions for a regular hexagonal cell and reduces to produce equation 2-8:

$$\left(\sigma_{PL}\right)_L = (\sigma_{PL})_W = \frac{1}{4}\left(\frac{t}{l}\right)^2 \frac{\sigma_{YS}}{(\cos\theta)},$$ [2-8]

where σ_{ys} is the tensile yield stress of the base material. These equations were shown to produce a good agreement with experimental studies on rubber honeycomb samples. These equations produce an indication of bulk properties which are not dependent on sample dimensions. Onck et al. [45] investigated size effect on in-plane properties and developed relationships linking the ratio between cell size and sample width with in-plane compression and shear properties. The parameter ζ was introduced as a ratio between the sample width, L, and cell diameter, d, and indicates the number of cells along the width of the sample. An example of the variation in compression properties is shown in Figure 2-21 and was later compared with experimental research using foam materials [100], shown in Figure 2-22, which showed the estimated trends to be applicable to alternative foam materials.
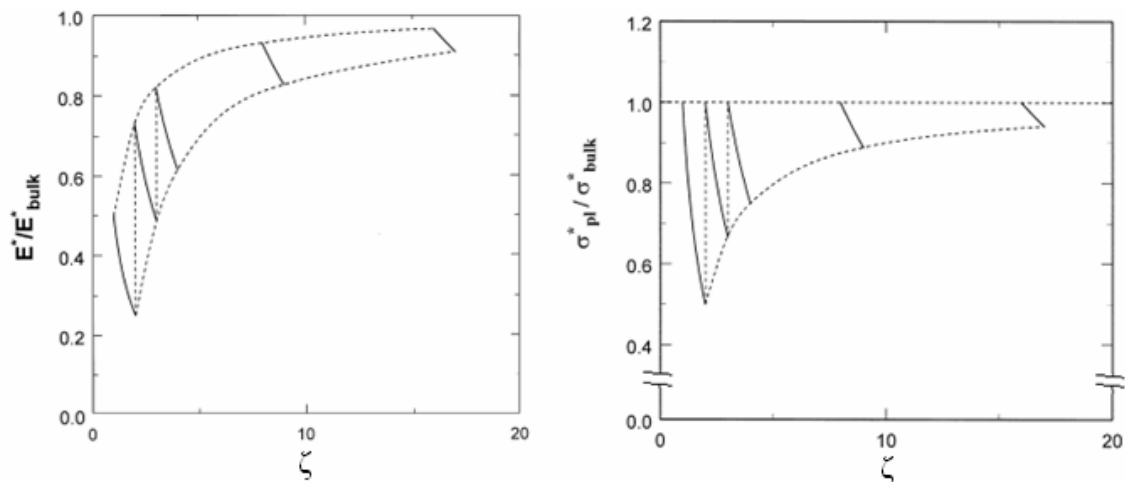
Figure 2-21: Example of the variation between in-plane compression properties depending on sample size [45]
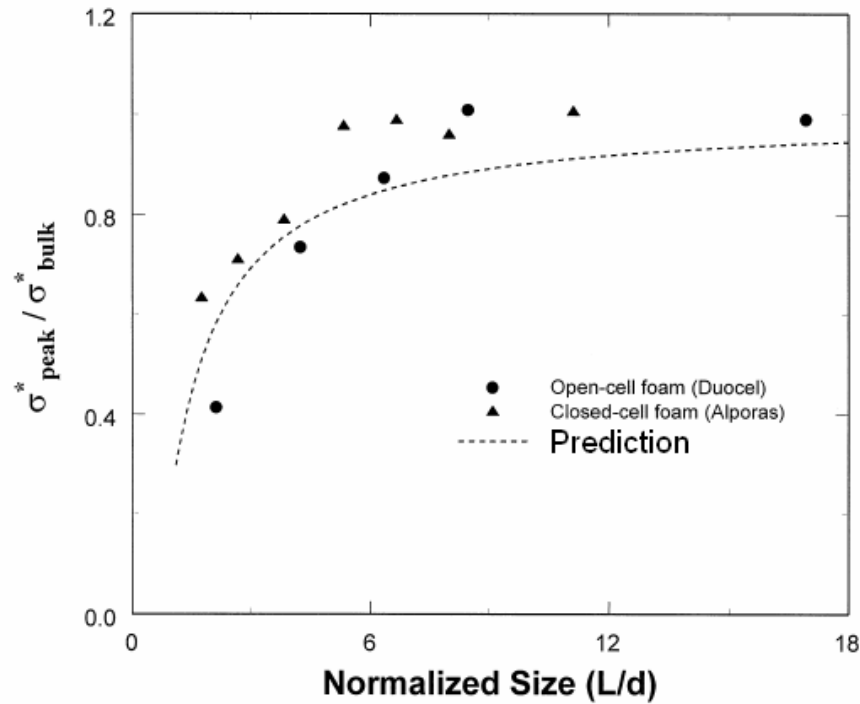
Figure 2-22: Comparison between theoretical size dependency influence on peak crushing strength and foam compression results [100]

Out-of-Plane Properties

The mechanics of deformation in the 'T' direction are based on the mechanics of folding walls. Figure 2-23 shows the regular folding pattern of a honeycomb cell under out-of-plane loading.
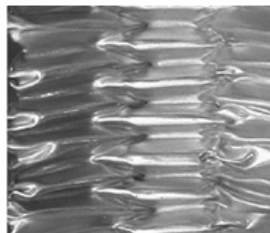
Figure 2-23: Deformed honeycomb due to out-of-plane compression loading [30]

Early research studies to determine the folding and energy absorbing mechanisms similar to those in honeycomb cells were confined to thin-walled cylinders; one such example was conducted by Alexander [31], producing the model shown in Figure 2-24. The Alexander model [31] mathematically describes the crushing process for cylindrical

22

structures; however, it did contain unrealistic assumptions concerning the folding profile and under-predicts the crushing strength of the structure.
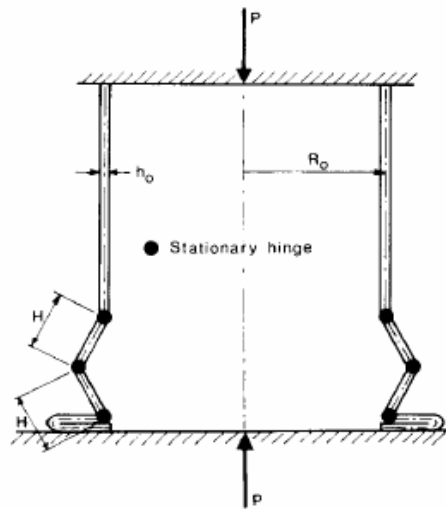
Figure 2-24: Alexander's model: Folding of thin walls in a cylinder [31]

In a later work, McFarland [32] presented a predictive method to determine the crushing strength in the out-of-plane direction based on a hexagonal cell structure. McFarland idealised the crushing mode to determine the mechanisms of collapse. The collapse profile, as shown in Figure 2-25, was used to relate the energy involved in the bending deformation to the mean crushing strength. This mechanism was simplified to introduce the effect of in-plane shearing during the 'T' direction crushing process.
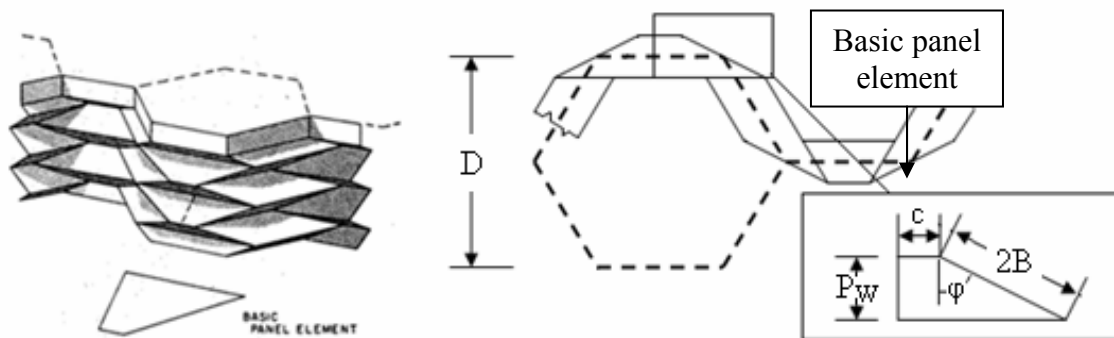
Figure 2-25: McFarland model: 'T' direction crushing mechanism [32]

Wierzbicki [33] also developed a method of determining the axial crushing of honeycomb cells. The model was further developed by including an analysis of the bond and thickness change between cells. Wierzbicki introduced an improved folding mechanism to the cell walls and comments on the effect of shear at the interface

between the cell walls. The research concluded that delamination must occur between adjacent cells for the folding mechanism to continue and proposed equation 2-9 to determine the plateau stress for a honeycomb;

$$\sigma_{P(T)} = 6.6\sigma_{YS}\left(\frac{t}{l}\right)^{\frac{5}{3}},$$
[2-9]

where σ_{YS} is the yield strength of the base material. In the same paper Wierzbicki also derived an equation to calculate the average fold wavelength λ, where $\lambda = 2H$ in Figure 2-24;

$$\lambda = 1.642\sqrt[3]{th^2}.$$
[2-10]

Out-of-plane shear, defined as 'TW' and 'TL', can also be predicted using the geometry of the cell and base material properties. The difficulty with predicting shear in this direction is that each surface cannot deform uniformly due to constraints imposed by surrounding cells. Kelsey et al. [22] provided two simple formulae to determine how shear stresses would distribute among the cell walls. Two methods were considered; a unit load method and a unit displacement method. The 'unit load' method considers the individual flexibilities of each of the cell walls in a unit area, Figure 2-26, and focuses on the shear stresses at four of the cell walls, where q is the shear flow in each wall, suffices a, b, c and d identify each wall, β is the direction of loading and τ is the shear stress. The 'unit displacement' method focuses on strains in the structure to determine the force required to deform the structure.
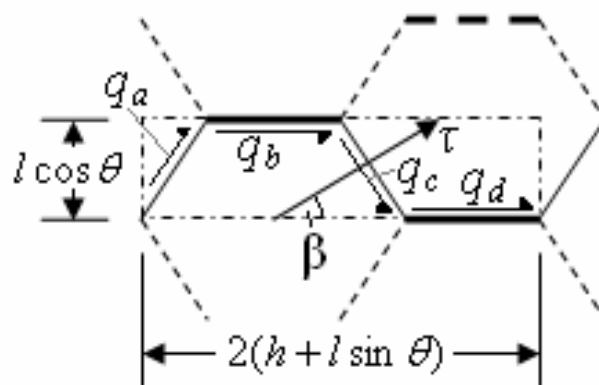
Figure 2-26: Shear flows in cell walls when honeycomb sample subjected to out-of-plane shear stresses [22]

Assuming regular hexagonal cells, the two methods produce the equations;

$$\frac{G_F}{G_S}\frac{\rho_S}{\rho} = \frac{9}{8\left(2+\sin^2\beta\right)},$$ [2-11]

$$\frac{G_D}{G_S}\frac{\rho_S}{\rho} = \frac{15}{8\left(3+2\sin^2\beta\right)},$$ [2-12]

where suffices F and D are the load and displacement methods respectively and the suffix S represents the base material. When $\beta = 0^0$ the calculated shear is in the 'TL' direction; at $\beta = 90^0$ the calculated shear is in the 'TW' direction.

Gibson and Ashby [17] also comment on the calculation of out-of-plane shear modulus. The theorems presented in [17] specify upper and lower bounds for shear modulus. The lower boundary for shear in the 'TW' and 'TL' direction are;

$$\frac{G_{TW}}{G_S} \leq \frac{\cos\theta}{h/l+\sin\theta}\left(\frac{t}{l}\right),$$ [2-13]

$$\frac{G_{TL}}{G_S} \leq \frac{1}{2}\frac{h/l+2\sin^2\theta}{\left(h/l+\sin\theta\right)\cos\theta}\left(\frac{t}{l}\right),$$ [2-14]

The upper boundaries are;

$$\frac{G_{TW}}{G_S} \geq \frac{\cos\theta}{\left(h/l+\sin\theta\right)}\left(\frac{t}{l}\right),$$ [2-15]

$$\frac{G_{TL}}{G_S} \geq \frac{h/l+\sin\theta}{\left(1+2h/l\right)\cos\theta}\left(\frac{t}{l}\right),$$ [2-16]

In the case of 'TW', the equations for upper and lower out-of-plane shear boundaries, equations 2-13 and 2-15, are identical and thus the method suggests that the shear modulus can be exactly determined. Under regular hexagonal conditions, the upper and lower shear modulus boundary equations for 'TL' become identical to 'TW', producing equation 2-17;

$$\frac{G_{TL}}{G_S} = \frac{G_{TW}}{G_S} = 0.577\left(\frac{t}{l}\right)$$ [2-17]

Since equations 2-7, 2-8 and 2-17 are independent of in-plane load direction of regular hexagonal honeycombs, these materials can be considered isotropic in the 'LW' plane. However, research presented by Hong et al. [28] show that aluminium honeycombs are not isotropic in the 'LW' plane. The equations presented here are developed for honeycombs with a constant cell wall thickness. Aluminium honeycombs have double

wall thickness regions due to the manufacturing method which produces a strong in-plane direction.

2.2.2 Composite Materials

This Section presents the types and benefits of available composite materials with specific focus on those used in the nosecone structure. Most commonly associated with aerospace applications [34], Formula 1 and other motorsport groups have pushed composite material development to optimise automotive components with high stiffness to weight ratios. Many researchers consider Formula 1 to represent the peak of exploitation of these materials due to the amount and complexity of the applications [4].

Composite Material Manufacture

Producing a structure from composite materials can be achieved in different ways, for example by resin infusion of dry fabrics or the use of pre-impregnated plies to form laminates that are cured in an autoclave. Resin transfer moulding (RTM) infusion methods require a manufacturer to arrange the fabric in the desired shape using a mould and then infuse with a resin; the method is shown in Figure 2-27.
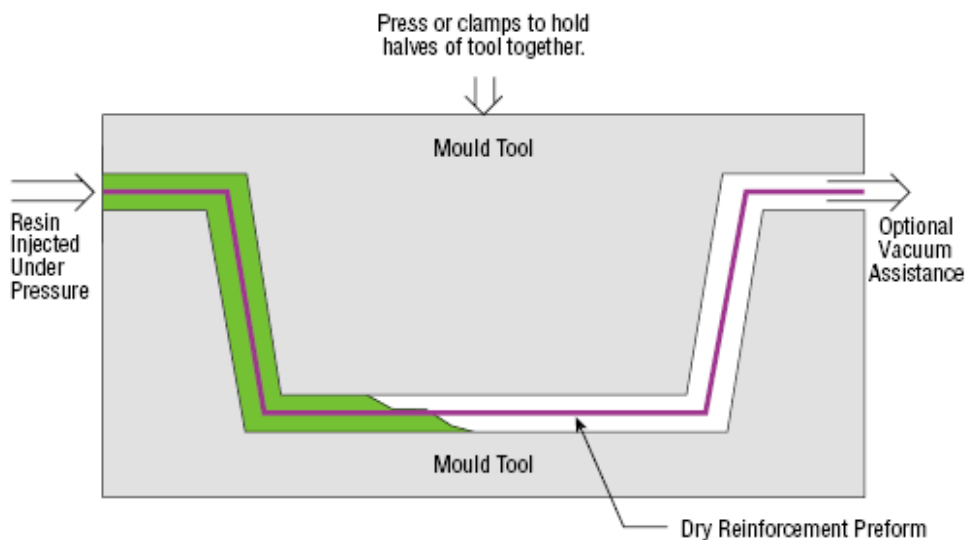
Figure 2-27: Resin transfer moulding method [35]

The benefits of RTM include the production of a safe manufacturing environment due to enclosure of the mould and increased flexibility in defining the component shape. The disadvantages include the expense of mould manufacture and control over the

component quality, such as resin voids, when compared with pre-impregnated composite components. RTM developed components are being introduced to an increasing number of aerospace and automotive applications, such as the bumper tube shown in Figure 2-28 used to absorb the energy from a frontal crash.
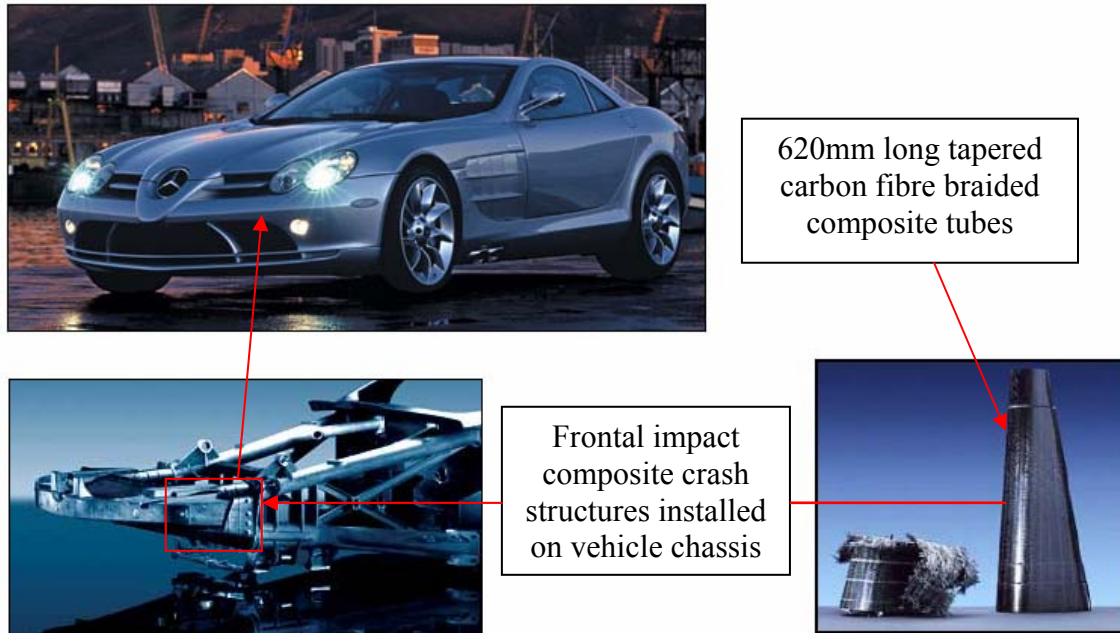
Figure 2-28: McLaren Mercedes SLR bumper tube [36]

The use of pre-impregnated composites is an alternative method to resin infusion. The material requires storage at a low temperature before use and has a limited shelf life. To produce a structural component, the material is cut to size and arranged as shown in Figure 2-29. The composite is bagged and consolidated under a vacuum; the mould is then transferred to an autoclave which subjects the composite to a high pressure/temperature cycle curing process. The method consistently produces components of a high quality with minimal voids and high fibre contents. The use of an autoclave does limit the part size and the production volume [37].
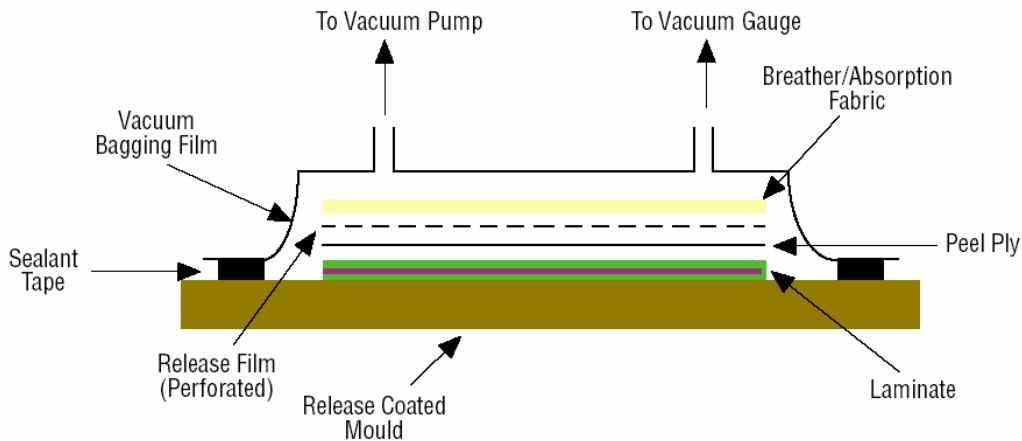
Figure 2-29: Pre-impregnated composite component manufacture [35]

The choice of fibre and resin type is of greatest importance when designing a structural component. There are three main fibre types:

- Glass: Produced by heating the ingredients of glass to around $1600^{0}C$ and then drawn through tiny holes to create thin filaments.

- Carbon: Carbon fibres are split into various categories depending on properties. Intermediate modulus (IM) and high modulus (HM) categories are often specified in product datasheets [38]. Carbon filaments are produced by controlling the graphitisation process during the production of fibres.

- Aramid: These fibres are extremely tough and have high specific tensile strength due to their low density. Aramid composites are more commonly known as Kevlar® and Twaron®. These materials are ideal for structures undergoing impact loading, such as bullet-proof vests. The material is not ideal for compressive applications and is difficult to manufacture with.

Table 2-1 compares the strength and stiffness of fibrous materials with aluminium and steel, thus highlighting the benefits of composites for low-mass applications. Hybrid fabrics, a mixture of fibre types such as aramid and carbon, can be developed to optimise properties for a specific application. Formula 1 teams with large budgets for material selection may invest in the development of hybrid fabrics to further optimise components. Alternatively, companies will be able to make selections from standardised fabrics developed by companies such as Cytec [39].

Property	Aluminium 5052 Grade	Mild Steel	Carbon/Epoxy (IM9/2020)	E-Glass/Epoxy
Ultimate Tensile Strength (MPa)	255	394	1084	1080
Tensile Modulus (GPa)	71	208	71	39
Density (g/cm^3)	2.7	7.8	2	1.58

Table 2-1: Tensile properties of composite materials compared with alloy materials [41] [42] [103]

The orientations and weave patterns of fibres in a composite component are of great importance to the laminate properties. The simplest orientation is unidirectional (UD) where all the fibres in a single ply lie in one direction; load capacity in this direction is excellent but very poor in the transverse direction. The fibres can alternatively be weaved in a regular pattern. The interlocking of fibres in a regular pattern produces a composite ply with built-in multi-axial properties. Figure 2-30 and Table 2-2 present three commonly used weave types and compare their properties.
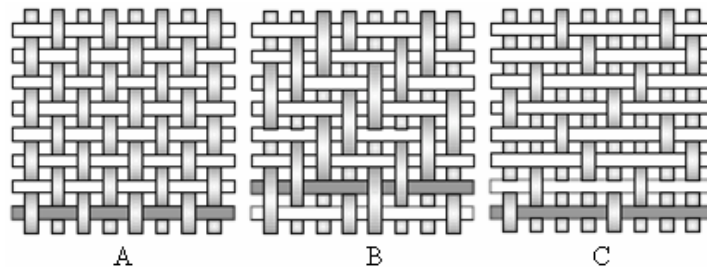
Figure 2-30: Weave types (A) plain weave, (B) twill weave and (C) satin weave [35]

From Table 2-2 it can be seen that twill weave composites possess the best all-round properties for manufacture. In the case of complex curvature sections, satin weaves might be employed, however, applying this material is often difficult due to its low stability. Since Formula 1 cars are increasingly using curved surfaces for aerodynamic purposes, it is likely that satin based weaves will be extensively used throughout the vehicle's bodywork.

Weave Type	Drapability	Stability	Balance
Plain	Poor	Good	Good
Twill	Good	Moderate	Moderate
Satin	Excellent	Poor	Poor

Table 2-2: Comparison of weave architectures [40]

For the Formula 1 nosecone the use of pre-impregnated materials is standard practice. The type of pre-impregnated composites used varies depending on team and application. In the case of the BAR-Honda 006 nosecone, the composite material uses IM9 carbon fibres arranged in a 2x2 twill weave embedded in a 2035 epoxy resin as shown in Figure 2-31.

Figure 2-31: 2x2 Twill IM9-2035 material used in the nosecone of the BAR 006

The IM9 carbon fibre has an elastic modulus of 290GPa and has a high strength in excess of 6GPa [38]. The IM9/2035 composite material used in the nosecone has a tow size of 6000 filaments and has a resin content, R_C, of 42±2%. The 2035 resin is an experimentally "super-toughened" epoxy resin jointly developed by Cytec [39] and BAR. The properties of the composite skin material are presented in Table 2-3. This shows how Formula 1 companies are actively involved in the development of new composite materials [41].

Property	Value	Property	Value
Tensile Strength	1184 MPa	In-Plane Shear Modulus	4.5 GPa
Tensile Modulus	74.4 GPa	$\pm45^0$ Poisson's Ratio	0.74
Poisson's Ratio	0.09	Flexural Strength	1348.5 MPa
Compression Strength	812 MPa	Flexural Modulus	77.9 GPa
Compression Modulus	71.7 GPa	Inter-laminar G_{IC}	792 J/m^2
In-Plane Shear Strength	151.7 MPa	Fibre Volume V_F	44%

Table 2-3: Property table of IM9/2035 composite material [41]

Failure Mechanisms of Composites and Methods of Analysis

As a composite material is loaded it will undergo damage mechanisms leading to ultimate failure. Damage mechanisms occur when fibre and/or the matrix undergo deformations that produce an irreversible effect on the loading characteristics of the material. These mechanisms can be categorised into three scales, which are the Micro-, Meso- and Macro-scale. These are described as follows:

- Micro-scale: This includes fibre fracture, matrix cracking and debonding at the fibre-matrix interface.

- Meso-scale: Failures which occur at the ply level, such as debonding between laminates.

- Macro-scale: Overall failure of the laminate.

Controlled testing is required to identify material properties and monitor the onset of damage propagation. Intra-laminar failure occurs through the thickness of the composite sample propagating through each ply, as shown Figure 2-32.
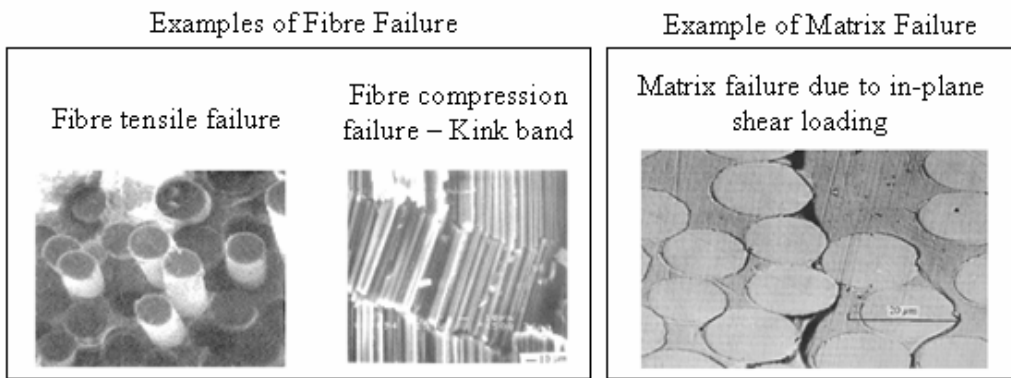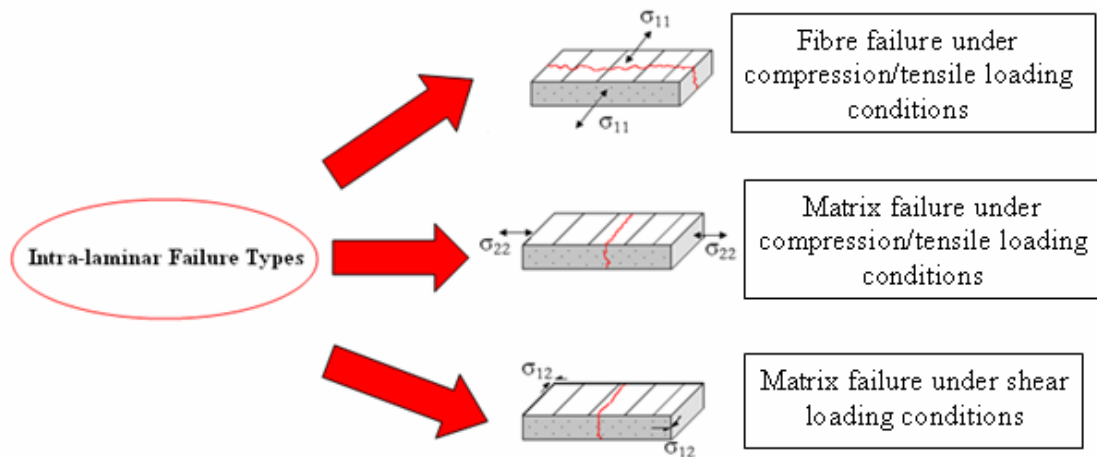
Figure 2-32: Intra-laminar failure types [42] [43]

Inter-laminar failure occurs when the plies are separated leading to eventual delamination. There are three inter-laminar delamination modes, shown in Figure 2-33. Inter-laminar failure strength is commonly characterised using the Double Cantilever Beam (DCB) test, shown in Figure 2-34, in which a composite laminate with a pre-initiated crack is pulled apart.
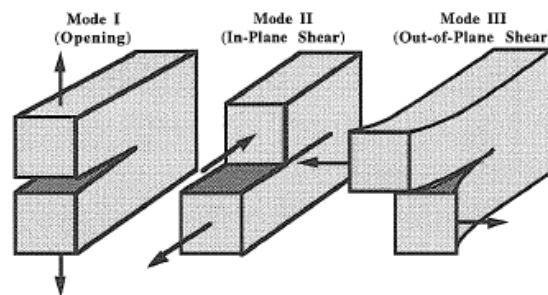
Figure 2-33: Inter-laminar failure types [44]
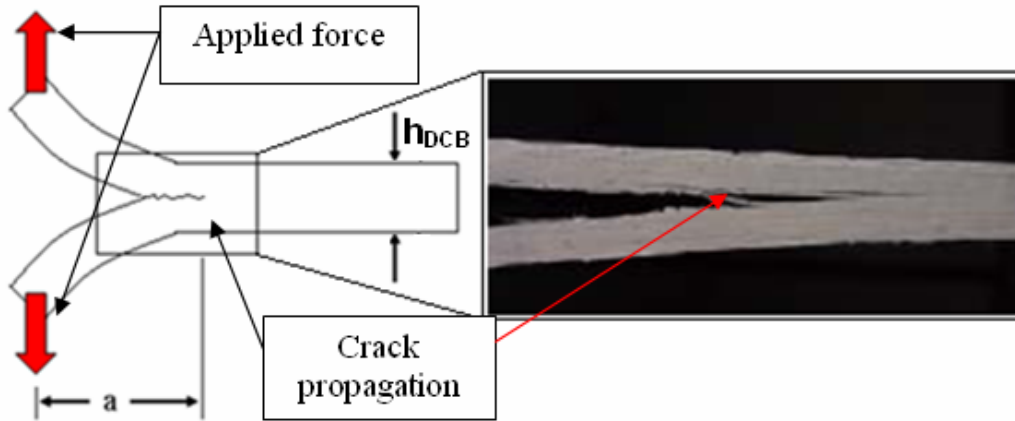
Figure 2-34: Mode-I inter-laminar delamination using DCB test [43]

The requirement of the test is to determine the strain energy release rate for Mode-I loading, G_{IC}, which is determined using equation 2-18 presented by Williams [46] and stated in ASTM D5528-01 [47].

$$G_{IC} = \frac{P^2}{2b}\frac{dC}{da},$$
[2-18]

where, P is the applied force, b is the width of the sample, C is the compliance, a is the crack length, b and h_{DCB} are the width and thickness of the sample respectively. The compliance at the crack tip can be determined using equation 2-19.

$$C(a) = \frac{\delta_I}{P},$$
[2-19]

where P is the applied force and δ_I the load point deflection. Table 2-4 presents a variety of methods to calculate G_{IC}. Equation 2-20 is the general solution produced by Williams [46].

Method	Equation	Notes	Equation
General Solution	$G_{IC} = \dfrac{3P\delta_I}{2ba}$	General solution produced by Williams [46]	2-20
Modified Beam Theory (MBT)	$G_{IC} = \dfrac{3P\delta_I}{2b(a+\lvert\chi\rvert)}$	χ is the crack length when $C^{1/3} = 0$	2-21
Compliance Calibration (CC)	$G_{IC} = \dfrac{nP\delta_I}{2ba}$	n is the slope of the curve observed when plotting log C against log a	2-22
Modified Compliance Calibration (MCC)	$G_{IC} = \dfrac{3P^2 C^{2/3}}{2A_1 bh}$	A_1 is the slope of the curve observed when plotting a/h against $C^{1/3}$	2-23

Table 2-4: Methods to determine strain energy release rate [46] [47]

A correction factor F/N can be applied to the calculated value of G_{IC} [47] to account for the large displacements and end-block corrections. The values of F and N are calculated using equations 2-24 and 2-25.

$$F = 1 - \frac{3}{10}\left(\frac{\delta}{a}\right)^2 - \frac{3}{2}\left(t\frac{\delta}{a^2}\right), \quad\quad\quad\quad [2\text{-}24]$$

$$N = 1 - \left(\frac{L'}{a}\right) - \frac{9}{8}\left[1 - \left(\frac{L'}{a}\right)^2\right]\left(t\frac{\delta}{a^2}\right) - \frac{9}{35}\left(\frac{\delta}{a}\right)^2, \quad\quad\quad\quad [2\text{-}25]$$

where L' and t describe the size of the loading block shown in Figure 2-35.
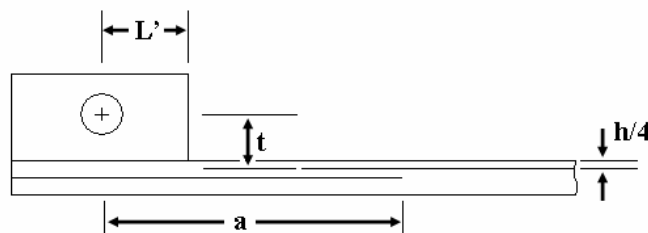
Figure 2-35: Definitions for large displacement and end corrections

In the case of the composite material used in the BAR 006 nosecone, G_{IC} has been found to be 792 J/m^2 [41] using a DCB test shown in Figure 2-36.
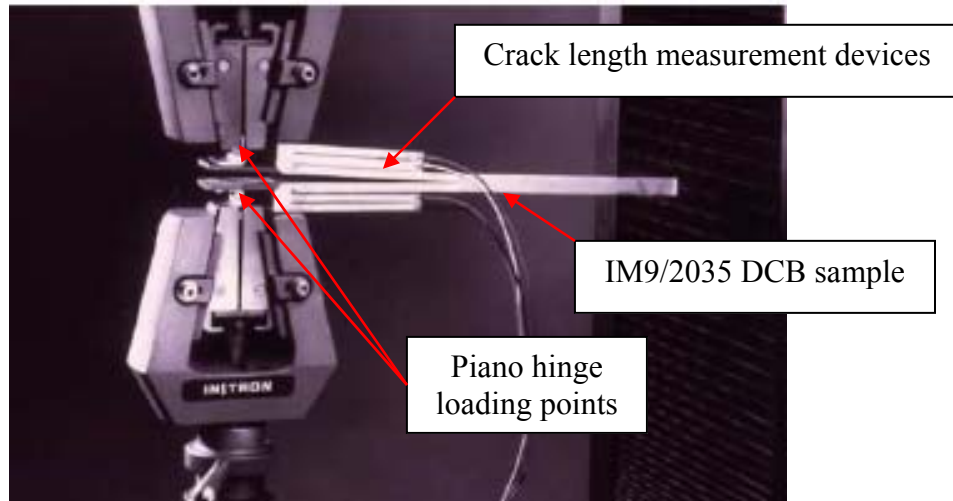
Figure 2-36: DCB test on a composite sample by Savage [41]

Theoretical Approximation of Intra-Laminar Properties

To determine the failure strengths of a composite material various failure criteria have been proposed. In practice, a composite material will contain flaws and variances throughout the structure which will influence deformation and failure of the sample. In order to simplify the ultimate strength prediction most theories have been developed to determine macro-mechanical failure; see for example the book by Daniel and Ishai [42]. Figure 2-37 shows how a selection of theories, in this case the maximum strain, maximum stress and the quadratic failure criterion, compare under loading conditions relative to the principal fibre directions. These theories commonly agree when loading is in the fibre and transverse direction but show variations when other loading directions apply.
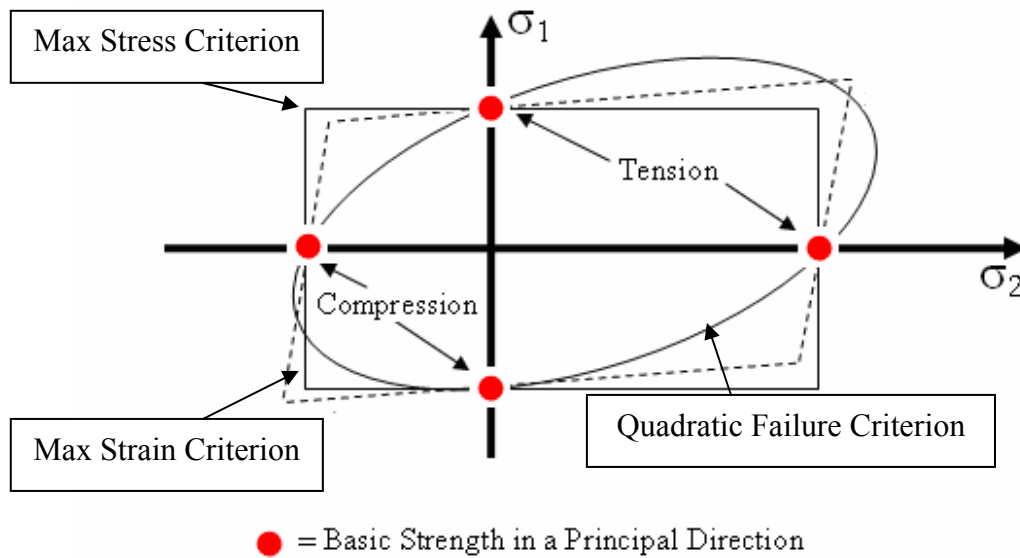
Figure 2-37: Comparison of failure prediction envelopes [42]

The number of theories available make it very difficult to determine the "best" theory, or set of theories, for a designer to use to predict failure strength for complex arrangements of composites. In an attempt to address this problem a study called the "World-Wide Failure Exercise" was conducted [48]. The study began with twelve of the leading theories being compared with experimental data, as the study progressed further theories were added. A finding from the World-Wide Exercise was that limitations were found in the theories with regards to matrix dominated loading, such as in-plane shear loading.

Ladevéze and Le Dantec [49] investigated and developed laws governing the damage properties of a composite when loaded in tension, compression and in-plane shear failure mechanisms, such as matrix cracking, fibre failure and debonding as shown in Figure 2-38 are considered in this model.
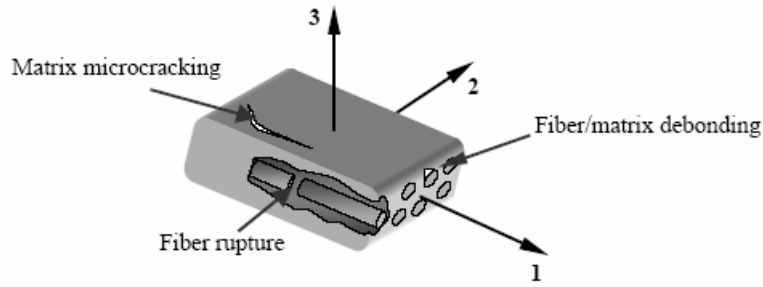
Figure 2-38: Failure mechanisms inclusive in the Ladevéze method [50]

To determine the progressive effect of damage, a cyclic loading procedure is conducted on a sample with fibres orientated at 45^0 to the load direction. Each cycle is analysed to establish the change in shear modulus and the onset of inelastic deformation through the shear loading process.
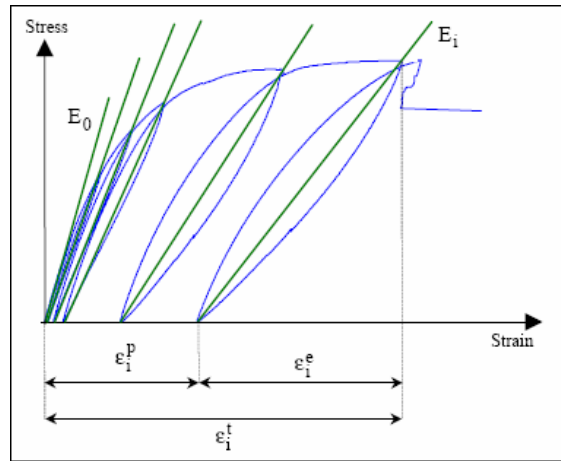
Figure 2-39: Cyclic loading effect on shear properties used to calculate damage and inelastic parameters for the Ladevéze model [50]

The damage-material strain energy is derived from a thermodynamic relationship and takes the form [49] [51];

$$E_D = \frac{1}{2} \underline{\underline{\sigma}} : \underline{\underline{\varepsilon}}^e$$

$$E_D = \frac{1}{2} \left[\frac{\sigma_{11}^2}{E_1^0} - \frac{2\upsilon_{11}^0}{E_1^0} \sigma_{11}\sigma_{22} + \frac{\langle \sigma_{22} \rangle_+^2}{E_2^0(1-d_{22})} + \frac{\langle \sigma_{22} \rangle_-^2}{E_2^0} + \frac{\sigma_{12}^2}{2G_{12}^0(1-d_{12})} \right] \quad [2\text{-}26]$$

where, d_{12} and d_{22} are shear and transverse matrix dominated damage parameters respectively, ε^e is the elastic strain and,

$$\langle\sigma\rangle_+ = \sigma \ \text{ if } \sigma \geq 0; \text{ otherwise } \langle\sigma\rangle_+ = 0$$

$$\langle\sigma\rangle_- = \sigma \ \text{ if } \sigma \leq 0; \text{ otherwise } \langle\sigma\rangle_- = 0.$$

Equation 2-26 can be rewritten with the stiffness matrix to produce equation 2-27;

$$\varepsilon^e = K^{-1}\sigma \Leftrightarrow \begin{cases} \varepsilon_{11}^e = \dfrac{\sigma_{11}}{E_1^0} - \dfrac{\upsilon_{12}}{E_1^0}\sigma_{22} \\[2mm] \varepsilon_{22}^e = \dfrac{\langle\sigma_{22}\rangle_+}{E_2^0(1-d_{22})} + \dfrac{\langle\sigma_{22}\rangle_-}{E_2^0} - \dfrac{\upsilon_{12}^0}{E_1^0}\sigma_{11} \\[2mm] \varepsilon_{12}^e = \dfrac{\sigma_{12}}{2G_{12}^0(1-d_{12})} \end{cases} \qquad [2\text{-}27]$$

The method distinguishes between compressive and tensile stresses in the transverse direction. When the transverse load, σ_{22}, is compressive, there is no degradation in strength. This is representative of a true UD composite in compressive transverse loading as micro-cracks in the composite would close. When a tensile load is applied to the transverse direction, the formation of cracks introduces a reduction in elastic properties and is accounted for in equation 2-27. It is also important to note that the method does not introduce any damage parameters when subjected to tensile loading in the fibre direction.

Damage evolution due to matrix failure is measured using Y12 and Y22. These are damage limitation properties derived from strain energy using equations 2-28 and 2-29,

$$Y_{12} = \left.\frac{\partial E_D}{\partial d_{12}}\right|_\sigma = \frac{1}{2}\frac{\sigma_{12}^2}{G_{12}^0(1-d_{12})^2}, \qquad [2\text{-}28]$$

$$Y_{22} = \left.\frac{\partial E_D}{\partial d_{22}}\right|_\sigma = \frac{1}{2}\frac{\langle\sigma_{22}\rangle_+^2}{E_{22}^0(1-d_{22})^2}. \qquad [2\text{-}29]$$

The relationship between damage limitation properties and damage is shown in equation 2-30, where the damage progression is assumed to be linear,

$$Y_{12} = Y_{12C}d_{12} + Y_{12(0)}. \qquad [2\text{-}30]$$

The method also requires derivation of a plasticity law from each cycle to evaluate matrix plasticity evolution. This is done using equation 2-31.

$$P_j = \sum_{i=1}^{i=j}\varepsilon_i^p, \qquad [2\text{-}31]$$

where P_j is the accumulated inelastic strain. ε_i^P is the inelastic strain for each cycle and is calculated using equation 2-32. A plastic hardening function $R_{(P)}$ is produced using equation 2-33.

$$\varepsilon_i^P = 2(1 - d_i)\varepsilon_{12}^p,\qquad\qquad\qquad\qquad\qquad [2\text{-}32]$$

$$R_{(P)} = \frac{\sigma_{12}^i}{1 - d_i} - R_0.\qquad\qquad\qquad\qquad\qquad [2\text{-}33]$$

These properties are then used to establish a plastic strain hardening relationship with the accumulated plastic strain, equation 2-34.

$$R_{(P)} = \Omega(P_j)^m,\qquad\qquad\qquad\qquad\qquad\qquad [2\text{-}34]$$

where the terms Ω and m are hardening coefficients determined from experimental testing. Table 2-5 summarises the tests and model parameters that are obtained from each tests. The parameter a represents a coupling factor between shear and transverse inelastic strains and b represents a coupling factor between the shear and transverse damage.

	Tensile Properties	Compressive Properties	In-Plane Shear Properties		
Experimental Fibre Angle	$[0^0]$	$[0^0]$	$[\pm 45^0]_S$	$[+45^0]$	$[\pm 67.5^0]_S$
Elastic Inputs	E_1^{0t}, υ_{12}^0	E_1^{0c}	G_{12}^0	E_2^0	
Damage Constraints	ε_{1l}^t, ε_{1u}^t, d_{1u}^t	ε_{1l}^C, ε_{1u}^C, d_{1u}^C	Y_{12C}, Y_{120}, Y_{12R}, d_{max}	Y_{22C}, Y_{220}, b	Y_{22R}, Y_{22C}, Y_{220}, b
Plastic Inputs			R_0, Ω, α	a^2	

Table 2-5: Summary of input parameters and experimental testing required for Ladevéze damage modelling [49] [51]

The Ladevéze method is used in the commercial FE package PAM-CRASH[TM] to model UD composite materials and is discussed in Section 2.3.4. Pickett and Fouinneteau [52] have successfully applied the model for braided composites with modification to the linear damage law equation 2-30.

2.2.3 Sandwich Structures

Briefly introduced in Section 2.1, the addition of a honeycomb core to composite skins produces a sandwich structure with improved flexural properties with only a minor penalty in mass. As a result sandwich structures are of great interest in the transport industry and especially aerospace. This interest has lead to the investigation of these structures subjected to various loading conditions and post-damage examination.

Benefits and Properties of Sandwich Structures

Sandwich structures consist of thin skin materials bonded to a low mass core material. A composite-honeycomb sandwich, as used for Formula 1 applications, uses composite laminates as skins bonded to a metallic honeycomb core as shown in Figure 2-40.
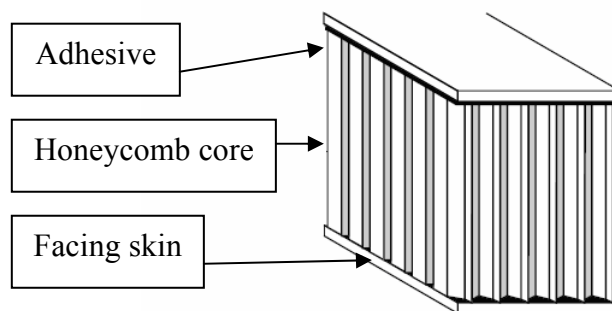
Figure 2-40: Honeycomb sandwich [53]

The addition of a core material to composite skins has a significant effect on relative flexural stiffness as shown in Table 2-6.
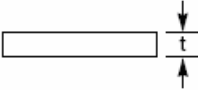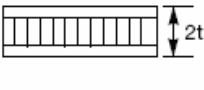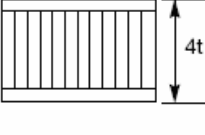
	Solid Metal Sheet	Sandwich Construction	Thicker Sandwich
	t	2t	4t
Relative Stiffness	100 %	700 % 7 times more rigid	3700 % 37 times more rigid!
Relative Strength	100 %	350 % 3.5 times as strong	925 % 9.25 times as strong!
Relative Weight	100 %	103 % 3% increase in weight	106 % 6% increase in weight

Table 2-6: Increase in flexural properties with additional core material [53]

The mechanical properties are dependent on the skin material when loaded in tension or compression in an in-plane direction. Without support, these skins would buckle and fold under compressive loading. With a supportive core, the skins are fixed relative to each other and thus buckling is prevented. In the case of bending, the structure can be likened to an I-beam as the introduction of the core increases the second moment of inertia and increases the flexural properties, as shown in Figure 2-41. This has been investigated by Styles et al [54] who found the thickness of the core to affect the flexural strength of the sandwich, more so than the number of plies in the skin. This study was conducted using a four point bending apparatus. The flexural properties can be found using ASTM C393-00 [55]. Similar research conducted by Lingaiah and Suryanarayana [56] using aluminium honeycomb and foam core specimens with a variety of skin materials. The samples with aluminium skins displayed delamination between the skin and core during three-point bend (3PB) testing as a result of a poor skin/core bonding.
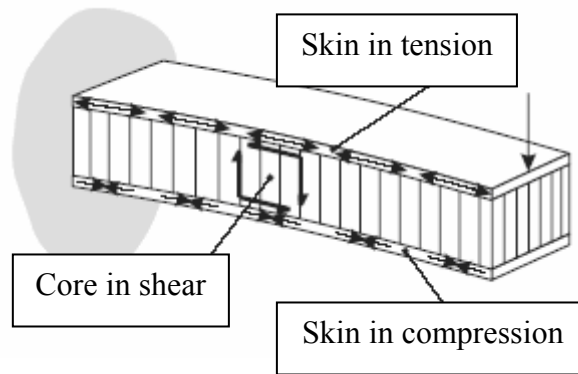
Figure 2-41: Tension, compression and shear forces in a sandwich beam [53]

The skins are bonded to the core material by use of an adhesive; this can be an adhesive film or resin fillets produced by the composite skins during the curing cycle. In a honeycomb sandwich the adhesive securely bonds the skins to the core by producing glue fillets, as shown in Figure 2-42. Foam cores tend to have a smaller cell size and produce less of a fillet effect and more of a simple glue line. The overall effect of adhesive on the properties of the foam core is very low, whereas a honeycomb core can be affected by the choice and amount of adhesive.
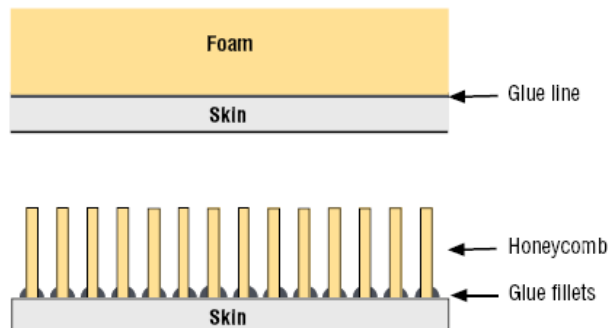
Figure 2-42: Comparison of glue-lines used in sandwich materials [35]

Research to determine the additional benefit through the choice and application of the adhesive bond has been conducted. Okada and Kortschot [57] investigated the effect on peel strength by the size of adhesive fillet. This study was conducted by varying the amount of resin in the skin panels and found an increase in G_{IC} with an increase in fillet size. A study conducted by Grove et al. [58] investigated the effects of varying the manufacturing parameters on the peel strength of composite-honeycomb sandwich. The composite skin resin content was 42% and this was considered high enough for direct

bonding without an adhesive film. The research found that varying the temperature of the cure cycle has a significant effect on properties as an increase in cure temperature increases the peel strength of the sandwich.

The properties of the adhesive bond can be investigated with a Cracked Sandwich Beam (CSB) test. This test is very similar to the DCB test described previously in Section 2.2.2 and is used to determine the strain energy release rate to debond the skin from the core using Mode-I test conditions. In this case a starter crack is produced between the core and skin material. Han et al. [59] experimentally investigated the adhesive strength of a sandwich structure, as shown in Figure 2-43, and found in this case that the failure crack propagated between the face sheet and the core. A new loading grip configuration using wire connections was used to achieve a point loading condition.
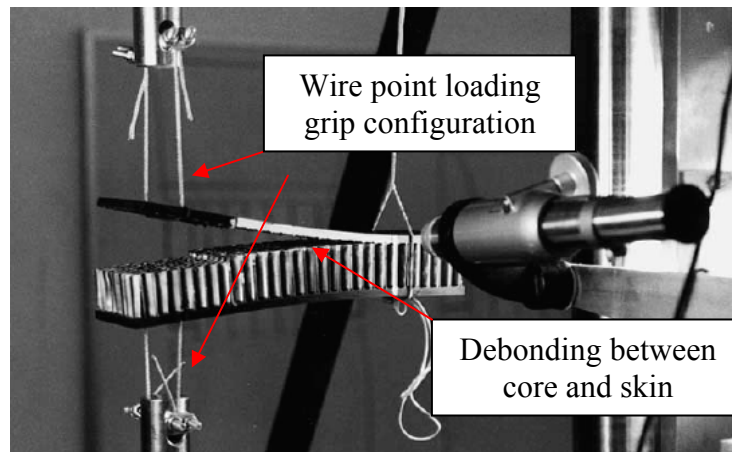
Figure 2-43: CSB test conducted by Han et al. [59]

Research conducted by Shivakumar and Smith [60] and Carlsson et al. [61] found that the crack direction can vary, as shown in Figure 2-44. Carlsson [61] studied the path of the crack propagation through a foam core to determine the factors that influence the kink angle, direction of crack through the core and stability of crack direction. A stable crack tip is defined as one that propagates at a constant location, for instance centrally or near a skin.
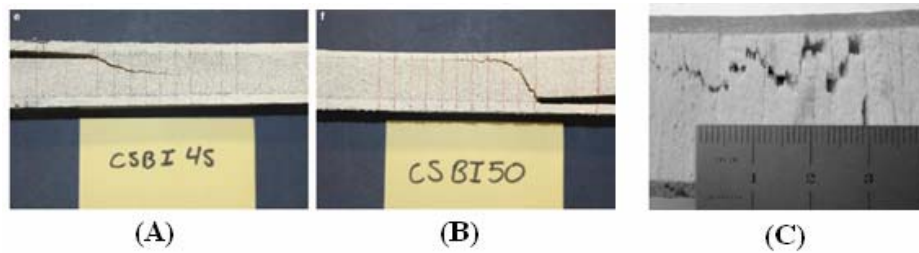
Figure 2-44: Variations in crack propagation; (A) & (B) Carlsson et al. [61] in foam cores and (C) Shivakumar and Smith [60] in Balsa wood core

Section 2.2.2 presented methods to determine strain energy release rate, G_{IC}, using the assumption that both arms in the DCB test are identical. This is not necessarily the case with the CSB where the crack can propagate at the core/skin interface. Shivakumar et al. [62] examined the current methods of determining G_{IC} using the methods presented in Table 2-4. The research found the methods to be in agreement with one another and it was recommended that the MBT method be used for CSB testing. Ural et al. [63] showed that the strain energy release rate was a function of the upper and lower beam dimensions and material properties. The researchers produced equation 2-35 to calculate strain energy release rate,

$$G_{IC} = \frac{P^2 a^2}{2b} \left[\frac{1}{E_1 I_1} + \frac{1}{E_2 I_2} \right],$$ [2-35]

where subscripts 1 and 2 are the upper skin and lower skin/core respectively. E and I are the elastic flexural modulus and second moments of inertia. The G_{IC} for sandwich structures can be approximated using CSB testing provided the crack propagation remains stable.

Manufacture of Sandwich Structures

There are three main manufacturing methods to produce a composite-honeycomb sandwich structure. These are:

- Press method in which the sandwich structure is arranged in a hot-press and formed. The method is only capable of producing a flat panel and is a single shot process where skins are cured at the same time as bonding the skins to the core.

- Match moulding method to produce curved structures. The core is pre-shaped and then the skins and core are placed between two faces of the mould and cured

in a single shot process. Some Formula 1 aerodynamic components are produced this way.

- The vacuum bagging method. A Section of honeycomb is cut oversize for the required component and the edges sanded to make a 45^0 angle; this prevents the edges from collapsing under the vacuum pressure. The sandwich is covered by pre-impregnated skins before bagging as shown in Figure 2-45. The method can be performed in a single stage. It is recommended that the lower skin be cured before the honeycomb core and upper skin in a two stage process [64].
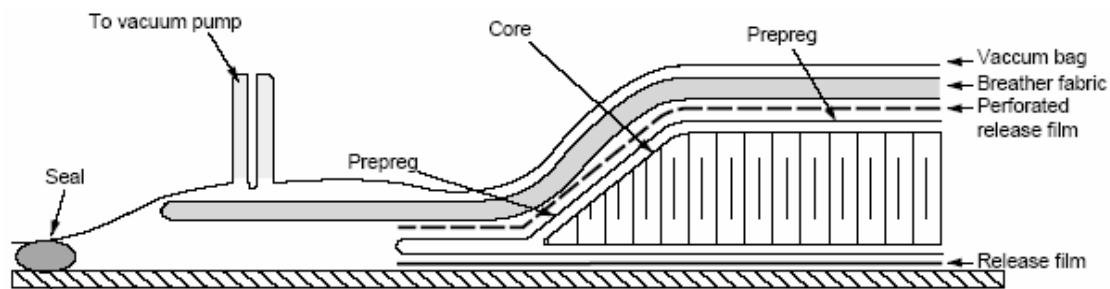
Figure 2-45: Sandwich construction using vacuum bagging method [64]

Effects of Damage on Sandwich Properties

The strength of the sandwich is a result of a combination of properties from the skin, core and interface. Any damage accumulated in one, or more, of these base materials will have an overall effect on the properties of the sandwich. It is imperative to understand how potential damage accrued in service will affect structural performance.

The most likely form of damage is obtained when the structure receives an impact on one of the skin surfaces, such as bird-strike and debris impact in aircraft applications. Experimental studies have been conducted to determine the effects of surface impacts on the in-plane properties of composite sandwiches, for example Lacy and Hwang [65], Kosza and Sayir [66] and Dear et al. [67]. These studies have investigated the damage progression in a sandwich when subjected to an impact load on the surface of the structure. The type of damage varies depending on impact energy, core material, skin material and adhesion between skin and core. The most common form of damage is shown in Figure 2-46.
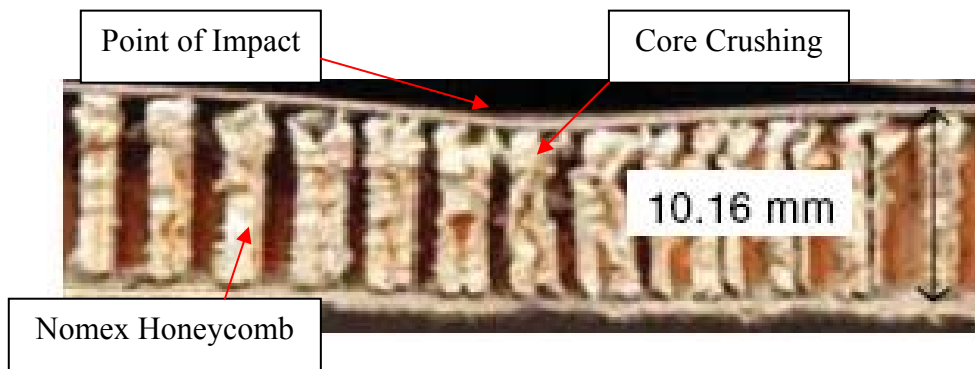
Figure 2-46: Damage in sandwich structure: indentation of laminate and partially crushed core [67]

The introduction of damage to the core and laminate in this way compromises the overall structural integrity of the sandwich. With potential debonding and localised damage to skin and/or core, the structure may no longer be able to perform to designed requirements.

Schubel et al. [68] investigated the effects of loading a PVC core structure with woven carbon skins. A selection of sandwich materials was subjected to a drop tower test before the sandwich underwent edgewise compression loading. The post-impact damage included indentation to the composite skin and delamination between the skin and core. The results from this research, presented in Figure 2-47, show the effects in facesheet compressive properties due to impact loading. Mouritz and Thomson [69] examined the edgewise compression and flexural strength of a foam core sandwich after low and high-energy impact damage. The study showed the peak compressive and shear strengths were influenced by interfacial cracks which were manufactured into test samples using Teflon® film between the skin and core. Bending strength was not influenced by the presence of interfacial cracks; however failure strain is reduced. The research also presented the influence of impact damage on structural properties. Flexural strength can be reduced by as much as 75% by a low energy impact depending on location of impact.
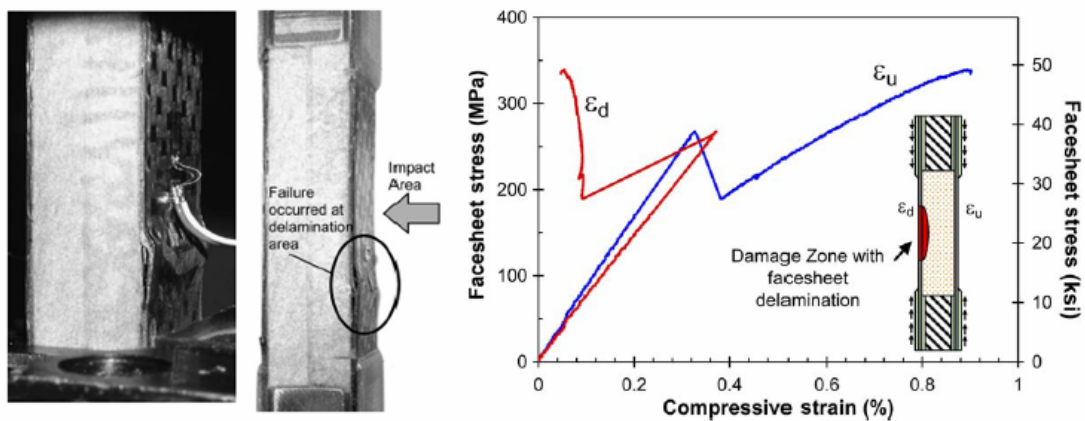
Figure 2-47: Pre-damaged sandwich study by Schubel et al. [68]

2.3   Finite Element Analysis

Finite Element (FE) analysis is a mathematical technique to acquire approximate solutions to physical systems subjected to a number of loading conditions [70]. The FE method breaks a problem into finite elements, where material laws and/or loads/boundary conditions can be applied. This is effective when dealing with complex structures undergoing multiple loading conditions.

There are two FE methods, namely implicit and explicit, which use different calculation methods to model deformation to the model mesh. Implicit FE is considered 'unconditionally stable' as the time step is independent of the properties of the model, such as mesh dimensions and stiffness, and is usually ideal for quasi-static and low loading rate modelling. Explicit methods are superior for highly non-linear events, such as impact modelling since the time-step is small enough to follow to phenomena. In general, dynamic non-linear events are best simulated using explicit codes, whereas quasi-static events are best simulated using implicit codes. The explicit calculation method is presented in Appendix B, the implicit method can be found in the PAM-CRASH^{TM} theory manual [71].

The FE code used during this research is the commercially available explicit code PAM-CRASH^{TM}. This Section presents the methods investigated to represent honeycomb, composite and sandwich structures using FE methods.

2.3.1 FE in Automotive Applications

In the last 20 years, automotive companies have made extensive use of FE methods to develop new vehicles. The use of these programs in the development of new vehicles has allowed engineers to produce safer vehicles whilst improving performance; one example is shown in Figure 2-48. FE companies and research bodies have been involved in the development of further material models to provide the necessary tools for future analysis of structures made from novel materials, such as composites and foams cored structures.

Figure 2-48: FE analysis of offset frontal impact [72]

2.3.2 Honeycomb Modelling

The development of constitutive material models for honeycomb materials is complicated due to the highly anisotropic properties of the material. This Section reviews different works that have attempted to model honeycomb materials using FE methods.

Solid Element Modelling using Macro-Scale Approximations

Macro-scale modelling of honeycomb material generally uses a three dimensional solid element shown in Figure 2-49. The principal directions of the honeycomb must be applied to the solid element and properties in each of these directions are specified for the constitutive law.
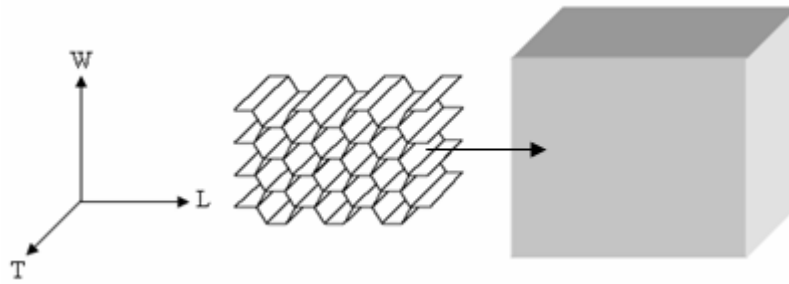
Figure 2-49: Solid block approximation of honeycomb

The most common approach to modelling honeycomb is to model the mechanical behaviour of the overall material, assuming the material as homogenous, and neglect the folding mechanisms of individual walls, such methods are referred to as phenomenological approach [73] [74]. Alternative methods of constitutive modelling have been considered using folding wall mechanisms such as [30] and [74]. Modern commercial FE codes, such as PAM-CRASH[TM] [50] and LS-DYNA[TM] [75], use phenomenological methods as they are more robust and easier to program.

The commercial FE code PAM-CRASH[TM] uses an orthotropic material model, MAT41, which assigns properties to three principal directions. The material model follows a standard stress-strain curve for compressing honeycomb materials in each of the principal directions, shown in Figure 2-50. In this figure, σ_{yT} is the yield stress, ε_{yT} is the yield strain, ε_C is the compaction strain, E_{0T} is the elastic modulus, E_{1T} is the first tangent plateau crushing modulus and E_{2T} is the compaction modulus.
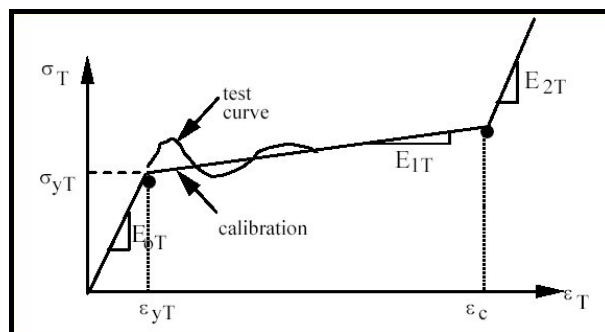
Figure 2-50: PAM-CRASH[TM] Approximation of 'T' direction compression [50]

The code replicates this curve by considering each phase of the compression process as a separate stage. The elastic region is calculated using equation 2-36; the crushing phase

49

is calculated using equation 2-37 and the eventual densification by equation 2-38. The code determines which phase the structure is undergoing by comparing the compression strain with the following requirements;

$$\sigma_i = E_{0i}\varepsilon_i; \text{ when } \varepsilon_i < \varepsilon_{yi}, \qquad\qquad [2\text{-}36]$$

$$\sigma_i = E_{0i}\varepsilon_{yi} + E_{1i}(\varepsilon_i - \varepsilon_{yi}); \text{ when } \varepsilon_{yi} \leq \varepsilon_i < \varepsilon_c, \qquad\qquad [2\text{-}37]$$

$$\sigma_i = E_{0i}\varepsilon_{yi} + E_{1i}(\varepsilon_c - \varepsilon_{yi}) + E_{2i}(\varepsilon_i - \varepsilon_c); \text{ when } \varepsilon_i \geq \varepsilon_c, \qquad\qquad [2\text{-}38]$$

where i is the principal direction, ε_i is the current strain of the element, ε_{yi} is the yield strain and ε_c is the compaction strain. Strain is calculated using;

$$\varepsilon = \ln\left(\frac{t}{t_0}\right), \qquad\qquad [2\text{-}39]$$

where t_0 is the original thickness and t is the new thickness after deformation. Also, E_{0i}, E_{1i} and E_{2i} are the modulus of loading in the elastic, crushing plateau and densification phases respectively. As discussed in Section 2.2.1, the properties in the principal directions are varied when a mixture of loading conditions are applied. Equations [2-36], [2-37] and [2-38] do not include any shear or transverse deformation terms and thus neglects any variance in principal direction properties due to mixed loading conditions. This is shown in Figure 2-51 where a mixture of out-of-plane shear and compression loadings, similar to that of the Arcan test, are applied to a solid element with the MAT41 material model. The shear and compression strength does not vary depending on the direction of loading. This is inaccurate when compared with the findings from Mohr and Doyoyo [25] shown in Figure 2-17.
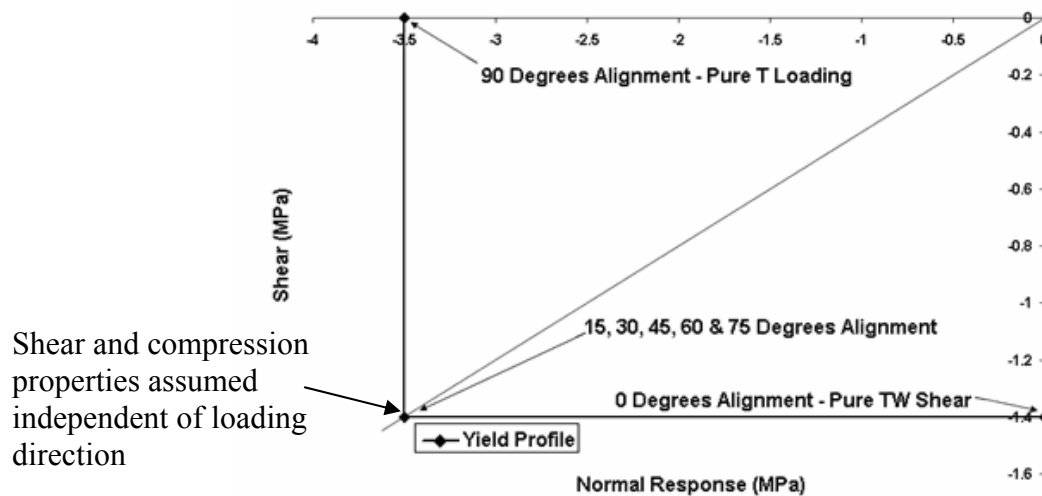
Figure 2-51: Standard response from macro-solid honeycomb model in commercial FE package to mixed shear-compression loading

Shell Based Modelling Methods using Meso-Scale Approximation

An alternative approach to model honeycomb materials is by use of detailed shell models of the cell walls. This method can be described as a meso-scale approximation as this form of modelling considers deformation at the individual cell wall scale. The benefit of this method is that the direction dependent energy absorbing behaviour of honeycomb, presented in Section 2.2.1, can be represented without the need for complex constitutive material codes. This method has been studied to investigate theories concerning the deformation of cellular cells. Mohr and Doyoyo [74] implemented a shell based modelling method to simulate the deformation in a single foil of honeycomb shown in Figure 2-52 and found the folding mechanisms during experimental mixed shear-compression loading to be accurately reproduced by the model.

This method can be applied to investigate variations in cellular geometries and complex loading conditions. Yamashita and Gotoh [76] applied the meso-modelling method to study the effects of varied wall angle on the structural response to dynamic loading. The method was used by Papka and Kyriakides [77] [78] to examine the biaxial properties of honeycomb and found the model to recreate experimental findings in terms of folding mechanisms and in-plane crushing strengths. Novel cell geometries have also been investigated this way, such as chiral honeycomb by Scarpa et al. [79] shown in Figure 2-53. These investigations have also shown that FE methods can accurately represent the crushing strength and deformation of novel core materials.
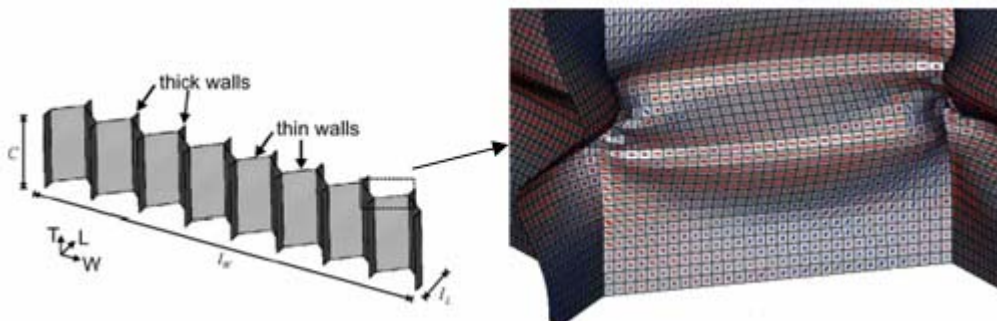
Figure 2-52: Mohr and Doyoyo model of honeycomb cell walls [74]
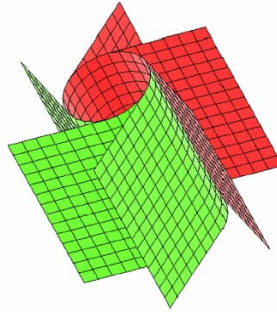
Figure 2-53: Chiral honeycomb modelling method used by Scarpa et al. [79].

2.3.3 Composite Modelling

As discussed previously in Section 2.2.2, the energy absorption and failure mechanisms of composite materials are complex in comparison to isotropic materials. Studies have been conducted in order to determine the failure criteria for a particular loading case and then applied these to an FE code. This is often difficult as there are many different modes of failure; often researchers will focus on only one particular type of failure criteria, such a shear damage or inter-laminar ply delamination.

Fibre/Resin and Tow/Resin Modelling of Composite Materials

The modelling of composite materials can be conducted at different scales. Modelling the composite at the tow/resin scale is referred to as meso-scale modelling, whilst the modelling at the filament level is referred to as micro-scale modelling. Examples of meso-modelling can be reviewed through the work of Tang et al. [80] [81], D'Amato [82] and Woo and Whitcomb [83]. These studies also investigated the effect of fibre geometry, for instance waviness and tow path, shown in Figure 2-54 and Figure 2-55. These investigations show how FE methods can be used to analyse the deformations and stress concentrations at the fibre level and potentially optimise a composite material prior to development.
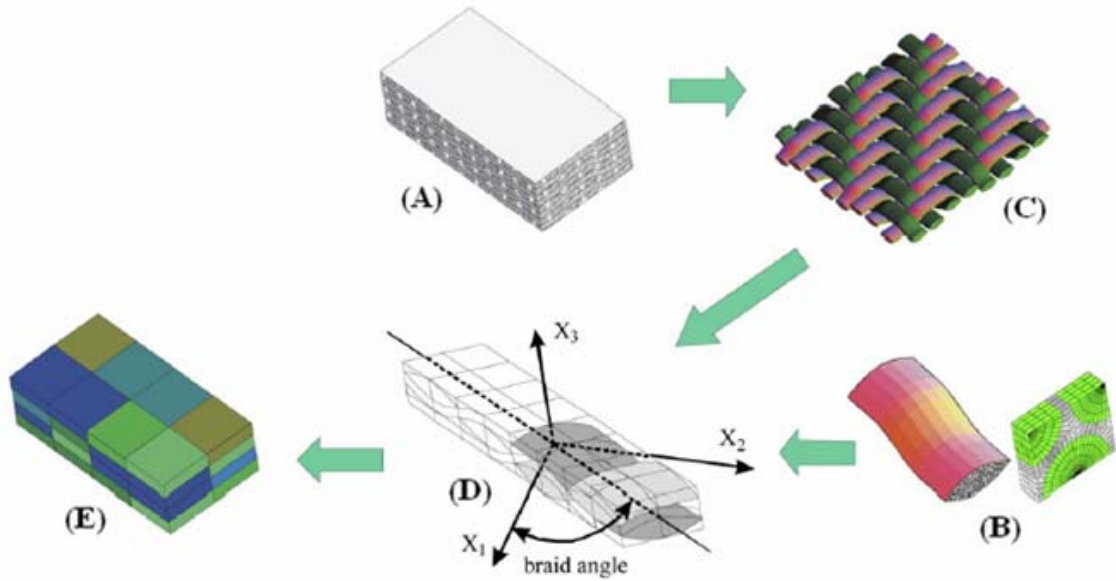
Figure 2-54: Micro-mechanical modelling of textile composites [80]. (A) Textile laminate, (B) Individual tow/matrix, (C) Textile mat, (D) Architecture at unit cell level (RVE), (E) Model at laminate level
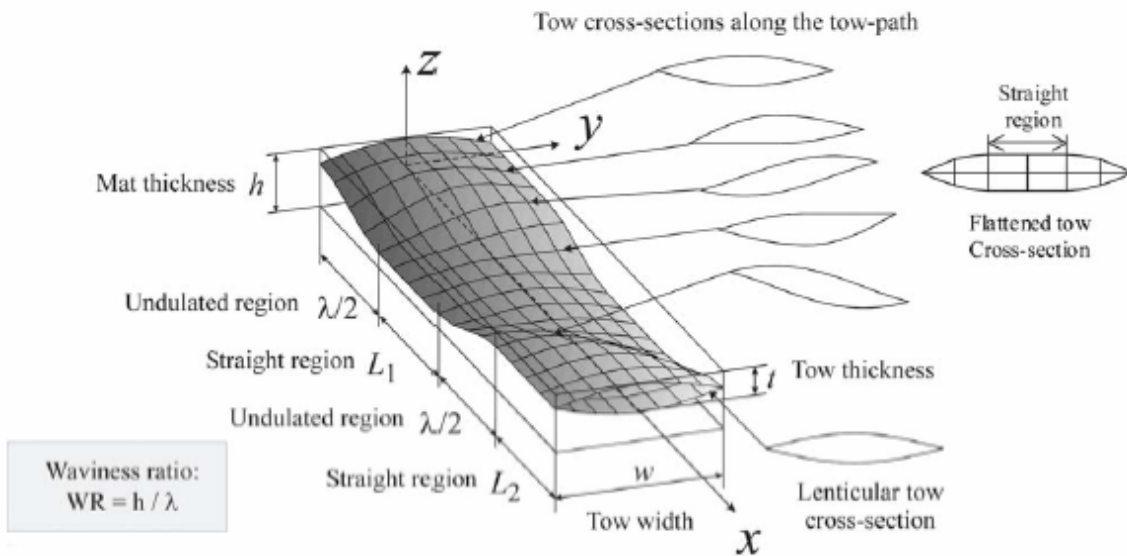
Figure 2-55: Detail of single tow path and waviness [80]

This method of modelling the composite is currently restricted to small samples. The capability of applying such methods to composite components is not currently available without access to supercomputers. The modelling of composites at the micro-scale level can be used to derive material properties for larger meso- or macro-elements which require less computational requirements. Woo and Whitcomb [84] have modelled the

tow/resin of a plain woven fabric to produce a macro-element with accurate properties. Figure 2-56 shows a schematic of the method. This method combines benefits of modelling at tow/resin level with the reduced computational requirements of the macro-modelling methods.
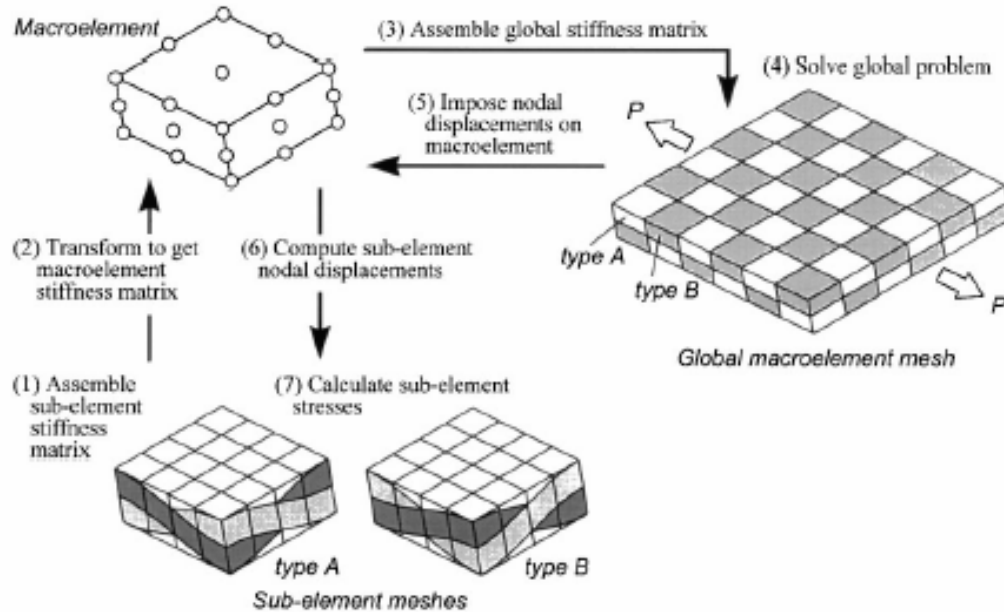
Figure 2-56: Schematic of modelling method by Woo and Whitcomb [84]

Damage Modelling using Shell based Meso- and Macro- Methods

In order to represent larger composite components, it is possible to simplify the mechanics of composites in such a way that application to shell or solid elements is possible, producing a macro-scale approximation of the composite material properties. Simplifying the composite in this way is advantageous as both the mesh requirements and process time are reduced. The introduction of damage parameters to represent failure mechanism effect on the composite are becoming increasingly available and of interest to researchers, such as Ladevéze and LeDantec [49], Iannucci and Willows [85] [86] and Boutaous et al. [87]. These models adhere to a specific failure model and thus neglect a number of failure mechanisms. This will often require information from material testing to specify the onset of damage.

The commercial FE code PAM-CRASH^{TM} contains a UD composite damage model based on the work of Ladevéze and Le Dantec [49]. The model is based on a multi-

layered single shell element where each of the layers represents a single ply with independent properties and orientation as shown in Figure 2-57. This method is a meso-based approximation as the computational code assesses the damage progression of each ply and the individual damage mechanism that can occur.
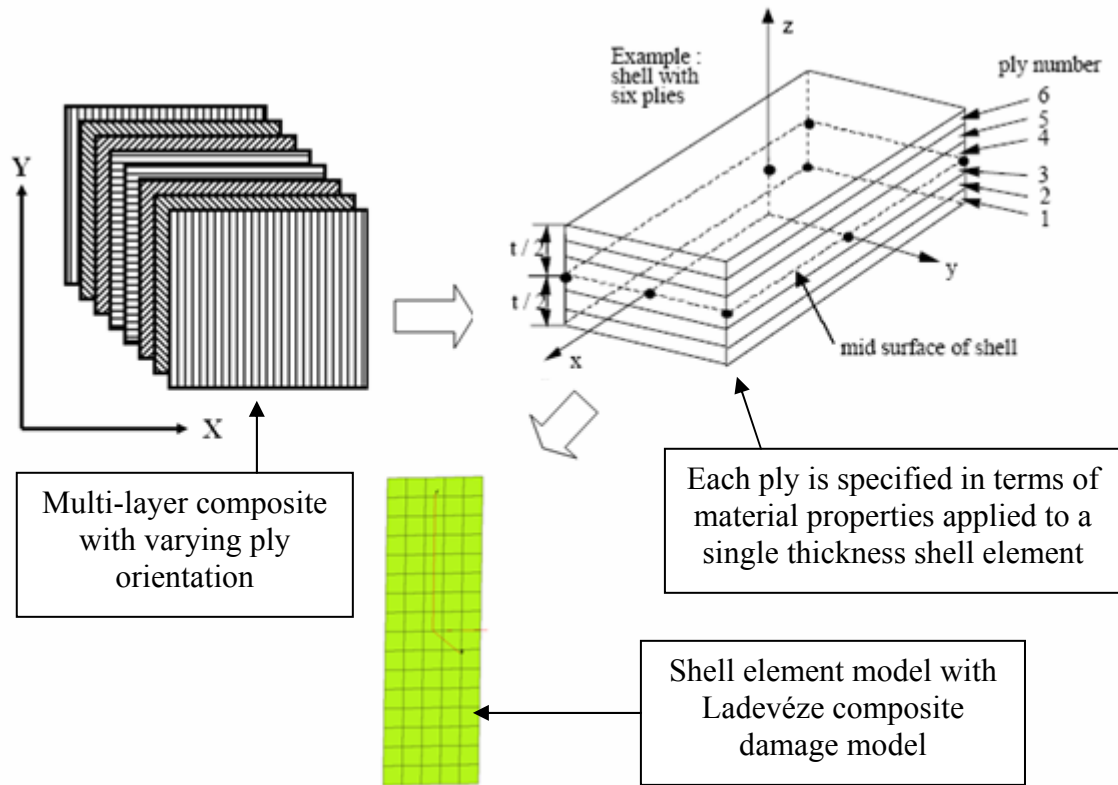
Figure 2-57: Multi-layered single shell element used in composite shell damage modelling [50]

The constitutive material code is based on the linear damage progression established by Ladevéze and Le Dantec [49], presented in Section 2.2.2, and is developed for UD composites only. The code does not currently contain options to vary the damage progression laws for woven fabric composites. Pickett and Fouinneteau [51] [52] introduced a non-linear damage law for braided composites and applied it to the modelling of a composite structure with increased accuracy as shown in Figure 2-58.
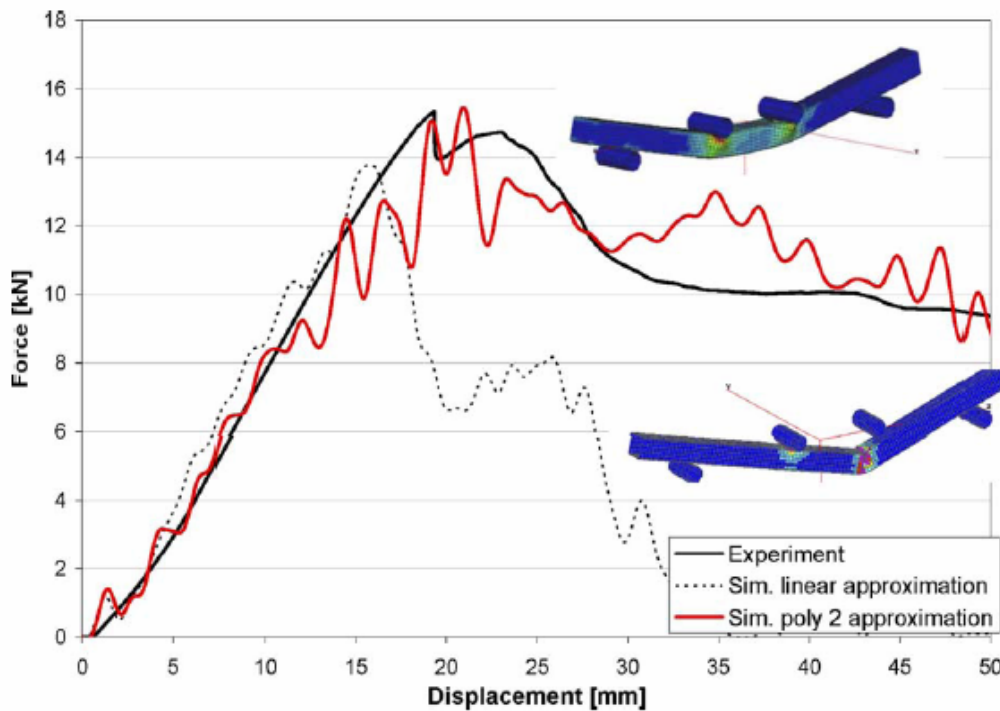
Figure 2-58: Non-linear damage progression modification to the Ladevéze method used in PAM-CRASH^{TM} [52]

Greve and Pickett [88] and Pickett et al. [89] introduced delamination effects to the composite damage model by applying a tie contact interface. Each ply of the composite laminate was modelled individually as a set of shell elements which were then tied together using a tied contact interface algorithm. In both cases papers, the properties of the tie link were established using DCB, end notch flexure (ENF) and mixed-mode beam (MMB) testing to derive mode I, mode II and mixed mode I/II properties. These tests were then successfully modelled using the tie interface model. In the case of the study by Greve and Pickett [88], the tie was applied to a model of a composite automotive component in a 3PB test configuration. The model was found to satisfactorily reproduce the force-displacement curve measured during full-scale testing. In the case of the study by Pickett et al. [89], the tie was used to model impact response on the surface of a composite panel. The study showed that by introducing the tie interface model and representing multiple plies in the composite using the Ladevéze model, as oppose to representing the entire composite as a single shell, the impact response of the composite could be more accurately represented.

2.3.4 Composite Sandwich Modelling

This Section describes the methodologies used to model a complete composite-honeycomb sandwich. Section 2.2.3 presented experimental research to investigate the effects of damage on the overall properties of the sandwich structure. Reproducing these effects using FE methods have been the subject of a number of investigations and are presented here.

Recently, Aktay et al. [90] have successfully predicted damage created by impact on composite skinned PVC and Nomex cored structures using PAM-CRASH[TM]. In this study the researchers applied a damage model to the composite skins and a crushable foam macro-solid model was applied to the PVC core. The Nomex was represented by a non-linear bi-phase macro-solid element model and not honeycomb model MAT41. The model was generated without any tie interface criteria between skin and core, thus potential delamination cannot be considered and only damage within the composite skin treated. The numerical model did reproduce the experimental test results satisfactorily, as shown in Figure 2-59. However, it is likely that this model will not accurately represent other loading conditions, such as edgewise compression or flexural loading, as vital material properties concerning the core are not included in this model.
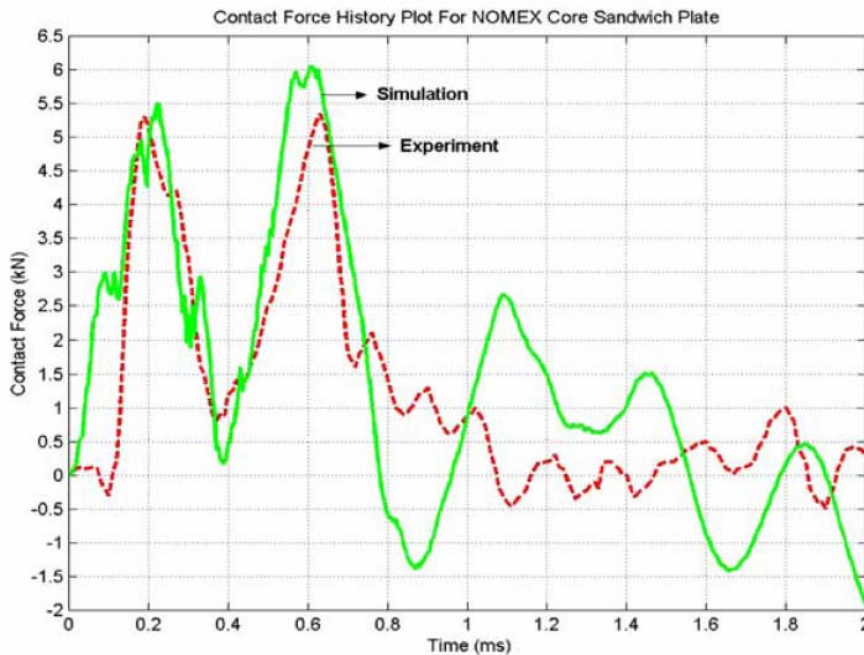
Figure 2-59: Comparison between experimental and numerical results for impact on Nomex[®] core sandwich [90]

The use of detailed shell elements models to represent the core cell walls has also been investigated to represent these structures. Foo et al [91] used the FE program ABAQUS to simulate impact loadings on composite sandwiches using the shell based core shown in Figure 2-60. The study yielded acceptable results in terms of both loading curves and physical deformation at the point of impact, as shown in Figure 2-61 and Figure 2-62. The tied interface region is not accurately represented and thus delamination between skin and core is neglected.
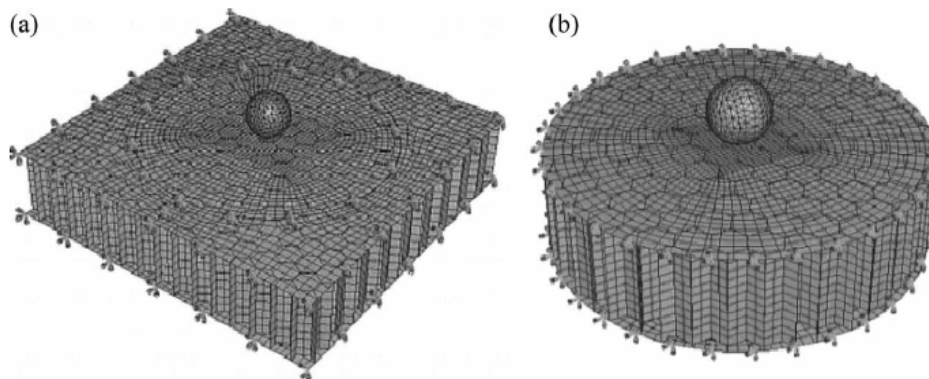
Figure 2-60: Meso-mechanical core models developed by Foo et al. [91]
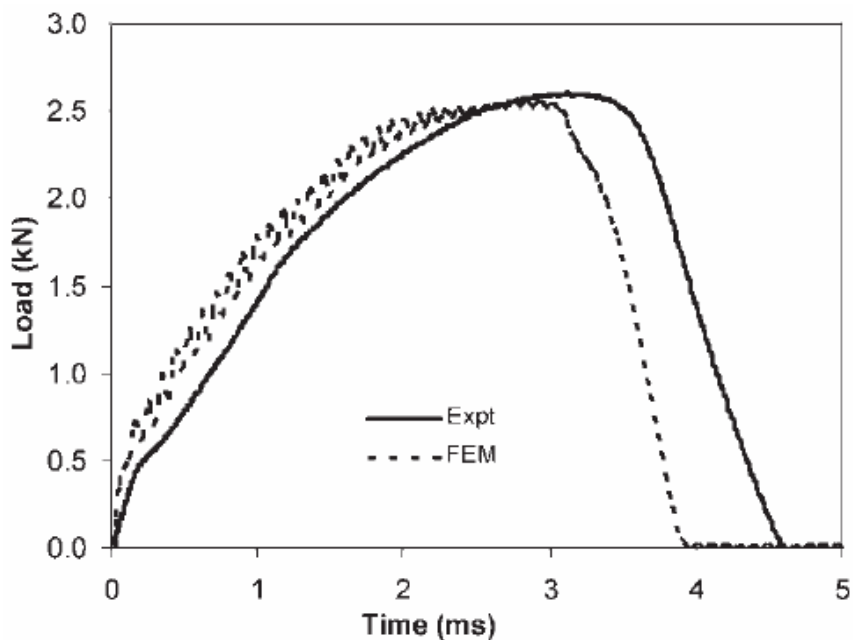
Figure 2-61: Comparisons between the experimental and numerical force history curves during 7J impact [91]
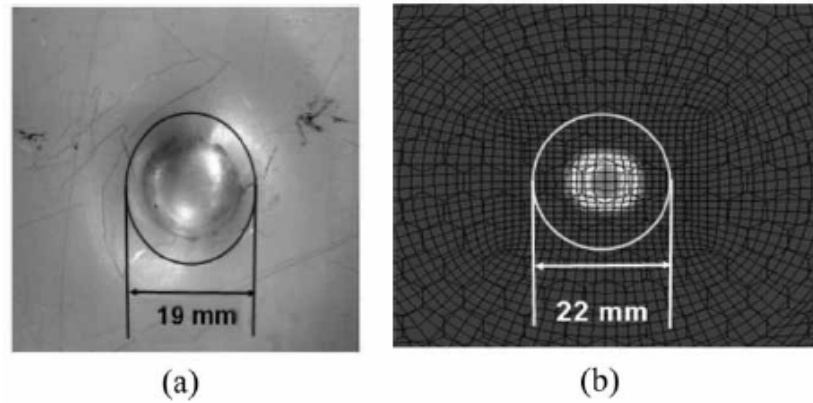
E_{imp} (J)	Experiment	Numerical
2.0	15.0	18.8
7.0	18.5	22.0
10.0	21.0	24.4
13.0	23.0	25.6

Figure 2-62: Comparison between (a) experimental and (b) numerical impact indentation size variation with impact energy [91]

2.4 Summary of Literature Review

This Chapter has presented published research to evaluate the current understanding of the composite honeycomb materials used in a sandwich construction. These materials are common in aerospace and motorsport applications as the low mass and high strength properties can be exploited to improve vehicle performance and efficiency.

The introduction of composite sandwich materials to replace traditional alloy materials in energy absorbent structures used in motorsport applications has improved crashworthiness of motorsport vehicles. Due to the stringent safety regulations imposed by the FIA, the injury and fatality rate of the sport has dropped significantly. The development of a new Formula 1 structure is currently limited since crashworthiness can only be determined using expensive prototype testing, computational methods can be used but currently lack the sufficient accuracy to be fully predictive.

The core of the sandwich structure is an aluminium honeycomb cellular material. This Chapter has discussed the properties and types of honeycomb material available.

Honeycomb is an orthotropic material where the properties in the principal directions vary depending on load direction. This research review has presented published works, such as those by Mohr and Doyoyo [25] and Hong et al. [28], where the properties in the principal directions have been expanded to include the effects of combined shear-compression. The methods to predict material properties based on the geometry of the cellular structure and properties of the base material have also been presented.

This review has investigated the methods used to represent honeycomb using FE methods. The use of phenomenological modelling approaches where the honeycomb is considered a homogeneous material is common place in commercial FE codes. These methods do not include coupling properties and currently cannot represent some mixed loading conditions accurately. Alternative methods to represent the core have been discussed, such as representing cell walls with shell elements and thus producing a geometrically accurate model.

The sandwich skin material used in the nosecone is a composite laminate. This review has presented the types, manufacture and benefits in terms of attractive high strength and low mass properties of these materials for motorsport and aerospace applications. The failure mechanisms and predictive methods have also been discussed, focusing specifically on the Ladevéze damage model as this is used in the FE code PAM-CRASH^{TM}. The use of a shell element to represent the composite material is a computationally efficient method which can be applied to large and complex geometry models. The Ladevéze damage model reproduces the effects of intra-laminar failure mechanisms to account for the onset of inelastic deformation. A tied contact interface has been used to represent inter-laminar delamination properties. This has been shown to improve the numerical representation of composite components.

This Chapter has also discussed the properties of composite-honeycomb sandwich materials. The addition of a low-mass core to the stiff composite laminates has a significant effect on the structural properties with only a small penalty in mass. Reviewed investigative studies have shown how damage, such as that produced by an impact on the composite skin, can reduce the structural properties of these sandwiches.

Methods to represent the composite sandwich have been presented. These include the use of solid and shell based modelling methods to represent the core material. Studies have shown that impact loading on the composite skins can be accurately represented and used to determine the response force and indentation dimensions on the composite skin.

3 FE Modelling of Composite-Honeycomb Materials

The present work follows the reviewed research into the development of FE methods to represent the composite-honeycomb sandwich material used in a Formula 1 nosecone structure. There has yet to be a recommended method using the material models in PAM-CRASH^{TM} to treat sandwich materials. An objective of this research is to establish the sandwich modelling capability of PAM-CRASH^{TM}. The energy absorbing properties of the individual composite-honeycomb sandwich materials are required to numerically represent the nosecone structure. This Chapter will describe the required material properties to represent the composite and honeycomb materials using the models available in PAM-CRASH^{TM}. This Chapter includes:

- A discussion of the deformation and energy absorption mechanisms which take place in the nosecone during the frontal impact test. The properties of the sandwich during these processes are required for numerical model development.

- The experimental and modelling strategy to improve the constitutive material law used in the PAM-CRASH^{TM} honeycomb model. The introduction of the shell based honeycomb modelling method is also proposed for core modelling applications.

- The requirements for representing woven composite using the UD composite damage model in PAM-CRASH^{TM}.

- The requirements to investigate and represent the properties of the sandwich structure using FE methods.

The nosecone structure displays a number of energy absorbing and deformation mechanisms when subjected to a frontal impact. As presented in Section 2.1.2, a Formula 1 nosecone will ideally be designed to collapse in a general Mode-1 progressive end failure mechanism as this maximises the energy absorption of the structure. It is difficult to determine from experimental testing, even with high speed video footage, whether the collapse mechanisms are Mode-1a or 1b as shown in Figure 3-1. It is likely that there will be a mixture of these mechanisms throughout the structure.
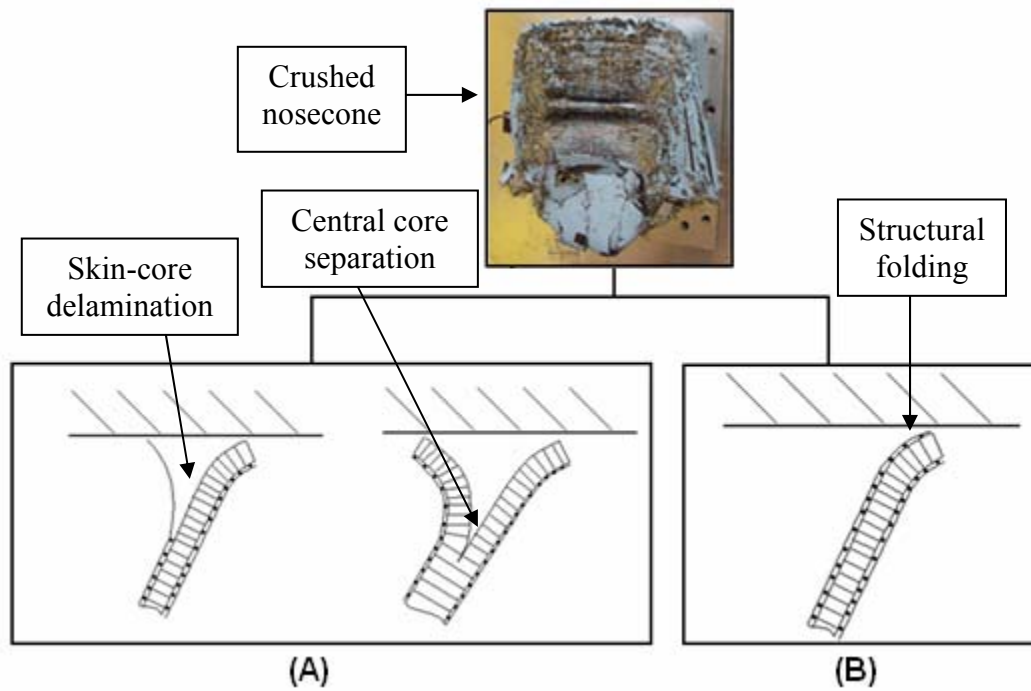
Figure 3-1: Axial collapse mechanisms, (A) Mode-1a skin-core debonding and core split, (B) Mode-1b sandwich folding

Figure 3-2 summarises the testing and modelling strategy for this thesis. Experimental procedures and results are presented in Chapter 4 and numerical results are presented in Chapter 5.

Core and Skin Analysis

Honeycomb Materials

Requirements: Section: 3.1

Experimental Analysis: 4.3
Numerical Analysis: 5.1

Composite Laminates

Requirements: Section: 3.2

Experimental Analysis: 4.4
Numerical Analysis: 5.2

Structural Sandwich Analysis

Cracked Sandwich Beam Testing

Requirements: Section: 3.3.1

Experimental Analysis: 4.5.2
Numerical Analysis: 5.3.2

Three Point Bend Testing

Requirements: Section 3.3.2

Experimental Analysis: 4.5.3
Numerical Analysis: 5.3.3

Impact Wedge Sandwich Testing

Requirements: Section 3.3.3

Experimental Analysis: 4.5.4
Numerical Analysis: 5.3.4

Formula 1 Frontal Impact Structure

Requirements: Section 3.4

Numerical Analysis: 5.4

Figure 3-2: Sandwich component testing and modelling strategy

3.1   Honeycomb Core Modelling Requirements

Computationally efficient modelling methods and constitutive laws are required to reduce CPU time and whilst being accurate enough to realistically represent the overall structural behaviour. The focus of this research thesis is the improvement of the orthotropic solid model, MAT41, in PAM-CRASH^{TM} to represent sandwich core materials. This has been previously discussed in Section 2.3.2 as a computationally efficient method of representing cellular solids, but currently lacks accuracy for complex loading conditions [20]. The MAT41 material model requires the user to specify the compressive properties in the three principal directions (L, W, T); these are discussed in Section 2.3.2. To obtain this information, standardised compressive experimental testing and manufacturer's property datasheets are required. The tensile failure stress is required for the numerical model. This is estimated to be 6.8MPa as the honeycomb material is 2.6% relative density to the aluminium base material.

The current constitutive code neglects the distinct peak loading effect observed during compressive loading in the 'T' direction shown in Figure 3-3. In order to improve the current material model MAT41 further tests in the 'T' direction are required, these are summarised in Table 3-1.
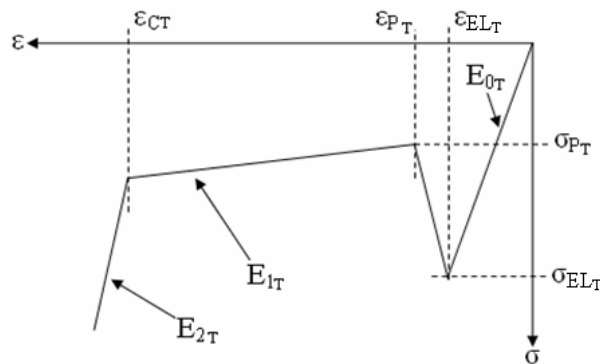
Figure 3-3: Required inputs for improved MAT41 material model - 'T' direction compressive loading

Property	Description	Notes
$\sigma_{EL(T)}$	'T' direction peak stress	Distinctive peak strength as the honeycomb cells collapse
$\sigma_{P(T)}$	'T' direction plateau initiation stress	After the initial fold, the core will settle into a constant crushing phase
$\varepsilon_{PL(T)}$	'T' direction plateau initiation strain	Used to establish a declination from peak to plateau crushing phases
$\varepsilon_{EL(T)}$	'T' direction peak strain	Compression strain at peak load
$\varepsilon_{C(T)}$	Compaction strain	Strain at which plateau crushing concludes and compaction begins
E_{0T}	Elastic modulus	Average elastic modulus before peak load
E_{1T}	1ST Tangent Modulus	Plateau crushing modulus
E_{2T}	2nd Tangent Modulus	Compaction modulus

Table 3-1: Further required 'T' directional material properties

It is unlikely that the core material will experience loading in only one principal direction in the nosecone, especially during the folding process, therefore the mixed shear-compression properties for this material must be established. Section 2.2.1 presented published research which showed honeycomb to produce a variation in normal and shear properties when mixed shear-compression loading is applied. The current material model for honeycomb representations has been shown to neglect these variations in [20] and Figure 2-51. In this work, the variation in normal and shear properties of the honeycomb material used in the nosecone structure is required for mixed shear compression loading conditions. This required the development and use of a modified Arcan apparatus for cellular solid materials, such as those produced in [24] and [25]. The developed apparatus and experimental results are presented in Section 4.3.3.

In addition, the effects of in-plane deformation on the 'T' direction compressive properties are not accounted for in this model. The compressive properties in the 'T' direction are dependent on the geometry of the hexagonal cell. The cellular geometry

will vary as the material is loaded in an in-plane direction. The influence of this variation has not been established in previous published work and an experimental study is required to examine the change in 'T' direction compressive properties after controlled pre-deformation in the in-plane directions. This investigation is presented in Section 4.3.2.

The deformation of the honeycomb core subjected to further complex loading conditions is difficult to produce and investigate experimentally. A potential solution to this is the use of a geometrically accurate shell based honeycomb model to predict the deformation in the honeycomb cells when loaded in multiple directions. The method was presented in Section 2.3.2 as an effective method to represent honeycomb materials with a reduced requirements from the user but increased computational requirements. This will also be used to represent the core when modelling the sandwich structure. This approach is examined and compared with experimental results in Section 5.1.2.

3.2 Composite Laminate Skins

For the purpose of this research, the composite laminate skins are represented using the UD composite damage model available in PAM-CRASH^{TM}. The method, presented previously in Sections 2.2.2 and 2.3.3, requires the user to specify properties of the individual plies, using PAM-CRASH^{TM} model 131(PLY1) in a multilayered shell element [50]. The model requires the compressive, tensile and in-plane shear modulus of the composite ply with shear, compression and tension strain limits. A failure initialisation strain is required to indicate the onset of plastic deformation and total failure is specified by an ultimate strain value with a corresponding damage value. As the composite fabric is a woven pre-impregnated structure, the input damage limitation properties to establish compressive damage evolution cannot be determined. The input requirements are summarised in Figure 3-4.

The model requires a secondary compressive property which specifies a non-linear compression modulus, denoted by E_1^γ in Figure 3-4. This parameter is not required for

the woven fabric as composite materials tend to produce a sudden brittle failure when loaded in compression.

Tensile and Compressive Fibre Damage

Properties applied to each ply

Shear Damage Progression

Tension	In-Plane Shear	Compression
E_1^{0t} ε_u^{ft}	G_{12}^{0} Y_C, Y_0, Y_R R_0, β, m	E_{11}^{C} ε_u^{fc}
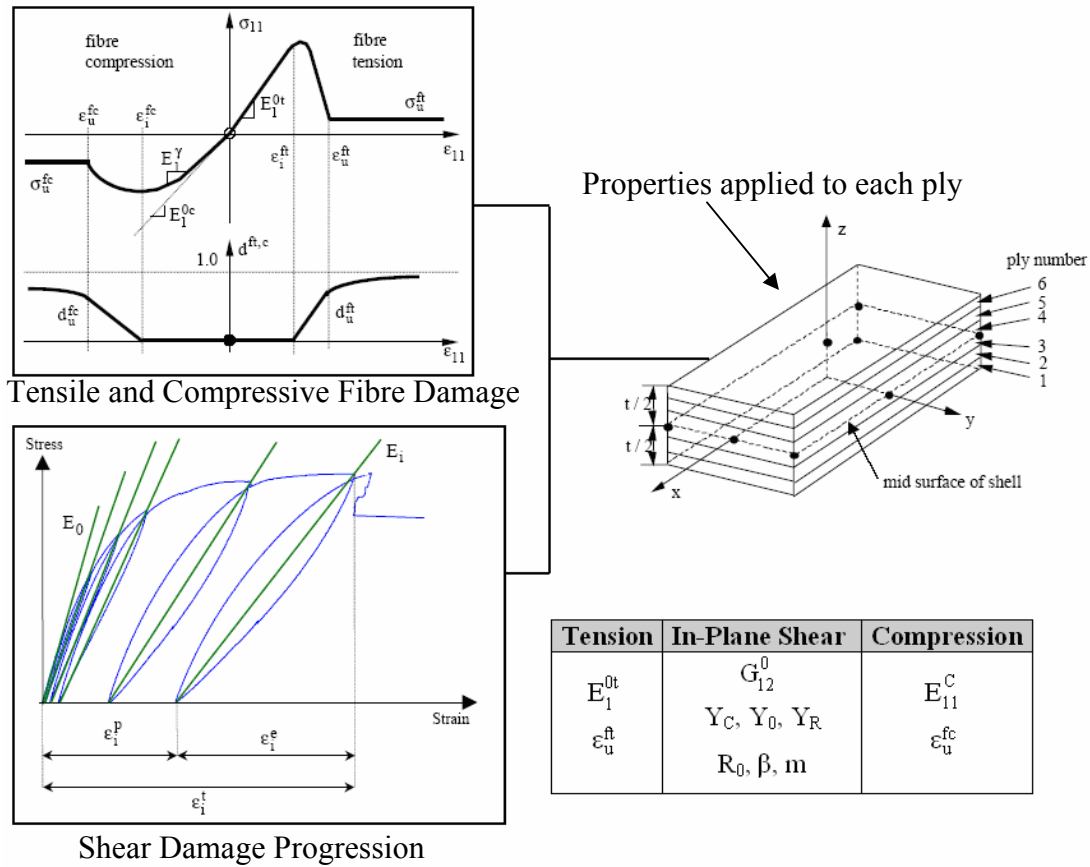
Figure 3-4: UD damage model with table showing required inputs from woven fabric examination [50]

The properties specified by the manufacturer indicate the ideal strength of the plies in tension, compression and in-plane shear loading conditions. The damage progression properties are not specified by the manufacturer and thus need to be established experimentally using a cyclic loaded tension-shear test.

As the material model is developed for UD composites, discussed in Section 2.3.3, the properties of the woven fabric must be represented using the UD property definitions. To achieve this, a single woven fabric ply is considered as two UD plies with one of these plies orientated at 90^{0} relative to the first ply as shown in Figure 3-5. Classical laminate theory is applied to calculate the equivalent transverse elastic properties of the

UD ply. Furthermore, an improved relationship between d_{12} and Y_{12} for the composite skins is derived for the woven composite material and introduced into the constitutive material code as shown from previous work by Fouinneteau [51] for braided composites. The experimental investigation to establish the new damage progression law is presented in Section 4.4.2 and improvements to the numerical model are presented in Section 5.2.
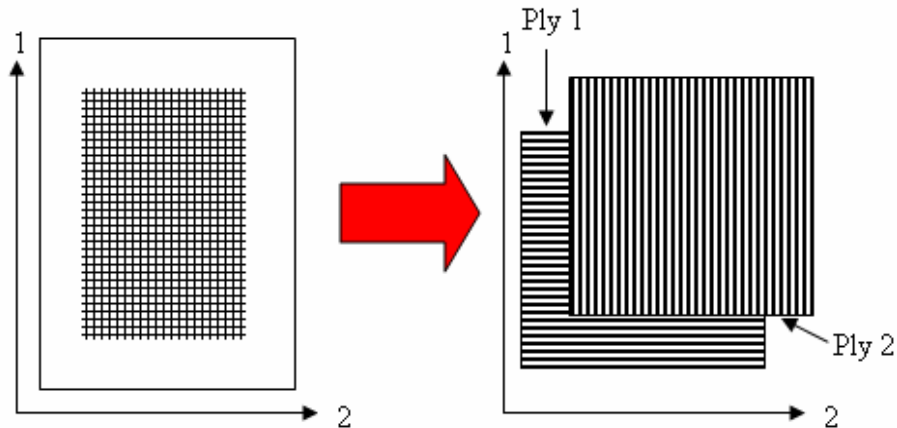
Figure 3-5: Conversion from woven fabric to UD composite representation

3.3 Sandwich Structure

There is currently no specific modelling method recommended for sandwich materials using the available material models in PAM-CRASH^{TM}. An objective of this thesis is to establish the most appropriate method to represent their crash behaviour using the available material models. A series of experimental investigations were conducted to determine their failure properties when subjected to a variety of loading conditions. These loading conditions are representative of those experienced in the nosecone structure during a frontal impact and create similar failure conditions; namely, debonding between the core and the skins, bending in the sandwich structure and edgewise in-plane crushing/impact.

3.3.1 Mode-I Crack Propagation

A likely failure criterion for the sandwich structure is crack propagation through the sandwich mid-plane; this could take the form of skin-core debonding or core splitting.

A tied interface method is available in PAM-CRASH^{TM} to represent crack propagation between surfaces. The tied interface used in PAM-CRASH^{TM}, material model MAT303, is a link element between a surface segment and a slave node on a contact surface developed by Pickett et al. [89] and shown in Figure 3-6. The movement of the slave node relative to the surface is measured in terms of perpendicular and parallel displacements. The failure mechanisms for both Mode-I and II are based on strain energy during crack propagation.
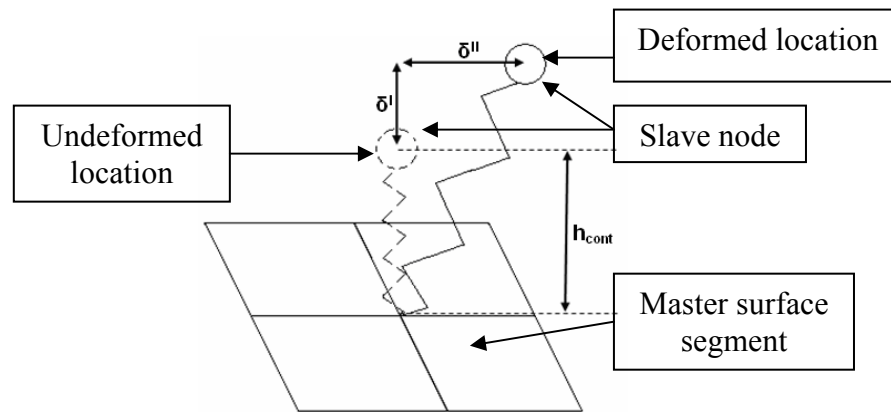
Figure 3-6: Contact interface MAT303 schematic

The energy limits are shown in Figure 3-7 for both Mode-I and II conditions. The interface undergoes failure when the elastic strain energy $G_{I/II}{}^0$ is exceeded. These are calculated using equations 3-1 and 3-2 for Mode-I and II respectively.

$$G_I^0 = \frac{\sigma_{max}^2 h_{cont}}{2E_0},$$
[3-1]

$$G_{II}^0 = \frac{\tau_{max}^2 h_{cont}}{2G_0},$$
[3-2]

where E_0 and G_0 are the normal and shear stiffness of the contact link element respectively and h_{cont} is the distance used for kinematic computation and must be greater than the distance between the slave node and the master surface segment.
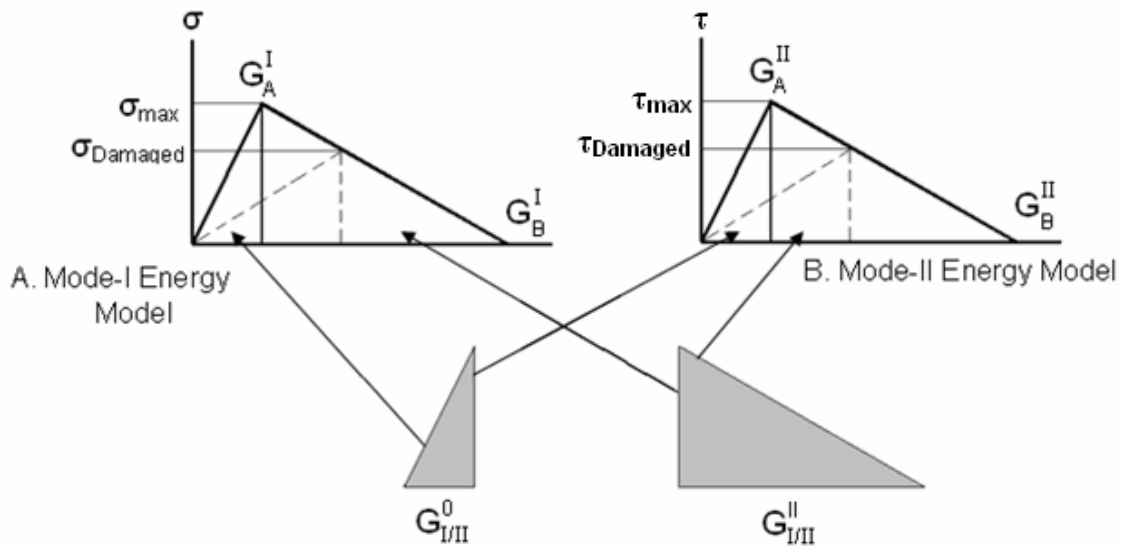
Figure 3-7: Mode-I and II strain release energy curve definitions [50]

A mixture of Mode-I and II loading is likely to occur in the nosecone structure. A linear coupling modelling has been implemented into the contact interface to represent these mixed mode failure mechanisms. Initial failure starts when G_{CONT} is exceeded in equation 3-3; this is also shown by the linear relationship in Figure 3-8.

$$\frac{G_I^i}{G_I^0} + \frac{G_{II}^i}{G_{II}^0} = G_{CONT} \, ,$$

[3-3]

where G^i is the instantaneous strain energy in both normal and shear loading. Once the failure criteria has been met, the stress required to continue propagation reduces linearly until an end limit condition is met using equation 3-4.

$$\frac{G_I^i}{G_I^{II}} + \frac{G_{II}^i}{G_{II}^{II}} = G_{CONT} \, ,$$

[3-4]
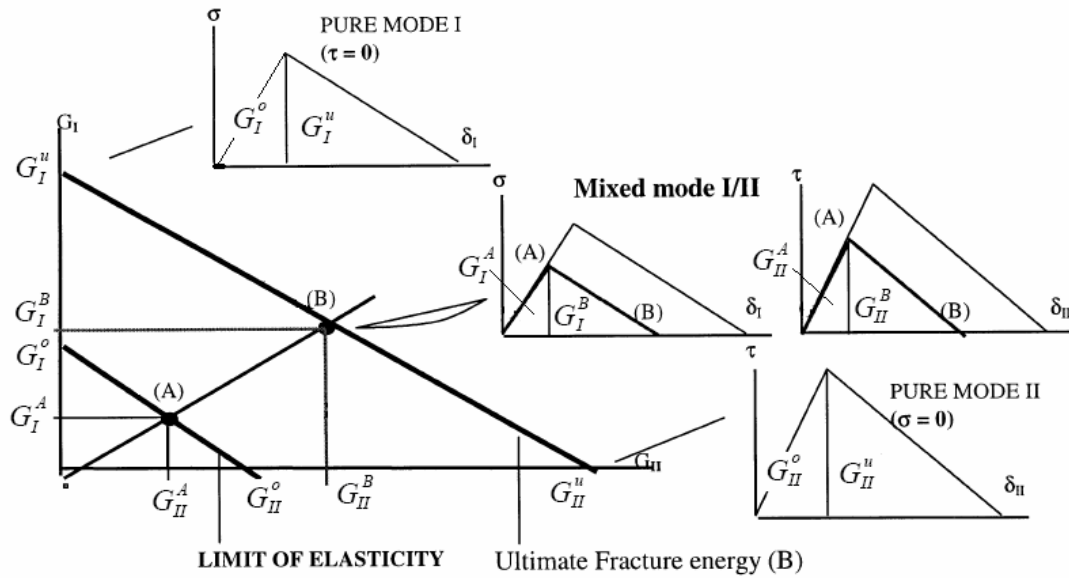
Figure 3-8: Linear coupling of Mode I and II failure mechanisms [89]

A CSB test is required to determine the input parameters for the contact interface. Mode-II failure parameters are not required as the honeycomb core is weak and will simply fold before possible crack propagation. The crack propagation properties are determined using quasi-static low-rate loading conditions as described in Section 2.2.2. This method has been used in previous work, such as Pickett [106] and Lourenco [107], to model the inter-laminar delamination failure in composite tubes during quasi-static crushing; these investigations displayed good correlation with experimental results. The CSB investigation using the sandwich material used in the BAR-Honda nosecone is presented in Section 4.5.2 and the numerical model calibration is presented in Section 5.3.2.

The effect of loading rate on G_{IC} is also of interest as a high-rate loading condition is a closer representation of the frontal impact conditions. To achieve this, a new test apparatus to produce a high-rate Mode-I delamination loading condition is introduced. The effects of loading rate are not required for numerical model development but are conducted to further investigate the energy absorbing properties of the composite-honeycomb sandwich. This investigation is also presented in Section 4.5.2.

3.3.2 Sandwich Flexural Properties

The walls of the nosecone structure can potentially fold during the frontal impact test. Therefore the flexural properties of the sandwich structure are required to investigate the folding deformation. This can be determined using the established 3PB test for composite sandwich structures shown in Figure 3-9 and the standard test method [55]. The experimental investigation is presented in Section 4.5.3. The findings from this investigation are used to validate the methods of numerically representing the sandwich material. The numerical model investigation is presented in Section 5.3.3.
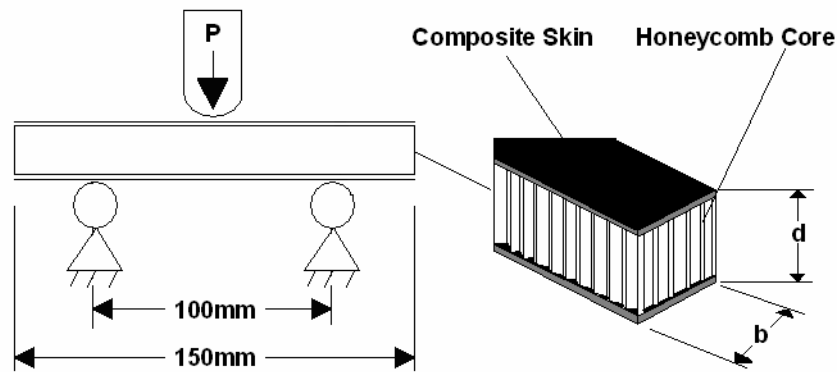
Figure 3-9: 3PB sample geometry

The elastic flexural modulus, flexural stress and strain of the sandwich component are then established using equations 3-5, 3-6 and 3-7 respectively [92].

$$E_B = \frac{L^3 P}{4Dbd^3},$$ [3-5]

$$\sigma_F = \frac{3PL}{2bd^2},$$ [3-6]

$$\varepsilon_F = \frac{6Dd}{L^2},$$ [3-7]

where, D is the displacement of the press and L is the distance between pivots, b and d are the width and thickness of the sandwich shown in Figure 3-9.

3.3.3 Wedge Impact Testing

The primary direction of loading in the nosecone structure is in the in-plane direction; the tip of the nosecone at an oblique angle to the impact wall shown in Figure 3-10.

This angle is approximately 27^0 to the horizontal. To the knowledge of the author the variation in strength of a composite-honeycomb sandwich when subjected to an axial and oblique in-plane impact has yet to be investigated. A similar study was performed by Mamalis et al [112] to investigate the edgewise loading energy absorption properties of a foam based sandwich. The samples were subjected to edgewise loading conditions specified in ASTM C364-99 [111] without the use of edge clamping lateral supports. A variation in core and skin material was investigated and three types of collapse mechanisms were identified. These failure mechanisms are described as follows:

- Type-I unstable buckling – The sandwich undergoes a buckling process which results in a sudden loss in structural strength. The deformation is shown in Figure 3-11.

- Type-II unstable sandwich debonding – The faceplate skins completely debond from the core. The skins buckle outward from the core and, like Type-I, a loss of structural strength is observed. The deformation is shown in Figure 3-12.

- Type-III stable end progression failure – The deformation is isolated at the crushing wall. The edgewise crushing strength is maintained throughout the crushing process. The deformation is shown in Figure 3-13.
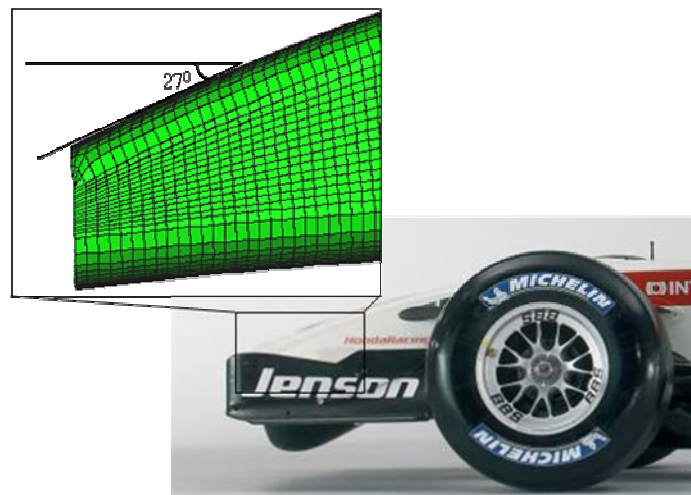
Figure 3-10: Oblique angle of BAR-Honda nosecone tip
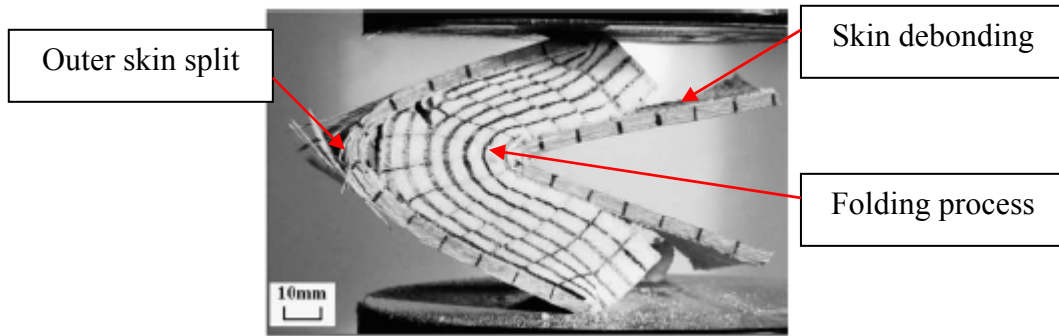
Figure 3-11: Type-I edgewise failure - Unstable sandwich buckling [112]
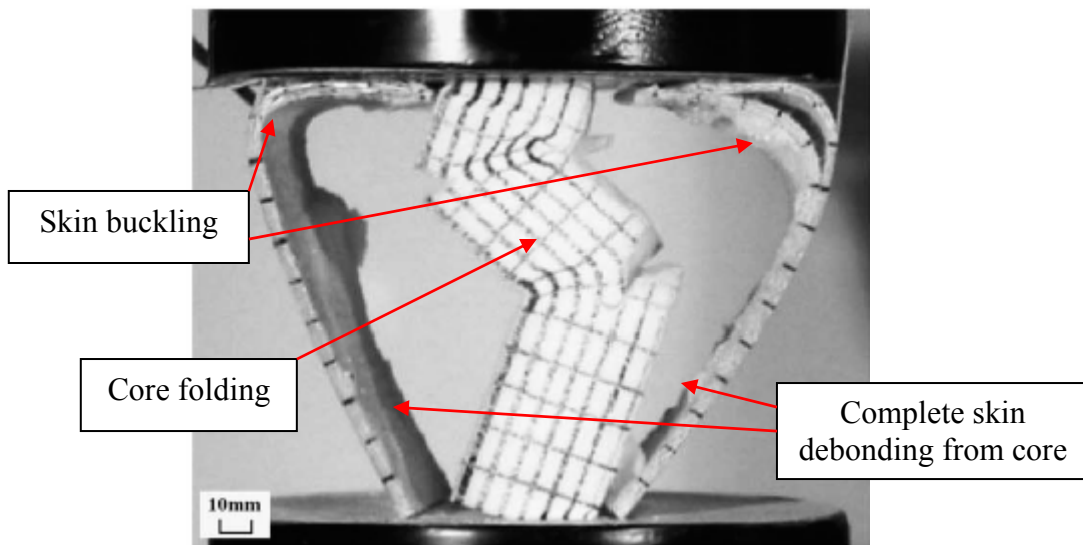
Figure 3-12: Type-II edgewise failure – Unstable sandwich disintegration with faceplate buckling [112]
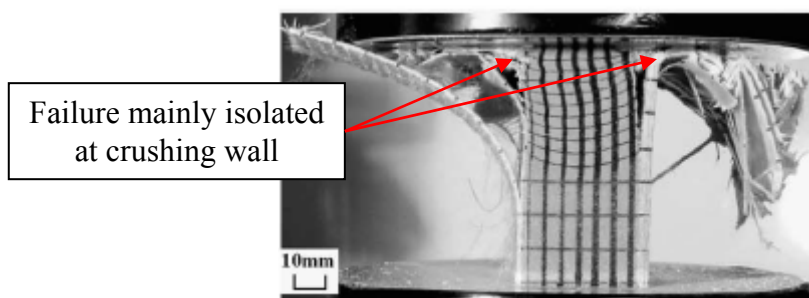
Figure 3-13: Type-III edgewise failure - Stable progressive end failure [112]

Composite-honeycomb wedge samples are used to determine the energy absorption and deformation mechanisms during edgewise loaded. The deformation, failure mechanisms and energy absorption of the sandwich material when loaded this way is examined using

quasi-static crushing. A further test series is conducted dynamically to examine rate effects on failure mechanisms using high-speed photography. The findings from both quasi-static and dynamic investigations are presented in Section 4.5.4. The findings from this investigation are used to validate the methods of numerically representing the sandwich material and are presented in Section 5.3.4

3.4 Nosecone Representation

The industrial interest in this material research is, ultimately, how to apply it to practical structures. In the case of this research, the practical problem is the crashworthiness evaluation of the frontal nosecone structure. The geometry of the nosecone is used to develop a mesh for numerical crashworthiness evaluation with the FIA frontal impact regulations as boundary conditions. The nosecone numerical model is used to assess the variations between the composite sandwich modelling methods. Unfortunately, crashworthiness evaluation information for this particular structure was not available; therefore, the nosecone model is compared with information gathered from Temple [93], where the details concerning a regulation passing structure are presented.

3.5 Section Summary

This Chapter has presented the experimental and modelling strategy that will be used to examine the capability of PAM-CRASH^{TM} to represent sandwich structures and investigate the energy absorbency of the materials used in the nosecone structure of a Formula 1 car. The potential failure mechanisms in the nosecone when subjected to a frontal impact have been considered and a series of tests to determine the properties of the sandwich structure have been introduced.

A test series to acquire the basic material properties for the current honeycomb material model and address deficiencies in the model for mixed loading conditions have been proposed. This Chapter has identified the mixed shear-compression conditions which occur in the sandwich during the frontal impact test and has stated that the response of honeycomb in these loading conditions is required. Further coupled directional properties are examined to relate the effects of pre-deformation on the properties in the 'T' direction.

The shell element used in this research to represent the sandwich skin has been identified in this Chapter as the Ladevéze damage model. As the material is a woven fabric, the experimental investigation to establish the material properties is conducted using the methods employed by Fouinneteau [51] for braided composites. An improved damage progression law for the material is required for improved representation.

This Chapter has also presented an experimental strategy to determine the energy absorption properties and deformation mechanics of the sandwich structure. The investigated conditions are representative of the mechanisms in the nosecone structure when subjected to a frontal impact loading condition and include:

- Low and high-rate crack propagation through the sandwich using Mode-I CSB testing methods.
- 3PB flexural beam testing.
- In-plane axial and oblique low and high-rate impact testing.

These are used to establish the capability and deficiencies with the current PAM-CRASH^{TM} code when representing sandwich structures.

4 Experimental Procedures and Results

This Chapter describes the experimental procedures and presents the results of the tests conducted on materials used in the BAR nosecone structure. The experimental research is focused on the core and skin materials separately, before studying the properties of the sandwich structure. This Chapter includes:

- A description of the optical measuring method used throughout the research.
- Experimental settings and apparatus, focusing on apparatus specially designed for this research.
- Experimental results for the individual sandwich materials and the complete sandwich.

The properties of each component element of the sandwich are required to produce a numerical model of a sandwich structure. A series of experimental investigations have been conducted to determine the material properties and energy absorbing behaviour of these materials when subjected a variety of loading conditions.

4.1 Digital Image Correlation

The optical measuring system used throughout this research is the Digital Image Correlation (DIC) system produced by LIMESS GmbH [94]. The system measures the movement of a random speckle pattern, shown in Figure 4-1, on the surface of a test sample which is then used to determine displacement and strain distributions.
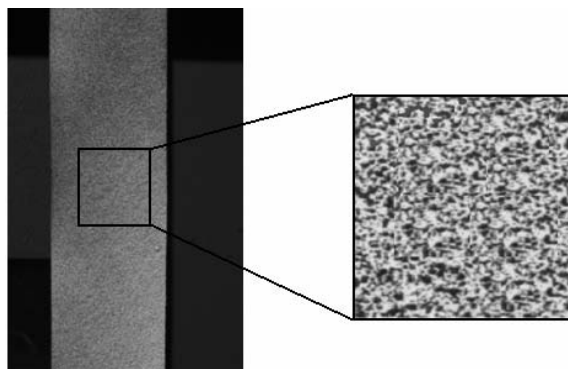
Figure 4-1: Example of speckle pattern on the surface of a composite test sample

There are two methods of using the DIC system, shown in Figure 4-2. The mono camera method is used in tests where there is negligible out-of-plane movement toward or away from the camera. The user must assure that the camera is pointing normal to the sample otherwise the recorded measurements will be inaccurate.
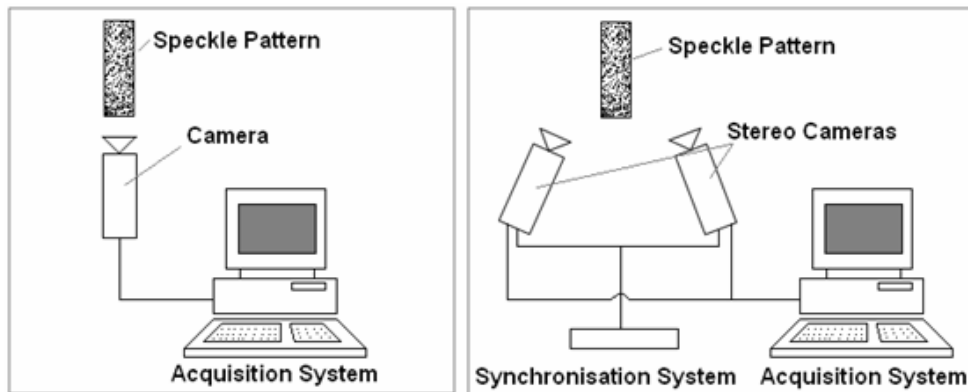
Figure 4-2: Comparisons of mono and stereo camera systems

The stereo camera method is used when there is likely to be some out-of-plane movement, such curved surfaces. In these cases, a calibration method is required to determine the relative positions of the cameras from the test sample surface. A calibration plate is placed in front of both cameras and images are taken and analysed; the process is shown in Figure 4-3.
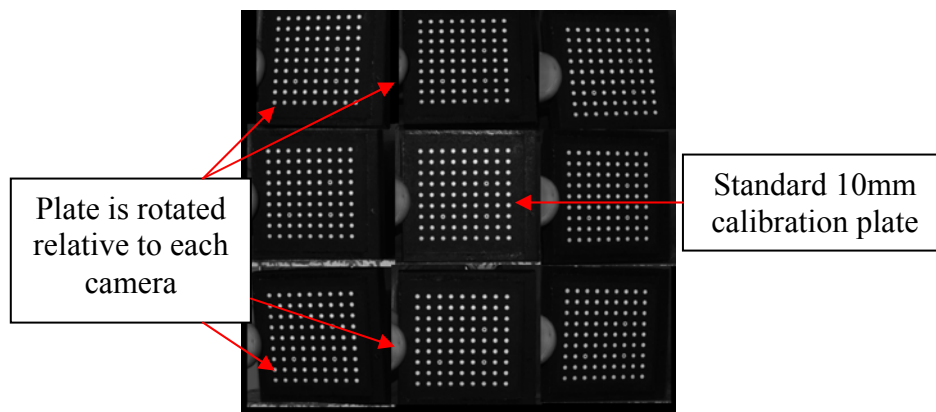
Figure 4-3: VIC3D calibration plate

The DIC system takes images of the sample surface at a constant rate during testing; these are referred to as deformed images. To analyse the deformation, a reference image and the deformed images are loaded into a post-processor, either VIC2D or VIC3D

depending on the camera arrangement, and an area of interest is selected. A subset and step size must then be chosen to assist with the analysis, where:

- The subset, shown in Figure 4-4a, is the area used to determine displacements between images; this affects the size of the area of interest.

- The step size, L_S, shown in Figure 4-4b, is the space in terms of pixels for the analysis to be performed, for instance a step size of 1 would analyse every pixel whereas a step size of 2 would analyse every other pixel in the horizontal and vertical directions.
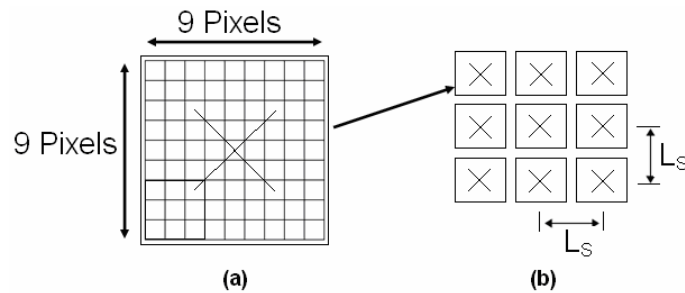
Figure 4-4: Definitions of (a) Subset and (b) Step sizes

The system then analyses each image and produces an output like that shown in Figure 4-5. Any point in the area of interest can be examined closer to determine displacements and strain in that region.
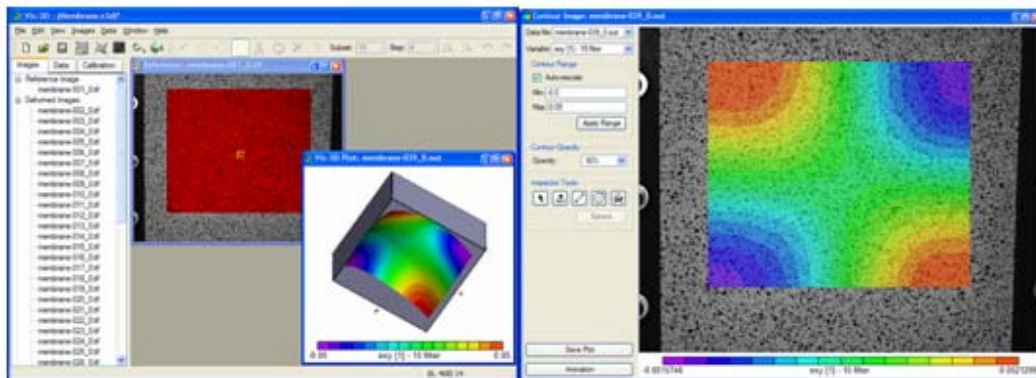
Figure 4-5: Example of VIC3D post-process analysis [94]

4.1.1 Benefits of Digital Image Correlation

Resistance strain gauges are the traditional method of measuring strain in a coupon. These are limited in performance and reliability, for instance they need to be positioned

in the region of interest, which on a composite sample can sometimes be difficult to predict in advance and they can detach from the surface of the sample during large deformations. The displacement of a test apparatus and sample is determined using with the use of displacement measuring devices, such as a linear displacement transducer. These devices are often positioned away from the sample, for instance in the Arcan apparatus developed by Mohr and Doyoyo [25], and thus deformation in the test apparatus can introduce an error to the sample deformation measurement. Optical techniques can be introduced to monitor the deformation of the sample with increased accuracy.

The above mentioned difficulties and limitations can be overcome with the use of optical measuring methods. Furthermore, the location of maximum deformation and eventual failure does not need to be identified in advance and the measured strain of the sample can be much greater than that of the strain gauge, which will typically fail at 3-5% [95] longitudinal strain. However, the system is limited by the formation of cracks in the white surface which will begin to disturb the monitoring of the speckle pattern and accuracy of the ability to measure strains.

The applications of full-field optical measuring techniques are increasing. Lichtenstein and Schreier [113] have applied the method to analyse the deformation of a car body panel when subjected to an impact. The method was successfully used to measure the deformation of the body panel and to validate FE models of the component. Ambur et al [114] have also used the method to evaluate the failure mechanisms in a stiffened composite panel when subjected to a picture frame shear loading. These findings were also used to validate FE models in ABAQUS. Fouinneteau [51] used the method extensively when characterising the progression of failure in glass and carbon fibre braided composite materials before applying the method to a 3PB test of a glass and carbon fibre beam. Strain deformations in the samples were calculated, from which fibre reorientation, damage progression and failure mechanisms occurring in the samples and the beam structure.

4.2 Test Samples

To determine the properties of materials used in the nosecone Section of the BAR Formula 1 car, a selection of composite coupon, honeycomb and composite-sandwich test samples have been produced. The selection of specimens is based on the requirements specified in Chapter 3 of this thesis. It is important that these samples are produced in the same laboratory conditions as the nosecone structure, therefore these samples were produced at the Honda Racing F1 facility in Brackley. The samples are shown in Figure 4-6.
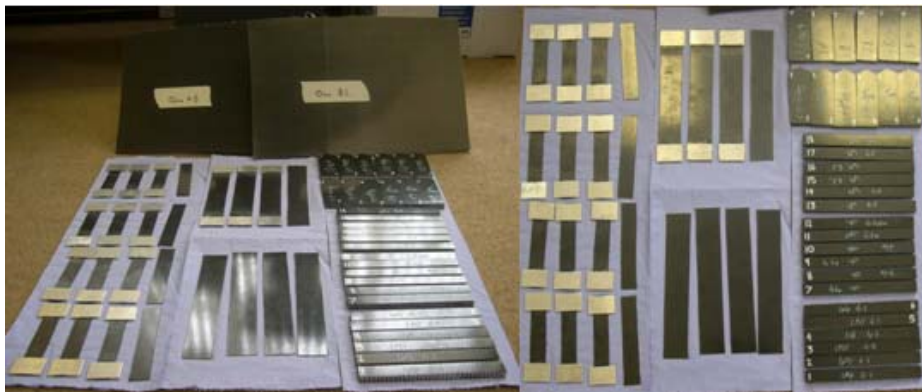
Figure 4-6: Selection of test samples produced by Honda Racing F1

4.3 Honeycomb Experimental Testing

For the purposes of this research, the investigation of honeycomb materials is focused on the low-density (72kg/m^3) honeycomb as only a small portion of the nosecone uses the high-density (129.7kg/m^3) material and is situated near the rear of the structure. The objectives of this investigation are to;

- Produce the required input parameters for the standard MAT41 material model used in PAM-CRASH^{TM}

- Determine the effects of in-plane deformation on the out-of-plane compression properties of honeycomb. The results from this investigation are compared with the standard MAT41 material numerical model. The relationships between in-plane deformation and out-of-plane compression properties are applied to the material model for improved representation of honeycomb.

- Establish the relationships between mixed shear-compression properties and loading direction using an improved Arcan apparatus. The relationships are

introduced into the MAT41 material numerical model to improve the representation of mixed shear-compression loading.

This investigation is focused on the properties of the low density ($72kg/m^3$) honeycomb material due to the amount of this material in the nosecone structure; however, some testing has been conducted on the high-density ($129.7kg/m^3$) honeycomb material and presented here.

Property	Honeycomb material type	
	1/8-5052-0.001-4.5 72kg/m^3 density	1/8-5052-0.002-8.1 129.7kg/m^3 density
'T' Elastic Modulus	1.03 GPa	2.41 GPa
'T' Peak (Yield) Stress	2.79 MPa (Minimum) 3.93 MPa (Typical)	7.58 MPa (Minimum) 10.76 MPa (Typical)
'T' Plateau (Crushing) Stress	1.79 MPa	5.17 MPa
'TL' Shear Modulus	486.2 MPa	930.8 MPa
'TW' Shear Modulus	213.7 MPa	372.3 MPa
'TL' Shear Stress	1.97 MPa (Minimum) 2.34 MPa (Typical)	4.62 MPa (Minimum) 5.52 MPa (Typical)
'TW' Shear Stress	1.16 MPa (Minimum) 1.52 MPa (Typical)	2.76 MPa (Minimum) 3.24 MPa (Typical)
Density	72 kg/m^3	129.7 kg/m^3
Wall Thickness	0.025mm (Minimum)	0.054mm (Minimum)

Table 4-1: Published honeycomb properties [18]

4.3.1 Principal Direction Compressive Properties

The in-plane and out-of-plane compressive properties of honeycomb are established from standard compression testing using the ASTM C365-03 [19] standard for flatwise testing of sandwich core samples. The standard specifies the honeycomb sample cross-sectional area based on the dimensions of the hexagonal cell, the honeycomb test samples were cut to 5625mm^2, 75mm x 75mm. The compression rate of loading was 0.5mm/min.

The experiments were conducted using an INSTRON Test machine. Two steel plates were used to compress the samples and the DIC system was used to monitor the relative displacement of the upper and lower steel plates, shown in Figure 4-7. The experiments were conducted with the mono-camera method as out-of-plane movement is negligible.
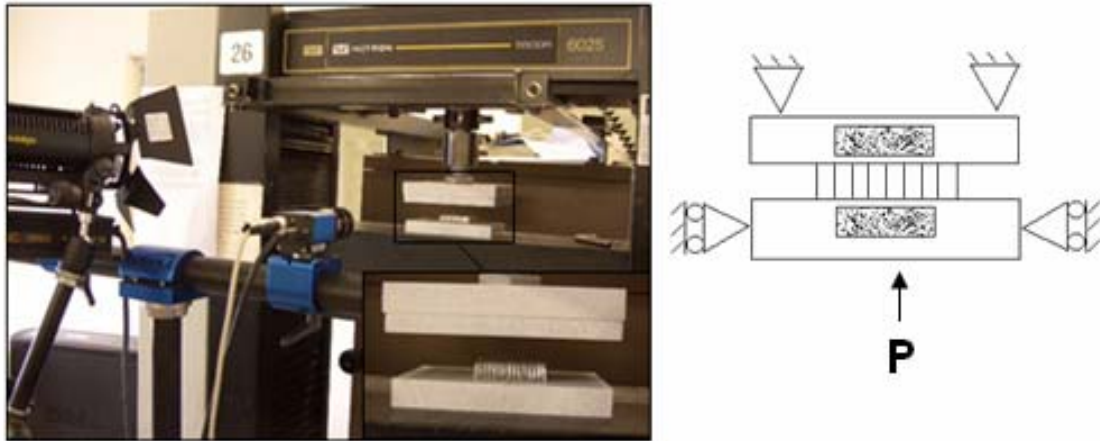
Figure 4-7: 'T' direction compression testing – Experimental arrangement

An image was taken with a marked ruler against the speckle pattern, shown in Figure 4-8. These were used to determine the number of pixels-per-mm as the single camera method displays displacements in terms of pixels. The movement of both steel plates were determined using VIC2D as shown in Figure 4-9.
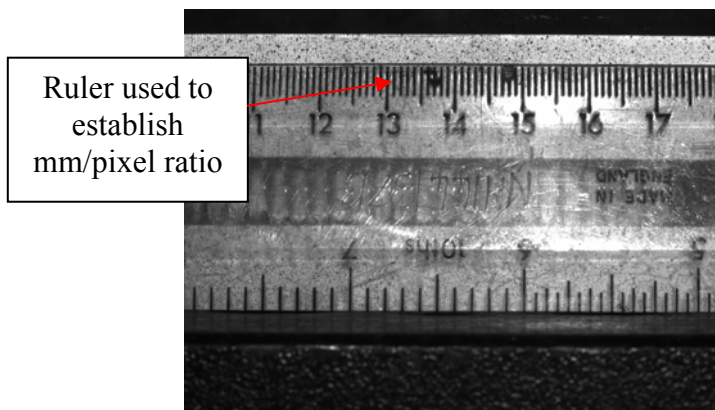
Figure 4-8: 'T' direction compression testing - Initial image with dimensions
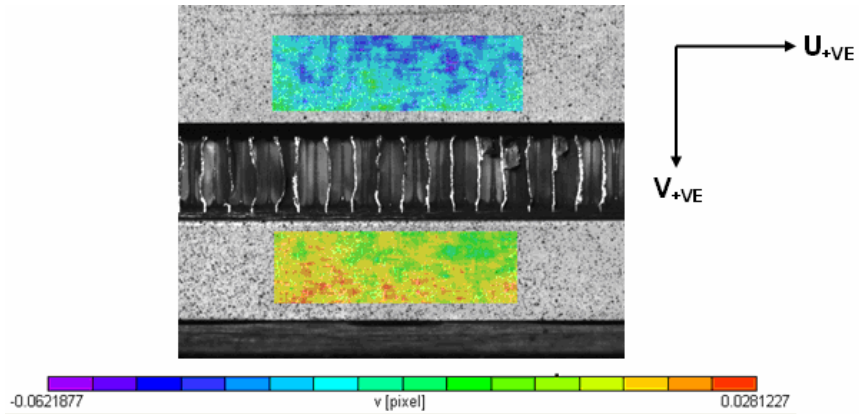
Figure 4-9: 'T' direction compression testing using DIC analysis

The movement of both plates was used to determine the stress-strain relationship, using equations 2-2 and 2-39, of the honeycomb under out-of-plane compression loading and produces the curve shown in Figure 4-10.
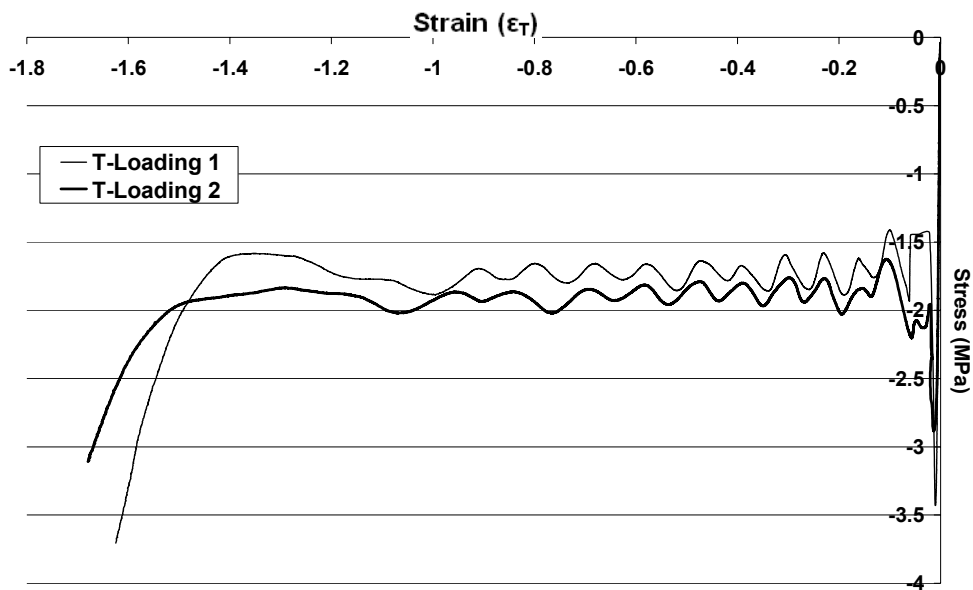
Figure 4-10: 'T' direction compression results

The cell walls were observed to buckle and fold once the initial peak load had been surpassed, producing a regular waveform during the plateau phase. The increase in loading during these periods occurs after a fold has occurred, at the peak a new fold is established which then weakens the honeycomb leading to a load reduction.

A different method was used to test the compression strength in the 'W' and 'L' directions. The loading apparatus was a compression tray shown in Figure 4-11 and the compression rate of loading was increased to 1mm/min. Friction between the upper and lower compression plates is considered negligible and is not accounted for. Friction will influence the deformation of the sample; however, the compression strength of the honeycomb in the in-plane directions is based largely on the folding and deformation of the cells walls as described by Gibson and Ashby [17].
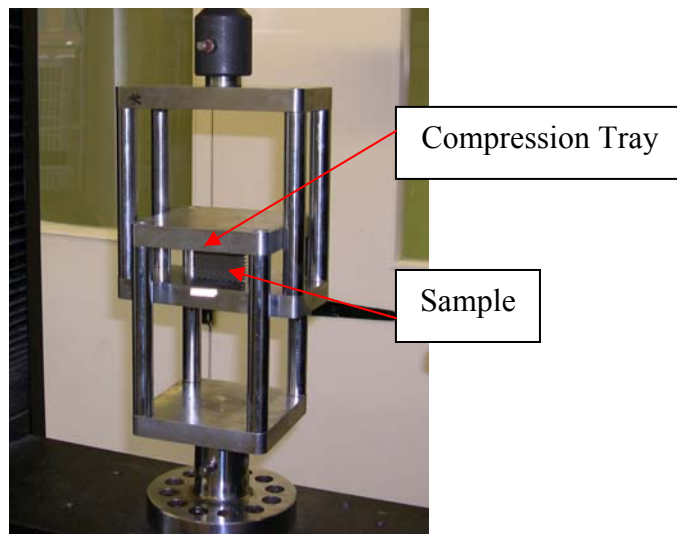
Figure 4-11: In-plane compression testing – Experimental apparatus

The stress-strain compression relationships in the in-plane directions are presented in Figure 4-12 and Figure 4-13. During in-plane loading, no initial peak loading was observed and the plateau stress is constant without any waveform. The 'L' direction is stiffer and produces higher crushing plateau strengths than the 'W' direction due to the strength of the shape of the hexagonal cell and double thickness walls at the interface between cells. These influences produce a 50% increase in crushing strength when loaded in the 'L' direction. There is also a variation in compaction strain between the two in-plane directions. The 'W' direction is folded flat leaving no gaps in the hexagonal cells at compaction. The cells cannot fold completely in the 'L' direction and produces small triangular cells at compaction. Thus 'L' direction compaction strain will always be lower than the 'W' direction.
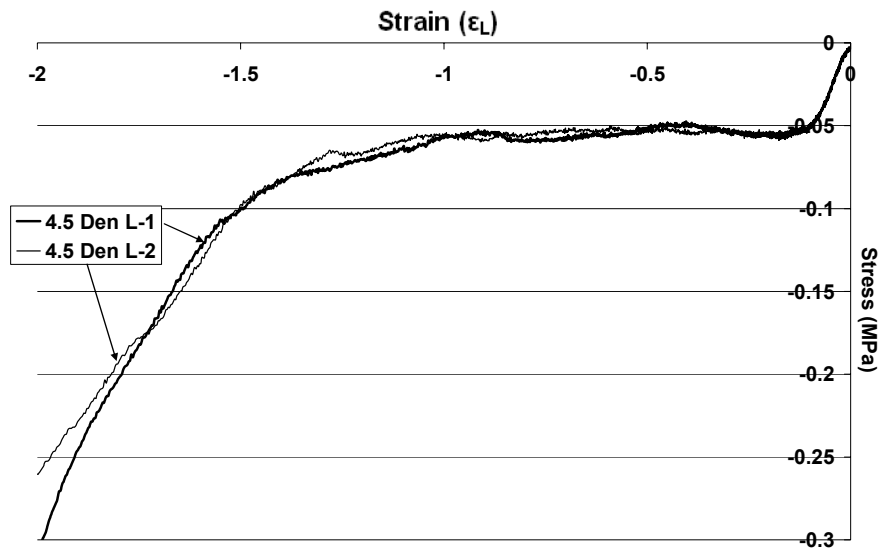
Figure 4-12: Experimental results for 'L' direction compression tests
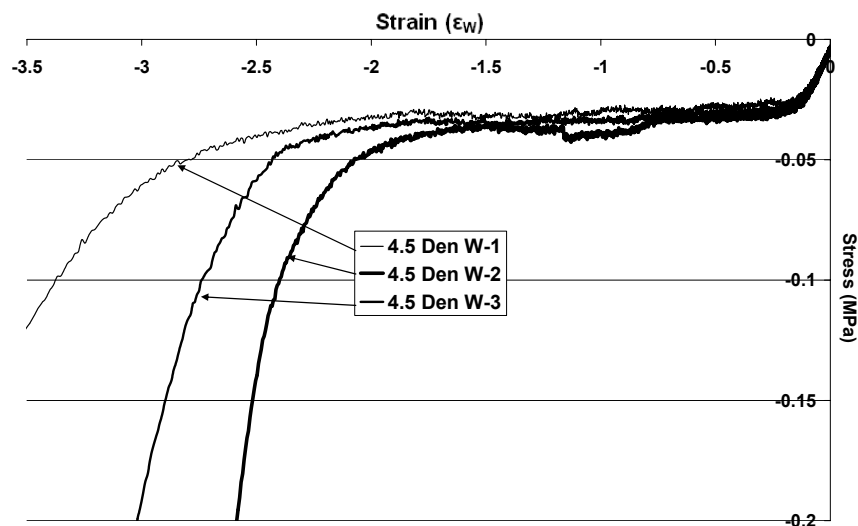
Figure 4-13: Experimental results for 'W' direction compression tests

The compression properties of honeycomb in each principal direction are summarised in Table 4-2. The peak and plateau stresses are comparable to the manufacturer's datasheet; however, out-of-plane elastic modulus is approximately one third of that stated by HEXCEL^{TM} [18]. It is likely that this is due to an experimental error where the upper and lower plates are rotating and deforming around the sample. This is shown in Figure 4-14 where d_{actual} is the actual deformation of the sample and $d_{measured}$ is the measured deformation of the sample. The $d_{measured}$ is greater than d_{actual} due to

deformation in the loading plate and reduces the calculated elastic modulus. A change in the size of the loading plates will likely overcome this error.
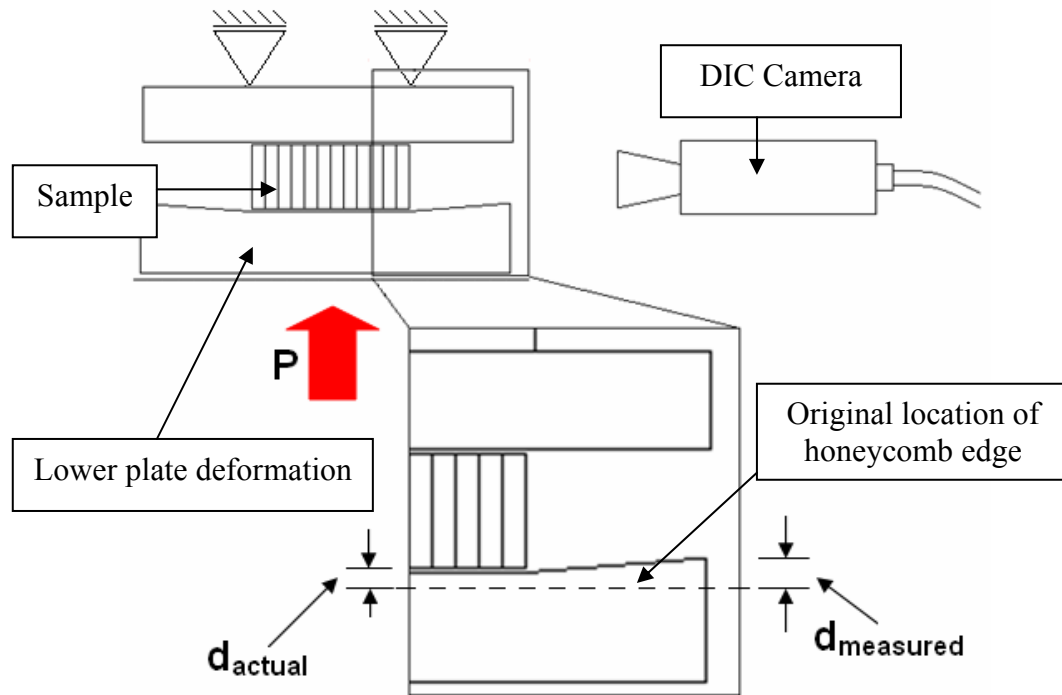
Figure 4-14: Example of apparatus deformation during 'T' compression tests

Property	Direction		
	T (HEXCEL^{TM} [18])	W	L
Elastic Modulus (MPa)	320 (1030)	0.17	0.5
Peak Stress (MPa)	-3.5 (-3.93)	-	-
Plateau Stress (MPa)	-1.75 (-1.79)	-0.035	-0.055
Compaction Strain	-1.45	-2.5	-1.4

Table 4-2: Summary of compressive properties

The compression tests in each of the principal directions have provided the required input values for the honeycomb material model, MAT41. The elastic modulus in the 'T' direction provided by HEXCEL^{TM} will be used as potential inaccuracies with the experimental results have been raised. These properties are used to calibrate the MAT41 honeycomb model and are presented in Section 5.1.1. The compression properties in the

'T' direction are also used to assess and validate the meso-shell approach to honeycomb modelling; these are presented in Section 5.1.2.

4.3.2 Pre-Crushing In-Plane effect on Out-of-Plane Properties

In some loading cases the honeycomb may undergo in plane compaction prior to out-of-plane crushing. Current constitutive models for honeycomb materials (in PAM-CRASH^{TM}) ignore the effects of such pre-deformation and, consequently, a further experimental study has been undertaken to investigate and quantify this effect. Three different types of pre-crushing are considered, they are:

- Series 1 – Transverse direction (L) locked with pre-crushing in the (W) direction as shown in Figure 4-15.
- Series 2 – Transverse direction (L) free with pre-crushing in the (W) direction as shown in Figure 4-16.
- Series 3 – Transverse direction (W) locked with pre-crushing in the (L) direction as shown in Figure 4-17.
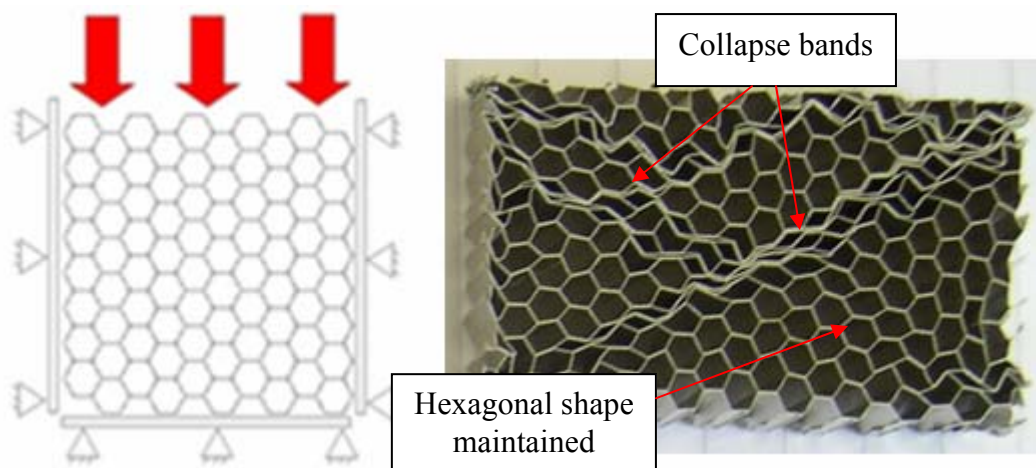
Figure 4-15: Transverse 'L' direction restricted whilst compressing in the in-plane direction
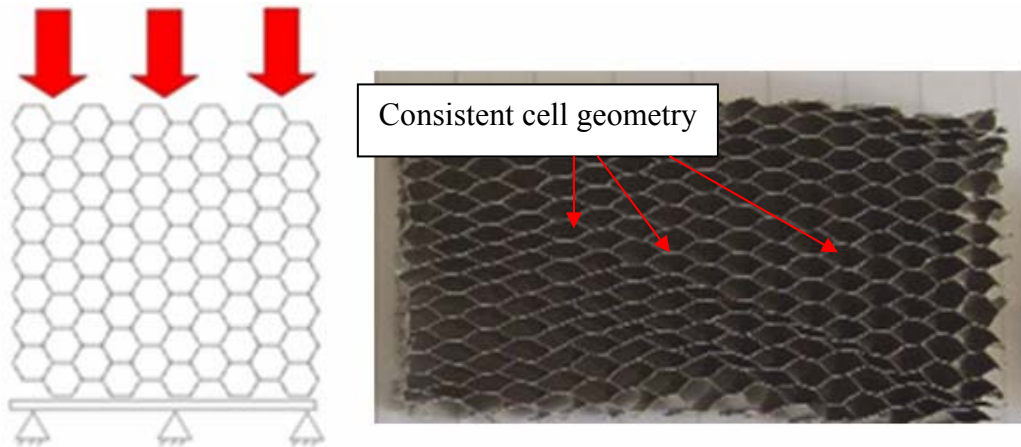
Figure 4-16: Transverse direction unrestricted whilst deforming in the 'W' direction
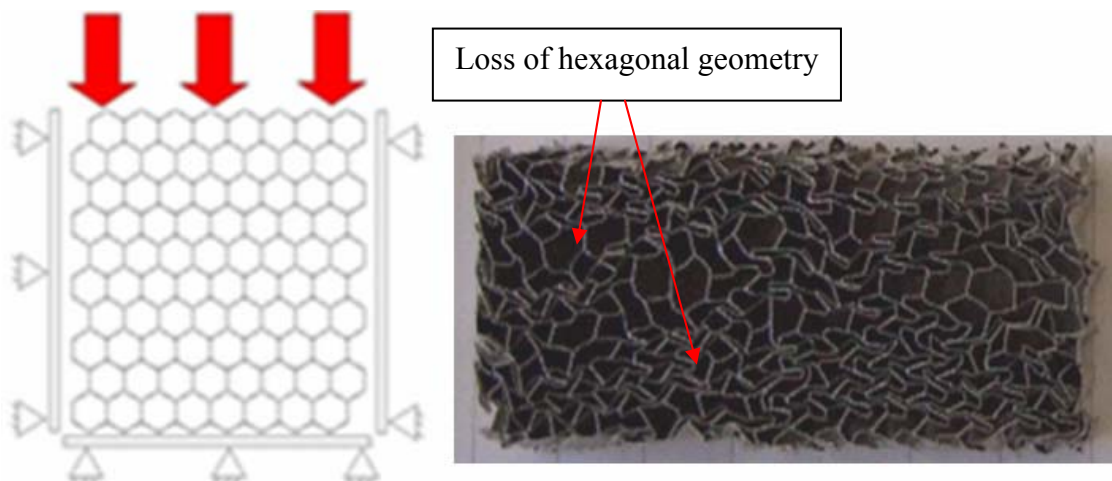
Figure 4-17: Transverse 'W' direction restricted whilst compressing in the in-plane direction

The test samples were cut having the dimensions 50mm x 50mm in the 'W' and 'L' directions. These were then compressed to produce the samples specified in Table 4-3. It was found that applying in-plane deformations, whilst imposing lateral constraints, leads to gross deformation of the cell structure; whereas removing the constraint allows the general structure of the cells to be maintained. The pre-deformed specimens were all tested using the compression apparatus shown in Figure 4-7, with the DIC system to measure compression deformations and strains. The following presents results of this study.

Pre-crush direction (Boundary condition)	Sample	In-plane compression strain and direction	Density (g/cm³)
W-Direction Compression (L-Direction Locked) Series 1	S1	-0.22 'W' Pre-crush	0.09
	S2	-0.5 'W' Pre-crush	0.1
	S3	-0.9 'W' Pre-crush	0.15
	S4	-1.6 'W' Pre-crush	0.33
W-Direction Compression (L-Direction Free) Series 2	S5	-0.22 'W' Pre-crush	0.08
	S6	-0.5 'W' Pre-crush	0.1
	S7	-0.9 'W' Pre-crush	0.15
	S8	-1.6 'W' Pre-crush	0.27
L-Direction Compression (W-Direction Locked) Series 3	S9	-0.22 'L' Pre-crush	0.09
	S10	-0.5 'L' Pre-crush	0.12
	S11	-0.9 'L' Pre-crush	0.18
	S12	-1.6 'L' Pre-crush	0.31

Table 4-3: Sample geometries for in-plane pre-crushed experiments

The test series with restrictions on the initial deformation show that the peak and plateau forces are approximately constant despite the amount of in-plane deformation as shown in Figure 4-18 and Figure 4-20. The cell wall folding mechanism was consistently isolated at the crushing wall; this is shown in Figure 4-21. Sample 12, the largest in-plane deformed sample in Series 3, displays a significant drop in strength during the plateau phase. This drop in strength is due to a single large fold that occurs in the cell walls. In the case of no restrictions imposed in the transverse direction during in-plane deformation, Series 2 experiments, there was a more pronounced drop in plateau strength as the in-plane deformation increased, Figure 4-19. These reductions in strength are due to larger folding mechanisms that occur in the 'T' direction during out-of-plane compression; the single large folding mechanism observed during Sample 8 testing is shown in Figure 4-22.
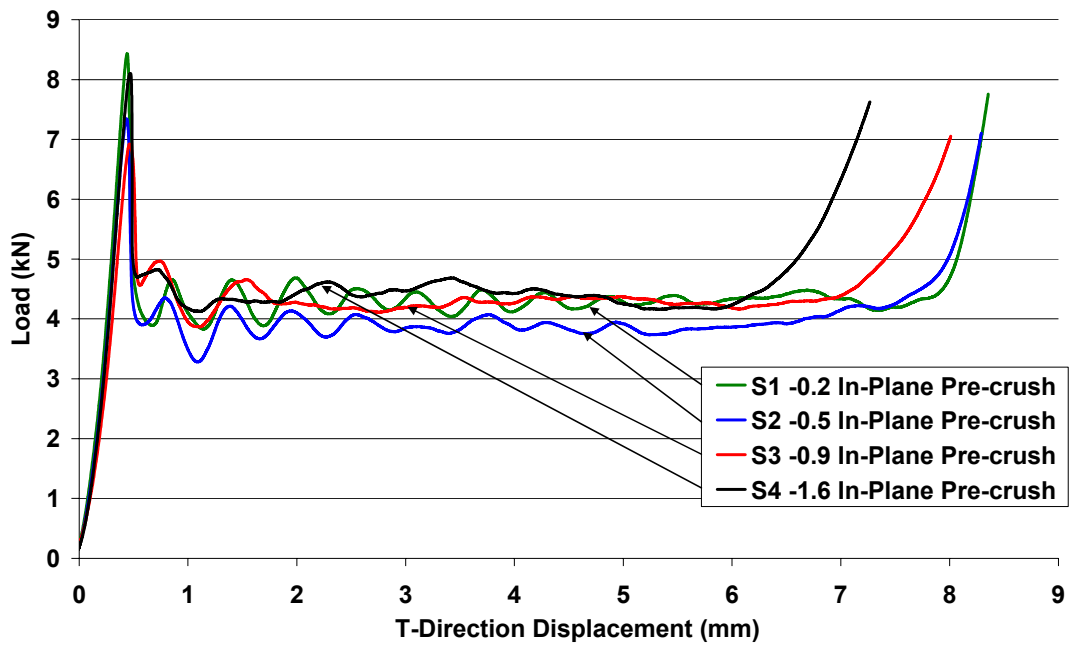
Figure 4-18: Force displacement results from Series 1 experiments
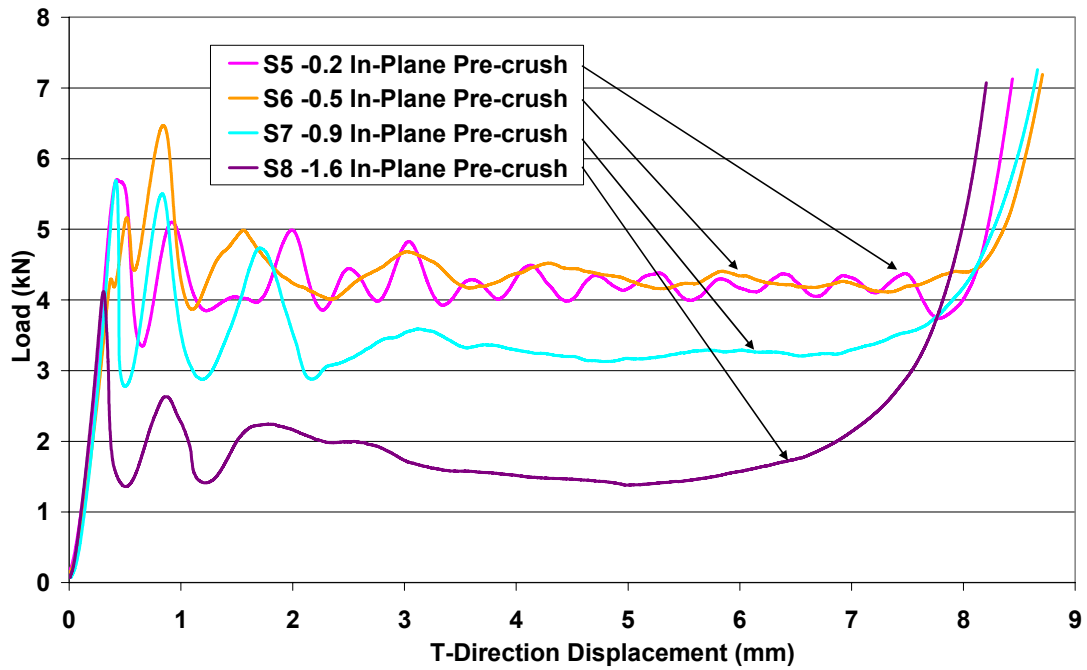
Figure 4-19: Force displacement results from Series 2 experiments
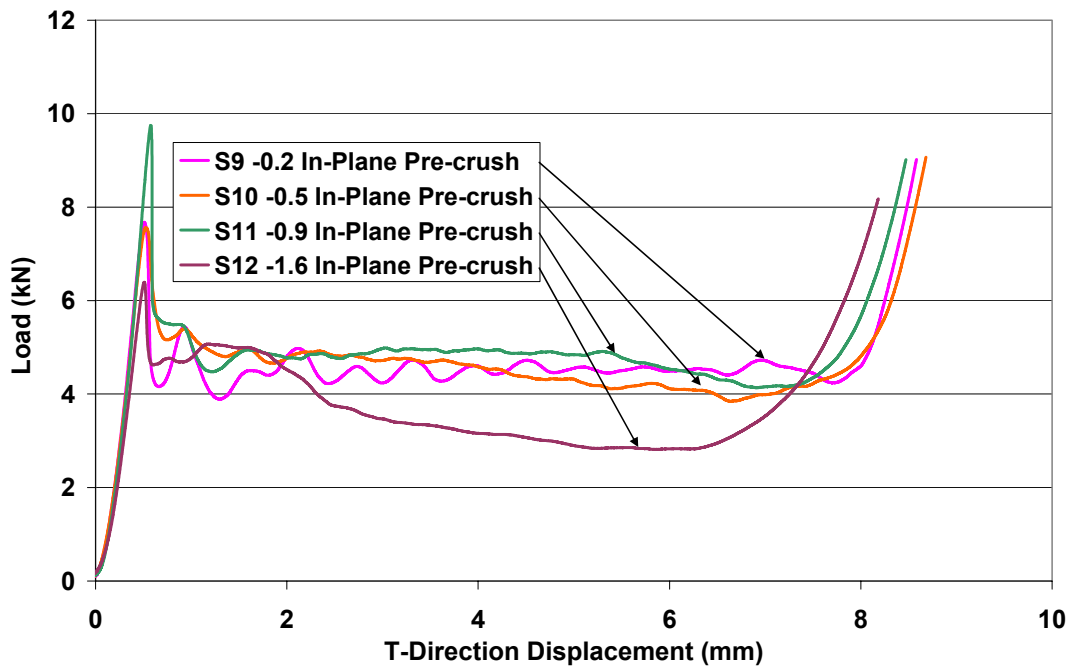
Figure 4-20: Force displacement results from Series 3 experiments
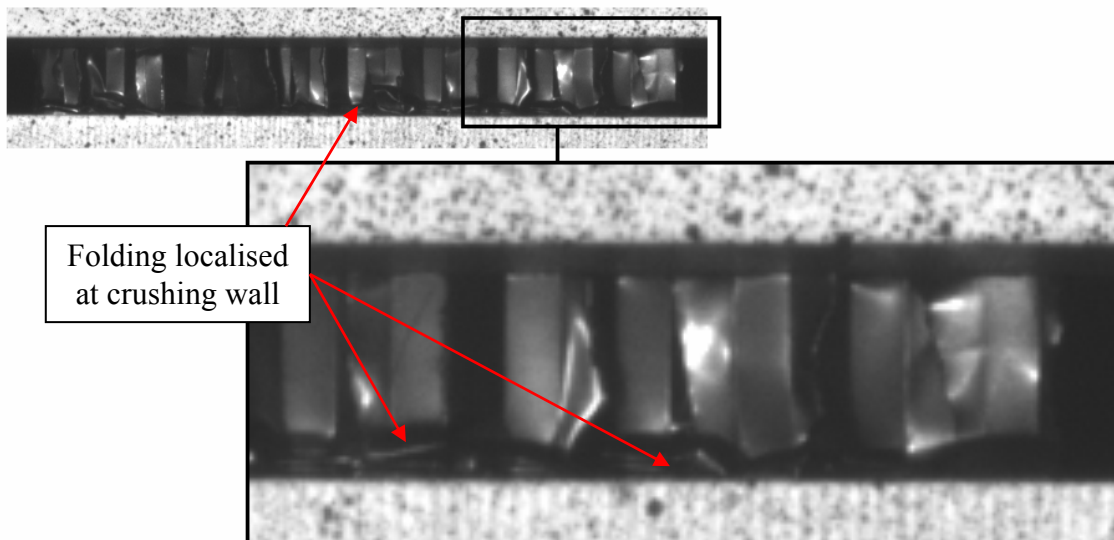
Figure 4-21: Sample 3 – Localised cell wall folding at $\varepsilon_T = 0.5$
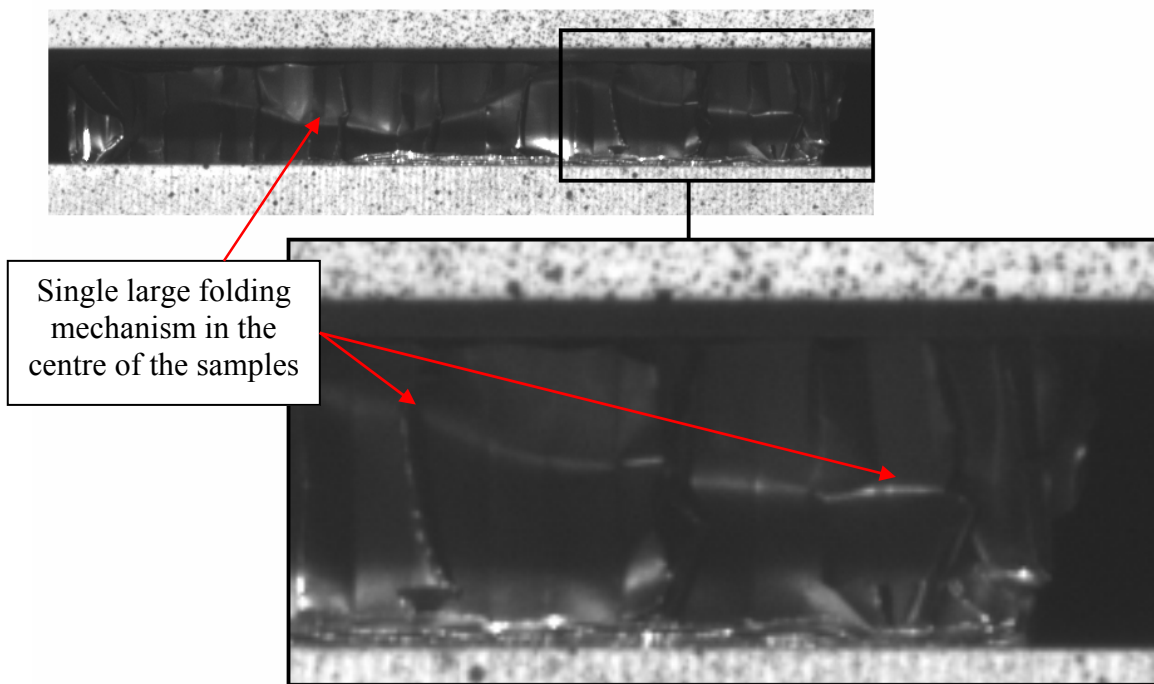
Figure 4-22: Sample 8 - Single fold at $\varepsilon_T = 0.2$

The average plateau strengths from all three series are shown in Figure 4-23 and Figure 4-24. The reduction in average plateau strength during the Series 2 experiments is shown in Figure 4-23 as the in-plane pre-crushing increases. As the transverse direction was unrestricted for this series the cells become less hexagonal and therefore the folding mechanism is less restricted. A strength reduction is also observed for Sample 12 from the Series 3 tests.
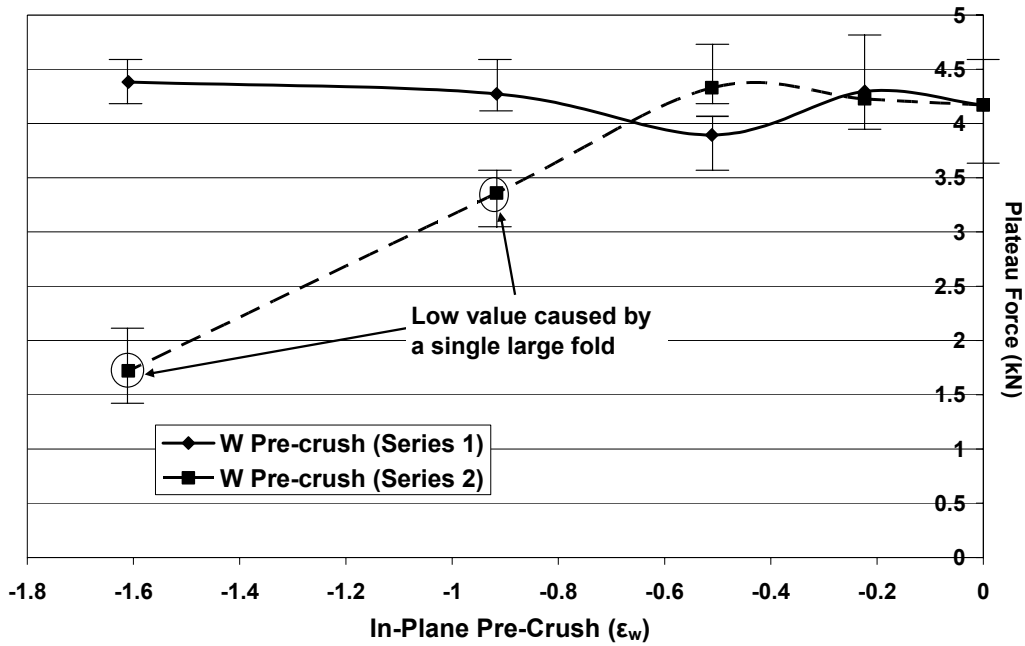
Figure 4-23: Plateau strengths from Series 1 and 2 experiments
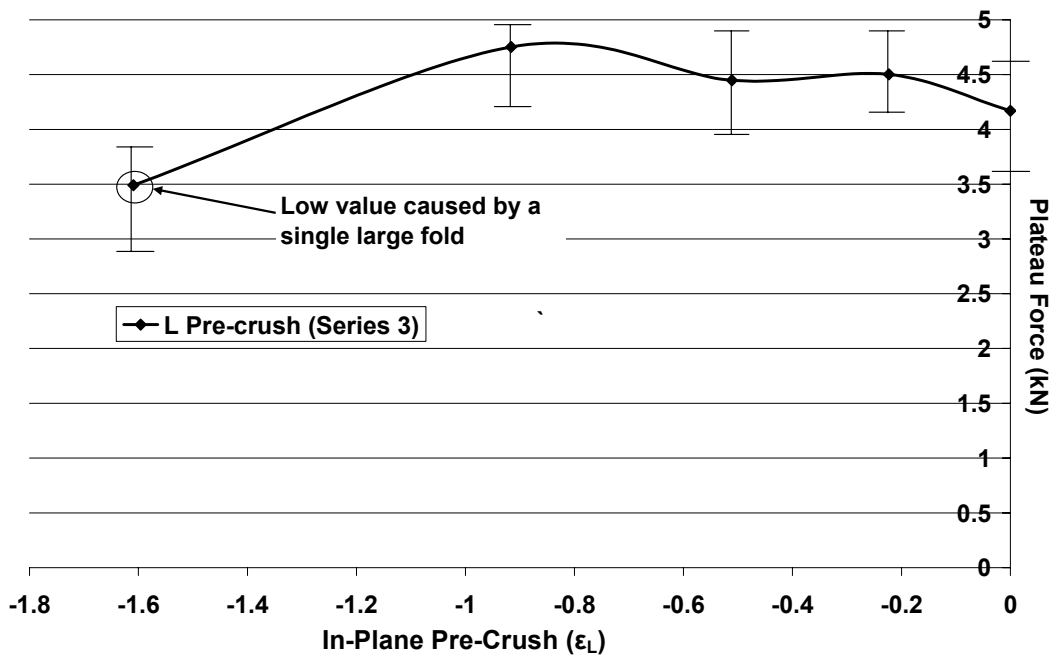
Figure 4-24: Average plateau strengths from Series 3 experiments

The plateau stresses must increase if plateau forces remain constant due to a reduction in cross-sectional area. Figure 4-25 shows a linear relationship between density and

95

average plateau stress for the Series 1 tests. This figure also displays the maximum and minimum plateau stresses observed during these tests. Figure 4-26 presents the relationship between plateau stresses and density for the Series 2 tests. In this case, a linear increase in average plateau stress is not observed. This is due to the advent of singularly large folding mechanisms occurring in the sample during out-of-plane loading described previously and shown in Figure 4-22. Figure 4-27 presents the relationship between plateau stresses and density for the Series 3 tests.

The change in plateau strength due to in-plane deformation can be represented by the following equation;

$$\sigma_{Tt} = \frac{\sigma_{T0}}{(e(\varepsilon_W)) * (e(\varepsilon_L))}, \qquad [4\text{-}1]$$

where σ_{TO} is the original undamaged plateau strength of the honeycomb and σ_{Tt} is the damaged plateau strength. Equation 4-1 is compared with Series 1 and 3 in Figure 4-25 and Figure 4-27 respectively. The new law is shown to be compatible with both loading conditions.
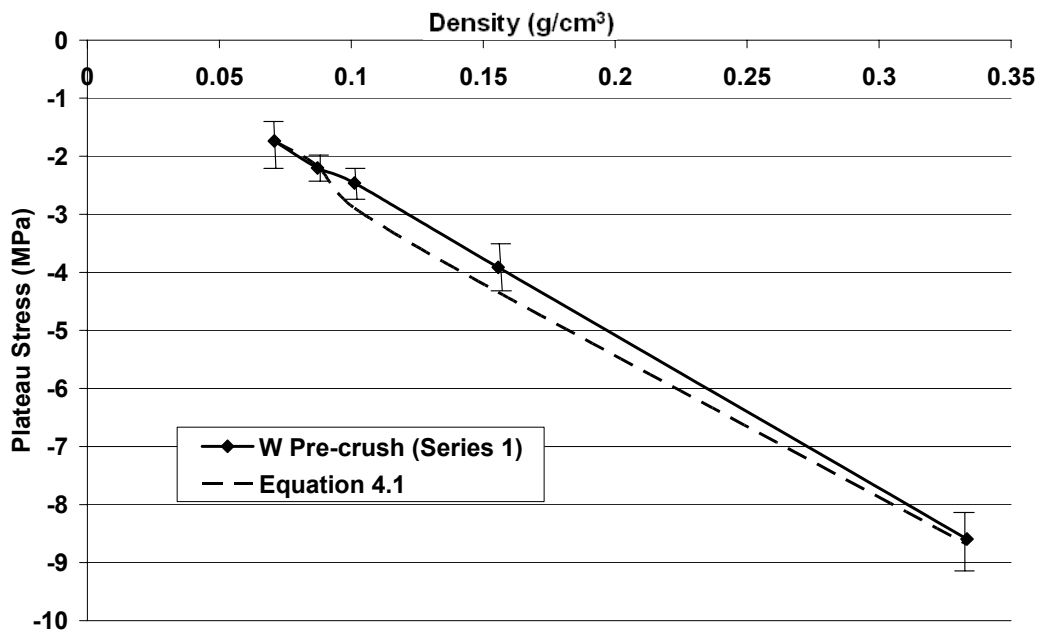
Figure 4-25: Average, maximum and minimum plateau stresses for test Series 1
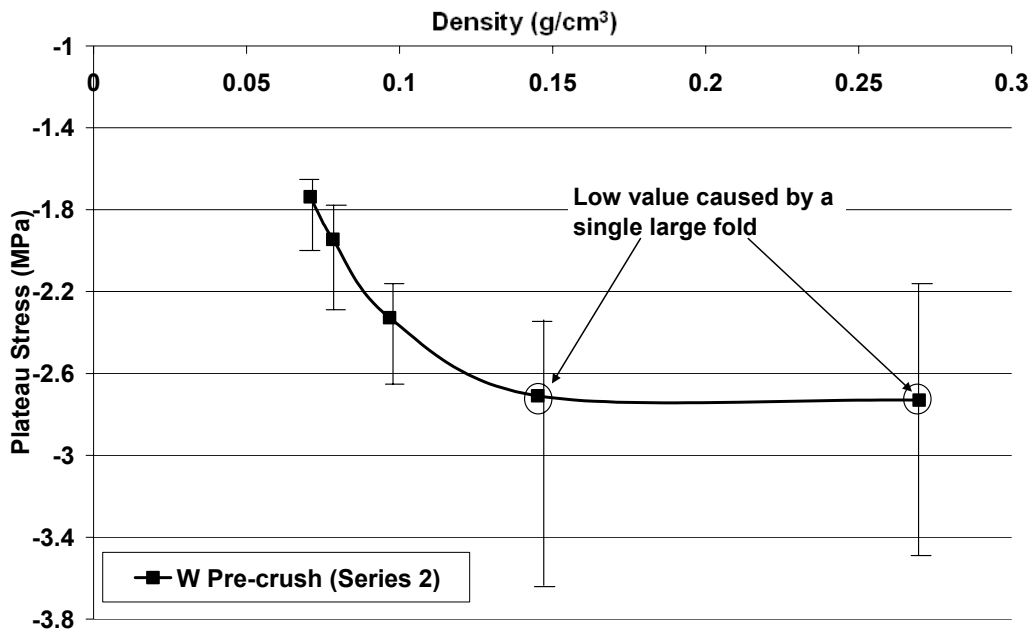
Figure 4-26: Average, maximum and minimum plateau stresses for test Series 2
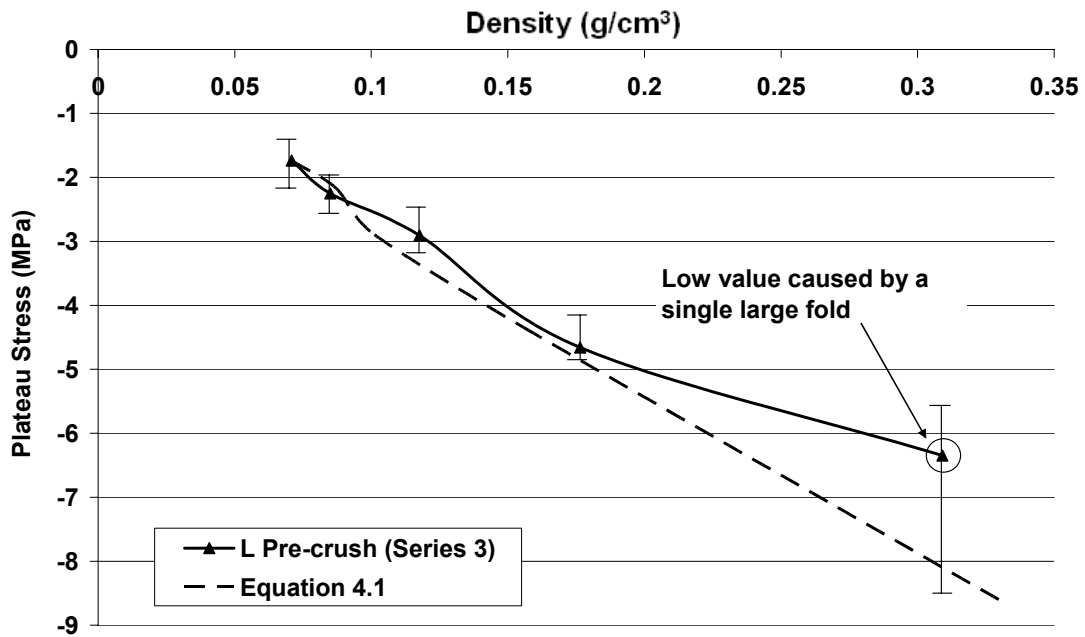
Figure 4-27: Average, maximum and minimum plateau stresses for test Series 3

In addition to plateau strength observations, variations in compaction strain are also observed. Figure 4-28 shows the variations of 'T' direction compaction strain due to in-plane deformation.
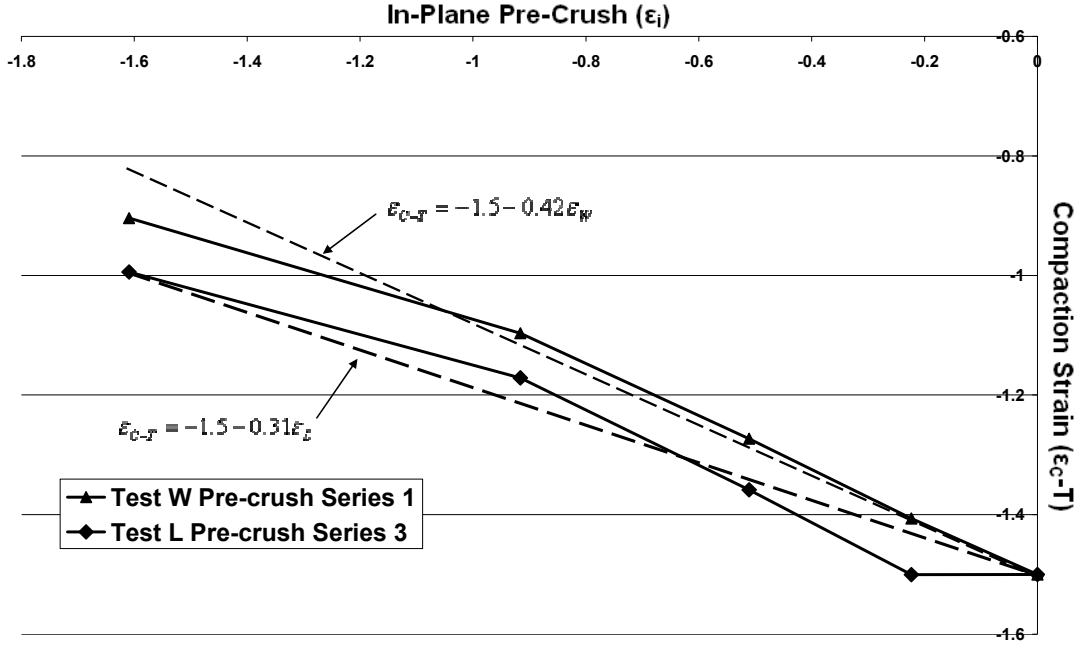
Figure 4-28: Compaction strain variation due to in-plane deformation

The variation in 'T' direction compaction strain due to in-plane deformation is approximated by equations 4-2 and 4-3, where ε_{C-T} is the 'T' direction compaction strain,

$$\varepsilon_{C-T} = -1.5 - 0.31\varepsilon_L,$$
[4-2]

$$\varepsilon_{C-T} = -1.5 - 0.42\varepsilon_W.$$
[4-3]

The variations in 'T' direction compression properties presented here are used to evaluate the MAT41 material model. These laws are also implemented into the MAT41 honeycomb model to improve the relationship between in-plane deformations on out-of-plane properties. The assessment and improvement of the honeycomb solid element model is presented in Section 5.1.1. An investigation of the meso-shell capability to reproduce the variation in 'T' direction properties due to in-plane loading is also presented in Section 5.1.2

In-Plane Pre-crushing Influence on the Out-of-Plane Compression Properties of High Density Core Material

To further investigate the influence of in-plane pre-crushing on the out-of-plane compression properties of honeycomb, an investigation using the high density core material present in the nosecone structure has been conducted. The samples were pre-crushed in the 'W' direction with restrictions in the 'L' direction; identical test conditions to the Series 1 tests described previously. The original sample size before in-plane compression is 50mm x 50mm.

Figure 4-29 presents the force-displacement curves from out-of-plane compression testing. The peak and plateau crushing forces remain the same regardless of the extent of pre-compression. The average, minimum and maximum compression forces are also presented in Figure 4-30 which also shows the variance between maximum and minimum plateau force reduces as the extent of in-plane deformation increases.
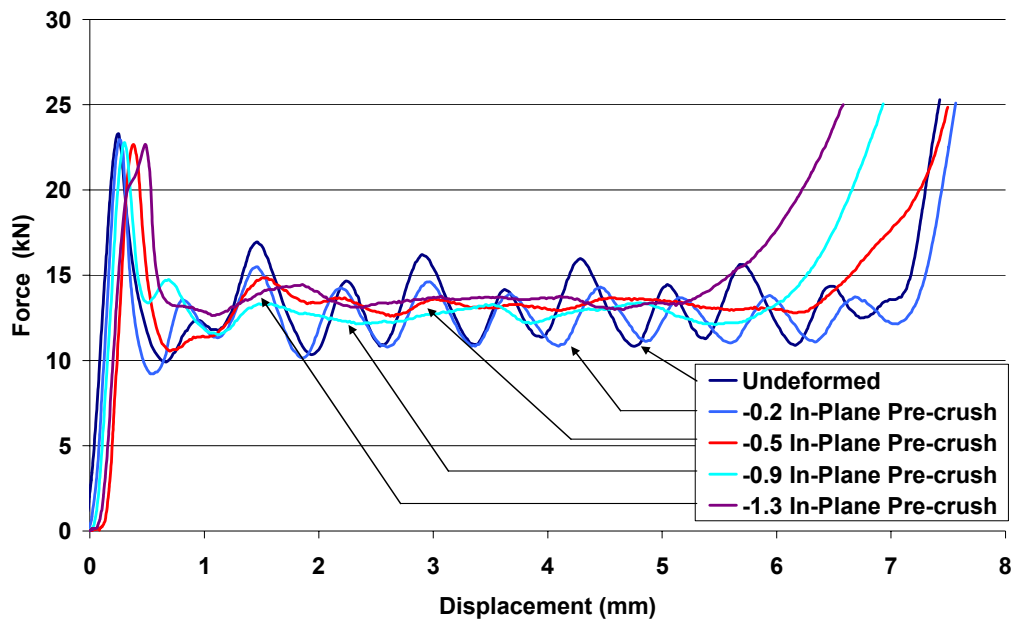
Figure 4-29: Force-displacement curves for the high density core investigation
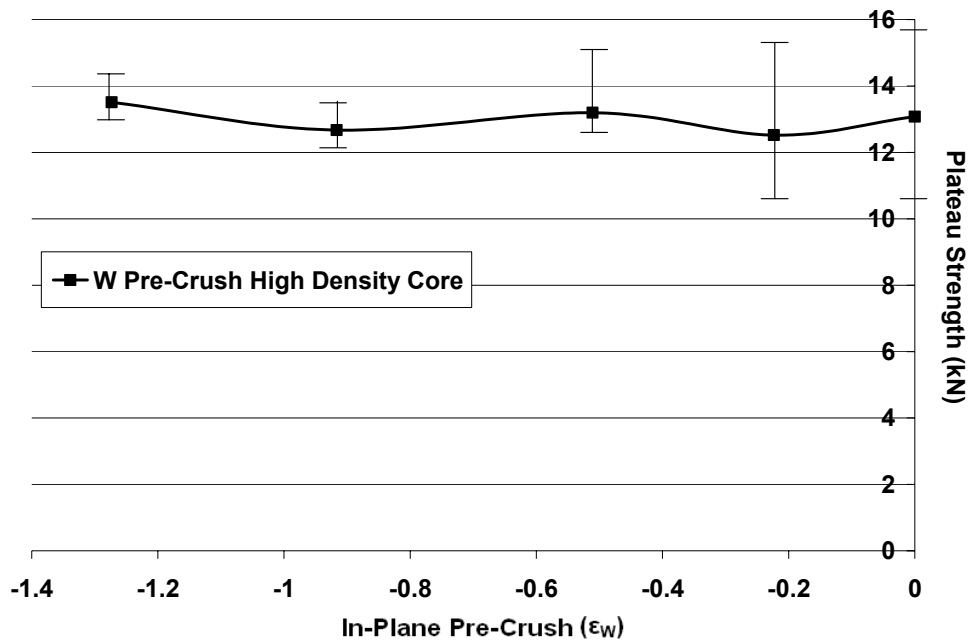
Figure 4-30: High density core plateau strength variation with in-plane pre-crush

Figure 4-31 presents the variation in plateau crushing stress with the increase in material density. The derived formula to determine the change in plateau crushing stress with in-plane deformation for the low density material, equation 4-1, is also shown in this figure. These results show that equation 4-1 is compatible with this honeycomb type without any modification. It is logical to suggest that similar sized hexagonal cell honeycombs will likely follow the same trend. A further study into the influence of in-plane deformation on larger cell honeycombs and possibly foams would be of value to determine the consistency or variance of this material law.

Figure 4-29 also shows a reduction in compaction strain as in-plane deformation increases. This reduction is shown in Figure 4-32 with a linear approximation of the change in compaction strain with in-plane compression strain. This approximation takes the form of equation 4-4.

$$\varepsilon_{C-T} = -1.25 - 0.39\varepsilon_W \qquad\qquad [4\text{-}4]$$

The compaction strain of the high density sample is lower than that of the corresponding low density sample. The slope of the curve is similar between both honeycomb material types. This research suggests a general relationship for this hexagonal cell size to be;

100

$$\varepsilon_{C-T} = \varepsilon_{C-T0} - 0.4\varepsilon_i, \qquad\qquad [4\text{-}5]$$

where, ε_{C-T0} is the compaction strain in the 'T' direction of a undeformed hexagonal cell honeycomb and ε_i is the in-plane compression strain. A further investigation would be of value to determine the change in compaction strain of larger cell honeycomb materials.
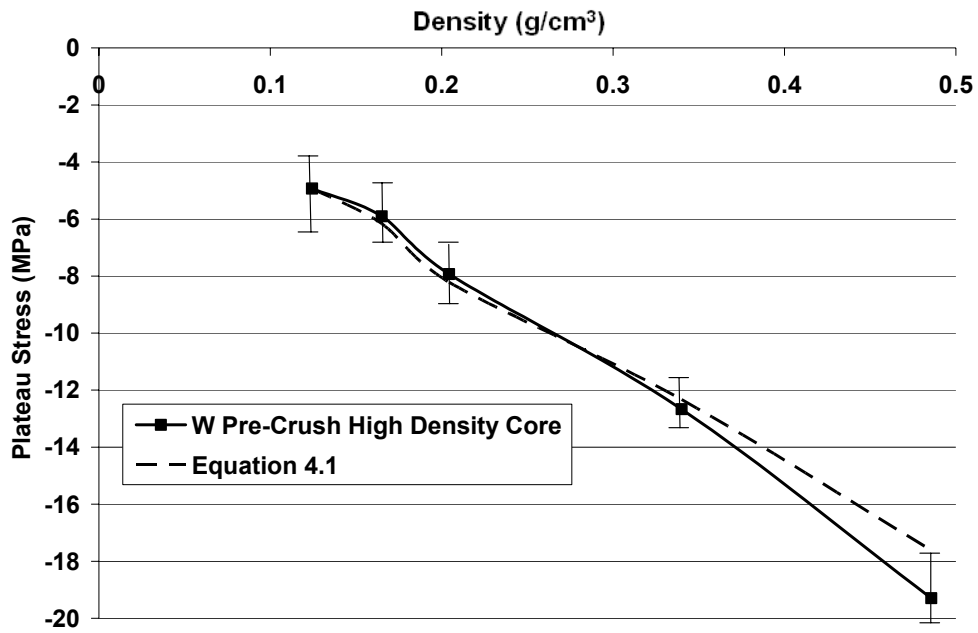
Figure 4-31: High density core plateau stress variation with density
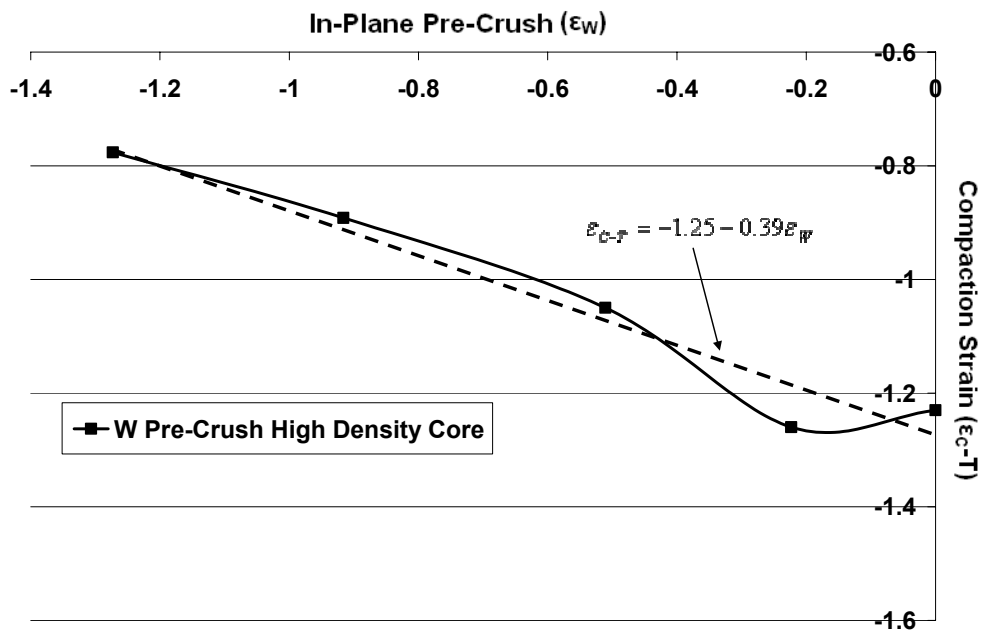
Figure 4-32: High density core compaction strain variation with in-plane pre-crush

4.3.3 Testing Procedure and Results for the Multi-axial Loading of Honeycomb Material

A standard Arcan apparatus has been modified to investigate the effects of mixed shear-compression loading and develop relationships between loading direction and the properties in the principal directions of the honeycomb material. The modified Arcan apparatus, shown in Figure 4-33 and presented in Appendix C, uses a new guiding rail mechanism. The rail reduces the rotational force at the load cell locking pin and thus prevents potential damage to test equipment. This also reduces the possibility of localised buckling of the honeycomb sample, as described previously in Section 2.2.1.
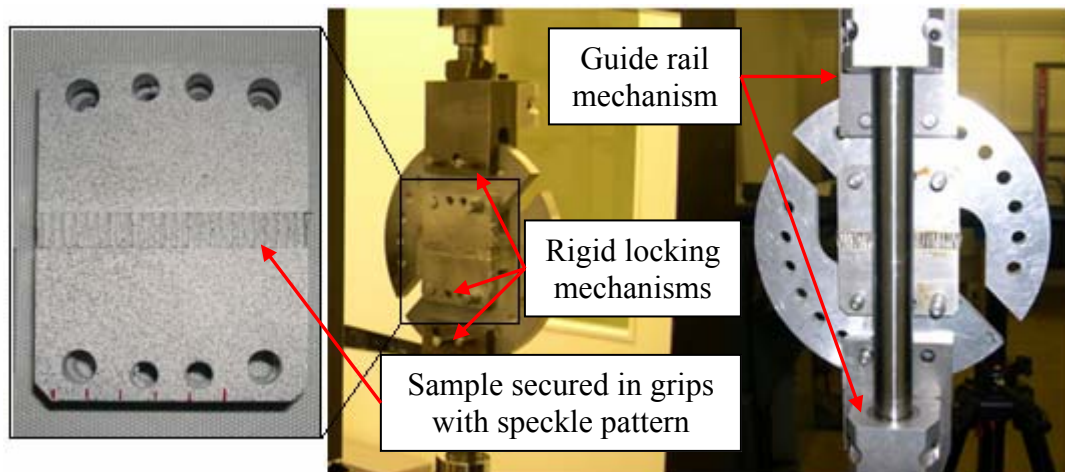
Figure 4-33: Modified Arcan apparatus

The sample is held between two aluminium grips and secured in place using Redux 330 film adhesive. A two part epoxy tabbing glue, such as Araldite 420A/B, could also have been used; however, it was found to be very difficult to maintain a consistent glue line thickness and this was found to influence results. The film adhesive produced a consistent glue line thickness with all specimens and was used for this investgation. A speckle pattern is applied to the grips and the optical measuring system is used in the single camera mode to determine relative displacement between the grips.

A method of measuring horizontal loading is required in order to obtain load components applied to the specimen. For this a method to determine horizontal loads

from the horizontal displacements of the sample grips was developed. The Arcan was configured to 45^0 and a low friction surface placed between the grips, as shown in Figure 4-34. In this configuration, the measured vertical force, F_V, will be equal to the horizontal force, F_H. The optical measuring system is then used to measure the horizontal displacement of the upper and lower grips giving dH_1 and dH_2 respectively, Figure 4-35.
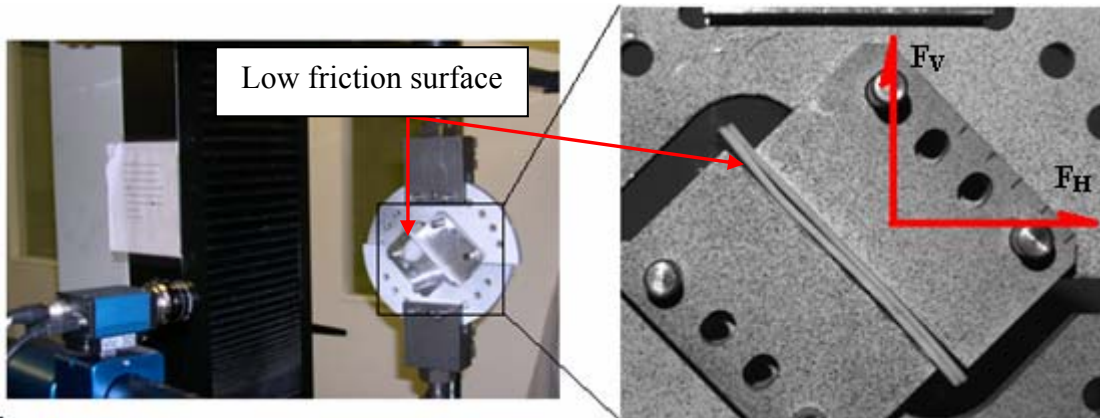
Figure 4-34: Horizontal force calibration method
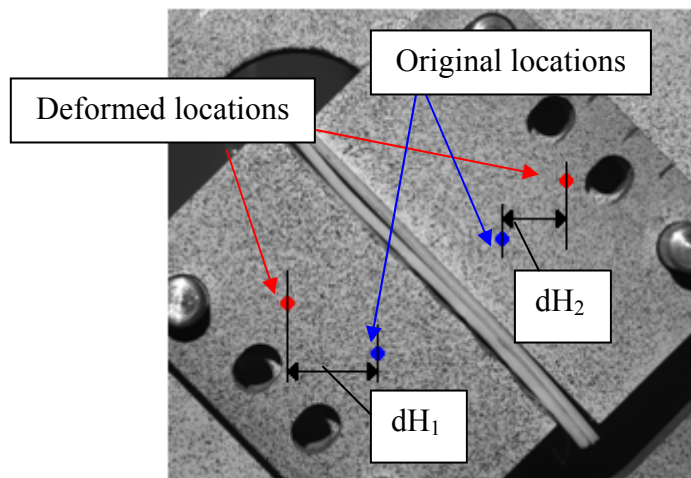
Figure 4-35: Horizontal displacement measured by DIC system

The relationship between total horizontal displacement and horizontal force is shown in Figure 4-36. The calibration 1 curve was produced before the honeycomb investigation, the calibration curves 2, 3 and 4 were produced after the honeycomb investigation. Figure 4-36 shows the horizontal stiffness of the Arcan apparatus remains constant throughout the testing series. A best fit relationship is established from experimental

data and gives equation 4-4. This relationship between horizontal displacement and force is defined as;

$$111.37(dH_{TOTAL})^2 + 126.1(dH_{TOTAL}) = F_H, \qquad [4\text{-}4]$$
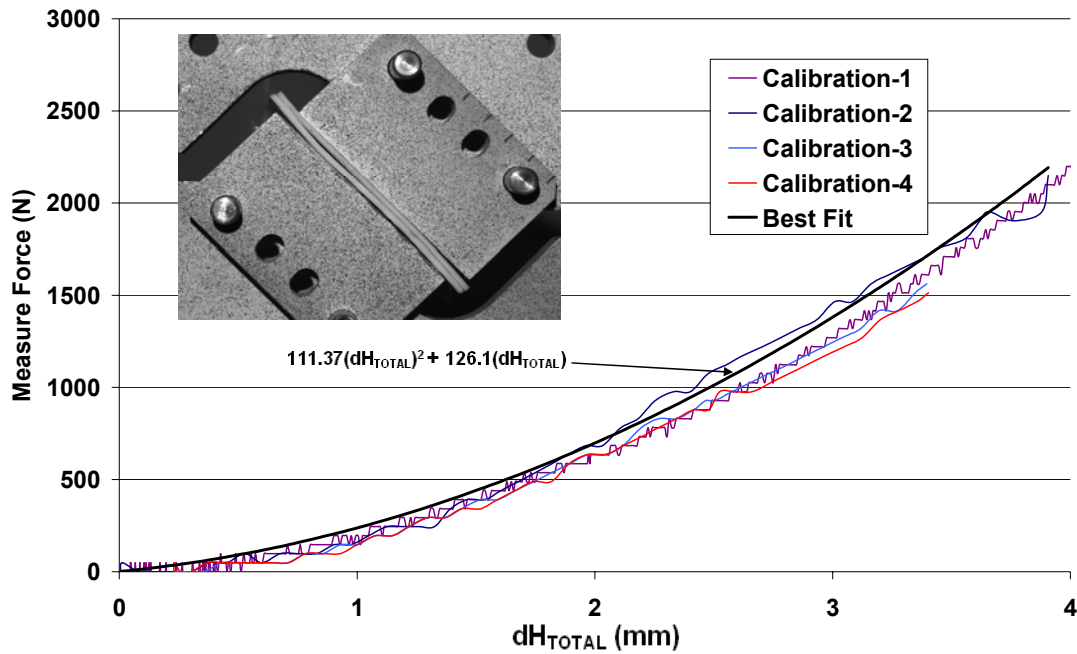
Figure 4-36: Total horizontal displacement and force relationship

From the recorded values for vertical force and the calculated value of horizontal force it is possible to use simple transformations to obtain the out-of-plane normal compressive and shear properties. Measurements are taken in the global frame and are then converted to a local frame as shown in Figure 4-37.
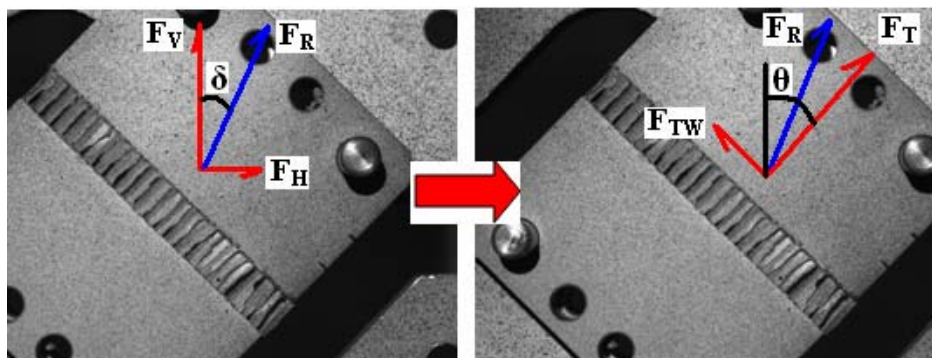
Figure 4-37: Conversion from (a) global system to (b) local system

The horizontal, F_H, and vertical, F_V, forces are used to establish a resolved force, F_R, and the resolved force direction, δ, using equations 4-5 and 4-6,

$$F_R = \sqrt{\left(F_V^2 + F_H^2\right)}, \qquad\qquad [4\text{-}5]$$

$$\delta = \tan^{-1}\left(\frac{F_H}{F_V}\right), \qquad\qquad [4\text{-}6]$$

where, F_R is the resolved force of the grips and δ is the direction of the resolved force. Equations 4-5 and 4-6 are then used to determine the stresses in the principal directions using equations 4-7 and 4-8,

$$F_T = F_R \cos(\theta - \delta) \Rightarrow \sigma_T = \frac{F_T}{A}, \qquad\qquad [4\text{-}7]$$

$$F_{TW} = F_R \sin(\theta - \delta) \Rightarrow \sigma_{TW} = \frac{F_{TW}}{A}, \qquad\qquad [4\text{-}8]$$

where A is the cross-sectional area of the honeycomb sample, θ is the angle between the direction of loading and the sample normal direction, σ_T is the stress in the 'T' direction and σ_{TW} is the out-of-plane shear stress. The resultant stresses are used to determine the peak, average plateau and plateau initiation normal and shear stresses; the normal stress definitions are shown in Figure 4-38. The investigation by Mohr and Doyoyo [25] found that at angles of loading approaching shear, the 'T' directional average plateau stress would indicate a tensile loading condition.
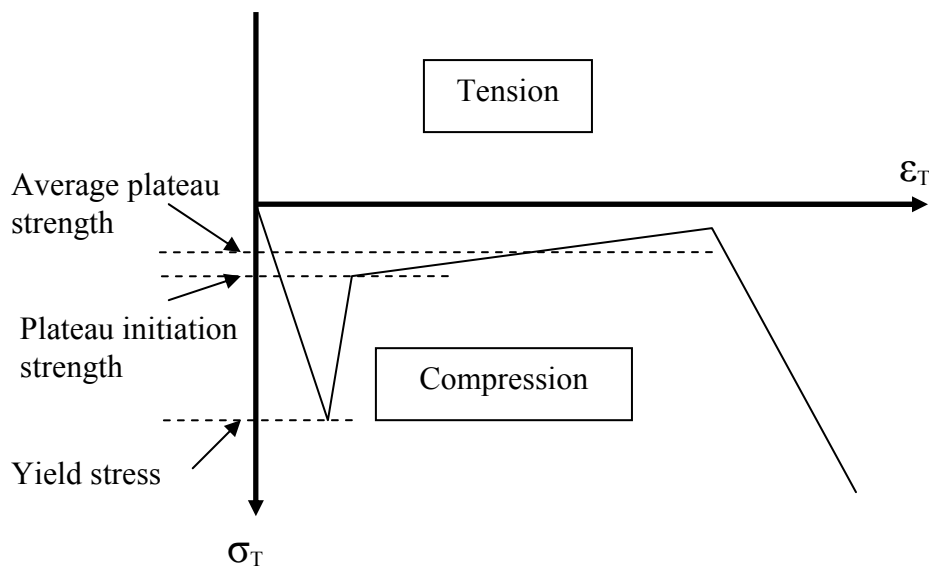
Figure 4-38: Definition of 'T' direction properties

The 'T-TW' loading conditions represent compression in the 'T' direction and shear in the 'TW' direction. The peak stresses for the 'T' and 'TW' directions are shown in Figure 4-39 and have been used to determine direction dependent laws for peak stress in equations 4-9 and 4-10 for normal and shear loads respectively.
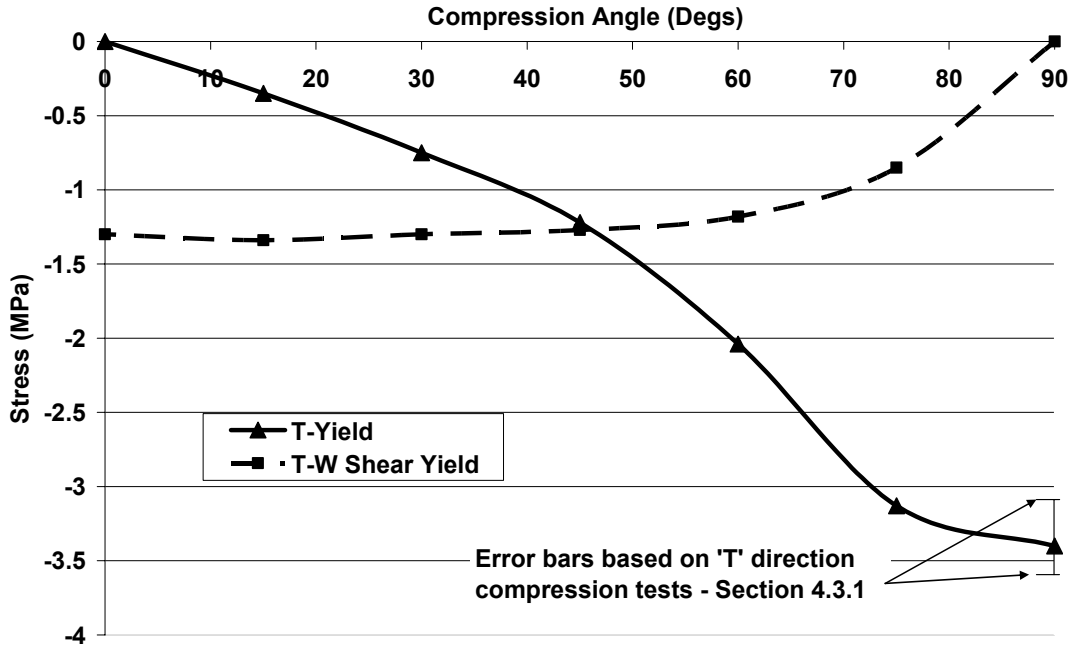
Figure 4-39: 'T-TW' loading yield stress variation with load direction

$$\sigma_{T-Yield} = 3e^{-7}\alpha^4 - 5e^{-5}\alpha^3 + 2e^{-3}\alpha^2 - 0.05\alpha, \qquad\qquad [4\text{-}9]$$

$$\sigma_{TW-Yield} = 8.e^{-8}\alpha^4 - 1.045e^{-5}\alpha^3 + 5e^{-4}\alpha^2 - 8.2e^{-3}\alpha - 1.3, \qquad [4\text{-}10]$$

where α is the loading direction. A near linear plateau initiation relationship between both normal and shear was observed as shown in Figure 4-40. This was also used to produce direction dependent laws for the normal and shear loading conditions, presented as equations 4-11 and 4-12 respectively.

$$\sigma_{T-Plateau} = 3.95e^{-8}\alpha^4 - 8e^{-6}\alpha^3 + 4e^{-4}\alpha^2 - 0.02\alpha \qquad\qquad [4\text{-}11]$$

$$\sigma_{TW-Plateau} = 9e^{-5}\alpha^2 - 1 \qquad\qquad [4\text{-}12]$$

The average plateau stress is shown in Figure 4-41. The 'T' direction is moves into a tensile loading condition at angles below 15^0.
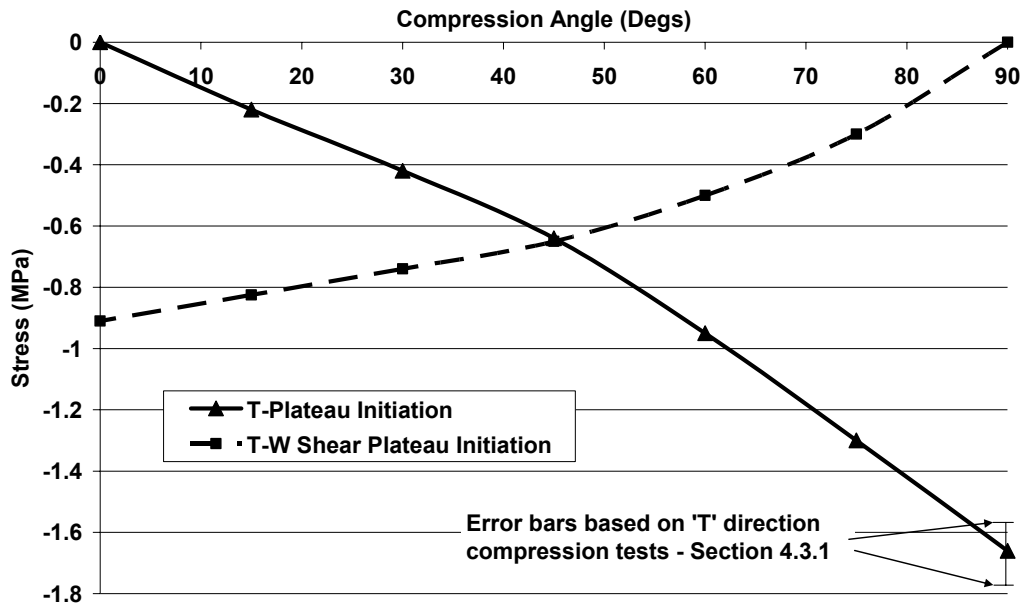
Figure 4-40: 'T-TW' loading plateau stress variation with load direction
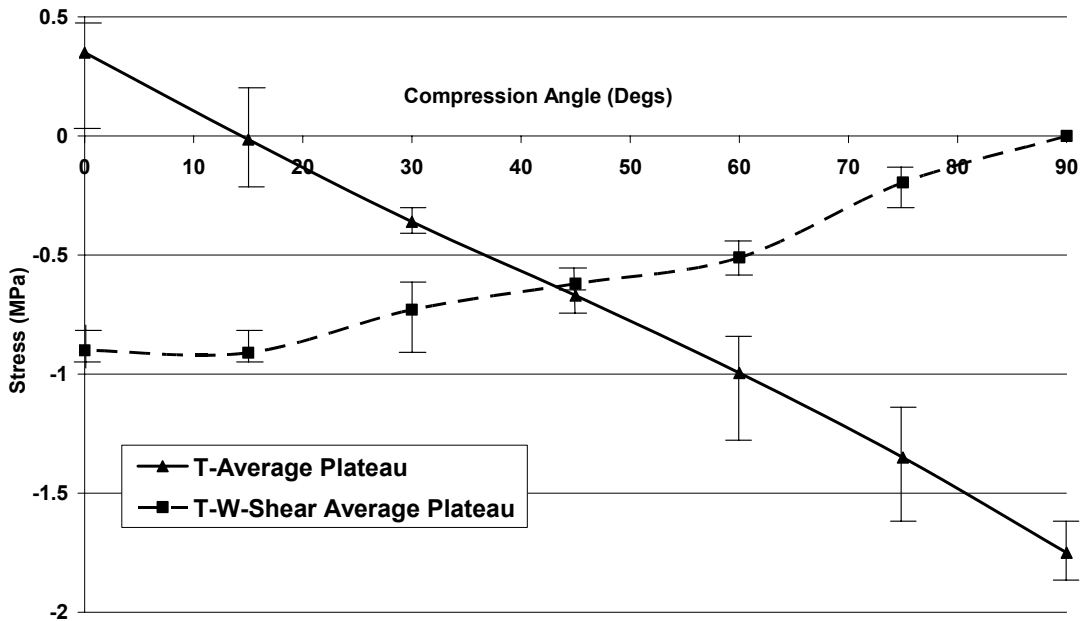
Figure 4-41: Average plateau stress variation with load direction

The results for peak loading and plateau initiation can be presented together as shown in Figure 4-42. The peak loading is shown to follow an elliptical path, whilst the plateau stresses have an approximately linear relationship. The elliptical relationship is similar

to that observed by Mohr and Doyoyo [25] suggesting that hexagonal honeycomb materials exhibit this form of relationship.
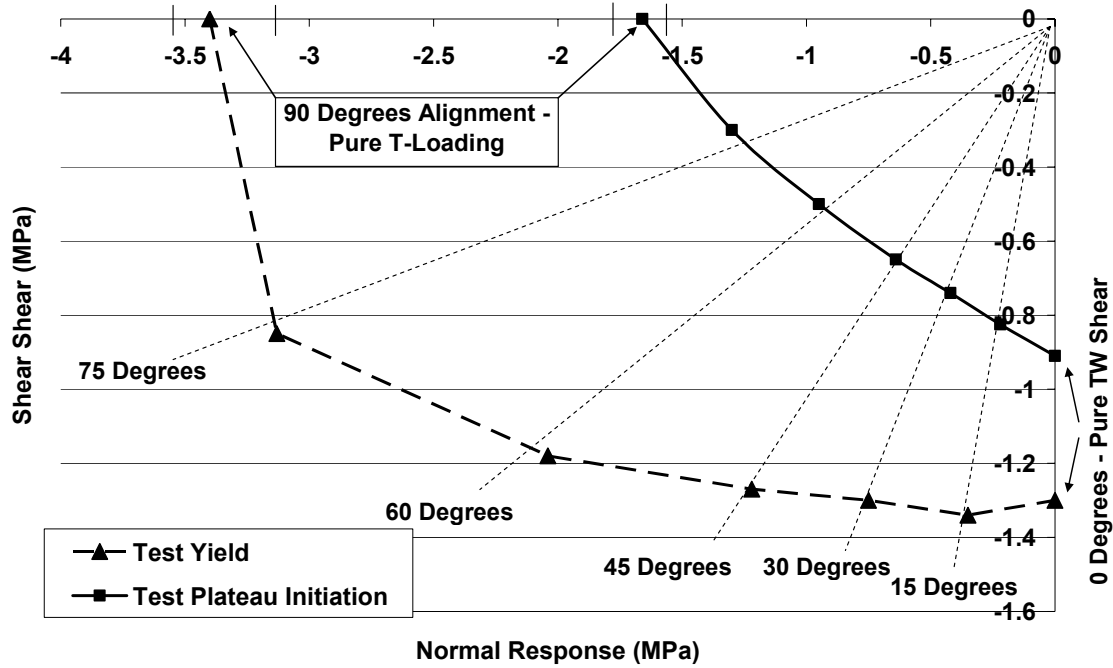
Figure 4-42: Yield and linear plateau initiation envelopes from 'T-TW' loading tests

Loading in the 'T-TL' normal-shear direction displays similar variations in peak and plateau properties when compared with the 'T-TW' investigation. The peak, plateau initiation and average plateau stresses are presented in Figure 4-43, Figure 4-44 and Figure 4-45 respectively. These stresses are higher than those produced by the 'T-TW' investigation. This was discussed by Hong et al. [28] as an effect produced by the double thickness bonded walls which produce the strong shear direction. These results presented the upper and lower bands out-of-plane mixed shear-compression for this particular honeycomb material.
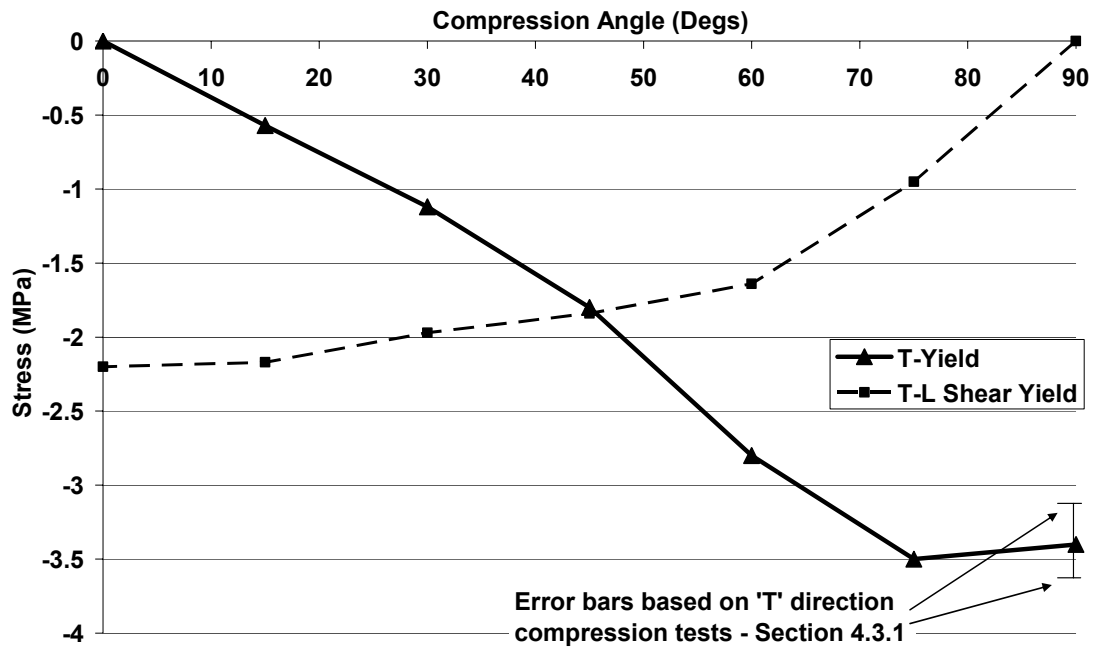
Figure 4-43: 'T-TL' loading yield stress variation with load direction
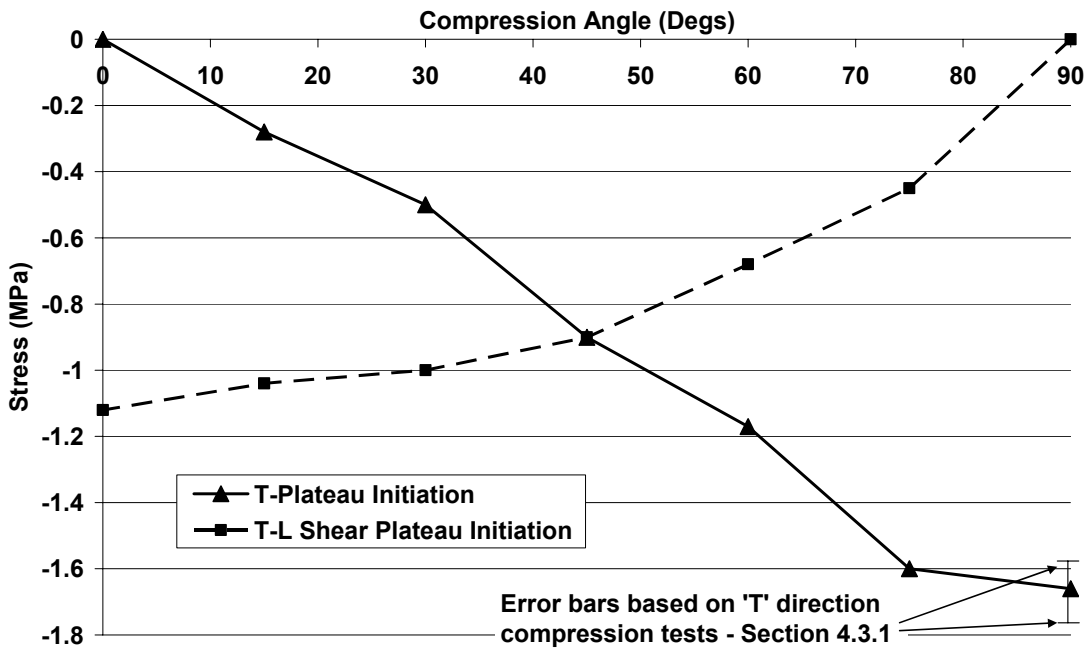
Figure 4-44: 'T-TL' loading plateau initiation stress variation with load direction
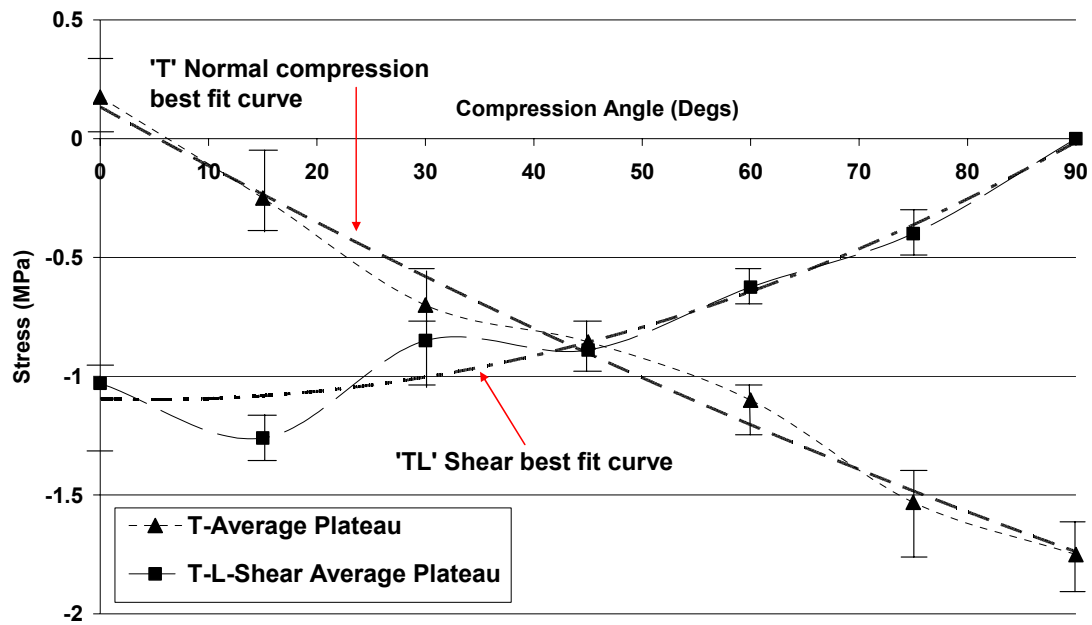
Figure 4-45: 'T-TL' average plateau stress variation with load direction

The variation of mixed shear-compression due to load direction has been summarised in Figure 4-46 for the 'T-TL' study. The relationship shows a similar elliptical band for the peak loading when compared with the 'T-TW' examination, but with a less linear plateau initiation relationship.
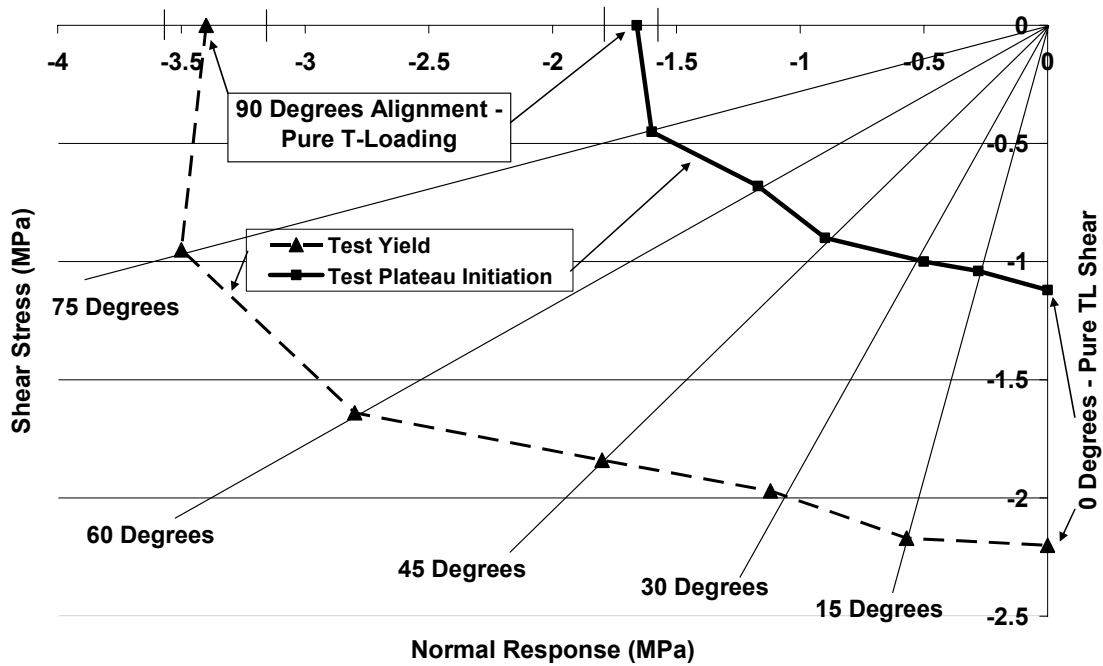
Figure 4-46: Yield and linear plateau initiation envelopes from 'T-TL' loading tests

The average shear stress between loading angles $0^0 \leq \alpha \leq 45^0$ was found to display large fluctuations, as shown in Figure 4-45. This variation was not observed in the 'T-TW' investigation. A possible explanation for these fluctuations is the influence of sample quality. During sample preparation, care was taken to maintain the consistency of the hexagonal cell; however, during the cutting and bonding procedure, inconsistencies to the sample are introduced. The consistency, or regularity, of the 'T-TW' examination results suggest the 'TW' out-of-plane shear properties are less affected by inconsistency of the hexagonal core than the 'TL'. These findings are not used for modification of the MAT41 material model in Section 5.1.1 as further testing is required to evaluate the scatter in average shear stress.

4.4 Composites Sample Testing

The composite skins used on the 006 BAR nosecone are constructed from IM9 fibres embedded in 2035 resin, as described in Section 2.2.2. The number of plies varies between four and five at locations around the nosecone and do not vary in orientation except for a small change due to conformity with the geometry. Composite samples

111

have been acquired from Honda Racing F1 to determine the required input parameters for the Ladevéze damage model. These include:

- Tensile samples where the fibre is orientated to the direction of loading.

- In-plane shear samples where the fibre is oriented at $\pm45^0$ to the direction of loading. These include cyclic shear loading samples for damage parameter acquisition.

- Compression sample with the fibre is orientated to the direction of loading..

These samples were produced using the same manufacturing techniques as the competition car to assure consistency.

4.4.1 Tensile Properties of the Composite in the Fibre Direction

The tensile strength of the composite material has been experimentally investigated. The experimental arrangement is shown in Figure 4-47 with the optical measuring system. The experimental procedure was conducted in compliance with those specified in ASTM D3039M-00 [96]. The geometries for the tensile loading samples are stated in Table 4-4;

Sample	Plies	Thickness (mm)	Width (mm)	Length (mm)		Mass (g)	Fibre
				Untabbed	Tab	Untabbed	Volume V_f
1	4	1	27.3	150.5	89.5	5.5	44%
2	4	1	26.7	151	90	5.3	42%
3	4	1	26	151	90	5.4	44%
4	4	1	26.7	151	-	5.5	43%
5	5	1.2	26.5	150	88	6.6	45%
6	5	1.2	27.1	151	90	6.7	43%
7	5	1.3	26.5	151	92	6.7	43%
8	5	1.2	26.6	151	-	6.8	44%

Table 4-4: Tensile Loaded Composite Specimens
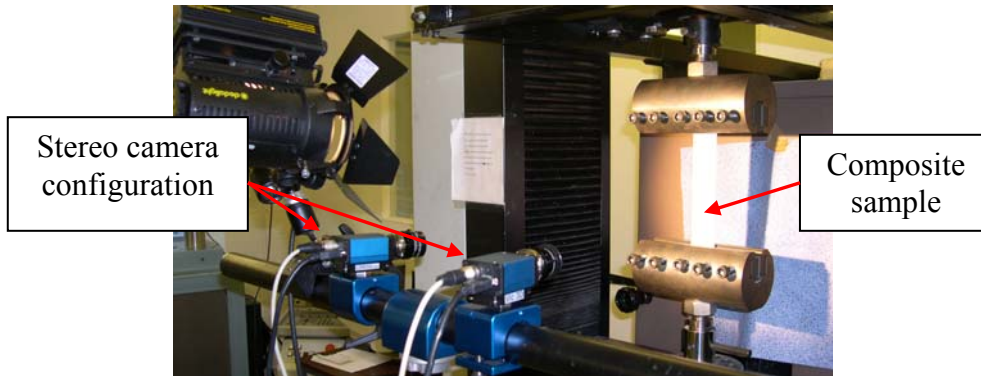
Figure 4-47: Experimental arrangement for composite coupon tensile testing with optical measuring system

The stereo camera system was chosen for this experimental investigation. The initial rotation analysis for Sample 3 is shown in Figure 4-48. Note that the analysis over-exaggerates the representation of the twist in the sample. A maximum of 0.5mm out-of-plane twist is recorded for this sample which relates to just over 1^0 twist at the top and base of the sample.
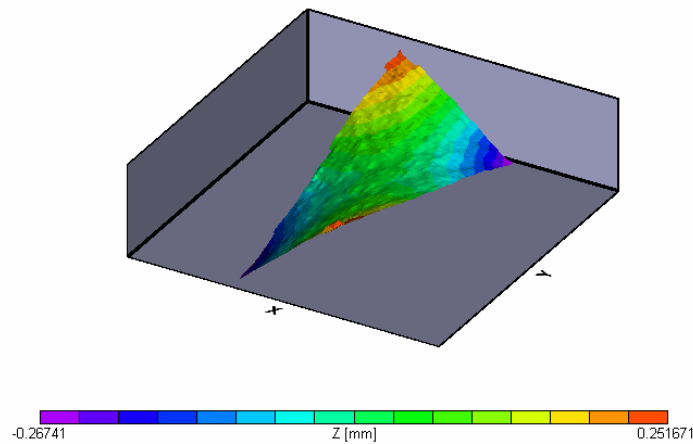
Figure 4-48: Sample 3 experimental set-up check to determine twist of sample

One of the benefits of the optical system is the ability to monitor the whole surface of the specimen whilst a traditional strain gauge would monitor only a small location on the sample, as discussed in Section 4.1. Composite samples frequently vary the location of ultimate failure thus making it difficult to produce consistent results. Figure 4-49 shows the surface deformation of Sample 3 near ultimate failure.
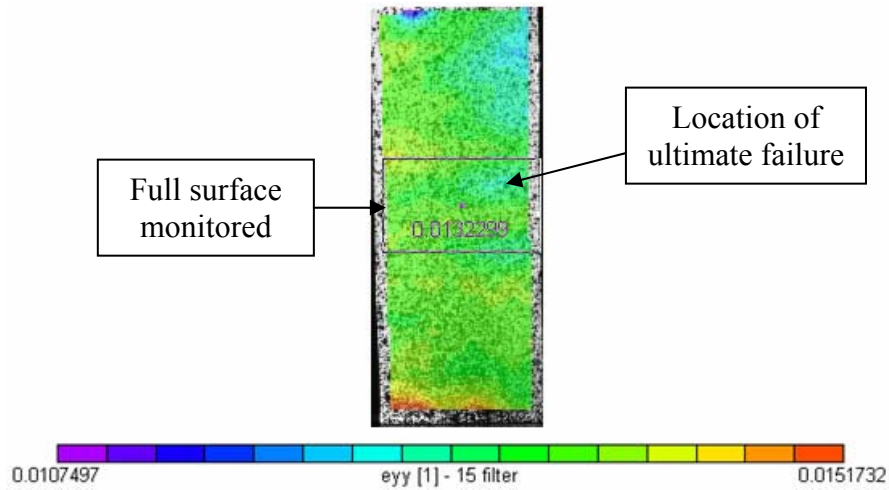
Figure 4-49: Sample 3 DIC image near failure

The elastic modulus of samples 3, 5 and 6 were found to be lower than the manufacturer's specification by as much as 5GPa (7%). This variation is possibly accountable to the quality of the samples where ply misalignment and sample preparation can greatly influence the laminate properties. Only two samples for each ply thickness were investigated due to research time constraints; more tests are required to reduce this scatter. The average fibre volume, V_f, of this composite was calculated as 43% using 42% resin content by weight stated in [41].
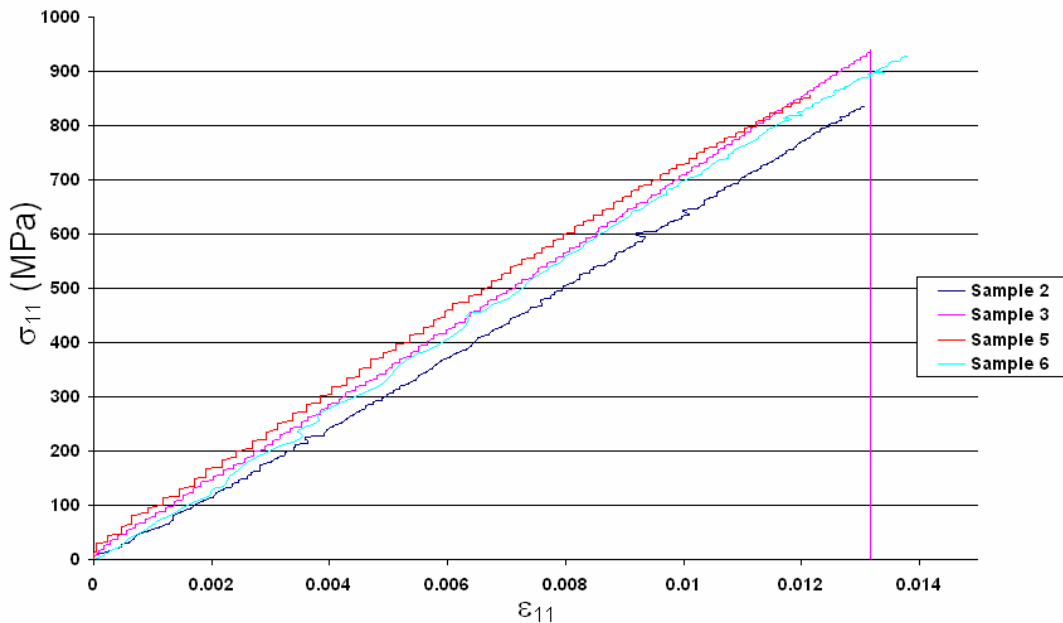
Figure 4-50: Pure tensile loaded sample results

Sample	Plies	Young's Modulus (GPa) E_{11}	Yield Strain ε_{11}
2	4	61.5	0.013
3	4	70.3	0.013
5	5	72.5	0.012
6	5	69	0.013

Table 4-5: Tensile properties of the woven composite

4.4.2 In-Plane Shear and Cyclic Shear Loading

The in-plane shear properties of the composite material are determined by loading samples with fibre orientation set to $\pm 45^0$ and complying with ASTM D3518M-94 [97]. A cyclic loading and unloading process is used to determine the progression of damage and evolution of plastic strains. The geometries of the in-plane pure shear and cyclic shear samples are presented in Table 4-6.

Sample	Plies	Thickness (mm)	Width (mm)	Length (mm) Untabbed	Tab	Mass (g) Untabbed	Fibre Volume V_f
9	4	1	26.4	153	93.5	5.5	46%
10	4	1	28	151	90	5.7	46%
11	4	1	27.3	151.5	-	5.6	43%
12	4	1	27	152	93	5.5	45%
13	5	1.2	27.4	151	-	6.8	45%
14	5	1.2	27	151	90.5	6.7	45%
15	5	1.2	28.3	151	90	7	45%
16	5	1.2	27.2	150.5	90	6.8	45%

Table 4-6: In-plane shear loaded specimens

The properties of shear strain and stress are established using,

$$\sigma_{12} = \frac{\sigma_Y}{2},$$
[4-13]

$$\varepsilon_{12} = \frac{\varepsilon_Y - \varepsilon_X}{2}.$$
[4-14]

The results from the pure in-plane loaded tests are presented in Figure 4-51 and summarised in Table 4-7. The results from the cyclic loaded samples are presented in Figure 4-52. The post yield strength of Samples 9 and 15 suggest that these samples contained flaws, such as void or prior fibre damage, which produced the lower strength and premature failure.
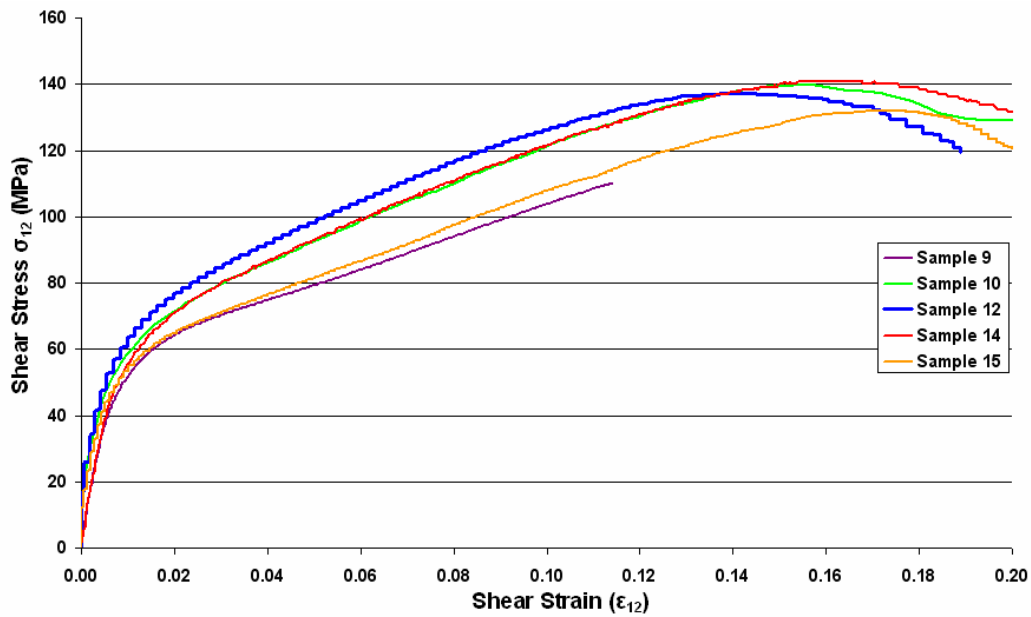
Figure 4-51: In-plane shear loaded sample results

Sample	Shear Modulus (GPa)	Ultimate Shear Strength (MPa)
9	3	124
10	4.3	139
12	4	137
14	4	140
15	4.2	132

Table 4-7: In-plane shear sample properties

Sample	Plies	Thickness (mm)	Width (mm)	Length (mm)		Mass (g)	Fibre
				Untabbed	Tab	Untabbed	Volume V_f
21	5	1.2	40.3	251	189.5	13.6	44%
22	5	1.3	42.1	251	-	14.1	45%
23	5	1.2	42.6	250	190	14.4	44%
24	5	1.2	42.7	252	190	14.6	45%

Table 4-8: In-plane Cyclic Shear Loaded Specimens
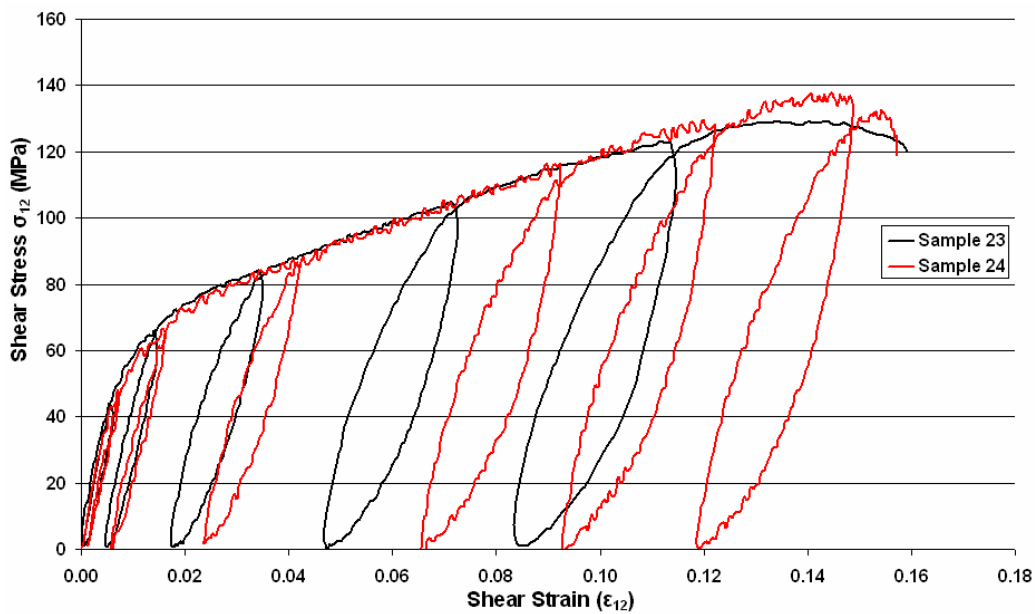
Figure 4-52: Cyclic loading samples

As a composite sample is sheared in the in-plane direction the fibres undergo a reorientation process. This can be monitored using,

$$\delta = \tan^{-1}\left[\frac{1 + \varepsilon_X}{1 + \varepsilon_Y}\right],$$
[4-15]

where, ε_X and ε_Y are the strains in the global x and y directions respectively and δ is the angle of the fibre relative to the direction of loading. The assumption for this calculation is that the carbon fibres are inextensible. The variation in change in fibre angle with loading is shown in Figure 4-53. The fibre direction is observed to changes from 45^0 to

35^0 for each test with the exception of Sample 14 which continues to carry load longer than the other shear samples and in which the fibres continued to rotate.
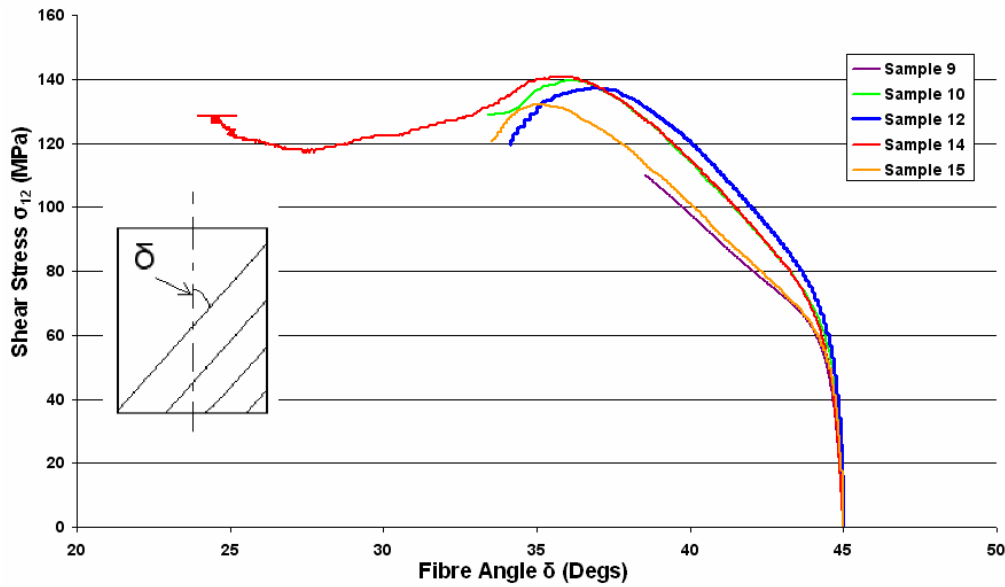
Figure 4-53: Fibre reorientation in shear samples

Changes in fibre orientation can be introduced to determine shear stress and strain in the material accurately. In addition, the change in cross-sectional area is also accounted for in the calculation of shear stress using,

$$\sigma_{12} = (\cos\delta)(\sin\delta)\frac{P}{(A_0(1+\varepsilon_X))}, \qquad\qquad [4\text{-}16]$$

$$\varepsilon_{12} = (\cos\delta)(\sin\delta)(\varepsilon_Y - \varepsilon_X). \qquad\qquad [4\text{-}17]$$

The effects of fibre reorientation on the results gathered from Sample 24 are shown in Figure 4-54. There is a clear increase in the ultimate shear strength from 137MPa to 157MPa. It is unclear if Honda Racing F1 and Cytec used this method to obtain the material specification as fibre reorientation adjustment is not specified in the standard for testing in-plane shear properties of composite.
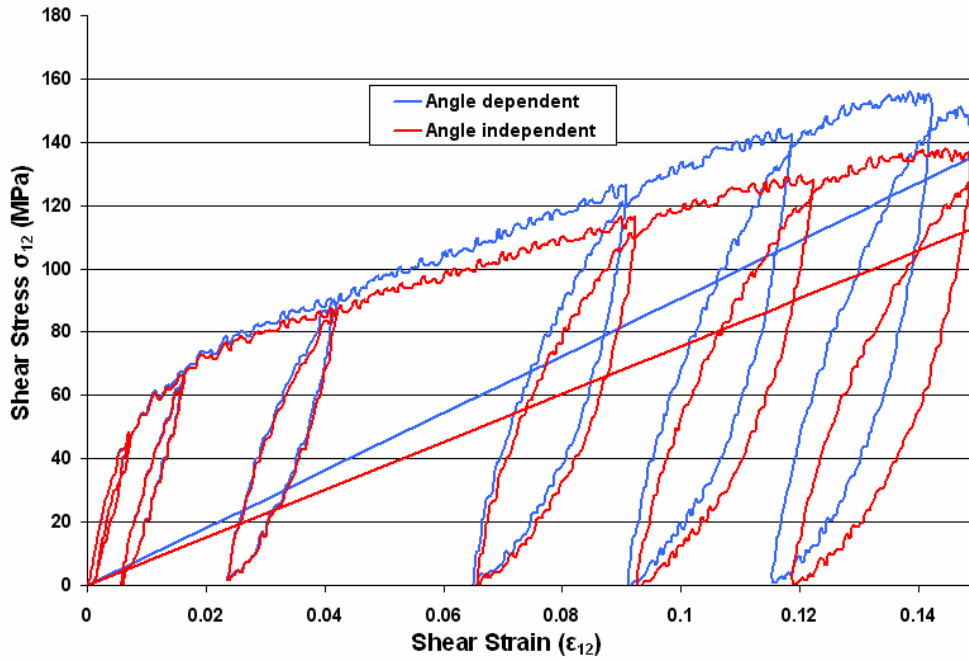
Figure 4-54: Effect of fibre reorientation on cyclic shear Sample 24

The change in shear modulus and plastic strain is measured at each cycle to determine damage progression. The value of Y_{12} at each cycle is acquired using equation 2-28. The evolution of damage is then assessed using equation 2-30 presented in Section 2.2.2. This relationship is shown in Figure 4-55. As with the findings of Fouinneteau [51] for braided composites, the damage progression is not linear for this woven fabric composite.
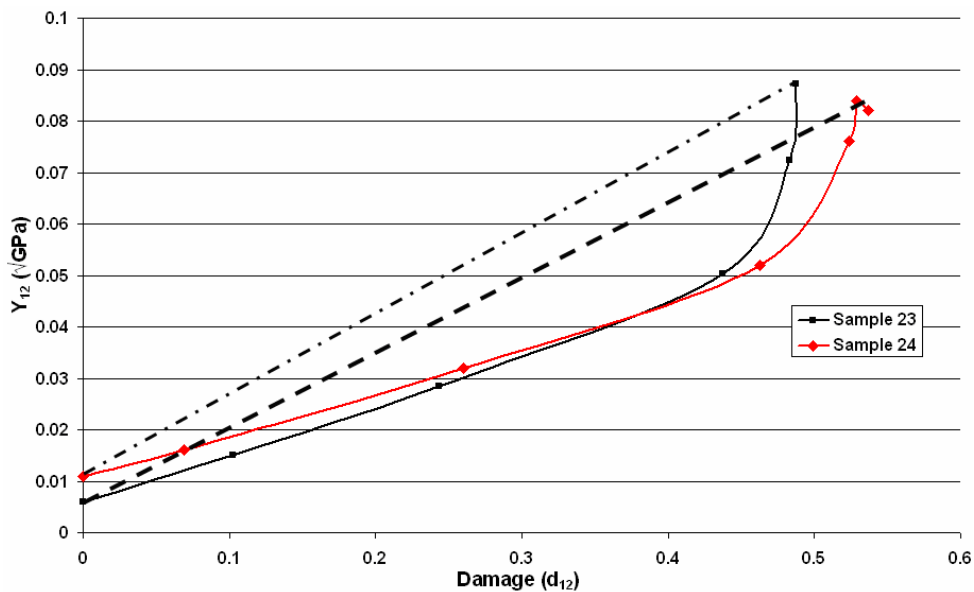
Figure 4-55: Damage progression for both cyclic shear tests

A linear approximation from both tests produces the damage progression parameters presented in Table 4-9;

Property	Value
$Y_{12(0)}$	0.09 √GPa
Y_{12C}	0.13 √GPa
Y_{12R}	0.08 √GPa

Table 4-9: Average damage limitation property values

The improved non-linear damage progression law is shown in Figure 4-56 and produces the equation 4-18;

$$d_{12} = -96.944Y_{12}^2 + 15.118Y_{12} - 0.0952 \qquad [4\text{-}18]$$
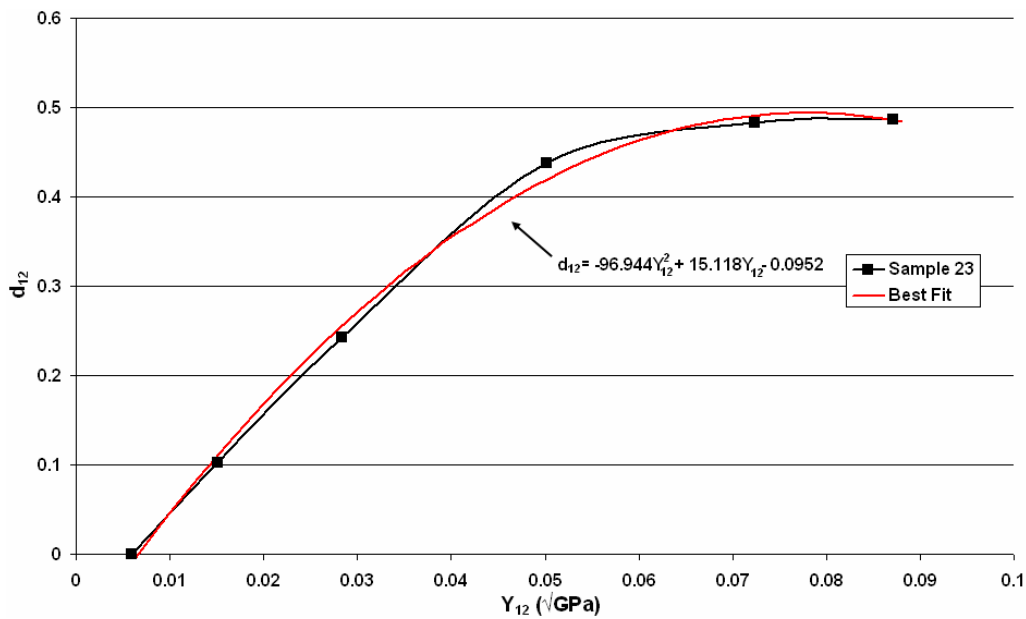
Figure 4-56: Improved non-linear damage progression law - Shear damage evolution d_{12} vs. Y_{12}

The plastic strain parameters are established using equations 2-32 and 2-33. The onset of plastic hardening is shown in Figure 4-57 and produces the relationship in the form of equation 2-34.

$$R(P_i) = 0.7986P_i^{0.5166} . \qquad [4\text{-}19]$$
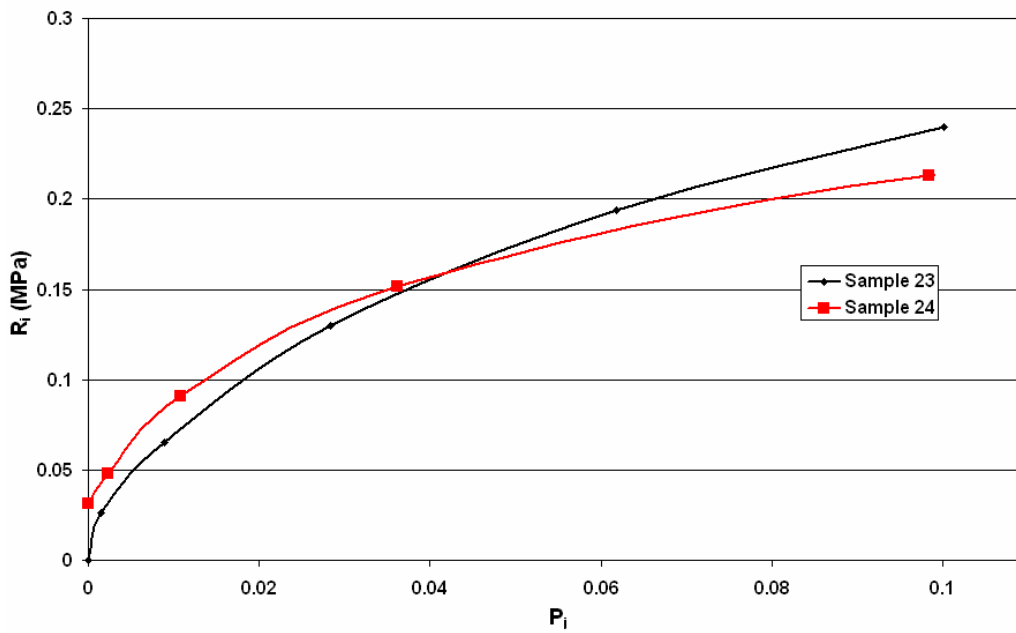
Figure 4-57: Plastic strain law

These damage parameters are used in Section 5.2 to validate the Ladevéze damage model for this material characterisation. Equation 4-18 is implemented into the PLY1 material model to provide non-linear damage progression.

4.4.3 Compressive Loading

The compressive properties of the composite skin material have been stated in Table 2-3; the composite material has a compression modulus of 71.7GPa and failure strength of 812MPa. This study was conducted to determine the suitability of a new test apparatus method. The difficulty with the current standard compression test, ASTM D3410M-03 [98], is that only a relatively small region is compressed and end grip constraints influence the stress field in this region [99]. The apparatus for the standard test is shown in Figure 4-58.

Figure 4-58: Composite compression apparatus [98]

A new method can potentially overcome these problems and expose a significantly larger gauge length. The apparatus, shown in Figure 4-59, uses two vertical guides which provide support to the sample along the length to prevent buckling and a compressive force directly applied to the sample via the end tabs.
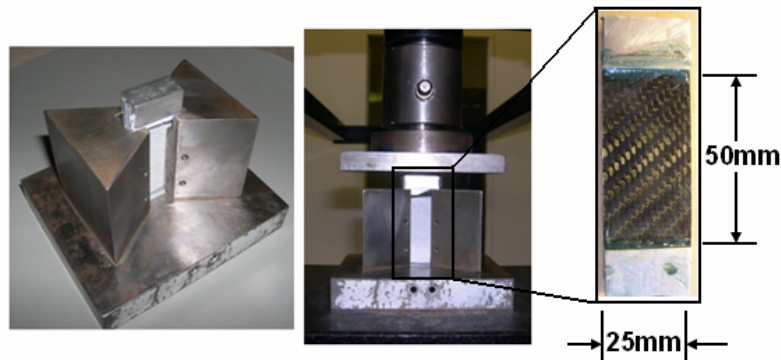
Figure 4-59: Composite compression apparatus and sample

The samples tested are ten plies thick and the test sample region measures 50x25x2.5mm. The stereo camera method was chosen as the sample may produce out-of-plane movement near the end of the test. The compression rate of loading is 1mm/min and the DIC equipment was used with a recording speed of one image per second.

Figure 4-60 shows the stress-strain relationship produced from the tests and the properties are presented in Table 4-10. The elastic properties are consistent with manufacturer's datasheets but the samples fail prematurely at approximately 35% of manufacturer values. The failure mechanism in these compression samples is shown in Figure 4-61; a central failure mechanism is shown to have occurred in both samples. It is likely that the apparatus has not completely restricted flexing of the sample and

allowed buckling to occur in the sample. Therefore, the method of supporting the sample in the apparatus is currently insufficient and requires further development.
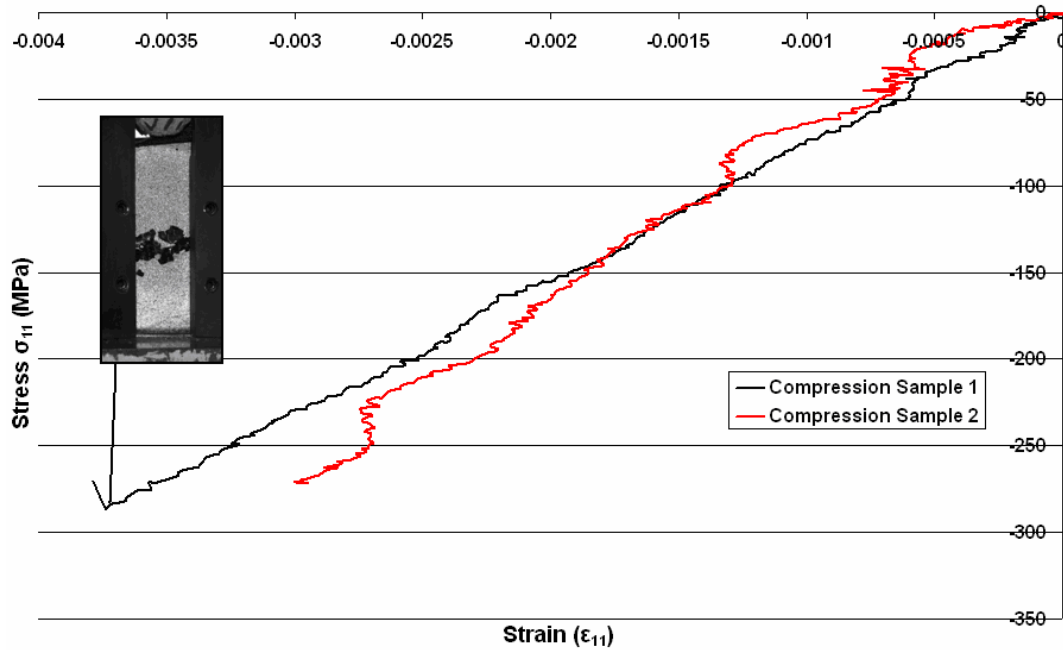
Figure 4-60: Composite compression results

Sample	No. Plies	Young's Modulus (GPa) E_{11}	Yield Stress (MPa) σ_{11}
1	10	77	-287
2	10	84	-270

Table 4-10: Composite sample compressive properties
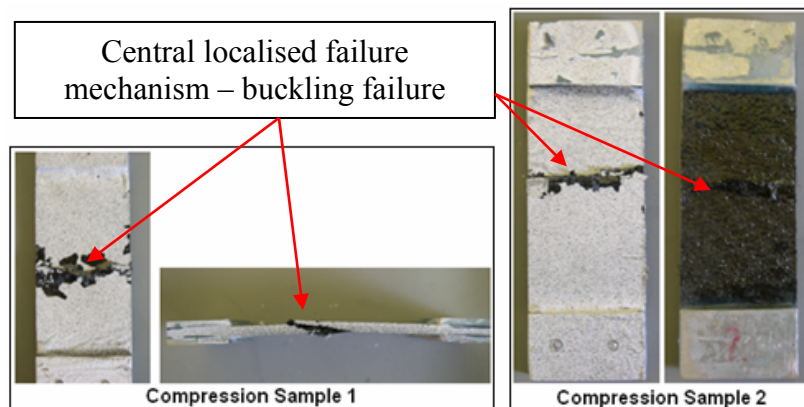
Figure 4-61: Compression samples post-test

These findings are not used to calibrate the numerical model of the skin material, presented in Section 5.2, as the failure strength observed is too low. The compression properties indicated by the manufacturer in Table 2-3, specifically compression strength of 812MPa and modulus of 71.7GPa, are used in the numerical model.

4.5   Composite Sandwich Structure

A series of tests have been conducted to determine the structural strengths and energy absorbent behaviour of the composite-honeycomb sandwich. The loading conditions are representative of the folding and failure mechanisms which potentially occur in the nosecone structure during frontal impact loading. The investigated conditions include:

- Out-of-plane compressive loading – This investigation presents the influence of the adhesive fillet on the crushing properties of the honeycomb core.

- Cracked sandwich beam testing – This investigation presents the crack propagation mechanisms through the sandwich when Mode-I loading conditions are applied.

- Three-point bend testing – The flexural properties of the sandwich beam are investigated using a 3PB test and presented here.

- Edgewise loading – The deformation mechanisms in the sandwich construction during edgewise and oblique loading conditions are investigated and presented.

4.5.1   Flatwise Loading Test

The 'T' directional properties of the honeycomb core have been established in Section 4.3.1. The addition of an adhesive bond-line introduces a restriction to the rotational stiffness at the skin-core interface which increases 'T' direction compression strength of the sample, as shown in Figure 4-62. This restriction will increase the 'T' direction elastic peak strength. The buckling load for a wall of length l is given by [17];

$$P_{CRIT} = \frac{KE_S}{\left(1 - \upsilon_S^2\right)} \frac{t^3}{l},$$
[4-20]

where K is the end constraint factor and υ_S is the Poisson's ratio of the base material. The end constrain factor varies from 2, completely free to rotate, to 6.2, locked in position. Gibson and Ashby [17] approximate K = 4 for honeycomb material as the cell

walls are neither completely free nor locked, thus producing the relationship for elastic buckling stress;

$$\frac{(\sigma_{el})_T}{E_S} \approx \frac{2}{(1-\upsilon_S^2)} \frac{(l/h+2)}{(h/l+\sin\theta)\cos\theta} \left(\frac{t}{l}\right)^3 , \qquad\qquad [4\text{-}21]$$

For regular hexagonal core materials and a Poisson's ratio of 0.3, equation 4-21 simplifies to become;

$$\frac{(\sigma_{el})_T}{E_S} = 5.2 \left(\frac{t}{l}\right)^3 , \qquad\qquad [4\text{-}22]$$

The inclusion of the adhesive fillet will increase the value of K toward 6.2 and thus increase the elastic yield (peak) stress of the material. The sample is compressed using the same testing conditions as the core alone 'T' direction compression tests described in Section 4.3.1.
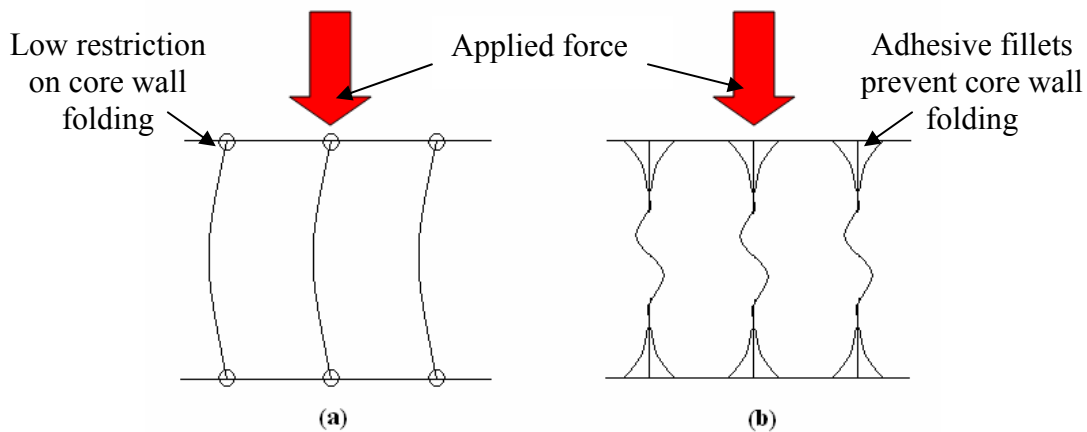
Figure 4-62: Adhesive fillet restriction on cell wall deformation. (a) Low restriction honeycomb core alone case. (b) Fillet restriction sandwich case

The results from the compression tests are presented in Figure 4-63. When compared with the findings shown in Figure 4-10, it may be seen that there is an increase in both peak and plateau stresses as summarised in Table 4-11.
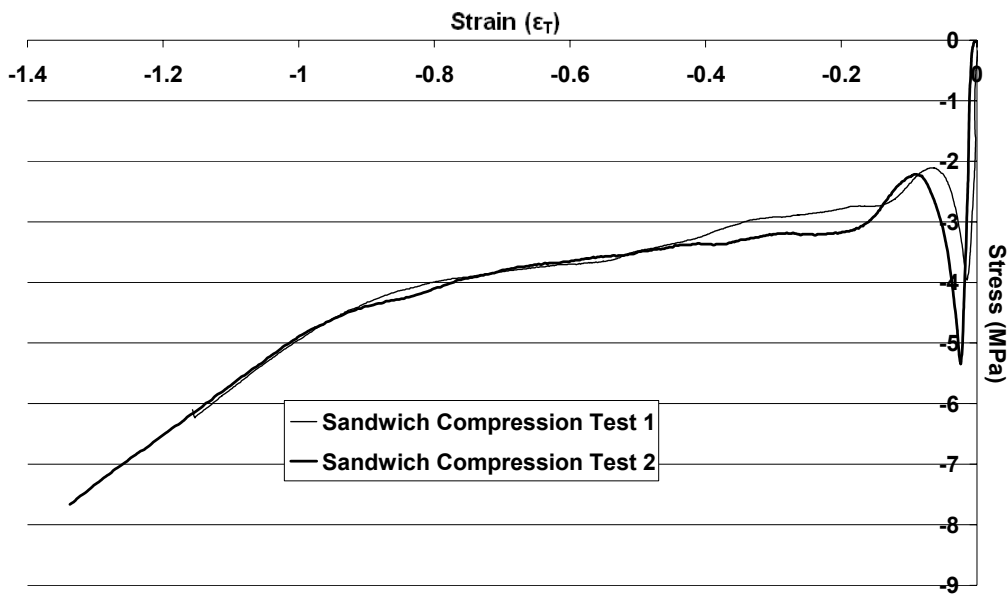
Figure 4-63: Sandwich material out-of-plane compressive test curve

Property	Core Alone	Sandwich
Elastic Modulus (MPa)	320	370
Peak Stress (MPa)	-3.5	-4.6
Plateau Initiation (MPa)	-1.75	-2.8
Plateau Modulus (MPa)	Negligible	1.9
Compaction Strain	-1.45	-0.85

Table 4-11: Sandwich compression properties compared with core alone

Assuming regular hexagonal cores, the end corrective factor, K, becomes 5.2 for this particular sandwich. It is likely that the size and strength of the fillet has a contributing factor as K is not 6.2 to represent full locking end constraints. The properties of the composite skin material produce a negligible effect on the sandwich 'T' directional properties and an increase in plateau crushing stress is observed without any waveform. The reason for this is unclear, under examination the cell walls have folded similar to those of the core alone tests.

The mathematical approximations of crushing strength by Gibson and Ashby [17], McFarland [32] and Wierzbicki [33] is based on the plastic work per unit length of the cell wall to continue folding and so should not be effected by end constraints. A

possible explanation for this is that the glue bond-line is preventing some folds from taking place and imposing restrictions on further folding, as shown in Figure 4-64 and Figure 4-65. The adhesive fillets prevent an average of 0.75mm of cell wall from folding at the interface. This investigation shows that the choice of adhesive plays an important role in changing the properties of the honeycomb material by supporting the cell walls and inhibiting buckling collapse.
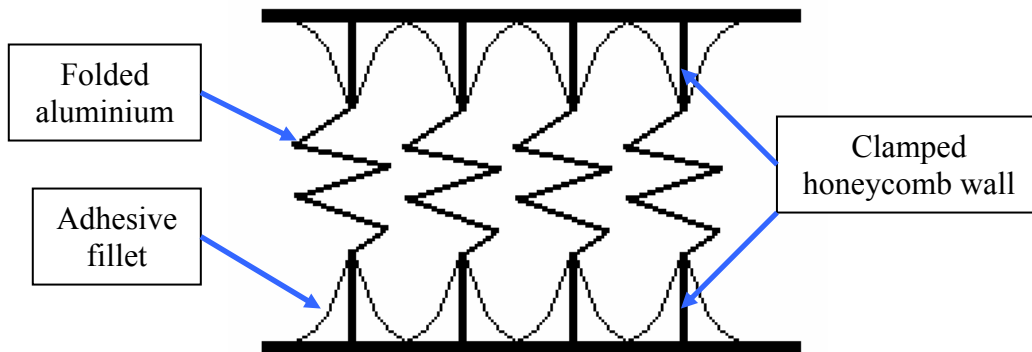
Figure 4-64: Adhesive reinforcement of honeycomb walls
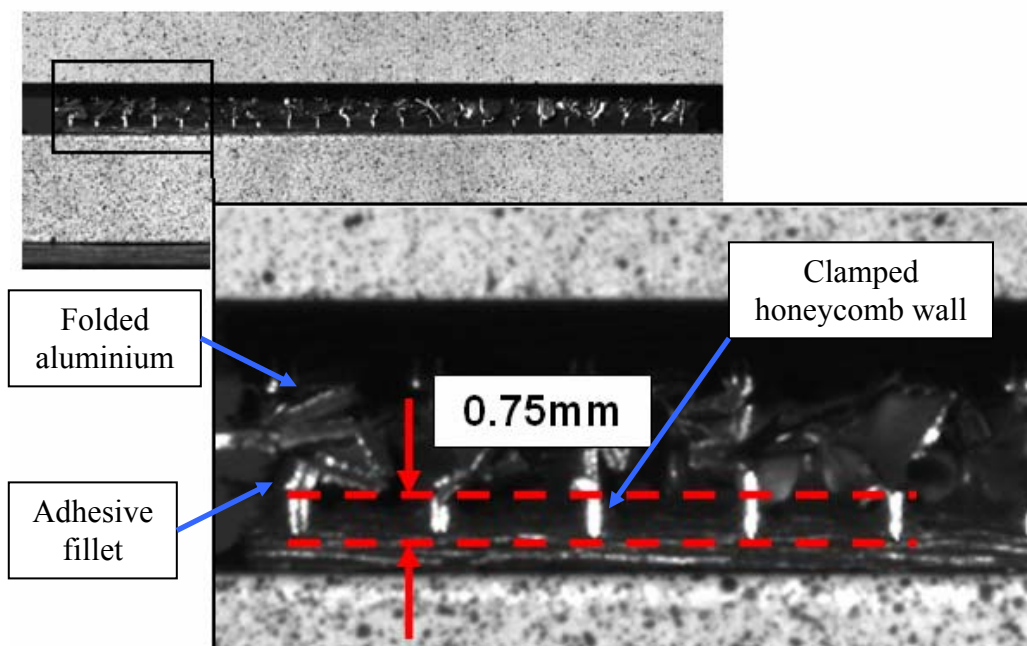
Figure 4-65: Adhesive fillet restriction on cell wall folding

The influence of adhesive on the 'T' direction compression properties is used in the MAT41 honeycomb model when applied to sandwich materials; this is presented in Section 5.3.1. The elastic modulus is assumed identical to the unsupported honeycomb

modulus of 1GPa as the experimentally measured modulus is low. The low modulus was identified during 'T' direction bare compression testing presented in Section 4.3.1 and identified as a flaw with the experimental apparatus. The measured elastic modulus for the sandwich is similar to that measured in the bare compression test; thus the assumption that elastic modulus is the same is valid.

4.5.2 Cracked Sandwich Beam Testing

A potential failure mechanism in the nosecone structure during impact testing is crack propagation through the sandwich. Reviewed papers on the crack propagation properties through a composite sandwich, presented in Section 2.2.3, indicated that crack propagation depended on the properties of the core, skin and adhesive interface. The crack propagation through the sandwich material used in the nosecone structure of the BAR-Honda 006 has not previously been investigated. The objectives of this research are to:

- Determine the strain energy release rate, G_{IC}, for the composite sandwich with a low density core.
- Identify the direction and stability of the crack propagation, i.e. central crack growth through the core.
- Investigate the influence of higher rates of loading on strain energy release rate.

CSB testing is required to determine the Mode-I crack propagation failure properties of the sandwich structure. Using the equations previously introduced in Table 2-4, G_{IC} has been calculated for the CSB samples. The tests were conducted in compliance with ASTM D5528-01 [47] and loaded at 2mm/min.

Aluminium blocks are applied to the samples to prevent the composite skins from breaking during loading. The dimensions of both the quasi-static and dynamic test samples are presented in Table 4-12 and Figure 4-66.

Dimension	Test Type	
	Quasi-static (mm)	Dynamic (mm)
Sample $_L$	200	200
Al $_L$	210	210
a_0	25	25
L'	3.5	5
Al $_T$	8	8
LB_C	3.5	5
h	28.5	28.5

Table 4-12: CSB sample geometries
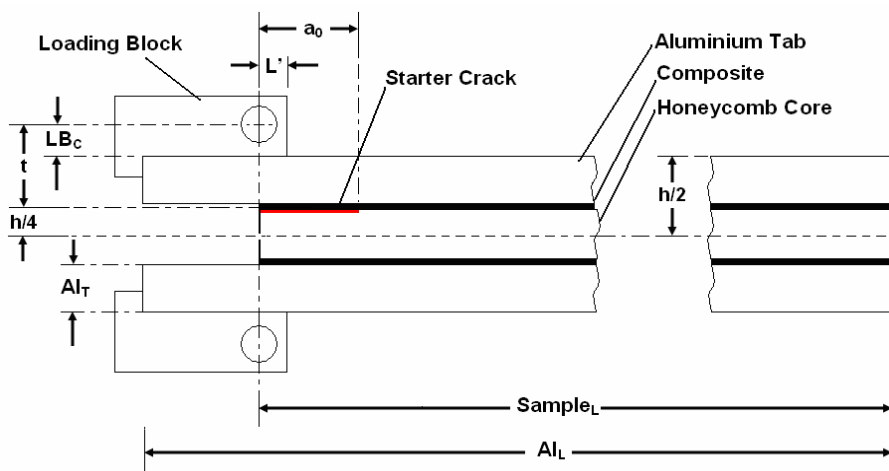
Figure 4-66: CSB sample geometry key

Two quasi-static tests were carried out to determine the G_{IC} of the composite-honeycomb sandwich. In both cases the crack propagated through the centre of the honeycomb core, as shown in Figure 4-67. The force-displacement curves for both tests are shown in Figure 4-68.
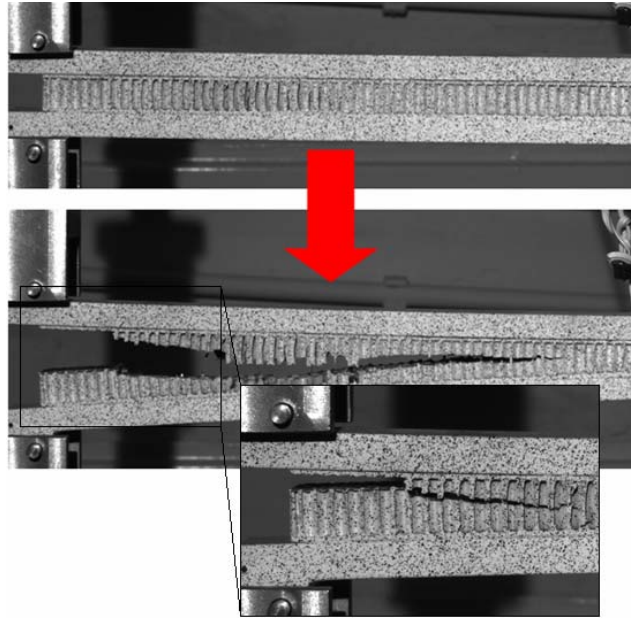
Figure 4-67: Crack propagation through sandwich Sample 9
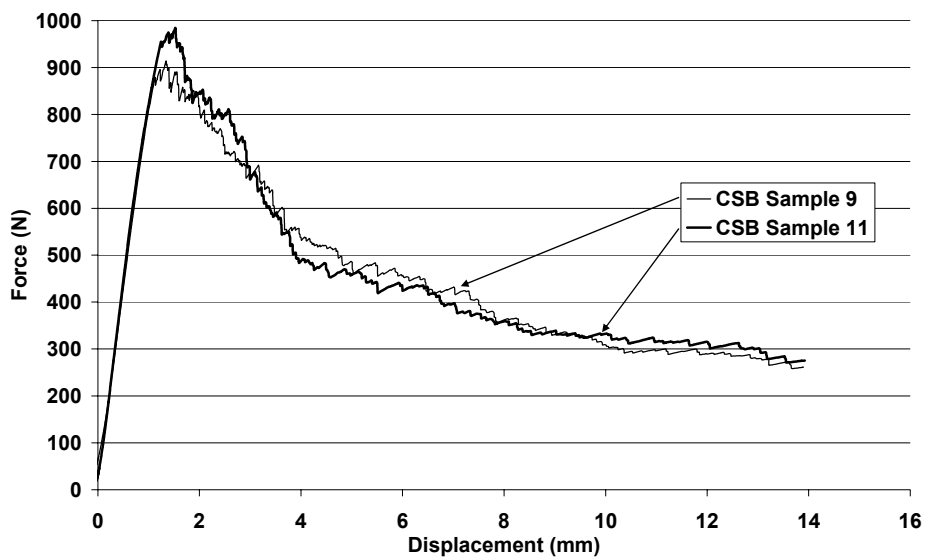
Figure 4-68: Results from quasi-static CSB tests

The corrective factor χ is required to determine G_{IC} for the modified beam theory using the graphical method, shown in the Figure 4-69. These are determined to be -39.3mm and -52.4mm for samples 9 and 11 respectively.

130
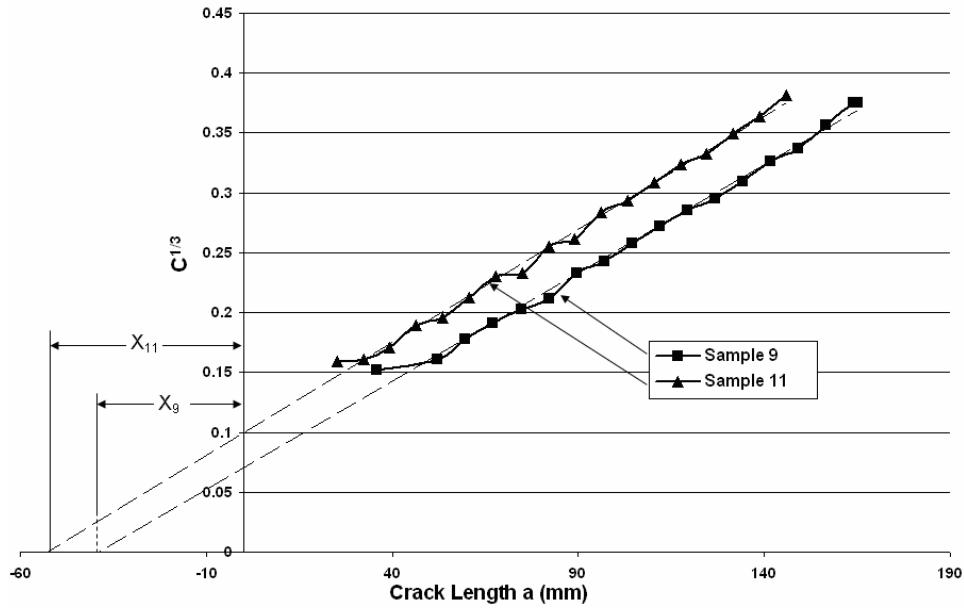
Figure 4-69: Corrective factor determination

The G_{IC} is calculated using the methods summarised in Table 2-4. A comparison of these methods is shown in Figure 4-70 for Sample 9. The average of these results is presented in Table 4-13.
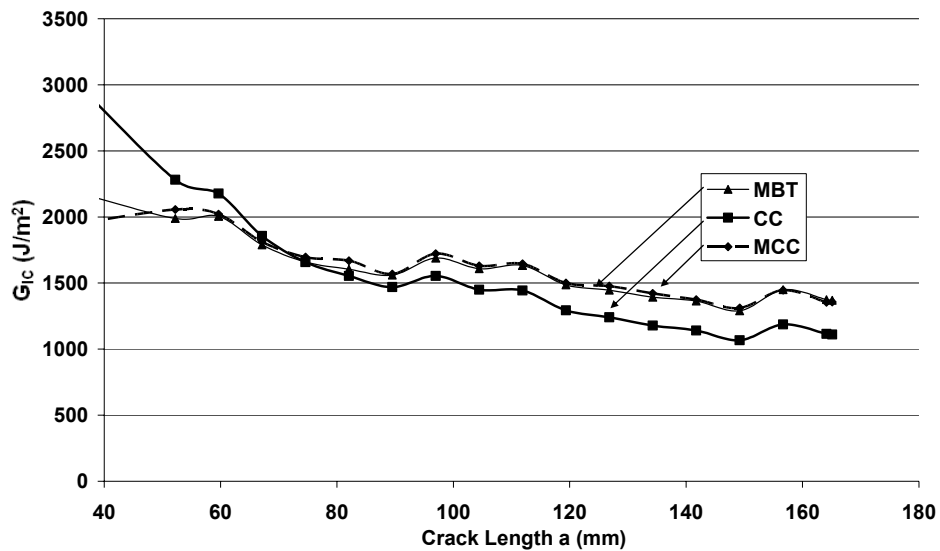
Figure 4-70: Strain energy release rate for Sample 9

Method	Sample 9	Sample 11
MBT (J/m^2)	1514	1652
CC (J/m^2)	1354	1375
MCC (J/m^2)	1532	1661

Table 4-13: Average approximations of strain energy release rate

The strain energy release rate is used in the tied contact interface numerical model, MAT303, presented in Section 5.3.2. In addition, the central location of the crack propagation is represented in the numerical model by two solid honeycomb element beams with the contact interface between them. This is also shown in Section 5.3.2 with a comparison of force-displacement curves produced from testing and by the numerical model.

High-Rates of Loading Influence on G_{IC} in Composite Sandwich Materials

In impact applications the sandwich structure will debond at higher rates of loading than those tested quasi-statically. Research conducted by Silbermann [101] and May [102] have been used to develop an apparatus to apply loads at a high-rate to DCB samples. The apparatus, shown in Figure 4-71, uses a drop tower to strike a CSB specimen. The Photron 1024PCI high-speed camera is used to monitor crack growth and captures 2000 frames per second. The experimental arrangement is shown in Figure 4-72.
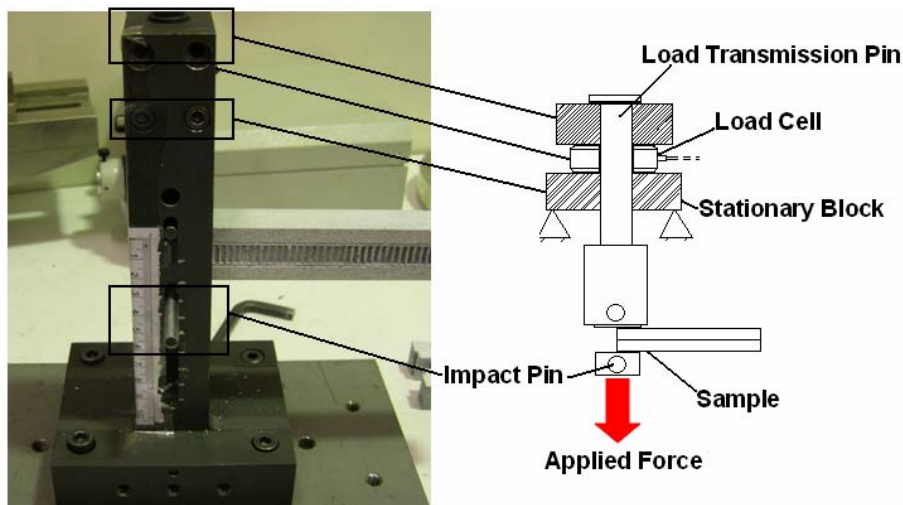
Figure 4-71: Dynamic delamination apparatus
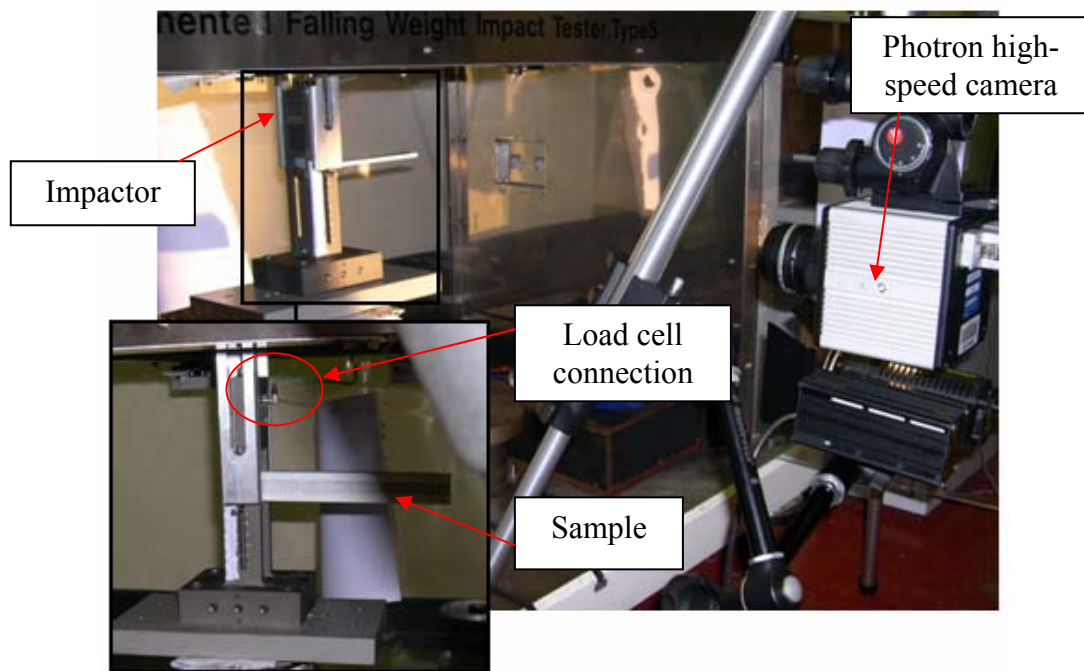
Figure 4-72: Dynamic delamination experimental arrangement

The average impact velocity during the test was recorded to be 1.3m/s. The crack propagates near the skin but is contained in the core material during high-rate loading. The modified dynamic delamination apparatus recorded a clear force displacement curve, presented in Figure 4-73, and is compared with the result from the low-rate quasi-static test Sample 11. The graph shows a clear increase in the initial peak load before settling close to the quasi-static load case.
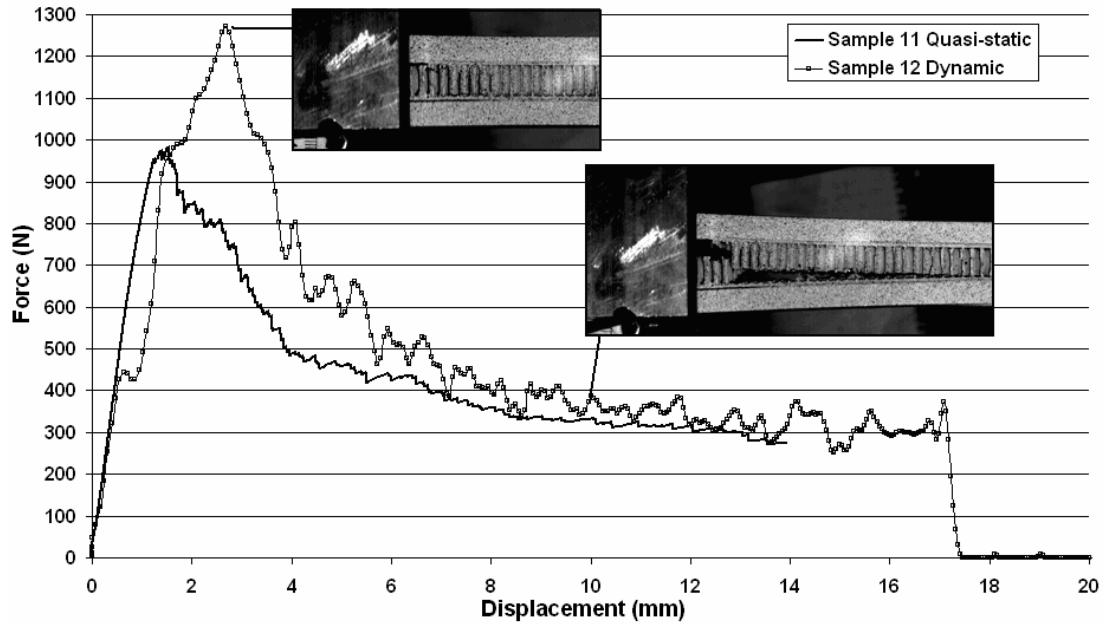
Figure 4-73: Comparison between quasi-static and dynamic CSB tests

The strain energy release rate is calculated using the same method for the quasi-static low-rate loaded tests. These values are presented in Table 4-14 and show an increase in G_{IC}. The increase in G_{IC} is possibly due to the increase in the failure strain of aluminium at high strain rate loading as presented by Smerd et al. [115]. It is feasible that this effect is increasing the strain energy release rate required for crack propagation through the aluminium core material. Further investigation is required to determine the change in G_{IC} due to load point deflection rate.

Method	Average quasi-static result	Dynamic Sample 12
MBT (J/m^2)	1583	2404
CC (J/m^2)	1365	2028
MCC (J/m^2)	1597	2541

Table 4-14: Strain energy release energy for high-rate case

The rate dependent strain energy release rate identified here is not used in the numerical modelling of the tied interface. This investigation was conducted to evaluate the new method of applying high rates of loading to CSB and DCB specimens. The apparatus was found to produce a clear force measurement which require no filtering and can be used on further CSB and DCB investigations.

4.5.3 Three-Point Bend Flexural Testing

A three-point bend test, 3PB, is required to determine the flexural properties of the composite sandwich. The objectives of this investigation are to;

- Provide force-displacement information required for evaluation of the sandwich modelling capability in PAM-CRASH^{TM} for 3PB representation.

- Identify the deformation and failure mechanisms in the core and skin materials during 3PB loading. These are also required for direct comparison with the numerical models.

The apparatus, shown in Figure 4-74, requires a sample to be placed on two pivots and a force applied at a constant speed of 2mm/min in the centre of the specimen. The sample geometries are dependent on the number of plies in the sandwich and are presented in Table 4-15. These tests were conducted in compliance with ASTM C393-00 [55].
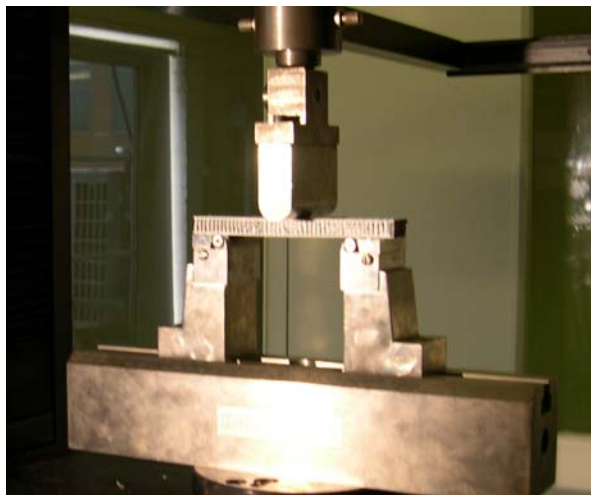
Figure 4-74: 3PB test apparatus

Dimension	4-Ply Samples (mm)	5-Ply Samples (mm)
Depth, d	11.6	12.1
Breadth, b	25	25
Length	150	150
Pivot Length, L	100	100

Table 4-15: General dimensions of 3PB samples

The force-displacement results are presented in Figure 4-75. In each test the samples undergo an elastic loading phase before settling into an approximately constant

deformation load. This load remains approximately constant until the upper skin fails in compression; this is marked by a sharp drop in strength as the load is transferred to the lower skin, which is in tension. The overall failure of the sample takes place when the lower skin fails; these failure processes are illustrated in Figure 4-76. In the case of the four ply samples the samples split completely in half whilst the five ply samples hold together, most likely by residual unbroken fibres.
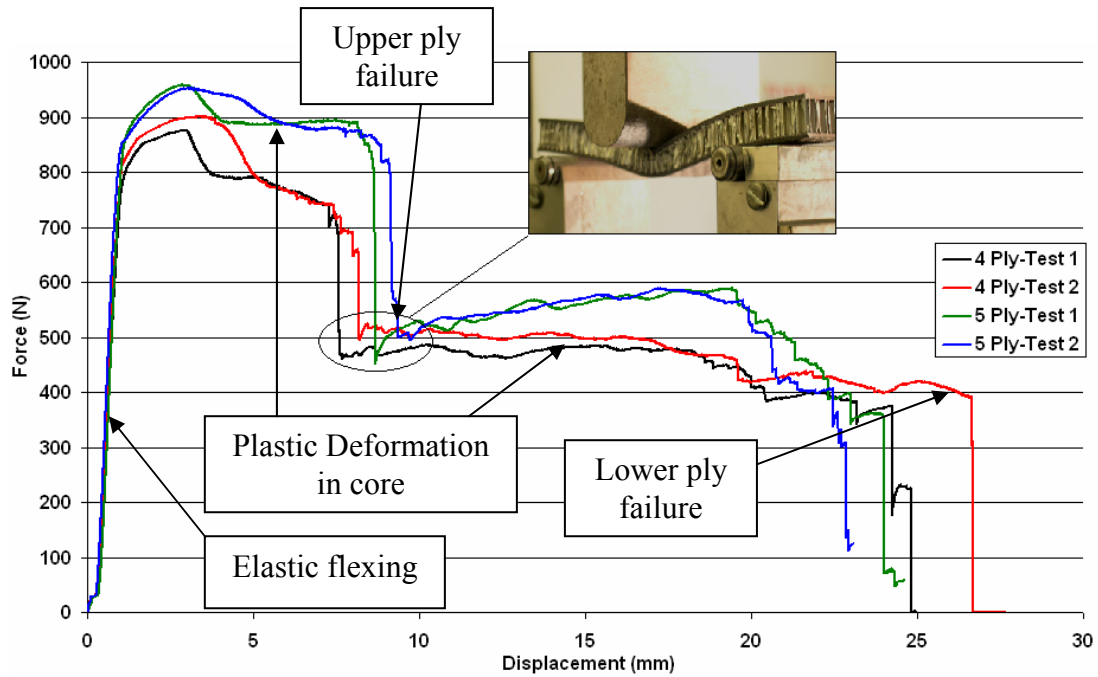
Figure 4-75: Results from 3PB tests
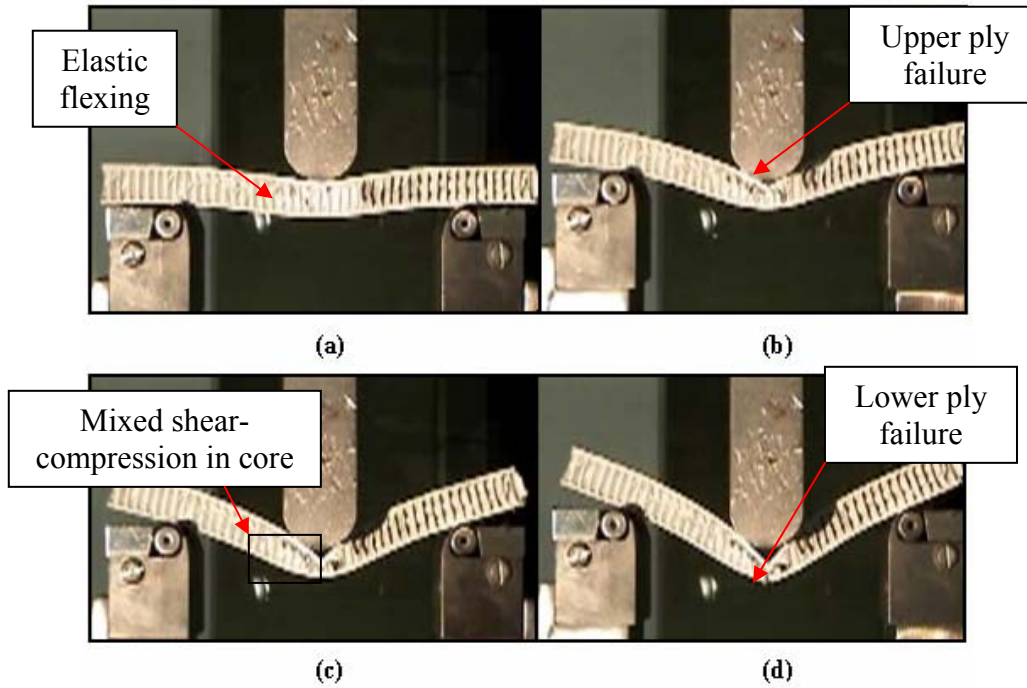
Figure 4-76: 3PB test images, (a) elastic flexing, (b) upper ply failure, (c) mixed shear-compression in core, (d) lower ply failure

Applying equations 3-5 and 3-6 to the 3PB test results produces the stress strain relationship shown in Figure 4-77. The elastic, plastic and failure properties are specified in Table 4-16. These findings show a consistent strength between samples regardless of ply composition.
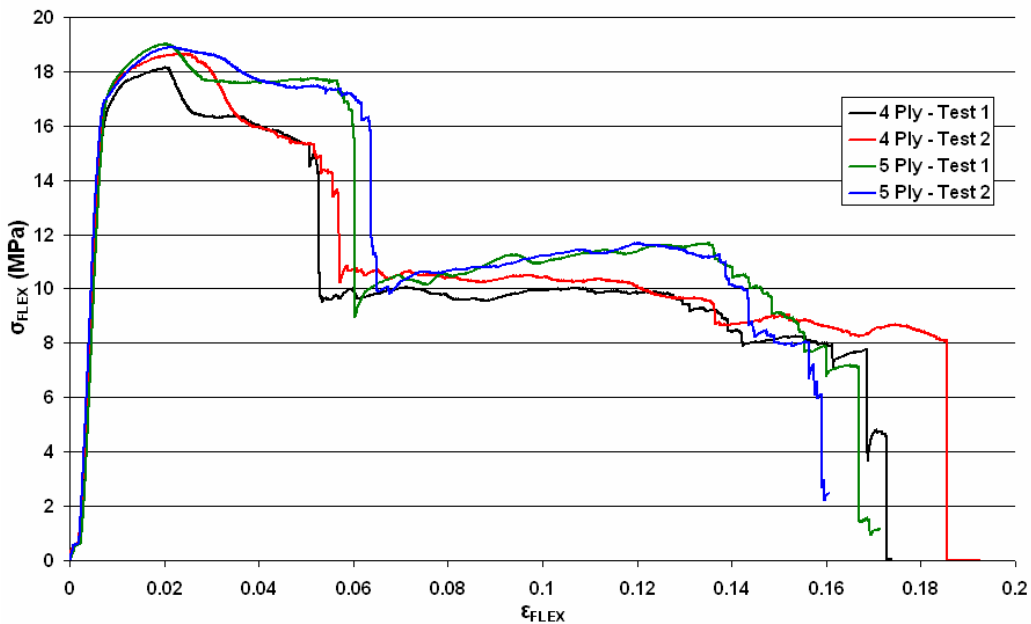
Figure 4-77: Flexural stress-strain results from the 3PB tests

Property	Test Sample			
	4 Ply (1)	4 Ply (2)	5 Ply (1)	5 Ply (2)
Flexural Modulus (GPa)	3.2	3.3	3.5	3.5
Yield Stress (MPa)	16.3	16.9	17	16.9
Peak Stress (MPa)	18	18.7	18.9	18.9
Upper Laminate Failure Strain	0.05	0.05	0.06	0.06
2nd Phase Average Flexural Stress (MPa)	9.3	9.6	10.6	10.6
Complete Failure Strain	0.17	0.19	0.18	0.16

Table 4-16: Sandwich flexural properties

A post-failure 5-ply sample is shown in Figure 4-78. The core of the sample has undergone a mixed non-proportional shear-compressive crushing process where the cell walls at the centre of the sample have folded and a shear band is visible leading outward from the centre of the sample.
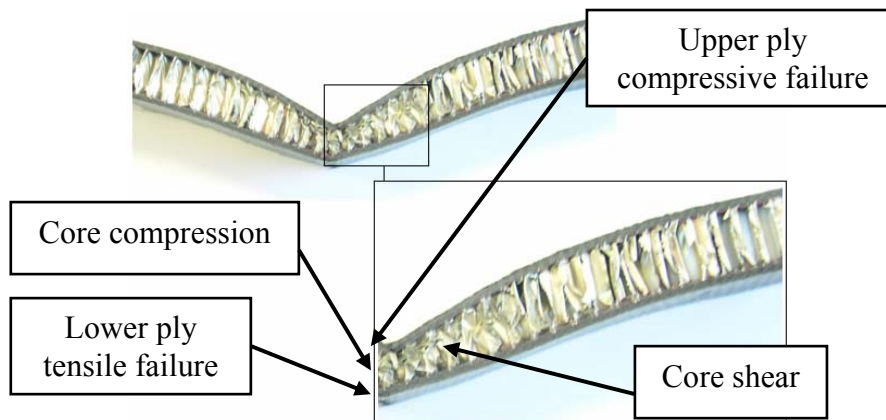
Figure 4-78: 5-ply test sample post failure

The force-displacement measurements presented here are used to assess the composite-honeycomb sandwich modelling capability of PAM-CRASH^{TM} in Section 5.3.3. The deformation mechanisms observed during testing are compared with those produced by the numerical model.

4.5.4 Axial and Oblique In-Plane Sandwich Loading

Edgewise loading tests have been conducted to determine the energy absorption and deformation mechanisms of the sandwich when loaded in the in-plane direction. The composite sandwich in the nosecone will be loaded dynamically in this direction during frontal impact testing. Wedge sandwich samples have been produced to investigate the in-plane impact structural properties of the sandwich. The objectives of this experimental investigation are to:

- Identify the failure mechanisms present in the sandwich during edgewise unsupported loading and their influence on energy absorption in the sandwich.

- Identify the failure mechanisms present in the sandwich during oblique edgewise loading.

- Provide force-displacement information required for evaluation of the sandwich modelling capability in PAM-CRASH[TM]. Failure mechanisms are also required for direct comparison with the numerical models.

- Investigate the change in failure mechanisms and energy absorption of the sandwich when a higher density core material is used.

The wedge geometry is shown in Figure 4-79 and individual sample dimensions are specified in Table 4-17.
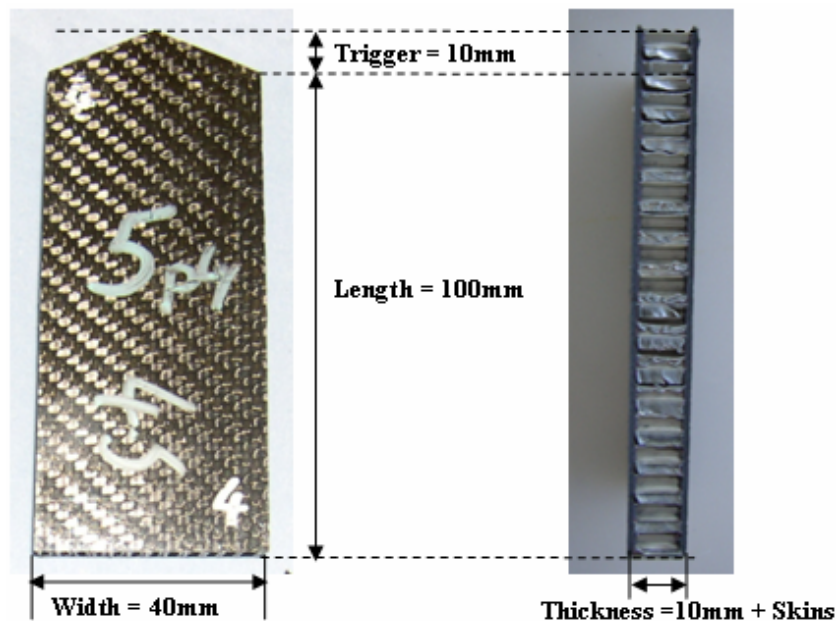
Figure 4-79: Wedge sample geometry

Sample	Plies	Core Density (kg/m^3)	Length (mm)		Width (mm)	Thickness (mm)	Mass (g)
			Edge	Centre			
1	4	72	99	109	39.8	11.8	16.1
2	4	72	100	110	40	11.8	16.5
3	4	72	100	110.5	40.3	11.8	16.8
4	5	72	100	109.5	39.3	12.2	19.2
5	5	72	98	109	40	12.2	19.2
6	5	72	98	107.5	39.8	12.1	19.2
7	4	129	99	108	39.8	11.6	19.4
8	4	129	100	109	40	11.6	19.1
9	4	129	99	108.5	40	11.6	18.7
10	5	129	99.5	108	39.3	12.1	21.7
11	5	129	99	109	39.8	12.1	21.9
12	5	129	100	109	38.5	12.1	21.4

Table 4-17: Wedge sample geometries

A series of statically loaded tests are required to determine the likely energy required for dynamic testing. The test apparatus is shown in Figure 4-80, which shows the wedge sample fixed axially and at an oblique angle of 15^0. The nosecone has a maximum oblique loading of 27^0, as stated in Section 3.3.3; however, the oblique loaded wedge samples are orientated at 15^0 to investigate the progressive effects of smaller loading angles. The sample is mounted in a holding device that locks the sample in place.
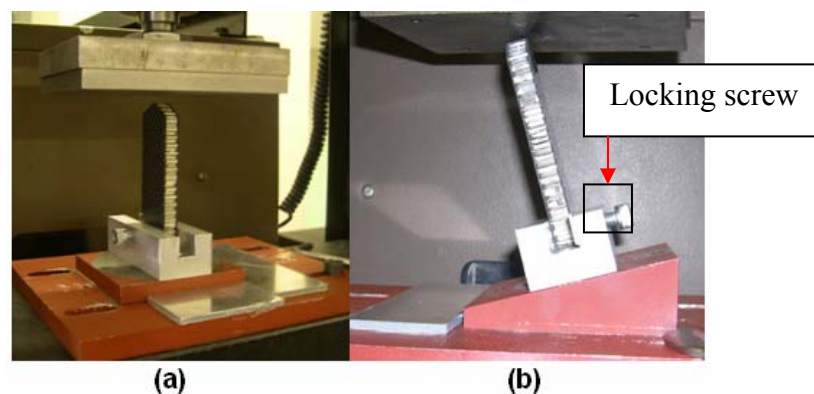
Figure 4-80: Compression apparatus. (a) Axial loading. (b) Oblique 15^0 loading

Low-Density Core Axial Compression Test

The skins within the trigger Section were observed to split and fold away from the core similar to the Type-III failure mechanism described in Section 3.3.3 and by Mamalis et al. [112]. Once the trigger had been passed, the core was observed to split and fold producing a stable failure mechanism. The deformation and failure mechanisms are shown in Figure 4-81 and Figure 4-82 for wedge specimens 1 and 3 respectively, which are both 4-ply skin samples.
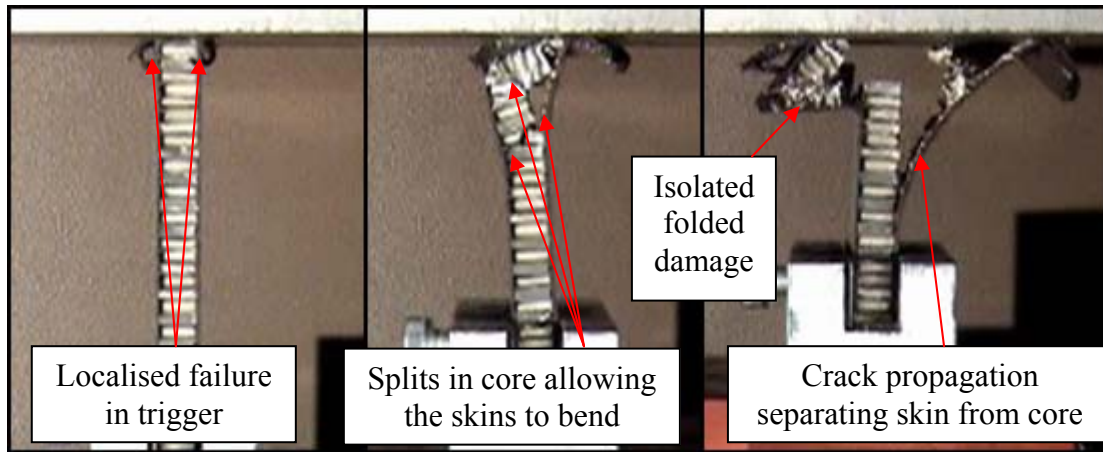
Figure 4-81: Failure mechanisms in Wedge-1
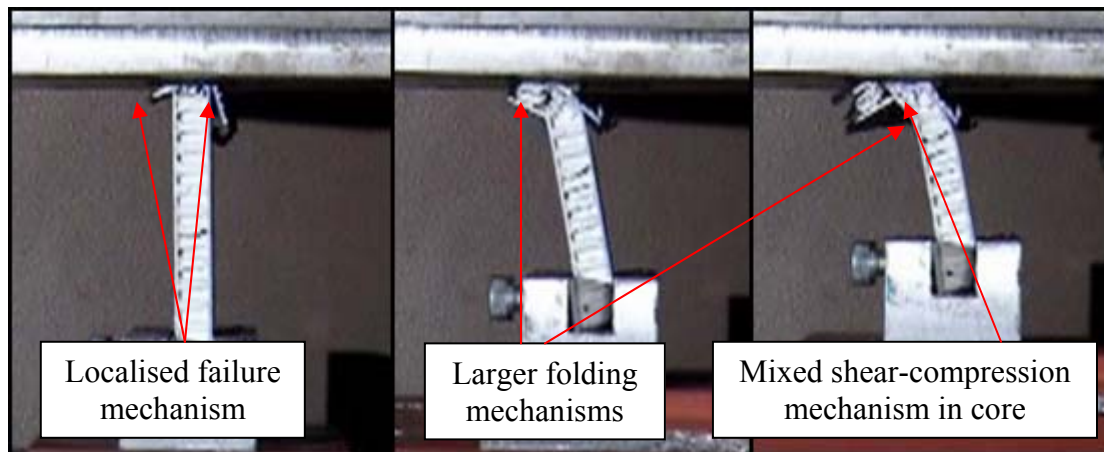
Figure 4-82: Failure mechanisms in Wedge-3

The variation in failure mechanism produces an oscillating loading profile as shown in Figure 4-83 and Figure 4-84. The folded Section of the sandwich is isolated and reduces the crushing strength of the sample at impact wall. These folds reduce the effective sample surface at the impact wall. The crushing strength increases when the isolated

damage is cleared. Wedge-6 produced a variation to this deformation as the sample failed by folding at its base.
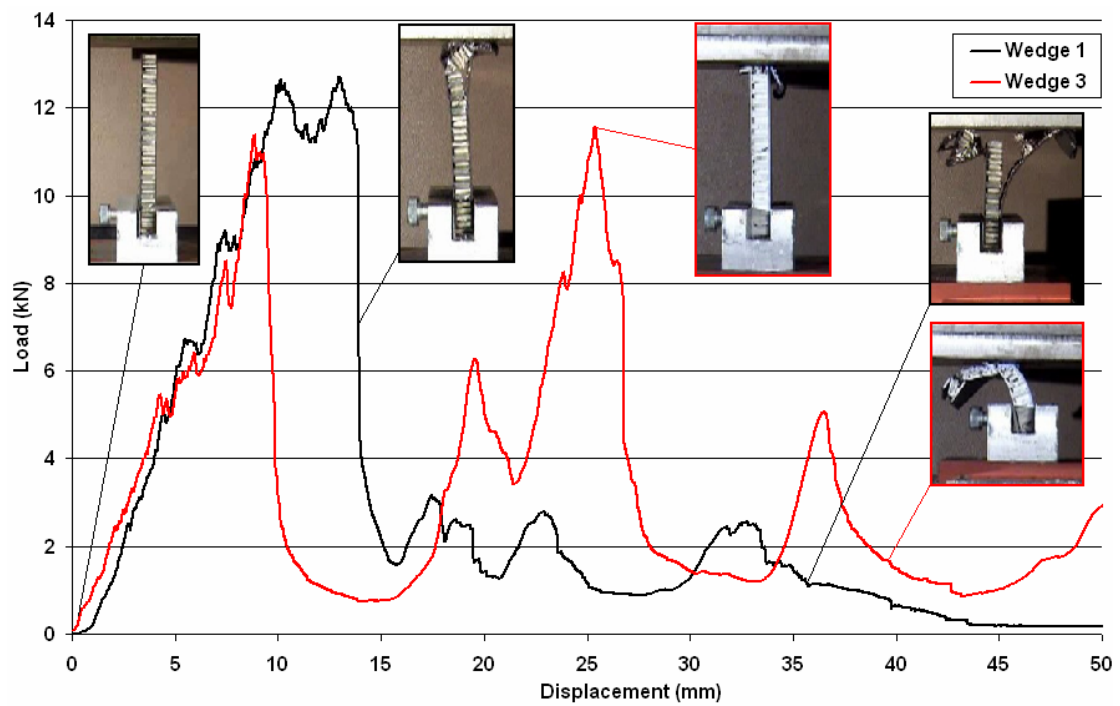
Figure 4-83: 4 ply low-density core wedge quasi-static compression results
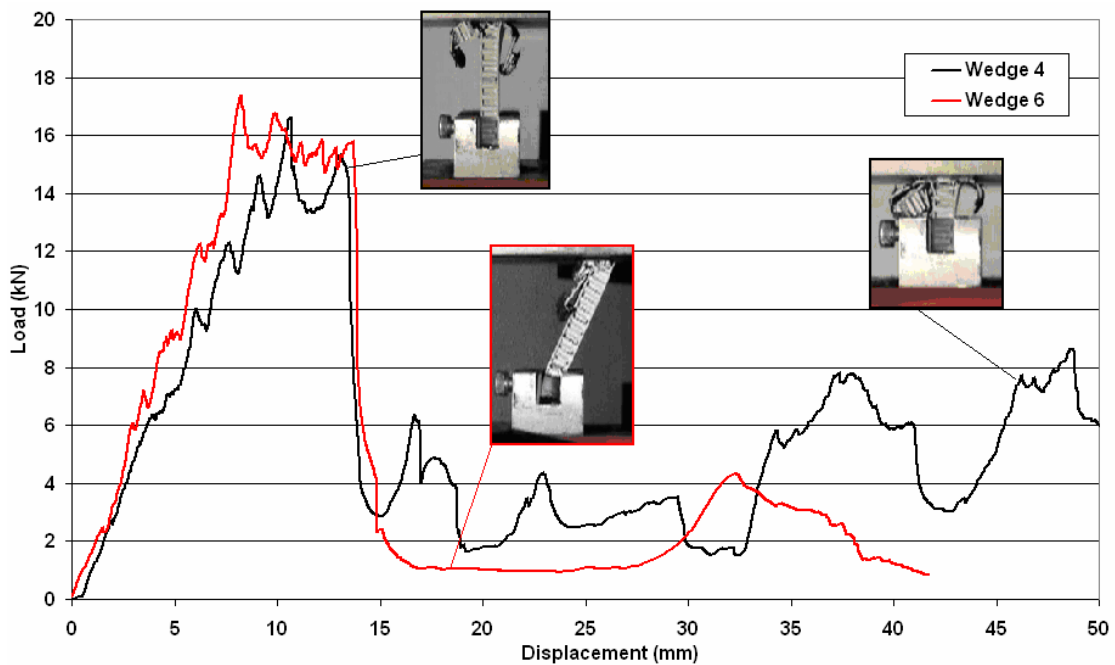
Figure 4-84: 5 ply low-density core wedge quasi-static compression results

In the case of Wedge-1 the skins were observed to delaminate from the core. Upon inspecting this sample aluminium was found in some of the bond-line fillets, this failure was therefore a mixture of tearing of the core material and failure of the bond-line as shown in Figure 4-85.
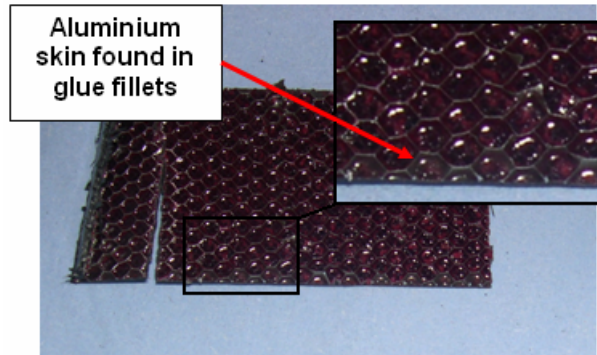
Figure 4-85: Aluminium located in glue fillets of Wedge-1 debonded skin

The force-displacement measurements and observed failure mechanisms in the four and five ply thickness axially loaded samples presented here are used in Section 5.3.4 to evaluate the capability of PAM-CRASH^{TM} for composite-honeycomb sandwich modelling.

High-Density Core Axial Compression Test

As discussed in [112], the choice of core material influences the strength and failure mechanisms in the sandwich when subjected to edgewise loading. In this investigation, the influence of a high-density core material on the edgewise properties of the sandwich is presented. These samples contain the 129kg/m^3 density honeycomb core and were subjected to the same experimental conditions as the 72kg/m^3 core samples.

The high density core samples produced greater stability during axial loading tests. A stable end progression failure mechanism, identical to the Type-III failure mechanism described in Section 3.3.3, was observed throughout the crushing process of each test. Figure 4-86 shows the deformation mechanism observed in Wedge-10. The deformation is initially isolated at the impact wall followed by crack propagation between the skin and core as the tests progressed. Upon examination, no aluminium core was found on any of the skins, thus suggesting an adhesive bond-line failure. A constant sample

surface is maintained at the impact wall. This consistency in failure mechanisms increases the energy absorbency of the samples and strengthens the samples as shown in Figure 4-87 and Figure 4-88.
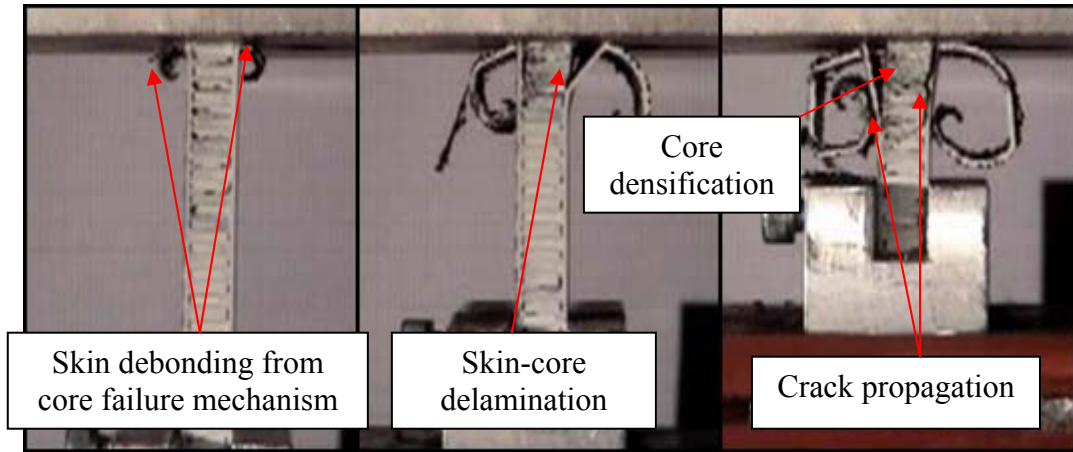
Figure 4-86: Failure mechanisms in Wedge-10
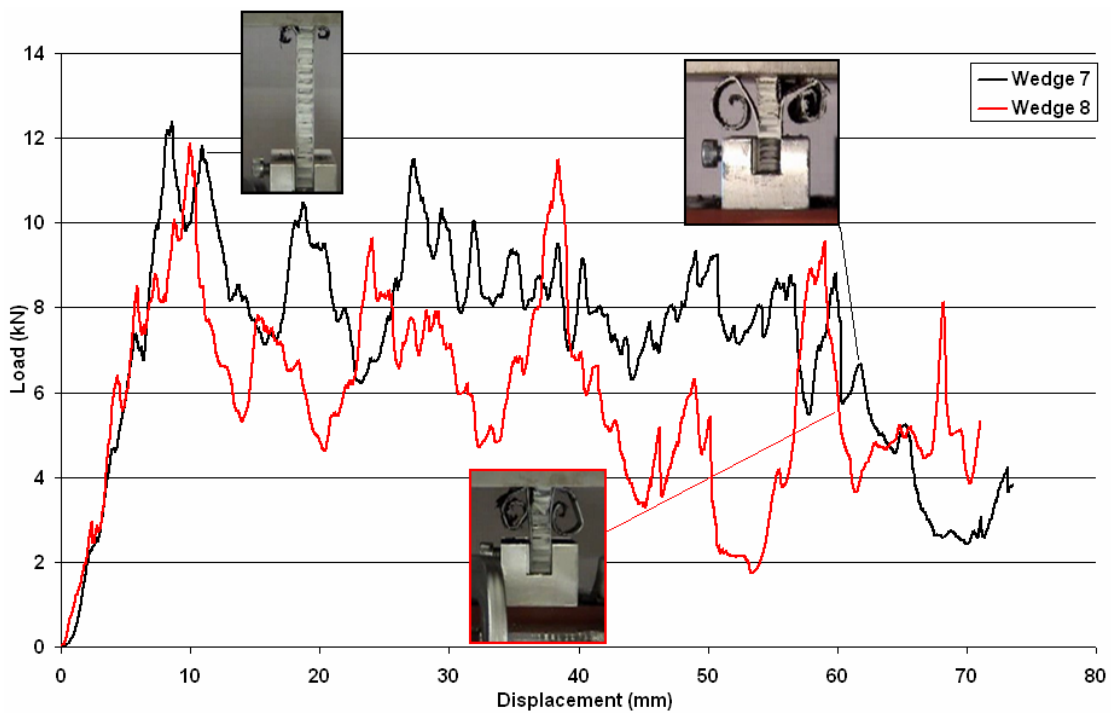
Figure 4-87: 4-ply high-density core wedge quasi-static compression results
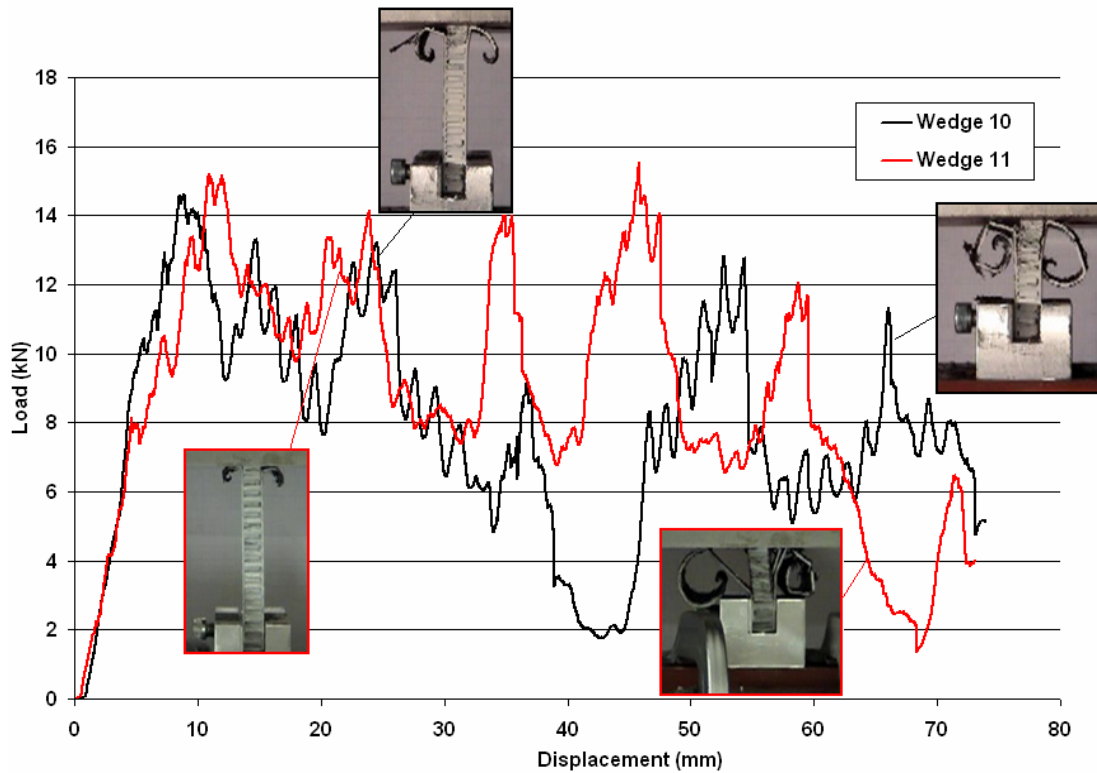
Figure 4-88: 5-ply high-density core wedge quasi-static compression results

Comparing the specific energy absorptions (SEA) of the axial loading tests, in Figure 4-89, it may be seen that there is a significant increase in energy absorption for samples to higher density cores compared with low-density cores. In the low density samples cracks propagate through the core and reduce the strength of the sandwich. In the case of the high density samples, crack propagation occurs in the adhesive bond-line and not in the core.
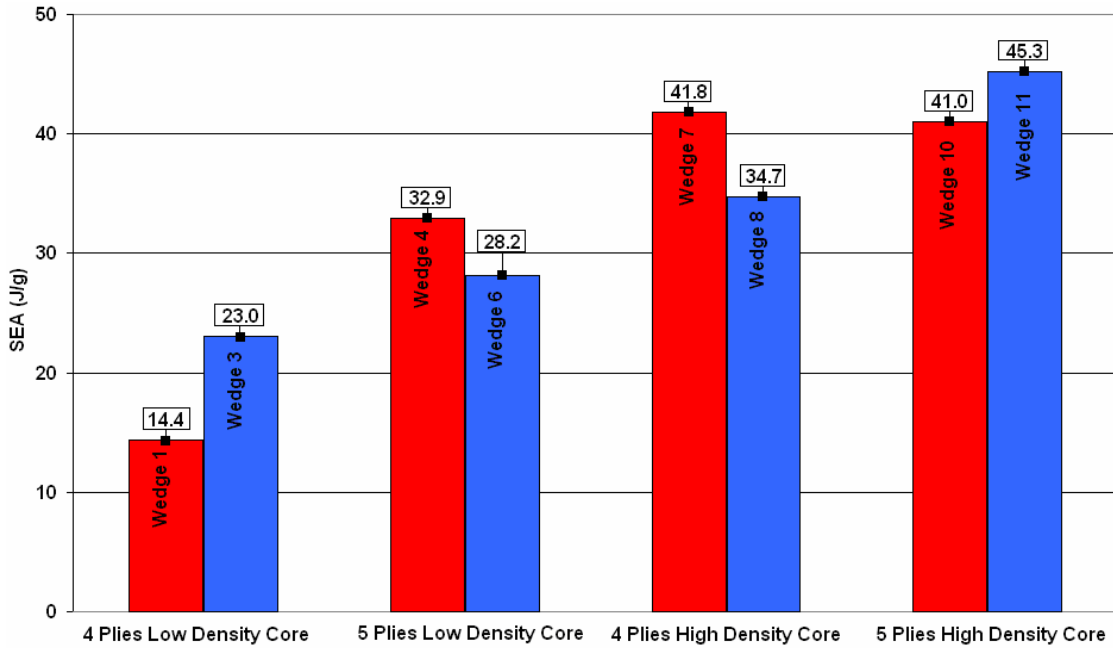
Figure 4-89: Specific energy absorption of wedge samples during edgewise loading

Due to the amount and location of high density core material used in the nosecone structure, the findings from this investigation are not used to evaluate the numerical model. This investigation has shown how the choice in core material can influence the stability of the sandwich during edgewise compression. The high density core material was observed to resist crack propagation and held the skins in position thus increasing the energy absorption of the sandwich. The failure mechanisms were isolated in the composite skins and adhesive interface between the skins and core.

Oblique Compression Test

The direction of the composite-honeycomb sandwich in the nosecone tip is not perpendicular to the impact wall. The angle of the sandwich has been shown in Section 3.3.3 to be 27^0 at the nosecone tip. Therefore, the influence of edgewise loading angle on the energy absorption of the sandwich is investigated and presented here. Only the low density core material was investigated as the high density core sandwich is located near the rear of the nosecone and is thus subjected to 0^0 axial edgewise loading conditions.

Low-density core samples were crushed at an oblique angle of 15^0; Wedge-2 contains a 4-ply skin and Wedge-5 contains a 5-ply skin. The 15^0 oblique loaded samples produce a consistent Mode-1b failure mechanism at the impact front as shown in Figure 4-90. These mechanisms include mixed shear-compression in the core and cracking of the matrix in the composite skins.

| Sandwich folding failure mechanism at tip | Mixed shear-compression in core | Damage consistently maintained at impact wall |
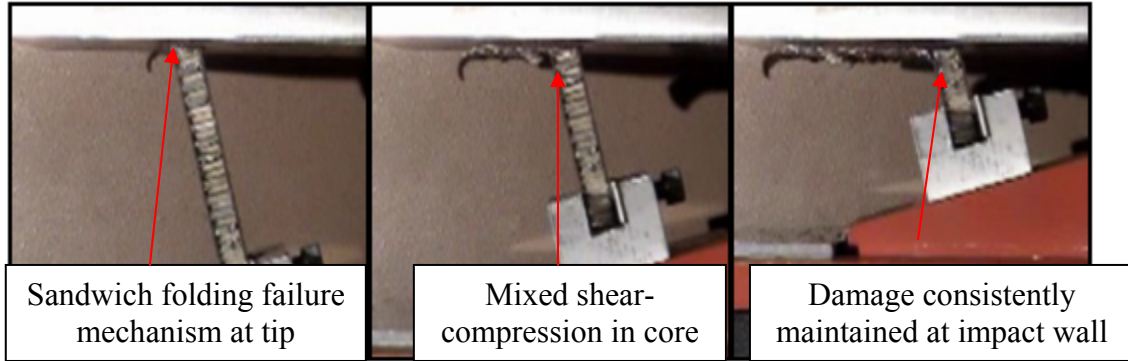
Figure 4-90: Failure mechanisms in Wedge-2

The low-density samples show a higher load bearing capability compared to axial loading when an oblique load angle of 15^0 is applied, as shown in Figure 4-91. Fluctuations in load are observed when sections of the sample fold. The reduction in load indicates the production of a fold in the sandwich and consequent hinging about that fold. The load increases once the folded region has been surpassed and remains until a new fold is produced. The peak load in Wedge 2 is shown to be consistently 13kN whilst the minimum load is consistently 6kN.
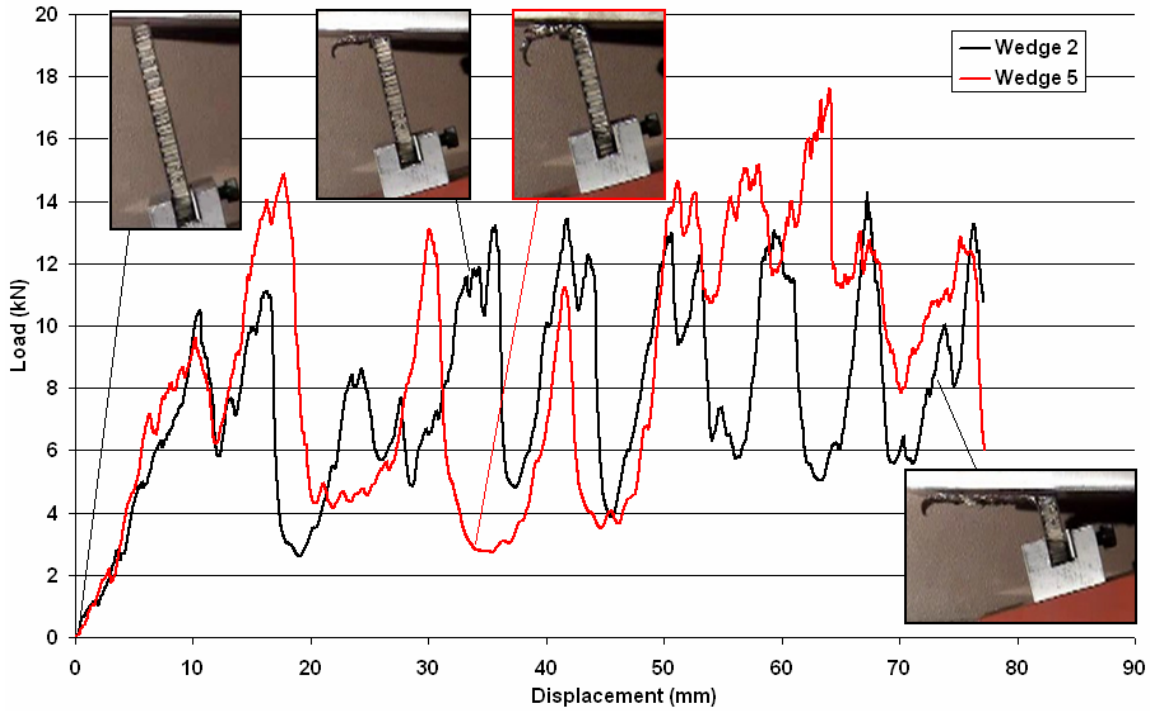
Figure 4-91: Oblique loading test results

Samples loaded at 15^0 to the impact wall show an increase in energy absorption compared with those tested axially, as can be seen in Figure 4-92. Axial tests produced buckling and failures down the length of the samples which reduce the strength of the specimen. These oblique tests show damage to be contained nearer the impact wall and that the skins remain bonded to the core, thus maintaining structural strength and increasing energy absorption.
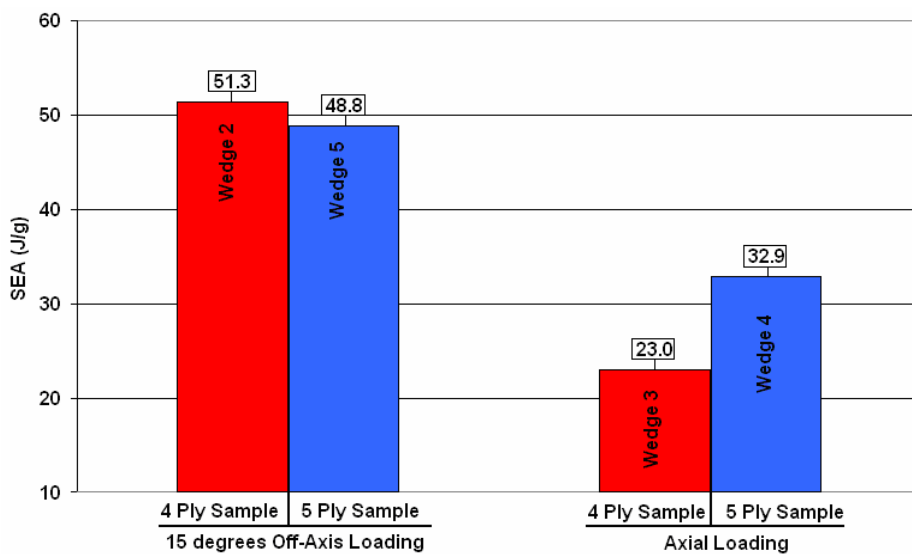
Figure 4-92: Comparison of SEA between oblique and axial tests

The force-displacement measurements and observed failure mechanisms in the four and five ply thickness oblique loaded samples presented here are used in Section 5.3.4 to further evaluate the capability of PAM-CRASH^{TM} for composite-honeycomb sandwich modelling.

Impact Loaded Wedge Samples

The energy absorbency measured from the quasi-static test series is then used to determine the input energy for dynamic testing. The Rosand drop tower is used with the Photron high speed camera as shown in Figure 4-93; the holding device is used to secure the sample.
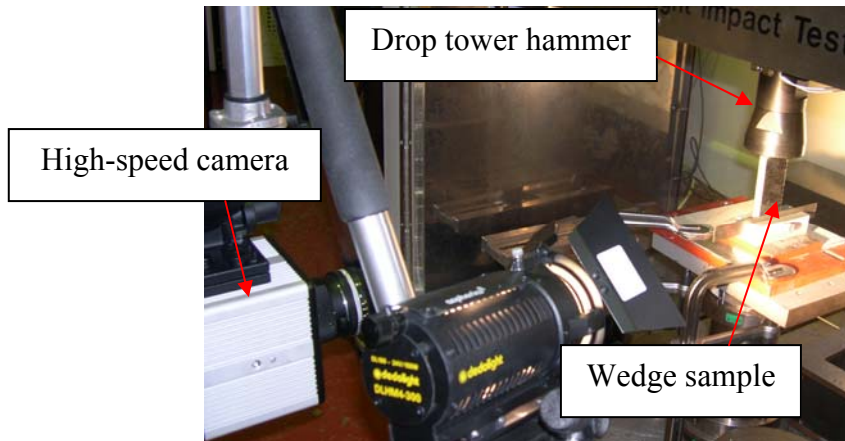
Figure 4-93: Wedge sample in drop tower impact apparatus

The dynamic test settings are based on the findings from the quasi-static investigation. A safety factor has been introduced to reduce the input energy to prevent any possible damage to test equipment. The input energies for the different wedges are shown in Table 4-18.

Wedge	No. Plies	Core Density (kg/m^3)	Velocity (m/s)	Energy (J)
20	5	72	3.44	297
25	4	129	3.44	297
26	4	129	3.46	300
27	5	129	4.84	588
28	5	129	4.42	490

Table 4-18: Input energy and velocities for dynamic testing

Failure mechanisms for the low-density core wedge sample are shown in Figure 4-95. The deformation begins with a stable end progression failure mechanism at the impact front. A crack was then observed to propagate through the core near one skin and create a fold in the sandwich near the impact front. The sample produces a fold as the strength of the sample is now biased on one side; the core flexural strength is insufficient to prevent this fold. This large fold produces a low resistance to the impactor after the sample trigger has been compressed as shown in Figure 4-94
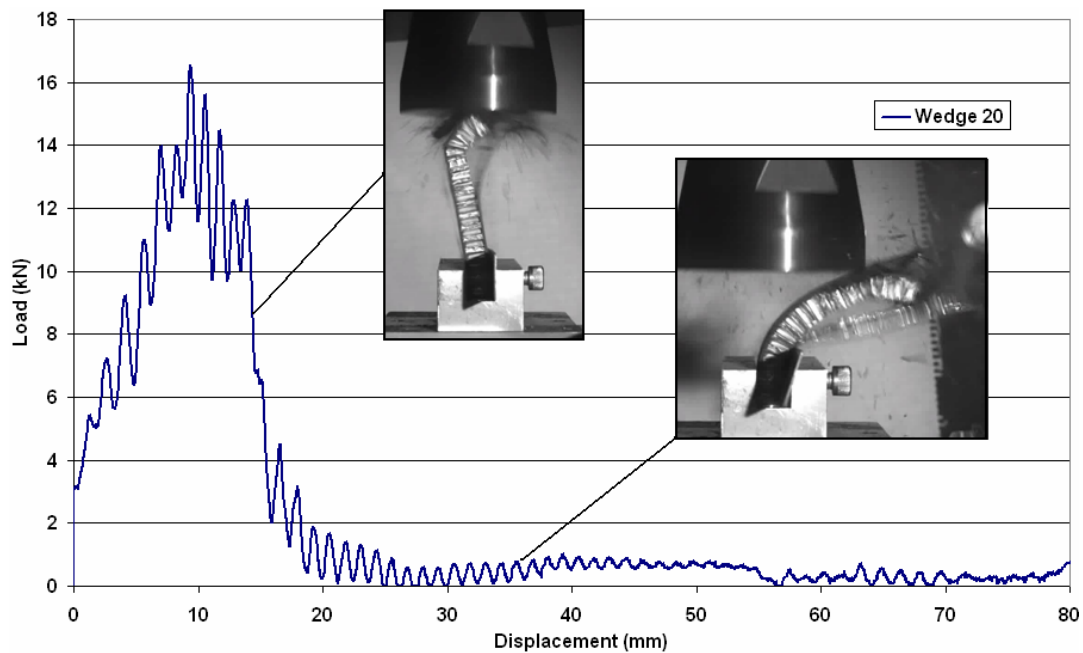
Figure 4-94: Low-density core impact wedge test
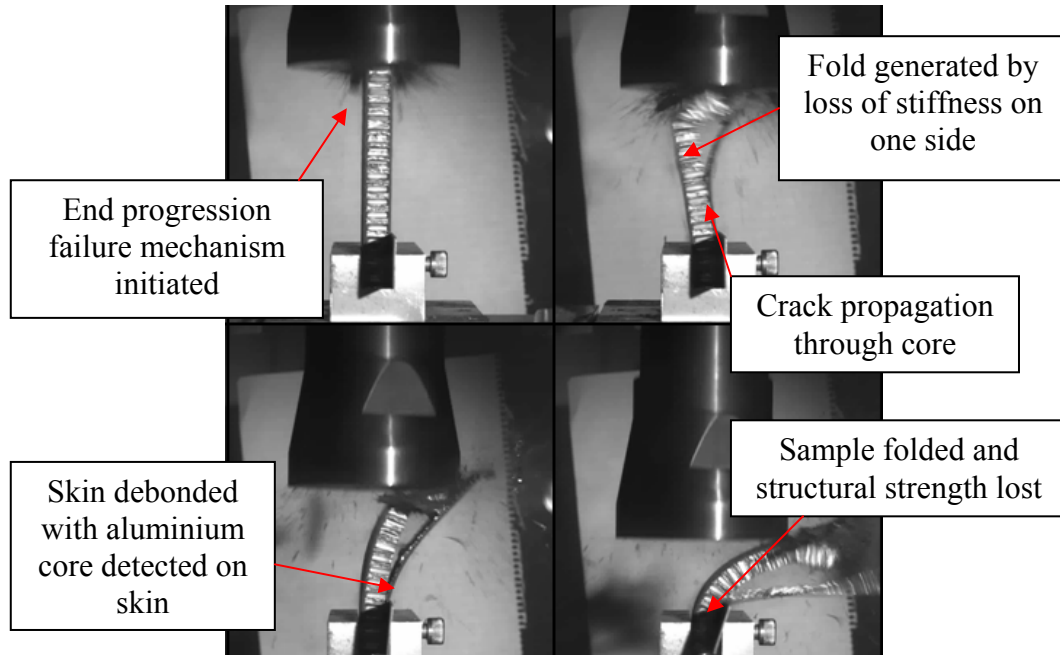
Figure 4-95: Failure mechanisms in Wedge-20

The high-density wedge samples provide greater stiffness to the impactor and resist folding. The 4-ply samples were observed to maintain deformation at the impact front conforming to the Type-III failure criteria, as shown in Figure 4-96. Larger cracks are then formed between the core and skin producing larger folds in the composite skins. The strength of the core prevents the structural folding observed in the low-density tests. The tests conclude with a complete delamination of one skin from the core material. The 5-ply specimens were observed to follow a similar series of deformation mechanisms. These mechanisms produce the increased and consistent strength shown in Figure 4-97 and Figure 4-98.
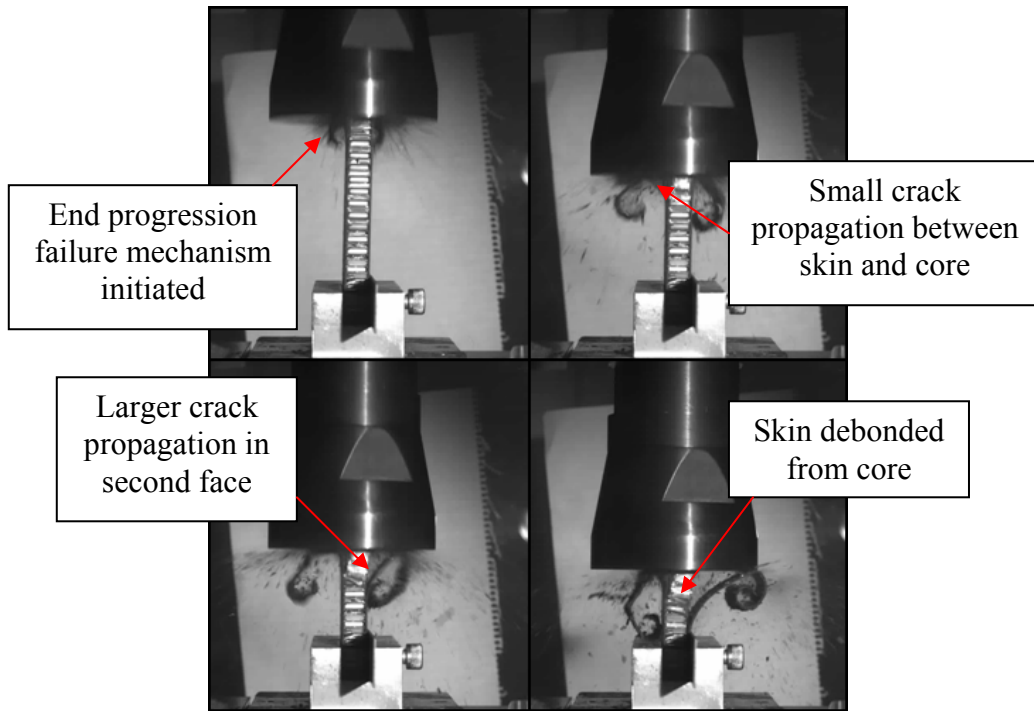
Figure 4-96: Failure mechanisms in the high density wedge sample 26
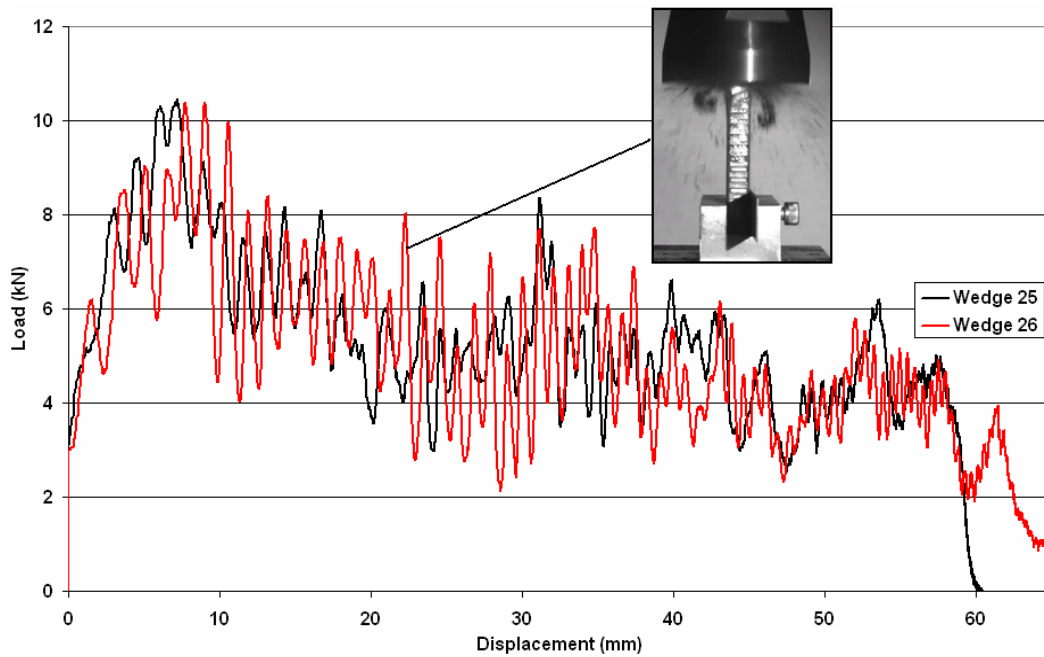
Figure 4-97: 4-ply high-density core impact results
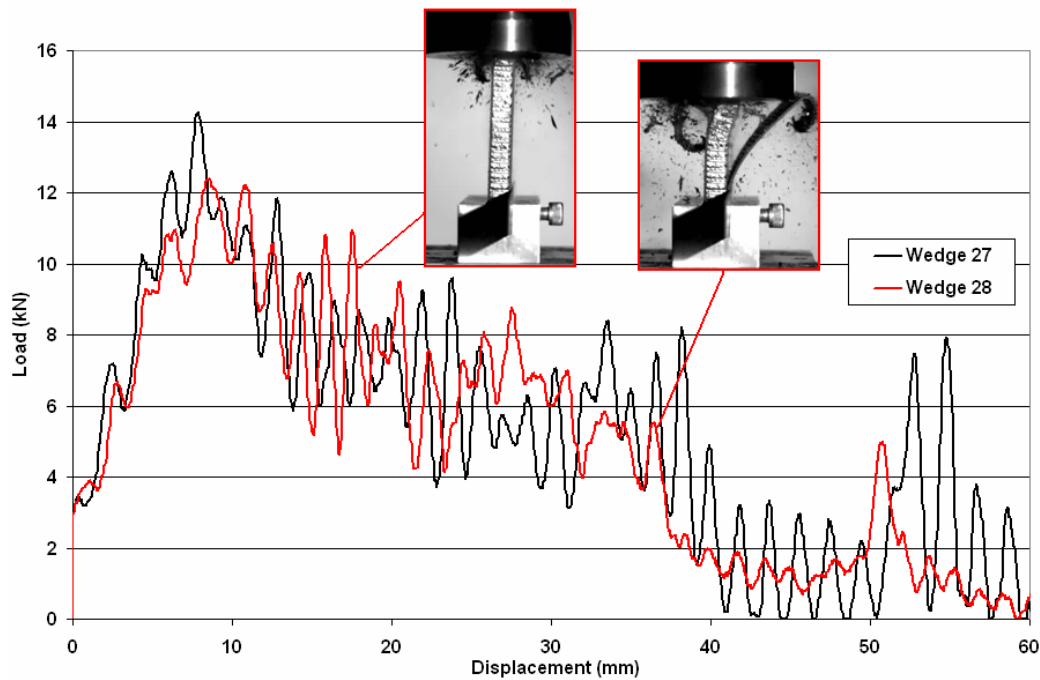
Figure 4-98: 5-ply high-density core impact results

When compared, the dynamically loaded wedge specimens show a reduction in energy absorbency in Figure 4-99. The 4-ply specimens were observed to maintain the failure at the impact front, whilst the 5-ply sandwich skins were observed to separate from the sample along the glue line. The impact may produce failure cracks in the composite skins which propagate and reduce the composite skin strength at the impact front. In the case of 5-ply samples a similar propagation may occur; however, the skins are stiffer and therefore separate way from the core. The skin-core debonding was found to propagate further ahead of the crushing wall than in the quasi-static tests. This may suggest a loading rate dependency on the adhesive properties.
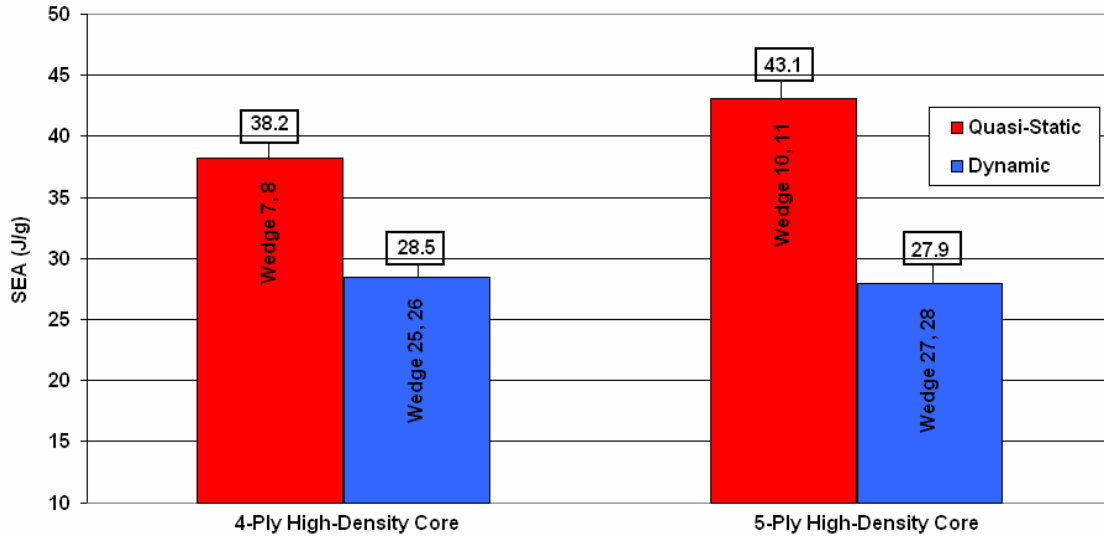
Figure 4-99: Comparison SEA quasi-static and dynamic test samples

The impact loading results are not used for further calibration or evaluation of the PAM-CRASH[TM] sandwich modelling capability. This investigation has shown how the failure mechanisms in the sandwich vary depending on the rate of loading. The properties of edgewise unsupported loading on a honeycomb core sandwich structure have not previously been investigated. This work has extended the research to include the influence of oblique loading angles and higher rates of loading.

4.6   Section Summary

This Chapter has presented the findings from the experimental investigation of the composite-honeycomb sandwich. The core and skin materials have been investigated separately before investigating the energy absorbing properties of the sandwich structure. The first objective of this investigation was to produce the required material properties for the material models used in the commercial FE code PAM-CRASH.[TM] The second objective was to investigate the variation in material properties of the core material when subjected to complex loading conditions and determine the non-linear damage progression relationship of the woven composite material.

The core material has been examined using standardised testing methods to establish the bare compressive properties. In order to investigate the direction dependent properties

of honeycomb in shear-compression, an Arcan apparatus has been improved for cellular solid testing. The research produced a series of relationships between load direction and compressive-shear properties including peak load and crushing properties in both the 'T-TW' loading direction. These relationships were found to be consistent with previous research, thus suggesting all hexagonal honeycombs produce similar relationships. The 'T-TL' properties were found to be highly sensitive to cellular inconsistencies.

A further investigation was presented to determine the effects of in-plane pre-deformation on the 'T' direction compressive properties. A series of honeycomb samples were pre-deformed in the in-plane direction before compression loading in the 'T' direction. This investigation produced relationships between pre-deformation and the change in the 'T' directional compression properties and specifically the effects on crushing strength and compaction strain.

The composite skin material has been investigated to provide input properties for the Ladevéze damage model. This has been conducted with the use of an optical measuring system to replace the traditional use of strain gauge measuring devices. The in-plane cyclic shear tests have been used to produce a non-linear damage progression law for improved computational representation. An examination of the composite material compressive properties has been conducted using a new testing method currently in development. The recorded failure strength was found to be approximately 35% of the manufacturer's specifications. The apparatus does not prevent the buckling process occurring in the composite sample; thus the recorded failure strength during this investigation is the buckling strength of the composite sample. The apparatus requires further development.

The composite sandwich has been examined under a variety of loading conditions. An investigation to determine the effects of glue fillets on the 'T' direction properties has been conducted. These fillets introduce additional constraint and support the cellular walls and have been observed to increase compressive peak and crushing strength of the core. The debonding strength of the sandwich is investigated using a CSB sample using

both quasi-static and high-rate loading with a new dynamic delamination apparatus. The investigation found an increase in the strength and G_{IC} when loading rate is increased. A 3PB investigation has also been conducted to determine the flexural properties of the sandwich structure and identified failure mechanisms.

The in-plane energy absorbency of the sandwich was studied using wedge impact samples. These samples were loaded axially and at an oblique angle of 15^0 to examine failure mechanisms that could potentially take place in the nosecone structure and the variation of direction on the energy absorption. In both cases failure was confined to the wall front, producing a localised Type-III end progression failure mechanism for the axial tests and a localised folding failure mechanism at the crushing wall for the oblique tests. The wedge samples displayed a reduction in energy absorption when tested dynamically compared with quasi-static testing. Crack propagation through the core material occurred separating the composite skins and reducing structural strength for the low-density core samples. Crack propagation through the adhesive interface was observed in the high-density core samples during axial quasi-static and impact loading. During impact loading, the crack propagation was observed to extend further through the sample than in the quasi-static testing. This decreased the energy absorption of the sample and indicates a loading rate dependency on the adhesive interface. High loading rate investigations using the new Mode-I DCB/CSB apparatus with high-density core samples are required to assess the rate dependency of the adhesive.

5 Computational Modelling of Sandwich Materials

This Chapter presents research work conducted to reproduce the energy absorbing properties identified during material testing using a commercially available FE code. Improvements to the constitutive material modelling in the code are undertaken to improve accuracy of the numerical methods.

Computational material models are based on observations made during testing from which theoretical laws are developed to approximate material behaviour. The modelling of complex materials, such as honeycomb and composites, are of keen interest to researchers and developers as the availability of robust and accurate simulation tools will assist the development of composite-sandwich components.

5.1 Honeycomb Modelling

Honeycomb cellular solids are a highly orthotropic material as discussed in Section 2.2.1. Numerically representing this type of material poses a number of challenges to FE code developers as modelling direction dependent behaviour adds significant complexity to the programming. The current PAM-CRASH^{TM} honeycomb model (MAT41) utilises a robust modelling method which considers uniform loading in the three principal directions only, without any complex relationships between load conditions and directional properties.

This Section presents improvements to the solid element "macro-representation" of the honeycomb material to account for the effects of multi-axial loading examined during the experimental Section of this thesis on the low-density honeycomb used in the nosecone structure of the 006 BAR-Honda F1 car.

A further examination using a shell element "meso-representation" of the honeycomb at the cellular wall scale has also been conducted to investigate the ability of this approach to examine the change in properties in the principal directions when subjected to multi-axial loading conditions.

5.1.1 Macro-Scale Modelling

As discussed in Section 2.3.2, the current honeycomb constitutive material model available in PAM-CRASH^{TM} [50] was developed primarily for applications in solid impact crash barriers and not sandwich materials. The model contains inaccuracies which must be addressed before the model can be used for sandwich applications. These simplifications include:

- The peak loading effect observed in the 'T' direction is neglected.

- The strain for full compaction is assumed to be the same in all three principal directions.

- The 'T' directional yield and crushing strengths are considered constant independent of loading direction and pre-deformation in the in-plane directions. The experimental research Section of this thesis has shown that there is a progressive increase in these strengths when in-plane compression has occurred before 'T' direction compression.

Using the information gathered from experimental testing and published HEXCEL^{TM} datasheets [18], the material model MAT41 solid element is calibrated to represent the compressive properties of the low density honeycomb material in the principal directions. For this single solid element model having the boundary conditions as shown in Figure 5-1 is used. The 'T' direction calibration is shown in Figure 5-2.
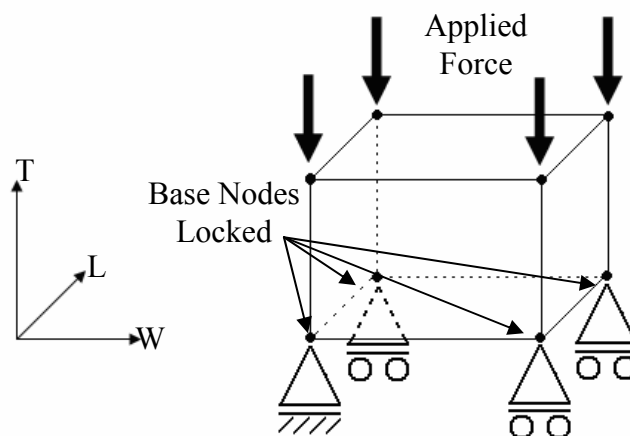
Figure 5-1: FE solid element loading and boundary conditions
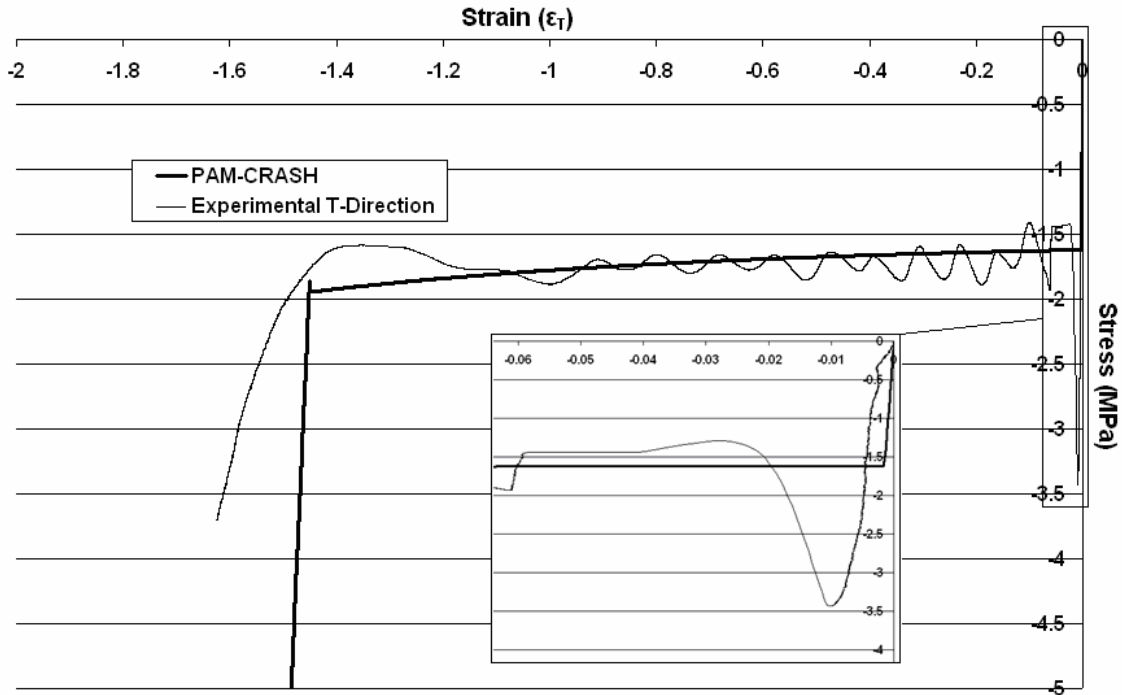
Figure 5-2: Standard MAT41 model compared with experimental results

Introduction of Peak Load Effect

The inset graph in Figure 5-2 shows a close-up of the difference between the experimental peak strength and the standard MAT41 numerical model. In this work, a simple modification to introduce this peak loading effect has been implemented into the constitutive material code. As discussed in Section 2.3.2, the constitutive material code calculates the stress during the peak load using equation 2-36. By re-specifying the value of yield strain within the plastic code, the plateau regime can be adjusted without affecting the elastic properties. In the case of the low density honeycomb used in the 006 nosecone, the average plateau strength is 42% of the peak strength. Using this approach, the current user input requirements remain the same as in the commercial code. Between the yield strain and compaction, the plateau stress is calculated using equation 5-1,

$$\sigma_{Ti} = \left[0.42 E_{0T}\varepsilon_{YT} + E_{1T}\left(\varepsilon_T - \varepsilon_{YT}\right)\right],$$
[5-1]

where E_{0T} is the 'T' direction elastic modulus, E_{1T} is the 'T' direction crushing plateau modulus, ε_{YT} is the 'T' direction peak strain and ε_T is the instantaneous strain in the 'T' direction . In order to avoid numerical problems a declination modulus is specified to prevent an instantaneous drop from the peak load to the plateau crush condition. The

159

validation of these improvements is shown in Figure 5-3. The inset image in **Figure 5-3** clearly displays the new peak load compared with the experimental result.
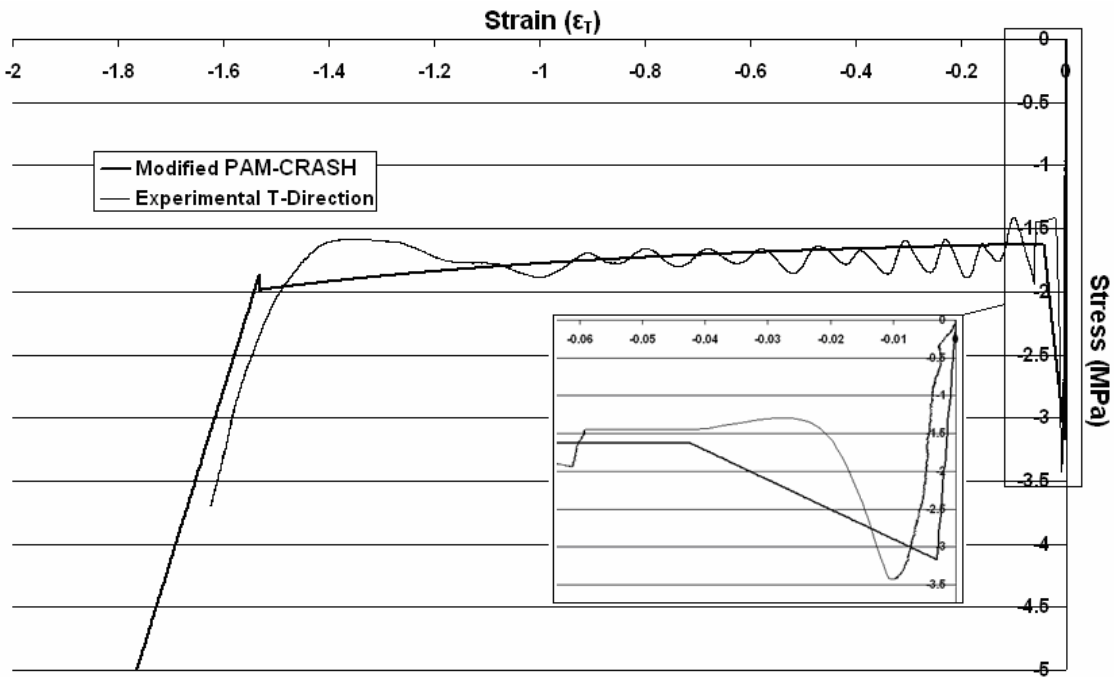
Figure 5-3: Validation of peak loading effect introduced into the MAT41 code

A limitation of the current code improvements for peak load is that it only works when there is one element in the 'T' direction. With more than one element the overall model will produce several peaks as each element must overcome the peak load criteria. To prevent this, the code must include a further "damage" parameter to remove the peak loading effect from adjacent cells along the direct 'T' direction once a single element has overcome the peak load, as shown in Figure 5-4.
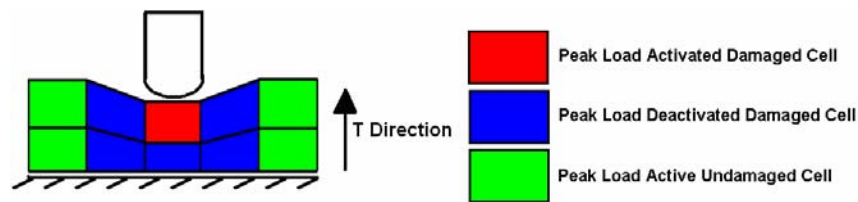
Figure 5-4: Multi-element damage dependent model

The red cell indicates that the element has produced the relevant peak load effect; the blue cells are the partially damaged elements which, if compressed, will not produce a peak effect. The green cells are elements which are undamaged and thus keep the peak

load effect. This modification has not been conducted as the required source code was unavailable during the course of this research.

Introduction of In-Plane Deformation of 'T' Direction Crushing Strength

The MAT41 code does not include any effects from pre-deformation in the 'W' and 'L' directions when calculating the 'T' direction crushing properties. The deformation from loading in the in-plane directions has been shown in Section 4.3.2 to affect 'T' direction compression properties. To reproduce this effect with the MAT41 material definition, a single solid element is produced with the boundary conditions shown in Figure 5-5 and loaded in two stages. The first stage compresses the element in an in-plane direction, either 'W' or 'L', by a specific displacement before the second stage compresses the element in the 'T' direction.
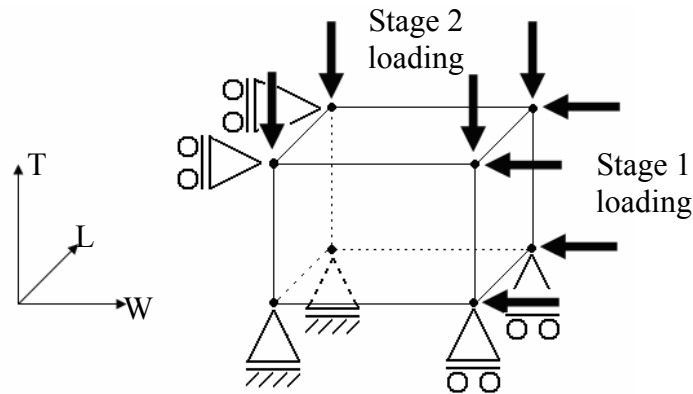
Figure 5-5: FE solid element boundary conditions for pre-crush loading

The calculated 'T' directional properties for plateau stresses are shown to be unaffected by in-plane deformation in Figure 5-6, this figure also shows the difference between the commercial computational code and experimental response stress.
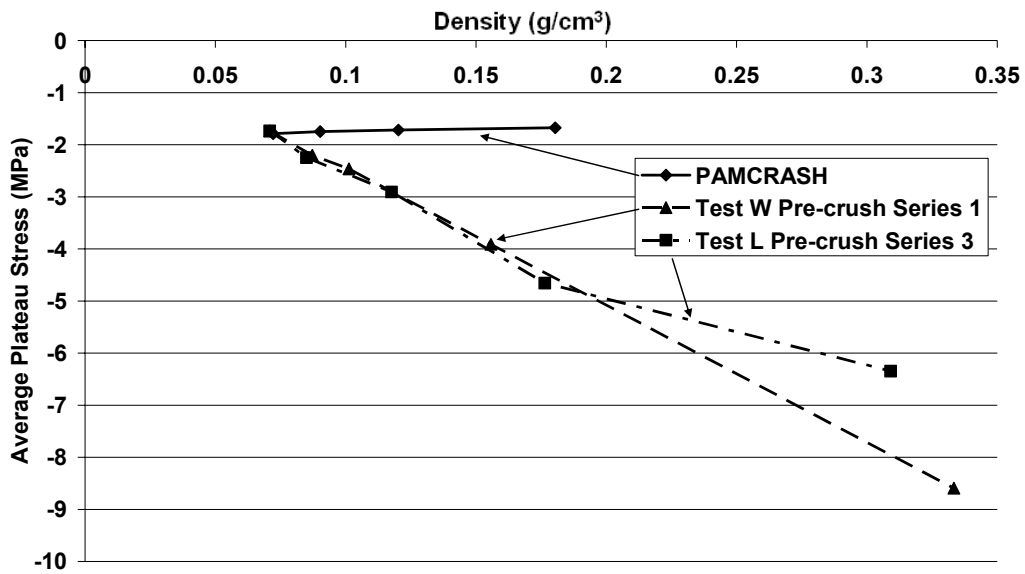
Figure 5-6: Constant plateau stress in the commercial PAM-CRASH[TM] code

From experimental testing presented in Section 4.3.2, the relationship between in-plane deformation and 'T' direction plateau stress has been established using equation 4-1. This law is applied to the improved plateau stress law, equation 5-1, to produce the plateau stress law, equation 5-2,

$$\sigma_{Ti} = \frac{\left[0.42E_{0T}\varepsilon_{YT} + E_{1T}\left(\varepsilon_T - \varepsilon_{YT}\right)\right]}{\left[\left(e(\varepsilon_W)\right) * \left(e(\varepsilon_L)\right)\right]},$$ [5-2]

where, ε_W and ε_L are the in-plane deformation strains in the 'W' and 'L' directions respectively. Implementation and application of the 'T' direction plateau properties produces the improved relationship shown in Figure 5-7.
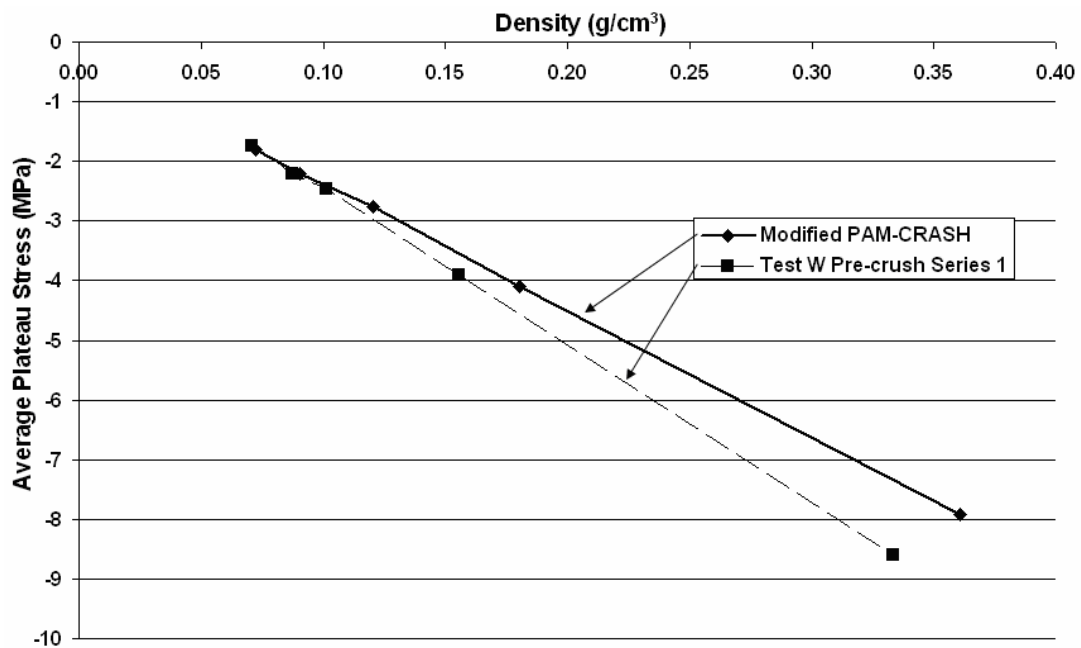
Figure 5-7: Modified MAT41 constitutive code to reproduce plateau stress variation for pre-crushed honeycomb

Introduction of In-Plane Deformation Effects on 'T' Direction Compaction Strain

The strain for full compaction in the 'T' direction has been observed to vary depending on the amount of in-plane pre-deformation, presented in Section 4.3.2. The commercially available MAT41 does inaccurately vary the compaction strain depending on in-plane deformation. The code utilises volumetric strain to determine the point at which the element is fully compacted. This method of varying compaction strain depending on in-plane pre-deformation is shown in Figure 5-8 using the same model boundary conditions presented in Figure 5-5.
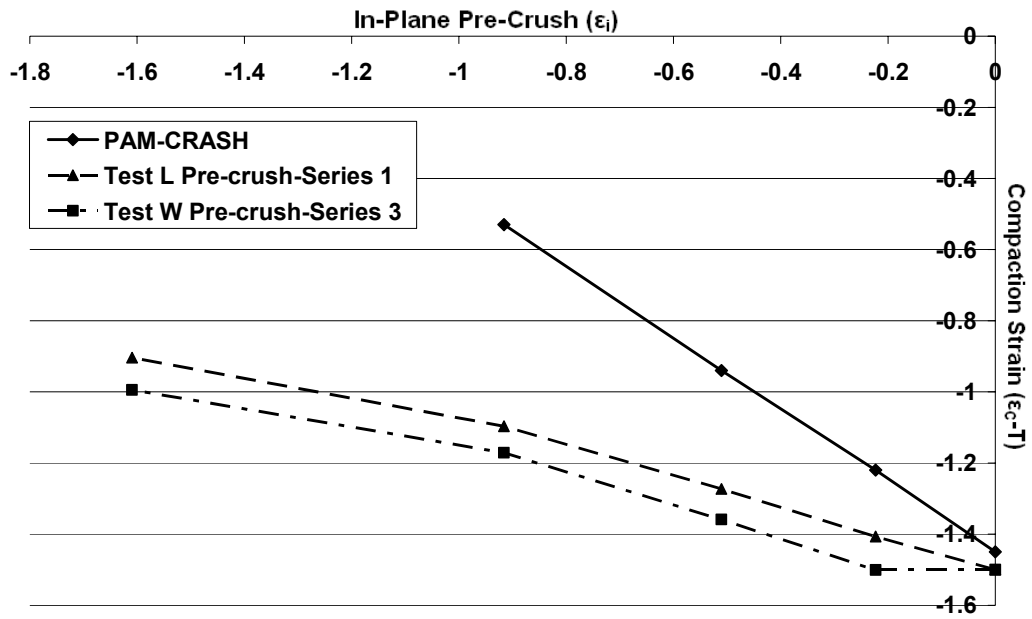
Figure 5-8: Comparison of compaction strain variation due to in-plane deformation between experiment and MAT41

The relationships observed from experimental testing, equations 4-2 and 4-3, are introduced to the MAT41 constitutive material code to improve the variation of compaction strain due to in-plane pre-deformation. Since compaction is based on using volumetric strain, the equation for compaction is;

$$\varepsilon_{V\lim T} = 0.58\varepsilon_W + 0.63\varepsilon_L + \varepsilon_{CT0}, \qquad\qquad [5\text{-}3]$$

where ε_{VLimT} is the volumetric limit strain for loading in the 'T' direction and ε_{CT0} is the user defined compaction strain in the 'T' direction for non pre-deformed cores. The result of this improvement is shown in Figure 5-9 and Figure 5-10.
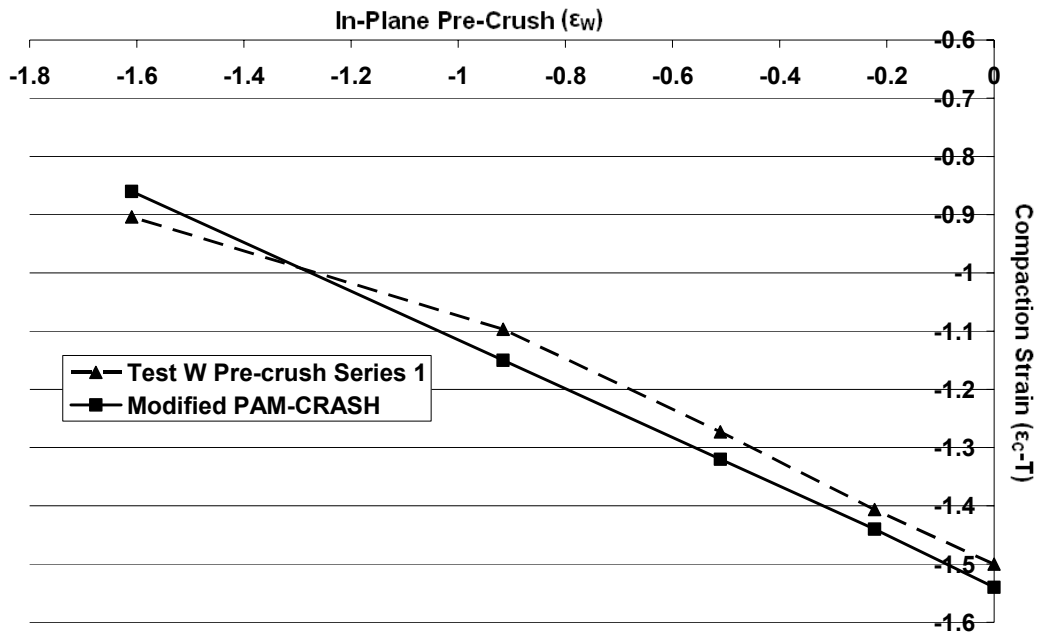
Figure 5-9: Compaction strain variation in the improved MAT41 for pre-crush in the 'W' direction
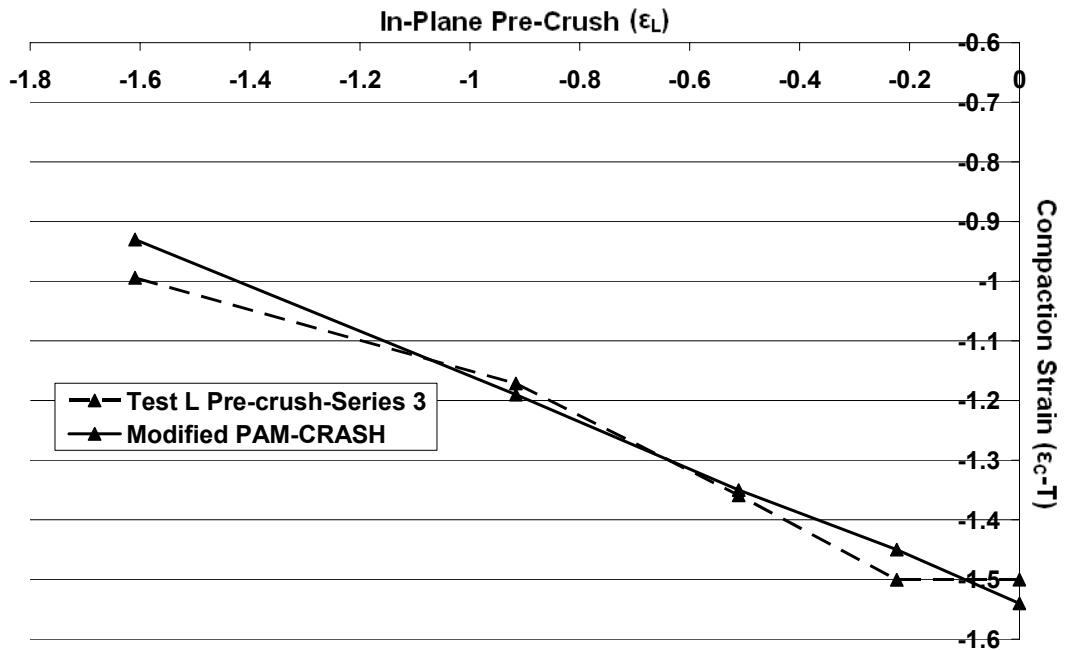
Figure 5-10: Compaction strain variation in the improved MAT41 for pre-crush in the 'L' Direction

165

Introduction of Mixed Shear-Compression Properties

Section 4.3.3 presented the relationships between mixed shear-compression loading condition directions and the influence on 'TW' out-of-plane shear and 'T' direction compression properties for the honeycomb material used in the nosecone structure. The standard MAT41 neglects this effect, presented in Figure 2-51, and therefore requires an improvement to the constitutive code. To account for the effects of load interaction and loading direction on shear and 'T' direction compressive properties, the relationships derived in Section 4.3.3 have been implemented into the MAT41 material code. A mixed shear-compression loading condition has been applied to a single solid element, shown in Figure 5-11. The improvements are compared with experimental findings presented in Figure 5-12.
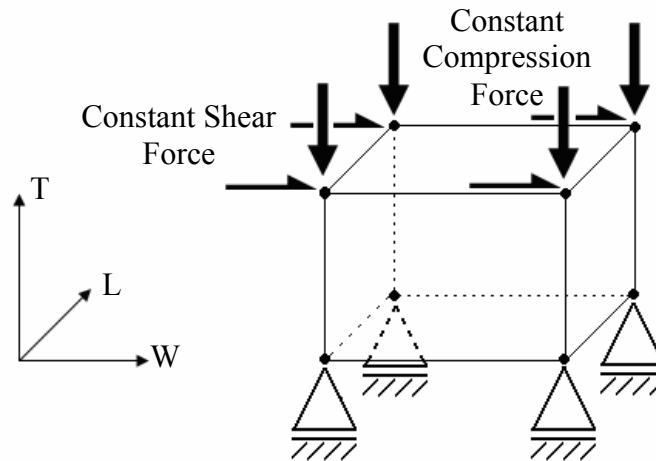
Figure 5-11: Boundary conditions for mixed shear-compression loading

At present, this improvement has the restriction that the loading angle must be manually introduced by the user. The introduction of an automated direction determination method would be possible with greater access to the FE code. This modification will not be used in the further numerical investigations of this thesis; however, the in-plane deformation effects on 'T' directional properties are used in further numerical investigations as this system is entirely automated.
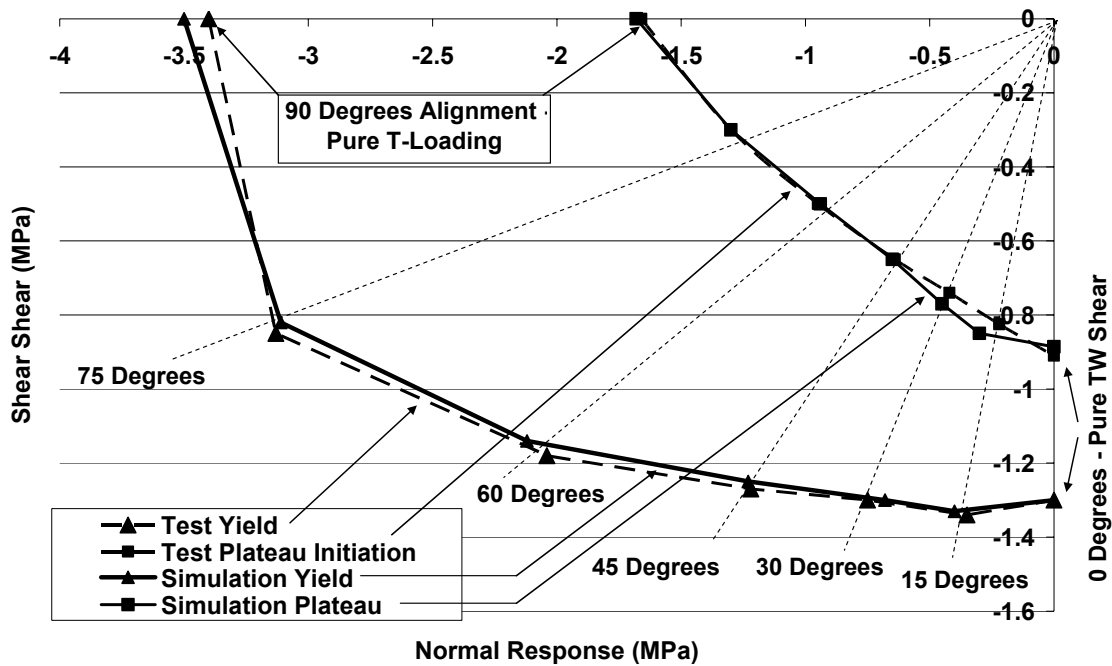
Figure 5-12: MAT41 improvements for direction dependent loading properties compared with experimental findings

5.1.2 Meso-Scale Modelling Investigation

The properties of honeycomb have been shown in this thesis and other published research to vary greatly depending on loading conditions. An experimental test procedure to investigate non-proportional multi-axial loading effects on the principal properties of honeycomb is difficult, in some cases impossible, with current testing technology. A potential solution to this is the use of an accurate numerical representation of the core where complex loading conditions can be applied in a controlled manner, similar to that of Papka and Kyriakides [77] [78]. Using the results from the pre-deformed and multi-axial loaded honeycomb a method of numerically modelling the honeycomb has been proposed. The properties of the aluminium material used to construct the cell walls were gathered from MATWEB [103]. The shape of the honeycomb cell is assumed to be consistent and regular with the size of the walls measuring 1.83mm in both the 'h' and 'l' directions thus producing a honeycomb cell internal diameter of 3.14mm.

The accuracy of the cell deformation is directly related to the number of elements used to make up a single cell wall. This is calculated using equation 2-10 [33] as 0.75mm for this material and geometry. Thus, for a 10mm sample in 'T' direction the shell size must not exceed 0.75mm. An investigation into the number of elements used to represent the cells has shown that 4 elements in the cell wall length 'h' and 40 elements in the 'T' direction, as shown in Figure 5-13(A), produces an adequate level of accuracy without being computationally expensive, such as a 50 'h' x 200 'T' elements cells shown in Figure 5-13(B) also studied during this research.
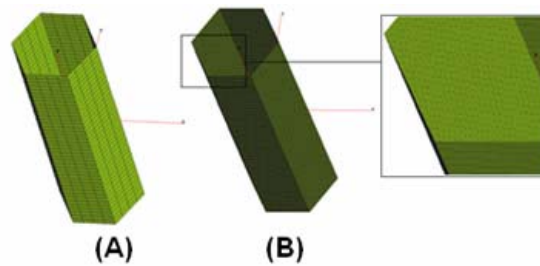
Figure 5-13: Individual cell mesh examination, (A) 4 x 40 elements, (B) 50 x 200 elements

When the cells are compressed, as shown in Figure 5-14, the fold thicknesses are compared with those from the 'T' direction compression tests. It has been found that the numerical model does reproduce the fold wavelength accurately. This reproduction in wavelength fold size and general deformation shows that the model can reproduce the physical deformations observed during compressive testing in the 'T' direction.
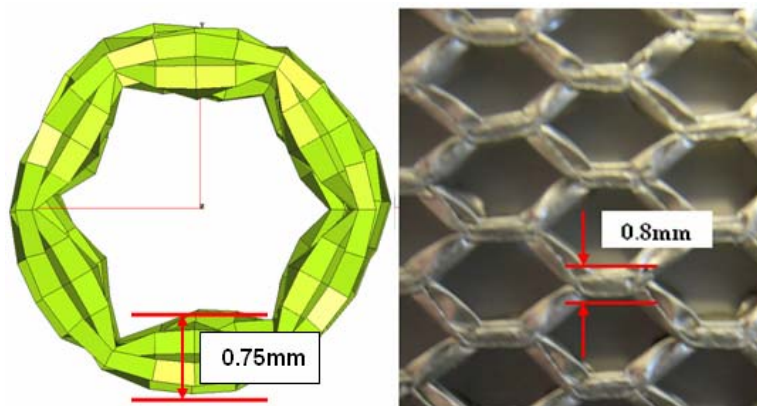
Figure 5-14: Comparison of fold thicknesses between numerical and experiment

This mesh density was then applied to a larger honeycomb mesh, shown in Figure 5-15, to numerically investigate the deformation of the cell walls and predict energy absorption of the honeycomb samples. The honeycomb mesh is 44mm x 25mm in the 'L' and 'W' directions respectively and contains 81,920 Mindlin shell elements. Furthermore, investigations of the effect of cell wall thickness at the interface between cells were also investigated. The three different modelling approaches to join cells were:

A. Single shell assumption, monolithic core, as shown in Figure 5-15(A), where the thicknesses of cell walls are constant throughout. This method does not account for bonding between cells or the double thickness of the cell wall but does produce the simplest model in terms of contacts, number of elements and materials definitions.

B. Double thickness at interface regions as shown in Figure 5-15(B). This assumes the interface regions as a secondary material with identical properties; however, the shell thickness for this material is double. This approach also ignores the effect of bonding at the interface.

C. Bonding at interfaces as shown in Figure 5-15(C). The whole model uses a single material and has a 0.1mm gap at the interface between cells. In this gap, a tied interface is applied.
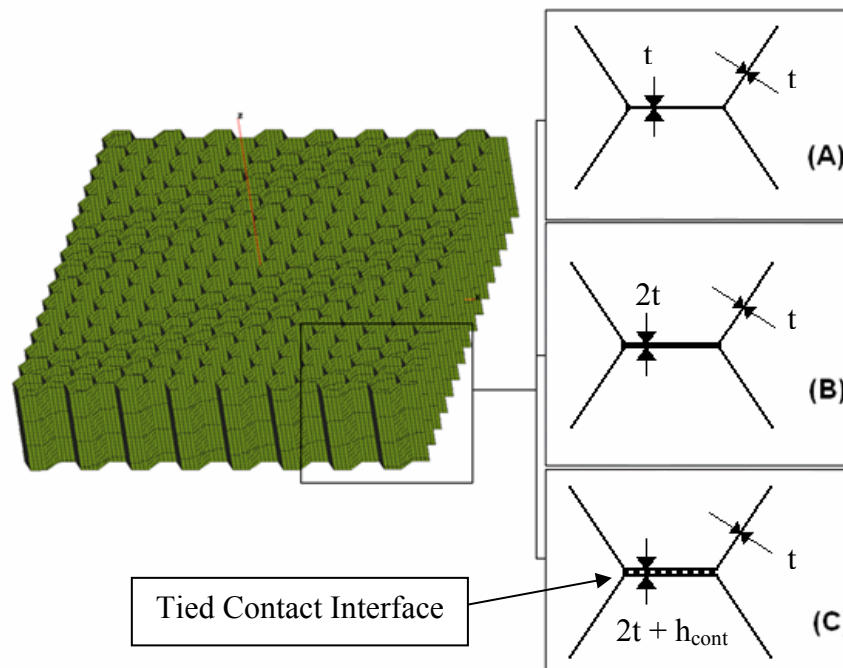
Figure 5-15: The three honeycomb model variants based on (A) single shell, (B) double material and (C) tie interface model

Since the strength of the bond at the interface cannot be determined as failure was not observed during experimental testing, an accurate failure criterion has not been assigned in this work. The comparison between each of these studies is shown with the experimental result and presented in Figure 5-16. From these results it may be concluded that:

A. The monolithic method produces the closest approximation with experimental results. The model neglects many flaws and characteristics of a true honeycomb sample, for instance damage to the base material during manufacture and inconsistencies in the cellular geometry introduced during storage and working with the material. The method is ideal due to the reduced requirements for the purposes of this research.

B. The double material method also produced an adequate result and only slightly over predicted the crushing strength of the honeycomb. This is an unusual result as the model is geometrically more accurate than the single material model. It is possible that the introduction of manufacturing flaws and inconsistencies between cell geometries will reduce the predicted crushing strength of the honeycomb material.

C. Tied interface modelling did not produce an adequate result. The peak and crushing strengths were over predicted by more than double the actual strength of the material. The distance between the two surfaces is likely to be the cause of this inaccuracy. A further study can be conducted to address this; however, the accuracy of the monolithic approach with the reduced modelling requirements is suitable for continued investigation.
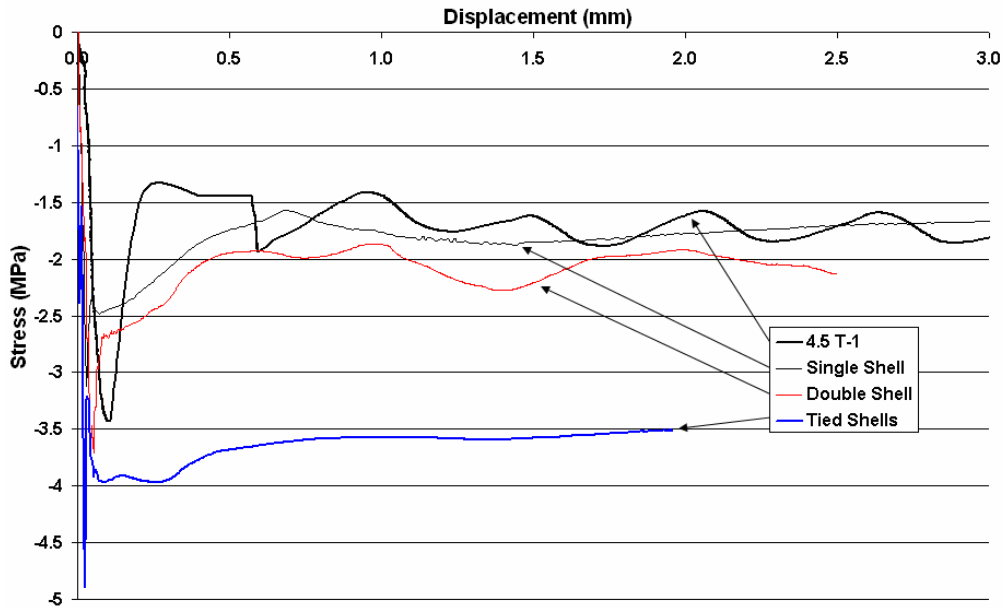
Figure 5-16: Comparison of meso-shell approaches with experimental result

Mixed Shear-Compression Investigation using Shell Modelling Method

In order to numerically represent the mixed shear-compression experimental testing of the Arcan apparatus, the meso-shell core is arranged between two rigid body shells and set at an angle to introduce a mixed shear-compression condition. The mesh and model are shown in Figure 5-17. The honeycomb shell mesh contains 61920 Mindlin shell elements and measures 45.7mm x 25.9mm in the 'W' and 'L' directions respectively. The upper rigid shell surface and bar element are assigned a constant velocity in the Y direction. The bar element, produced using material type MAT203, contains a further boundary condition that prevents the tip node to move in any other direction. The lower rigid shell surface is fixed to prevent any movement of the base.

The horizontal stiffness of the Arcan apparatus is duplicated by assigning a spring stiffness relationship, defined in equation 4-4 from experimental calibration tests, to the bar element attached to the upper rigid body, as shown in Figure 5-18.
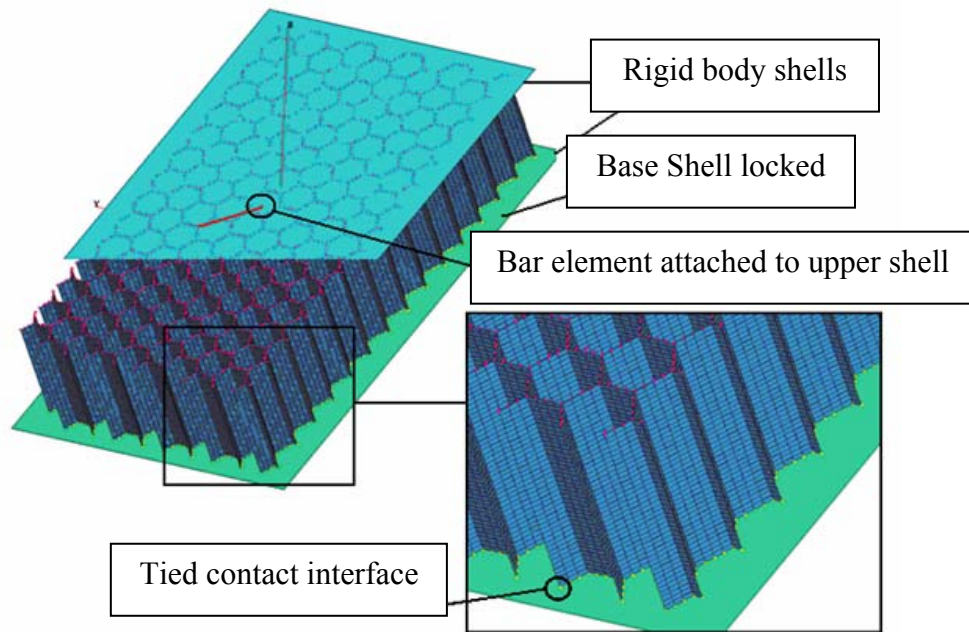
Figure 5-17: Numerical modelling mixed shear-compression of meso-shell model
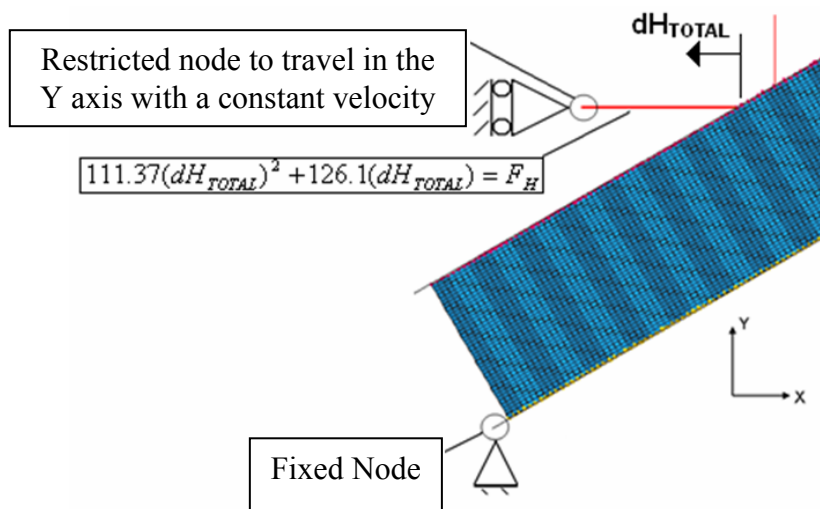
Figure 5-18: Boundary conditions and Arcan apparatus compliance

The results for the yield stress and plateau initiation stress using this modelling method are presented in Figure 5-19 together with the experimental findings. The average plateau stress is also presented with the experimental findings in Figure 5-20.

172
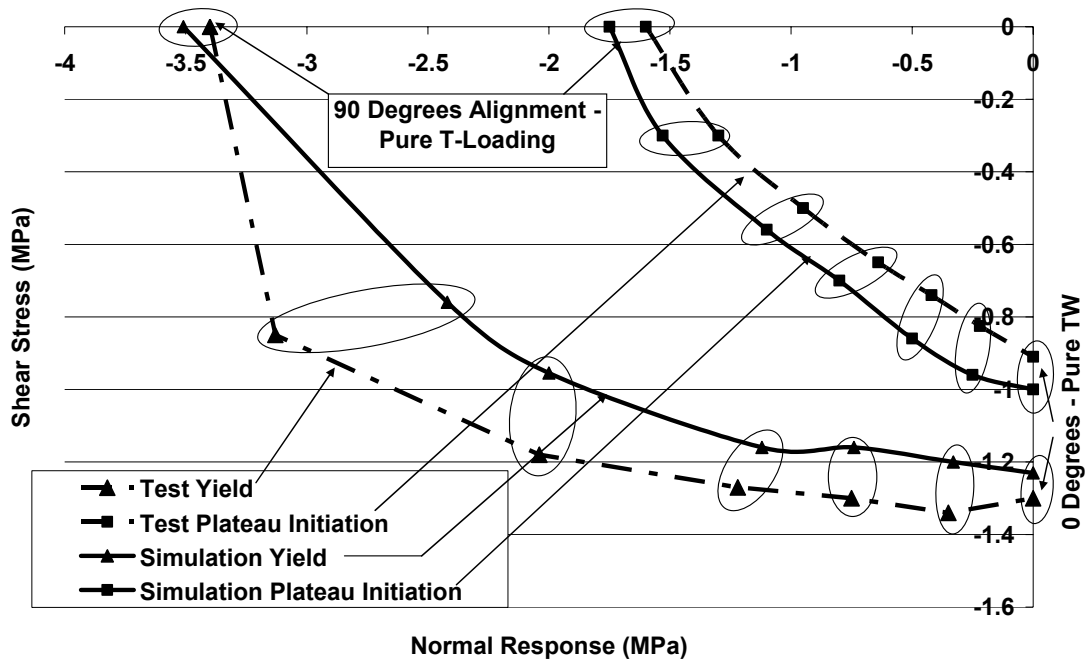
Figure 5-19: Meso-shell combined shear-compression modelling compared with experimental results

The shell based modelling method does produce similar variations in yield strength and plateau initiation stress to the experimental findings. In general, the yield strength is under-predicted by the meso-model; however, the plateau initiation strength is reproduced with a reasonable level of accuracy. The change in average plateau strength due to directional loading is similar to that observed during experimental testing and presented in Figure 5-20.
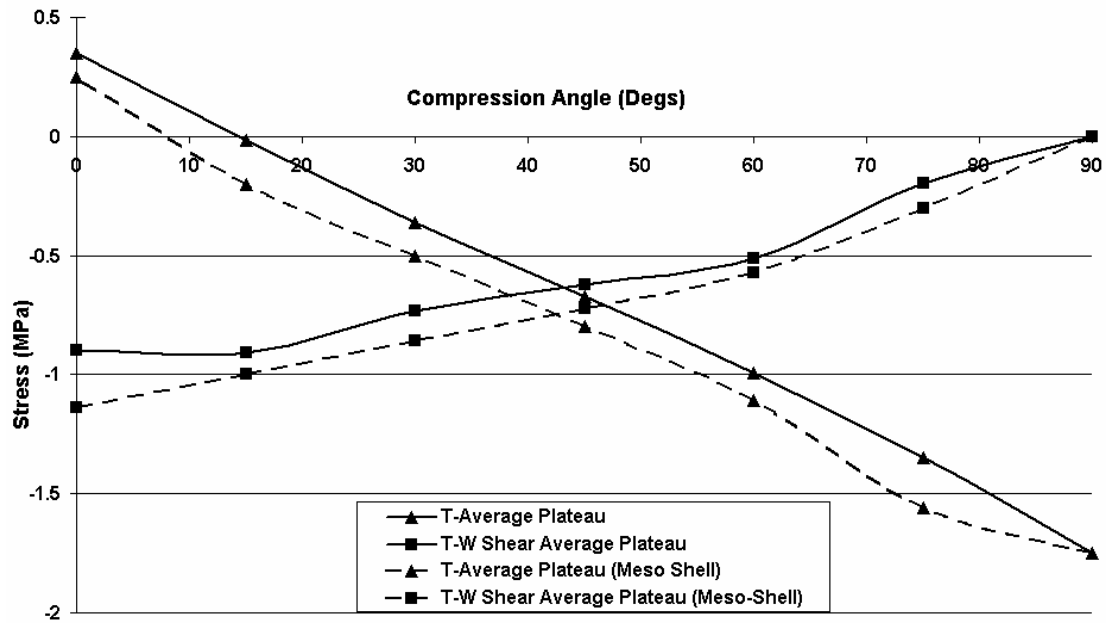
Figure 5-20: Average plateau stress variation due to load direction of the meso-shell model compared with experimental results

Pre-deformation Effects on 'T' Direction Compressive Properties

The effects of pre-crushing in the in-plane direction on 'T' direction properties have also been examined with the meso-mechanical shell model. The core representation consists of 163,840 Mindlin shell elements and measures 51mm x 44mm in size. The shell model is arranged between a series of rigid walls which impose the controlled in-plane compression in one direction, whilst the transverse directions are constrained as shown in Figure 5-21. After pre-crushing in the in-plane direction, the in-plane compressions and restriction walls are removed before another set of rigid walls compress the sample in the 'T' direction. The three compression cases investigated are:

- Case 1 – Pre-crushing in the 'W' direction with restrictions in the 'L' direction.
- Case 2 – Pre-crushing in the 'L' direction with restrictions in the 'W' direction.
- Case 3 – Pre-crushing in the 'L' direction with no restrictions in the 'W' direction.
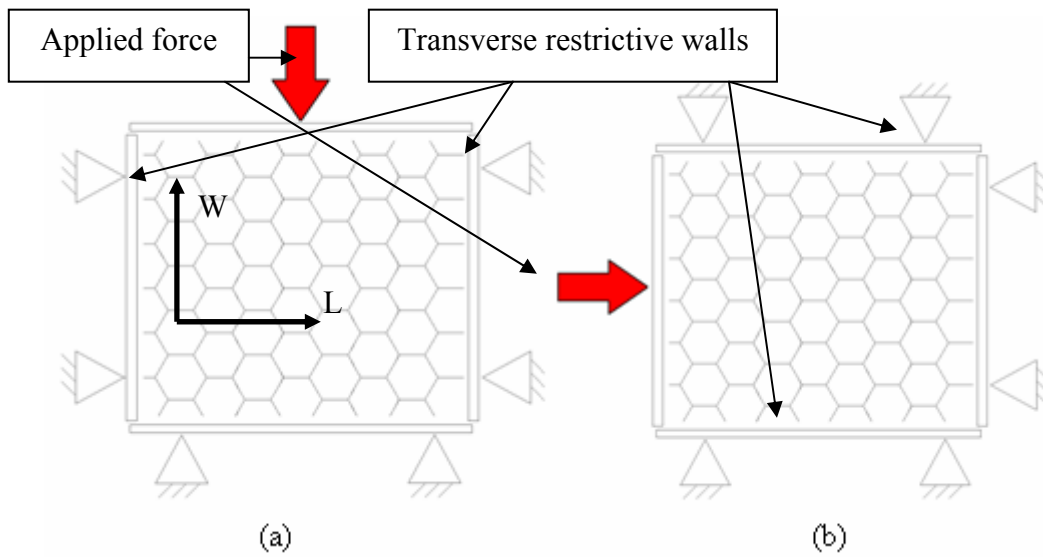
Figure 5-21: Meso-shell pre-deformation boundary conditions, (a) Case 1 boundary conditions, (b) Case 2 boundary conditions

Case 1: 'W' Direction Pre-Deformation with Restrictions in 'L' Direction

The model is compressed in the 'W' direction with restrictions in the 'L' direction. This loading is found to cause inconsistent deformation of the cells throughout the sample, as shown in the inset images in Figure 5-22. This irregular deformation is similar to that observed during the preparation of the experimental samples.
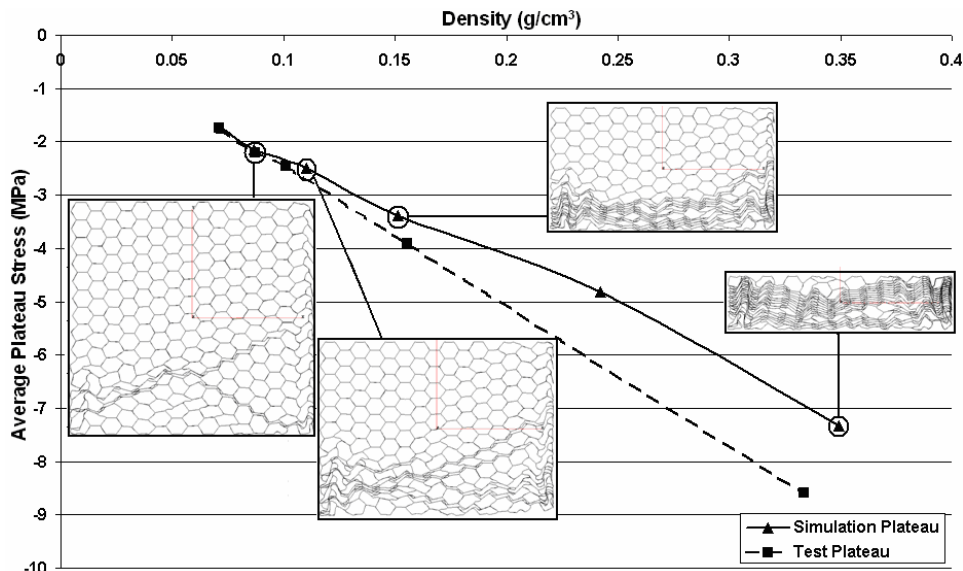
Figure 5-22: Case 1 average plateau stress variation with sample density

This model preparation displays a similar trend between the change in density and the average plateau stress as shown in Figure 5-22. The 'W' direction pre-crush with 'L' direction restrictions under-predict by as much as 10% as the density increases. However, this occurs at larger pre-deformations.

Case 2: 'L' Direction Pre-Deformation with Restrictions in 'W' Direction

The sample is compressed in the 'L' direction with the 'W' directions restricted. The cells deform in an inconsistent profile, as shown inset in Figure 5-23; however in this case the deformation is more evenly spread throughout the sample. The cell deformations observed are similar to the experimental samples. The 'L' direction pre-crush with 'W' direction restrictions produces an accurate representation of the change in plateau strength due to the increase in sample density as shown in Figure 5-23.
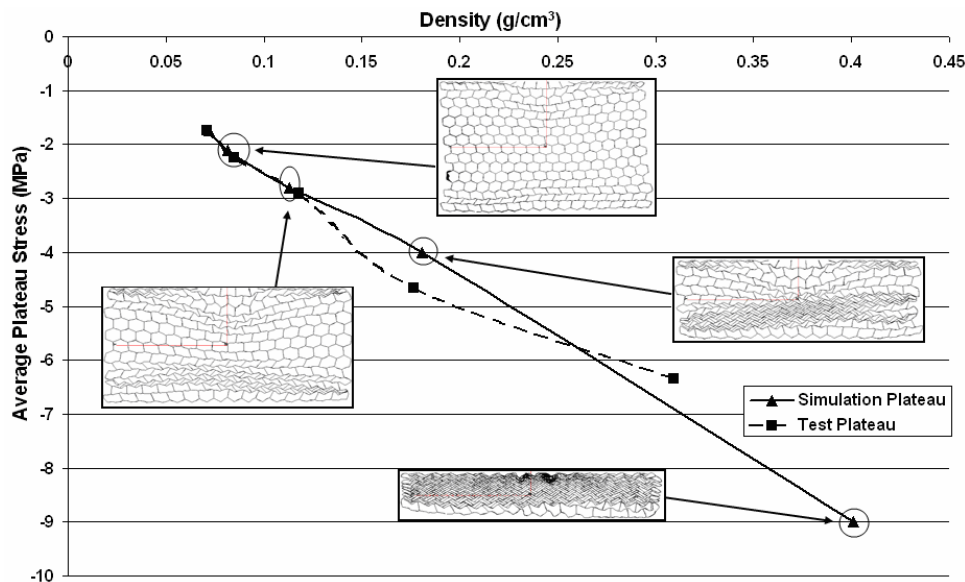
Figure 5-23: Case 2 average plateau stress variation with sample density

Case 3: 'W' Direction Pre-Deformation with No Restrictions in 'L' Direction

The cells are crushed in the 'W' direction without any restriction in the 'L' direction. In this case, the size of the sample in the 'L' direction is increased during deformation. The variation in average strength of the meso-shell model with density is compared with the experimental result and shown in Figure 5-24. The meso-shell model is shown to under-predict the plateau strength of the honeycomb sample as the degree of pre-deformation increases. As the hexagonal cells are not consistent throughout the sample, it is likely

that this variation in cell profile is responsible for the poor correlation at larger pre-deformations.
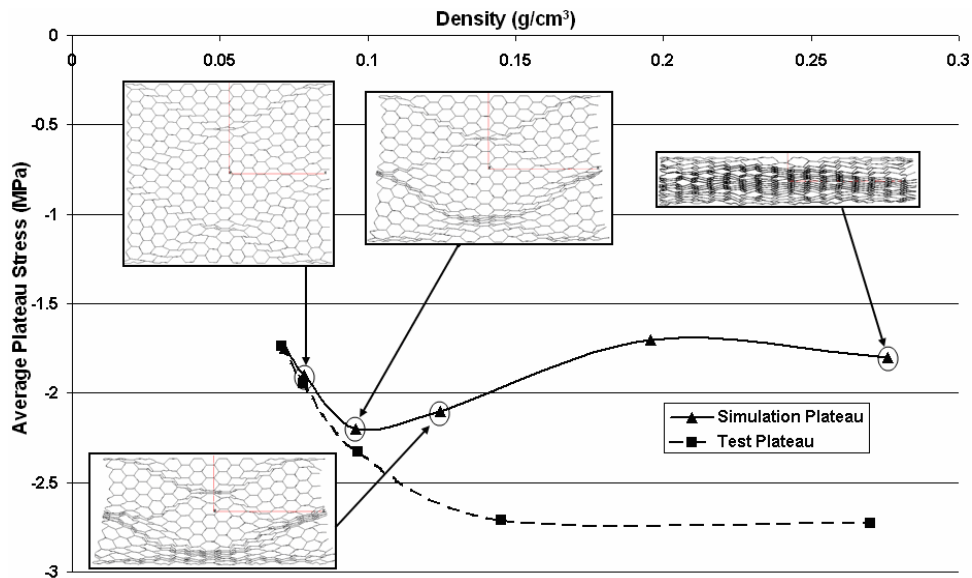
Figure 5-24: Case 3 average plateau stress variation with sample density

5.2   Laminate Modelling

Section 2.3.3 has reviewed some of the methods proposed to treat composite materials using FE analysis. These methods focus on either specific failure criteria or introduce progressive damage models to represent failure mechanisms, such as inter-laminar debonding, matrix cracking and fibre breakage. These methods also vary in the accuracy of the modelling, such as modelling the fibre and matrix specifically or building failure criterion into a meso- or macro-element approximation. Reduction in modelling complexity is required for large complex geometry structures; therefore, the use of shell elements to represent the composite skin is the focus of this research thesis.

Section 3.2 introduced the Ladevéze damage model used in PAM-CRASH^{TM} to numerically model the BAR Honda nosecone composite skin material. A comparison with experimental results presented in Section 4.3.4 and material property tables are made. This investigation extends to include the introduction of an improved damage progression law for the shell model, similar to that produced by Fouinneteau [51] for braided materials. The shell element model for this investigation is shown in Figure 5-25.
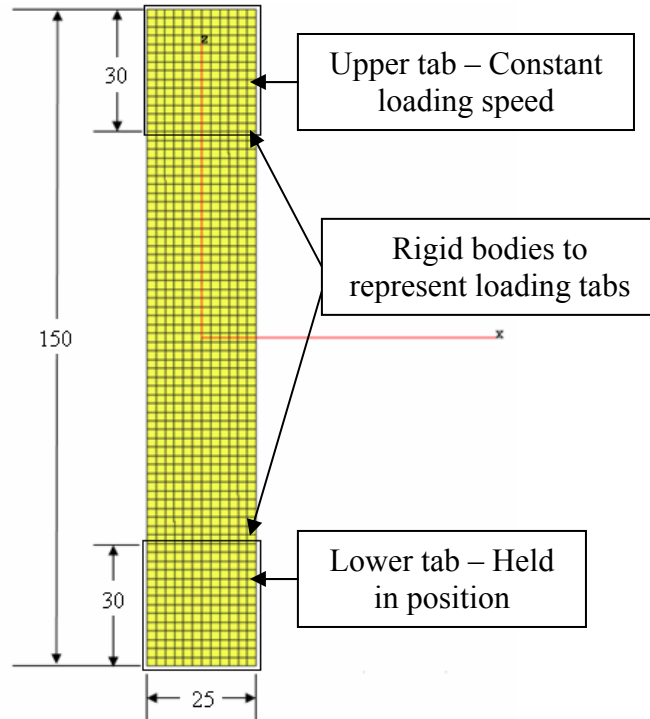
Figure 5-25: Shell model for composite tensile and shear property representation

The dimensions of the model are those of the experimental samples and it consists of 900 shell elements. The upper and lower grips are represented by rigid body elements. The lower grip is held in position whilst the upper grip has an imposed constant velocity in the Z direction.

Tensile Loading

From the experimental findings presented in Section 4.4.1 and manufacturer's datasheets [8], the tensile and compressive properties are introduced into the model. As stated in Section 3.2, eight UD plies are required to represent a four ply woven specimen. The CADEC program [108] was used to determine the equivalent UD ply elastic modulus in the fibre and transverse fibre directions. The elastic modulus in the fibre direction (E_1^{0t}) is 135GPa. The elastic modulus in the transverse fibre directions (E_2^{0t}) is 6.8GPa to produce a UD equivalent of the woven ply. The comparison between experimental and numerical results for tensile properties is shown in Figure 5-26. The compression properties are calibrated directly with the manufacturer's datasheets.
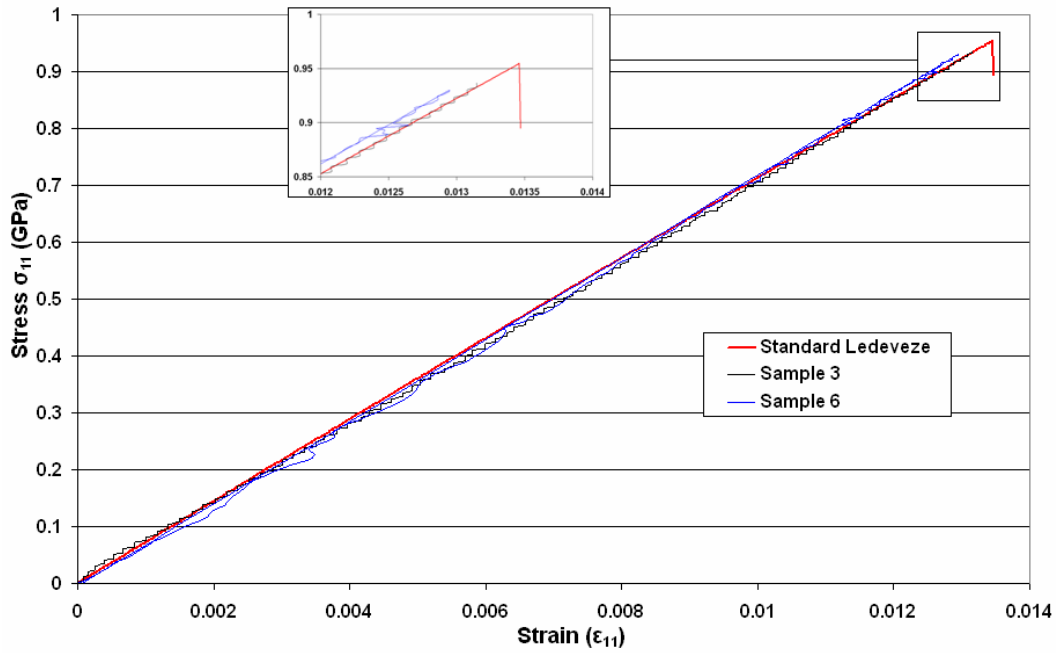
Figure 5-26: Comparison of standard Ladevéze method with experimental results

In-Plane Shear Loading

Using the same model setup shown in Figure 5-25, the tensile shear modelling is conducted by changing the ply orientations to $\pm 45^0$ with respect to the load direction. The standard damage progression input parameters, derived in Section 4.4.2, were applied to the ply properties and produced the shear stress-strain graph shown in Figure 5-27. This result shows that the standard PAM-CRASH^{TM} linear damage progression to determine the onset of damage for an in-plane shear loaded sample is not adequate for this woven fabric composite.
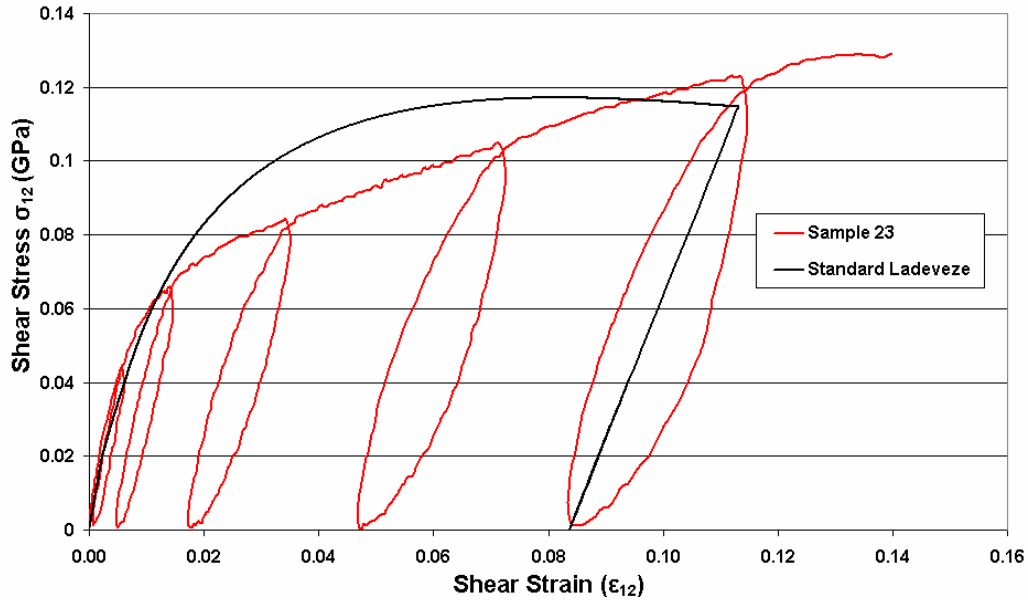
Figure 5-27: In-plane shear comparison between standard Ladevéze model and experimental results

A new non-linear damage progression law is applied to improve the in-plane shear representation. Based on the results gathered in Section 4.3.4, a quadratic damage progression law has been developed, equation 4-18, and implemented in the PLY1 material code. Results of this modified code are presented in Figure 5-28 and show a significant improvement in the representation of in-plane shear properties.
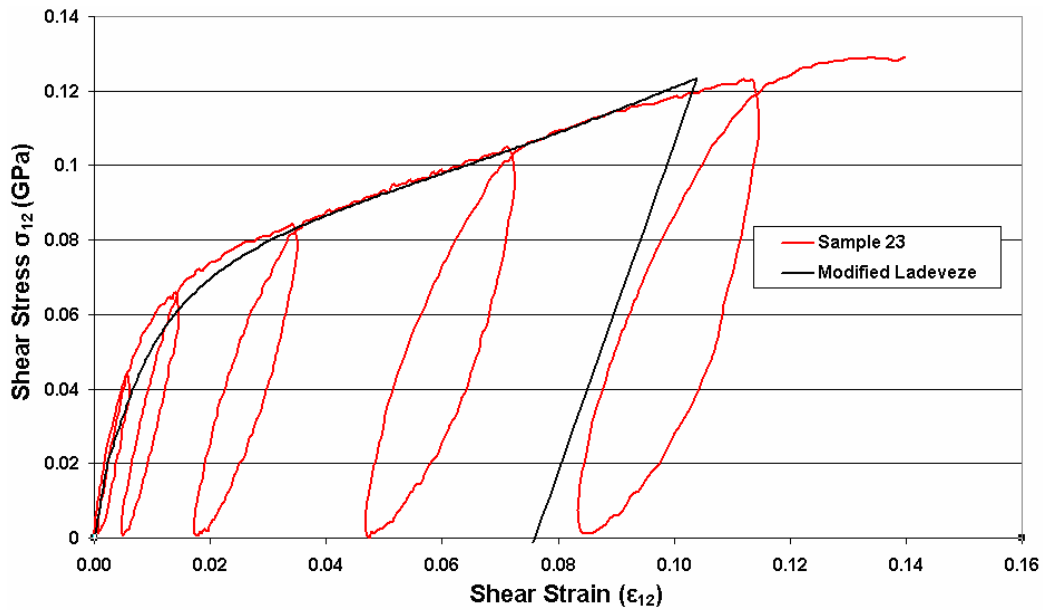
Figure 5-28: In-plane shear comparison between improved Ladevéze damage progression model and experimental results

5.3   Sandwich Modelling

A definitive method of representing composite-sandwich materials using the material models available in PAM-CRASH^{TM} has yet to be produced. This Section addresses the modelling of sandwich structures using meso-shell representations for the skin, using MAT131 with PLY1, and macro-solid representations for the core, using MAT41, and compares a selection of modelling methods with experimental research presented in Section 4.5 on the sandwich structure. This Section also includes the use of meso-shell based modelling methods for the core to represent the core, presented previously in Section 5.1.2, when applied to sandwich applications.

5.3.1 'T' Direction Sandwich Loading

The experimental compression test in the 'T' direction of the sandwich, presented in Section 4.4.1, showed that compressive strength properties of the core are increased when constructed in a sandwich structure. The addition of a glue-fillet introduces a restriction to the cell walls preventing rotation at the material surface and adding strength to the 'T' directional compressive properties, as summarised in Figure 4-62.

Calibrating the solid element properties with those determined from experimental testing of the core and honeycomb material datasheets will be insufficient when representing sandwich structures. The properties of the solid element must be calibrated with sandwich 'T' direction compressive test results presented in Section 4.4.1. This produces the comparison shown in Figure 5-29; the modified peak load effect introduced to the solid element in Section 5.1.1 is also calibrated and presented. This calibration is used for the 'T' directional properties for the core due to the greater accuracy and is used for further numerical modelling of the sandwich.
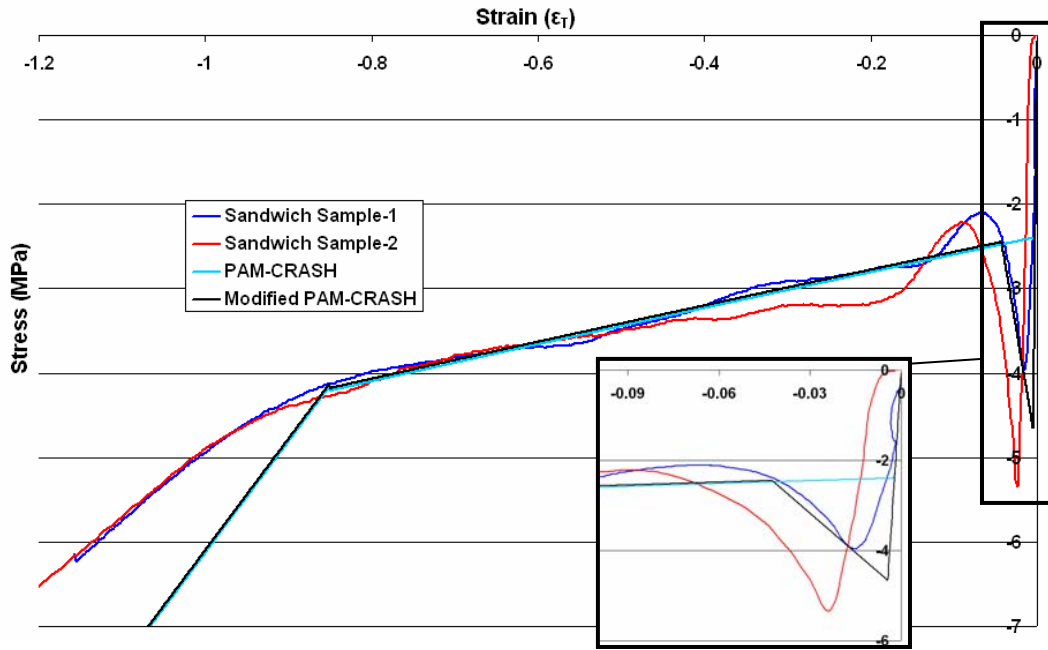
Figure 5-29: Calibrated MAT41 and modified MAT41 for sandwich applications

5.3.2 Crack Propagation Modelling

A crack at the interface between the composite and core in the sandwich construction used for the 006 nosecone does not fail at the adhesive bond line but undergoes a balanced tearing along the centreline of the honeycomb core identified during experimental testing presented in Section 4.5.2. The direct approach to representing this potential tearing in the numerical model is with a pair of solid element honeycomb cores with a tied interface, MAT303, between them. The model is shown in Figure 5-30.

The aluminium loading blocks are represented using material model 1 (MAT1), which is a solid element model used to describe isotropic materials. The loading tabs are represented using rigid bodies to reduce model complexity. In both rigid bodies, the centre-of-gravity nodes are specified at the centre of the pin holes. The lower loading tab is locked so that it cannot move in 5 degrees of freedom with rotational freedom about the Y axis. The upper loading tab is constrained with 4 degrees of freedom with a constant velocity in the Y direction and is allowed to rotate about the Y axis. The model includes the Ladevéze damage shells between the core and the aluminium grips. In

order to reduce the model complexity the adhesive glue-line between the materials is not modelled and the two parts share common nodes. The properties of the tied interface are stated in Table 5-1. Test and numerical results are compared in Figure 5-31.

Property	Input
G_{IC}	1500 J/m^2
Initiation Stress (σ_{IN})	25MPa
Propagation Stress (σ_{PROP})	10MPa
Elastic Modulus (E_1)	70GPa
Contact Interface Distance (h_{CONT})	0.5mm

Table 5-1: Input requirements for contact tied interface
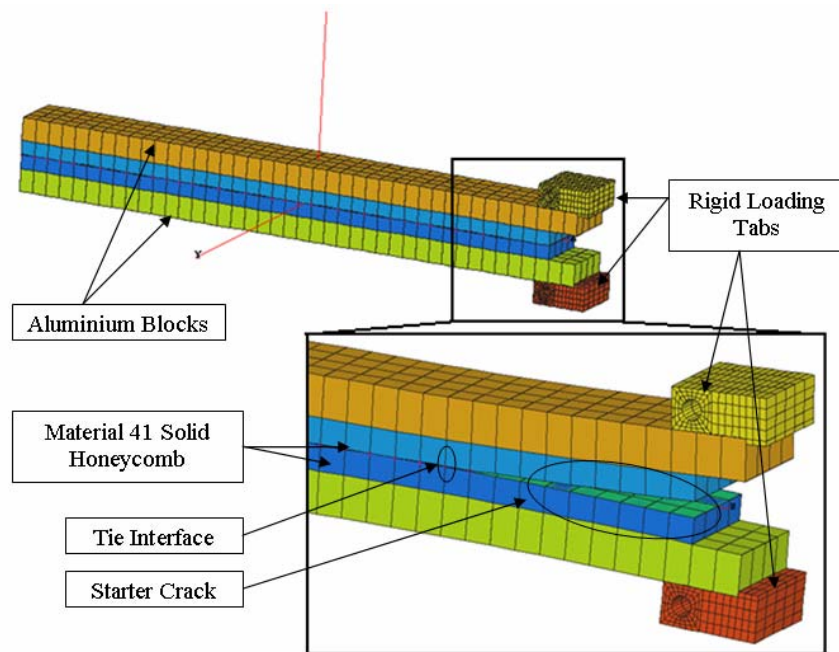
Figure 5-30: Description of CSB computational model
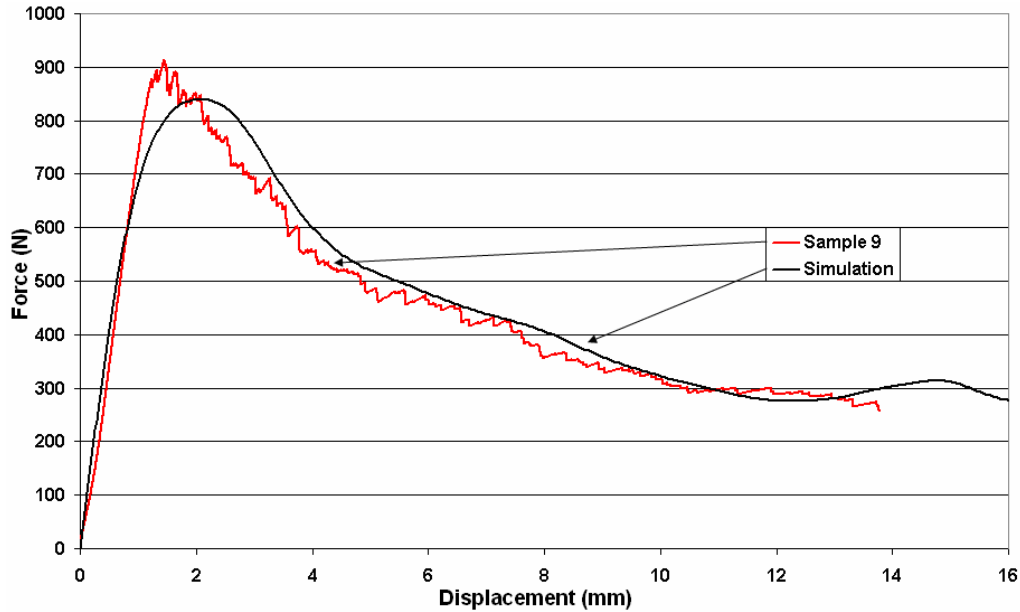
Figure 5-31: Comparison of quasi-static CSB test with computational model

The force-displacement curve produced by the computational model closely follows the recorded experimental result. The properties are based on tearing through the aluminium core material and not the adhesive glue-line. The adhesive glue-line has been shown in Sections 4.5.2 and 4.5.4 to resist failure when subjected to a variety of loading conditions and debonding shown to occur in the core. These properties are applied to all models using the tied interface at the central core and skin-core interface to represent tearing in the core.

5.3.3 Three-Point Bending Modelling

The 3PB tests, presented in Section 4.5.3, are used to establish the flexural properties of the composite-sandwich structure. Using the experimental layout, also presented in Section 4.5.3, the standard model arrangement is produced as shown in Figure 5-32. The impactor and pivots are modelled as rigid bodies to reduce complexity of the model. The pivots are locked in position and the impactor is restricted to move in the Z direction at a constant velocity.

184
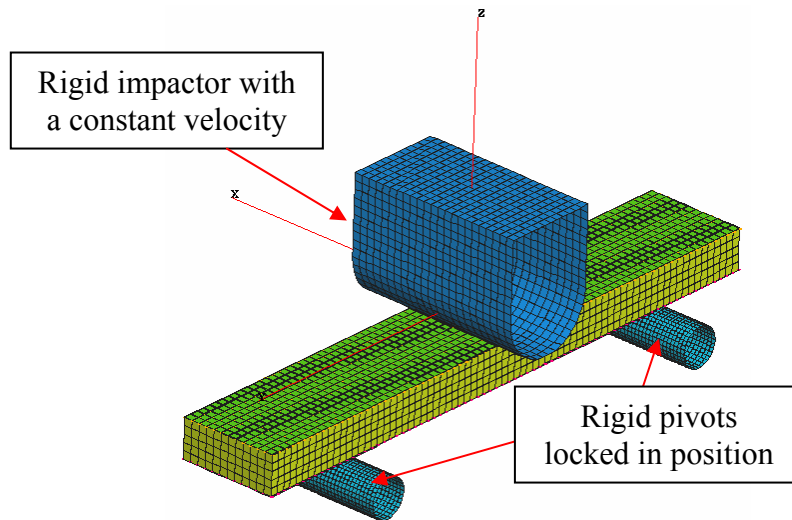
Figure 5-32: 3PB test using honeycomb solid arrangement

Macro-Solid Modelling of the Core

The core material of the 3PB sample is represented using the MAT41 model with properties in the 'T' direction presented in Section 5.3.1. Two methods of attaching the skin shells to the honeycomb core have been investigated. The first method, referred to here as the Type 1 method, is the simplest method in which the skins are directly attached to the core, using common nodes and neglecting debonding between core and skin. The second, Type 2, method uses a tied interface, MAT303, to attach the skin shell to the core using the properties developed from the CSB modelling, Section 5.3.2. The experimental research using the wedge samples, presented in Section 4.5.4, showed the honeycomb core tore as opposed to bond-line failure between core and skin, and thus this approach is acceptable.

The improvements to the constitutive codes presented earlier for the composite laminates and the honeycomb core are examined and compared with the standard numerical modelling codes available in PAM-CRASH^{TM}. The force-displacement curves from the numerical modelling examinations are shown in Figure 5-33 and Figure 5-34 for 4-ply samples and Figure 5-35 and Figure 5-36 for 5 ply samples. In each series, the numerical models are shown to initially produce similar curves to those shown in the experimental testing; however, as deformation continues the accuracy of the force-displacement curve reduces. These models do not accurately represent the flexural properties of the test specimens as further deformation occurs. The peak

strength is similar in the 4 ply thick models, although the deformation at this point is greater than that seen in test specimens. In the 5 ply samples, the numerical models over-predict the peak load by approximately 5%. The modifications applied to the core and skin shell material codes do not produce any improvement to the force-displacement curves for the 3PB models. The difference between the numerical models and test curves are largely due to the mixed shear-compression deficiencies in the honeycomb model. In addition, frictional forces acting at the pivots and loading point will require further investigation and improved modelling.
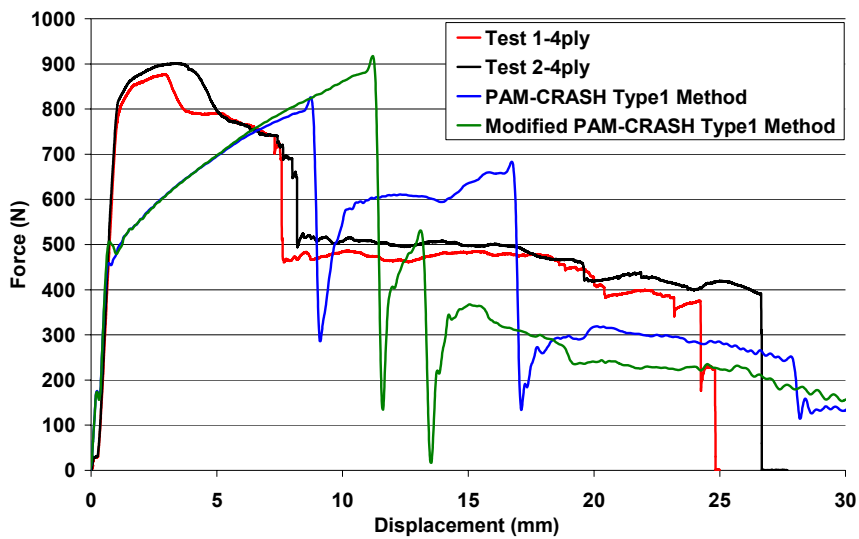
Figure 5-33: Type 1 model and experimental testing on 4-ply specimens
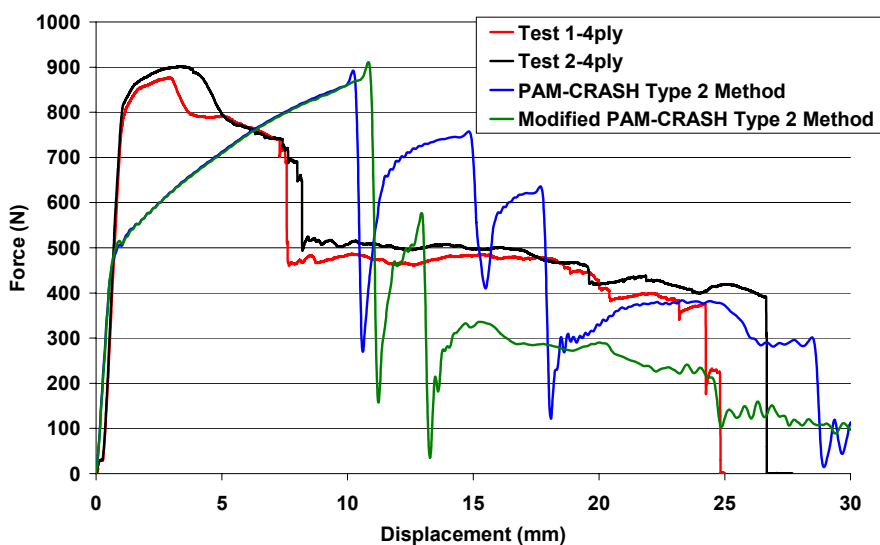
Figure 5-34: Type 2 model and experimental testing on 4-ply specimens
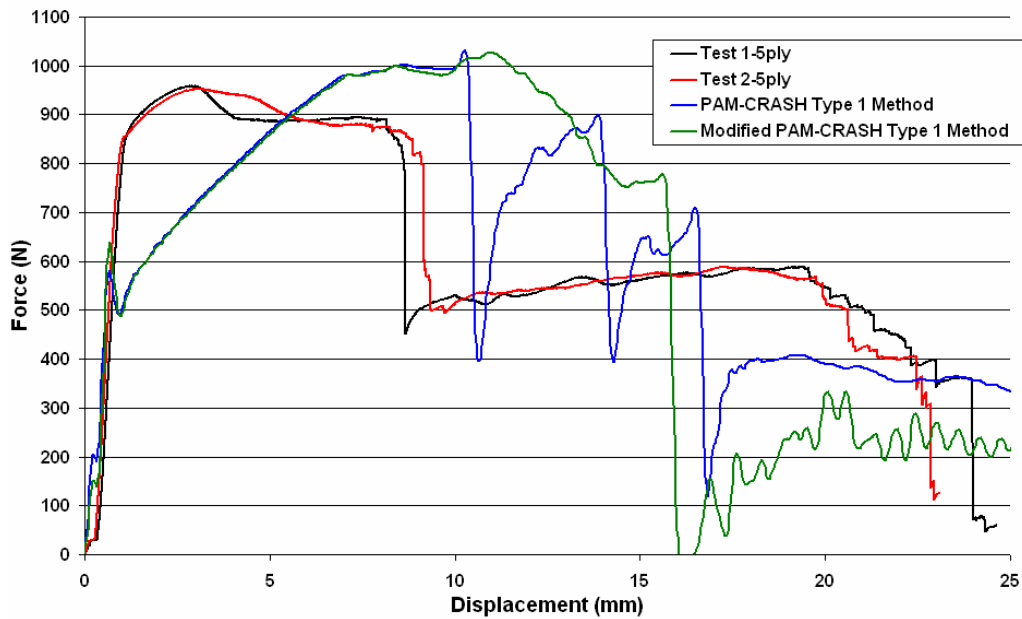
Figure 5-35: Type 1 model and experimental testing on 5-ply specimens
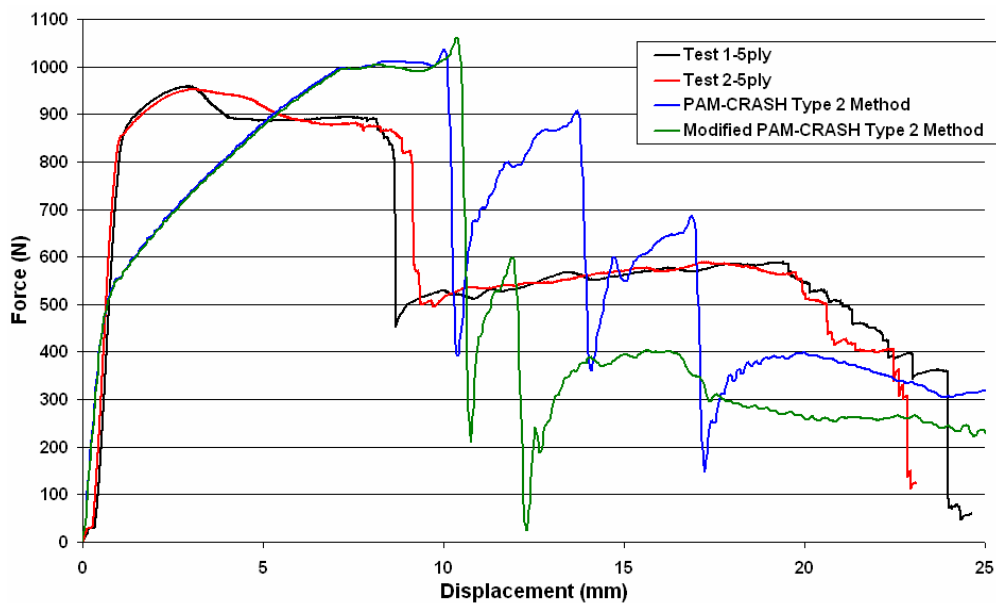
Figure 5-36: Type 2 model and experimental testing on 5-ply specimens

A comparison of energy absorption between simulation and test is shown in Figure 5-37 for 4-ply samples and Figure 5-38 for 5-ply samples. According to this method of comparison, the modified codes show an improvement in terms the amount of energy required to completely bend the sandwich material. For the 4-ply sandwich case, the

improved codes applied to the Type 1 model is shown to be the most accurate method, whilst the improved codes applied to the Type 2 model is more accurate for the 5-ply cases.
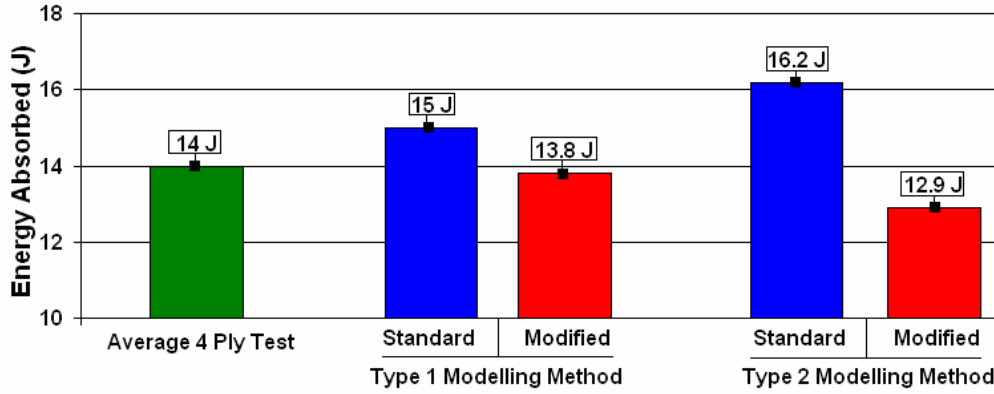
Figure 5-37: Energy absorption comparison between 4-ply test and models
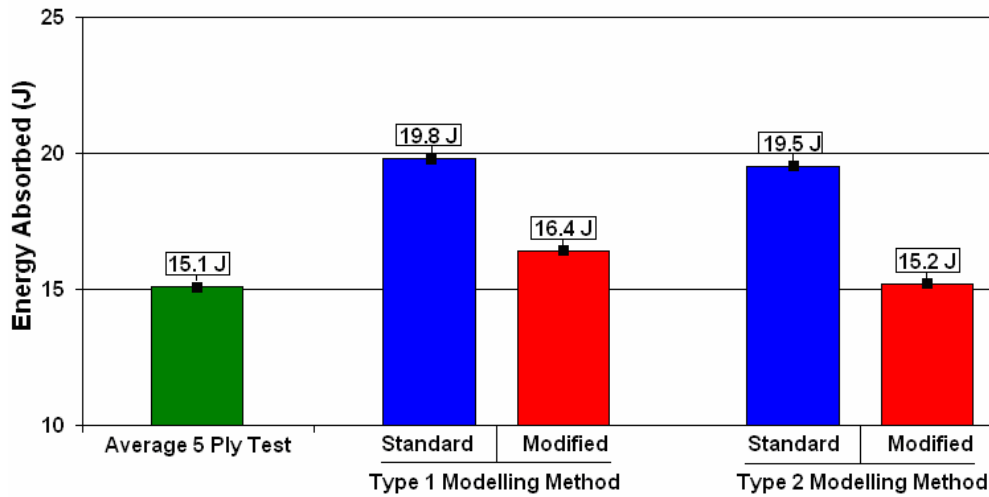
Figure 5-38: Energy absorption comparison between 5-ply test and models

The deformation of the sandwich is shown in Figure 5-39. The core displays a similar deformation process to that observed during the experimental testing. The core appears to undergo a pure compression process directly under the impactor, whilst a mixed shear-compression mechanism occurs in the surrounding area.
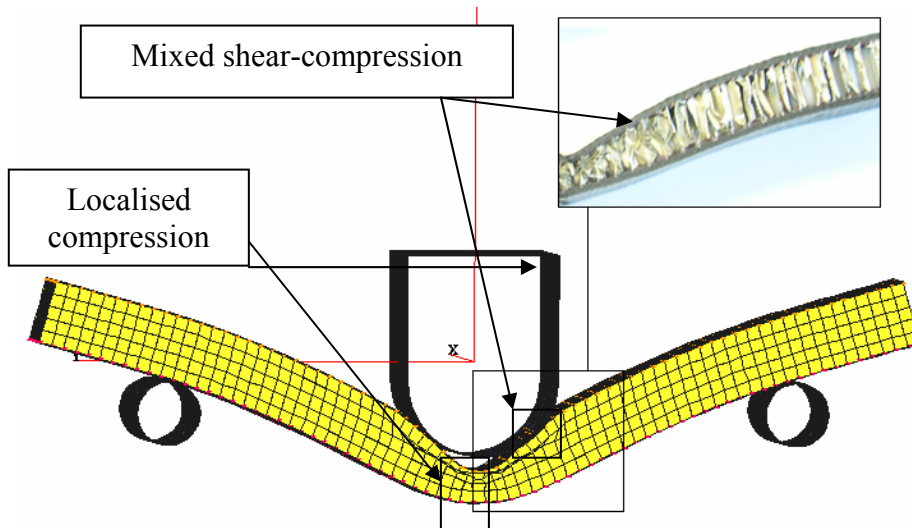
Figure 5-39: Deformation of the numerical sandwich model

The properties in the principal directions of the core when subjected to combined shear-compression loading have been shown in Section 4.3.3. It is likely that improvements to the solid element presented in Section 5.1.1 of this Chapter, to vary these properties depending on load direction, would improve the force-displacement representation of the structure; however, this cannot be confirmed without a method to determine loading directions.

Meso-Shell Modelling of the Core

A further study has been conducted using the meso-shell method to represent the core. The model arrangement is identical to that of the macro-solid core model and is shown in Figure 5-40. The core is attached to the skins using a Type 301 contact interface. From experimental testing, the glue-line was not observed to fail, thus a non-debonding tied interface is appropriate.
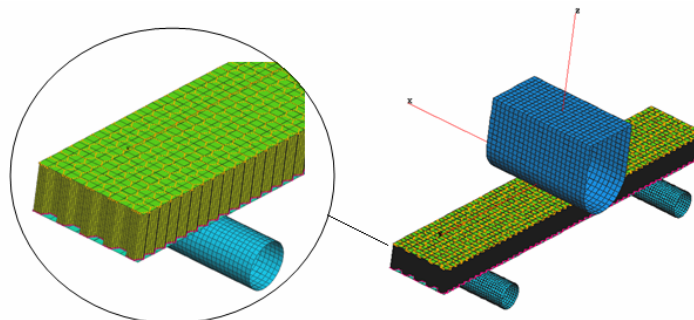
Figure 5-40: 3PB model using shell elements for the core

The force-displacement response curve is presented in Figure 5-41. The meso-shell modelling of the core is comparable with the experimental findings; more so than the macro-solid core approach. This is due to the model's ability to vary the properties in the principal directions due to the mixed shear-compression of the core during this loading process, as shown in Section 5.1.2. The deformation of the model is shown in Figure 5-42 where the mixed shear-compression deformation is visible.
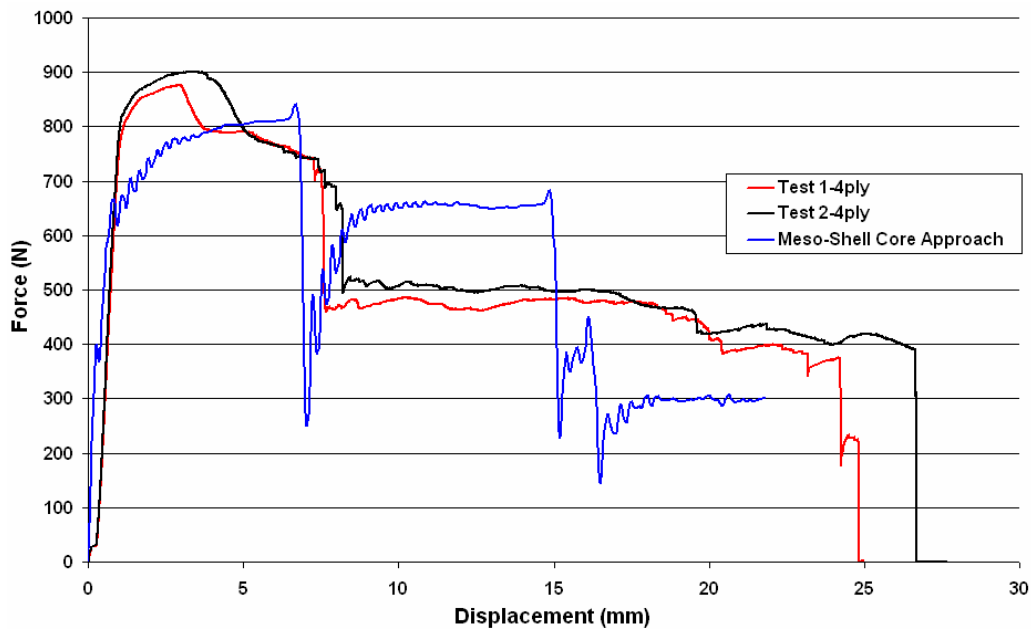
Figure 5-41: Comparison between meso-shell core approach and 4-ply test
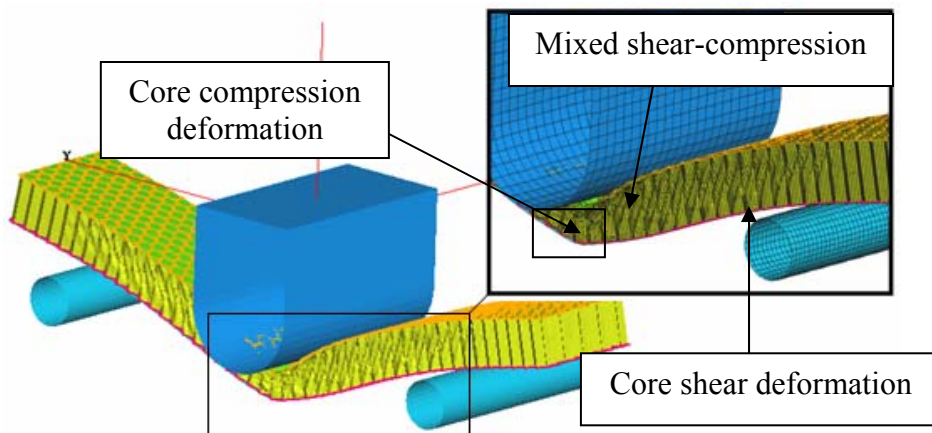
Figure 5-42: Deformation of the meso-shell core during 3PB testing

190

Despite the improved accuracy of the meso-shell core model compared to the solid-element core model, the force-displacement curve does not match very well to the experimental testing curve, suggesting that there are still some inadequacies with this model. It is possible that the failure criteria for the composite shells are inadequate. In the numerical models presented here the shells were set to completely fail when one or more of the plies fail. It is likely that, under bending conditions, this is not accurate as the plies in the skin will not fail simultaneously as observed in pure tensile loading cases. To further this investigation, a 3PB test can be conducted on the composite skins and used to calibrate the Ladevéze damage shell model and identify potential inaccuracies in the material code. In addition, the physical restrictions imposed by the glue-fillet have been neglected in the meso-shell model; it is possible that this restriction on the core folding and stiffening of the structure has a significant effect on the energy absorbing and deformation behaviour of the honeycomb core.

5.3.4 Impact Wedge Modelling

Wedge Modelling using a Solid Element Based Core

The wedge model is developed to determine the numerical modelling capability to represent the in-plane deformation and energy absorbency of the sandwich structure using PAM-CRASH^{TM}. The model boundary conditions and mesh are shown in Figure 5-43. In order to investigate the methods of attaching the skins to the core and debonding of the structure, three modelling methods using the solid element to represent the core have been investigated and are shown in Figure 5-44. The first two are identical to the joining methods Type 1 and 2 described in Section 5.3.3. The third variation makes use of the central core failure interface using a tied contact interface, the properties of which were given in Section 5.3.2.
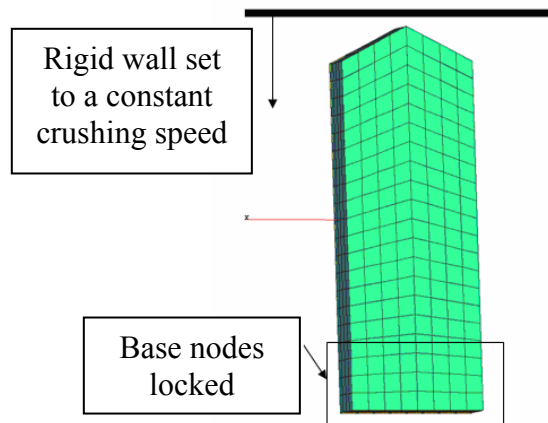
Figure 5-43: Wedge sample mesh with boundary conditions
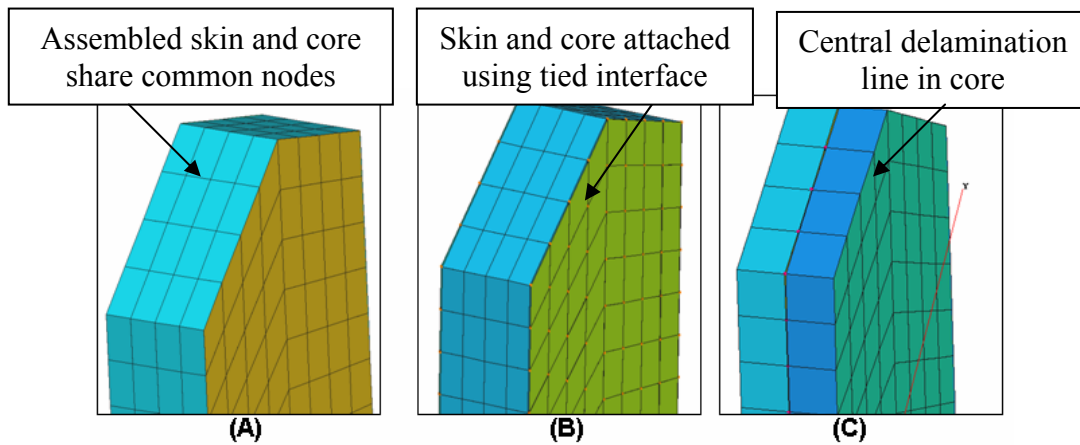
Figure 5-44: Modelling approaches (A) Type 1 (B) Type 2 (C) Type 3

Using these modelling methods the load displacement curves of the samples for axial conditions are shown in Figure 5-45 and Figure 5-46. As shown, the load displacement for each numerical method is comparable with the experimental tests. The fully assembled model, Type 1 model, is shown to over predict the peak load before producing a folding mechanism similar to that observed in testing. The Type 2 model produced the closest representation to the experimental results.
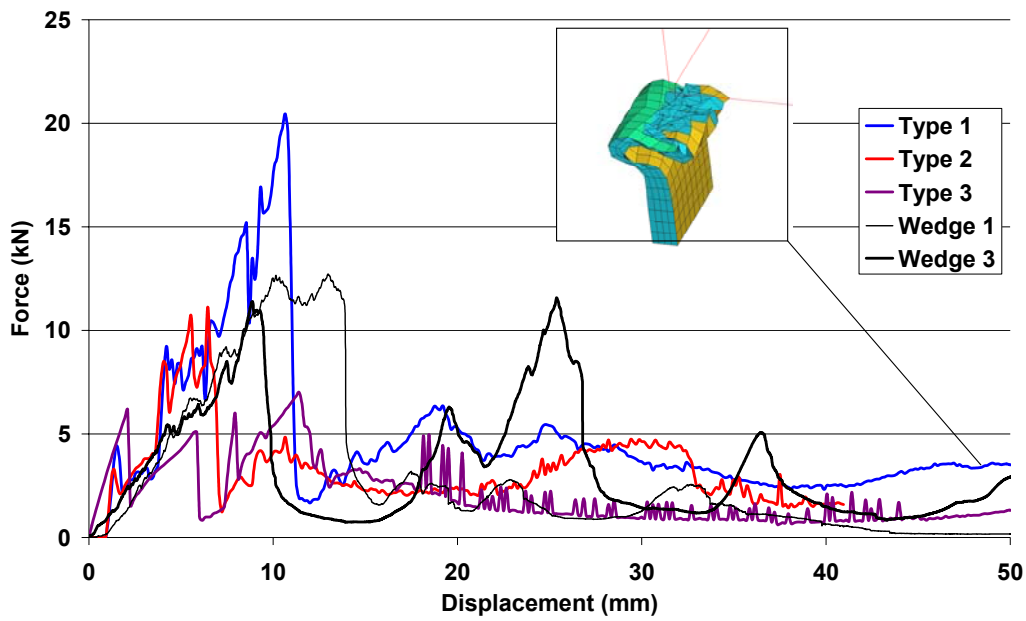
Figure 5-45: Comparison between standard PAM-CRASH^{TM} sandwich modelling and test results for 4-ply axial specimens
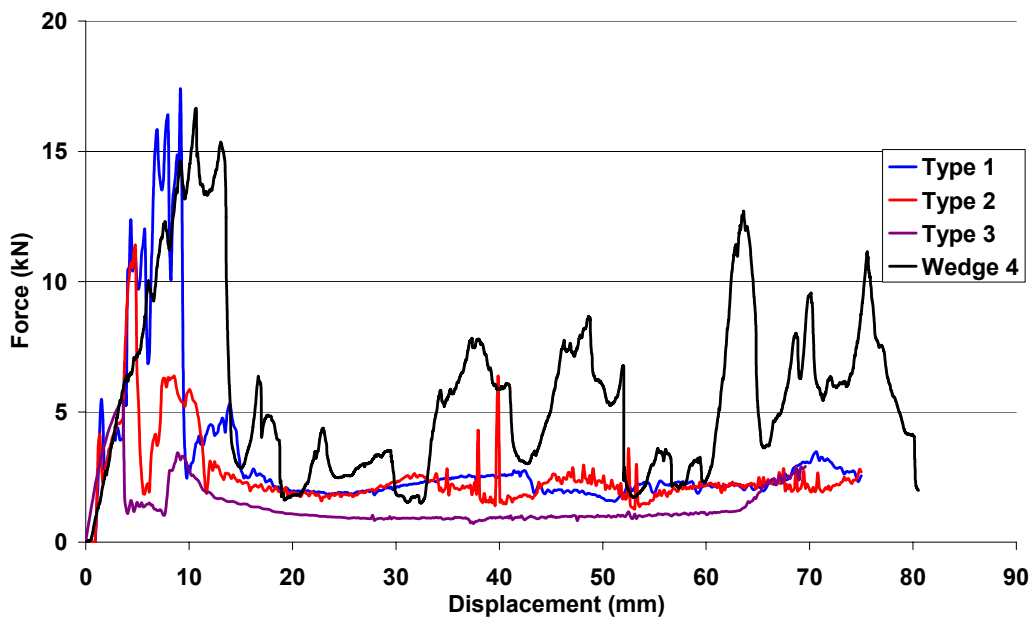
Figure 5-46: Comparison between standard PAM-CRASH^{TM} sandwich modelling and test results for 5-ply axial specimens

The experimental wedge tests, presented in Section 4.5.4, suggested that the properties in the composite skin at the impact front will be changed due to the propagation of

micro-cracks. The constitutive material model for the composite material cannot account for this degradation in properties; the stiffness at the wedge tip is over-predicted and produces an unrealistic fold. Figure 5-47 and Figure 5-48 present a comparison between modelling methods and experimental findings for oblique loading conditions.
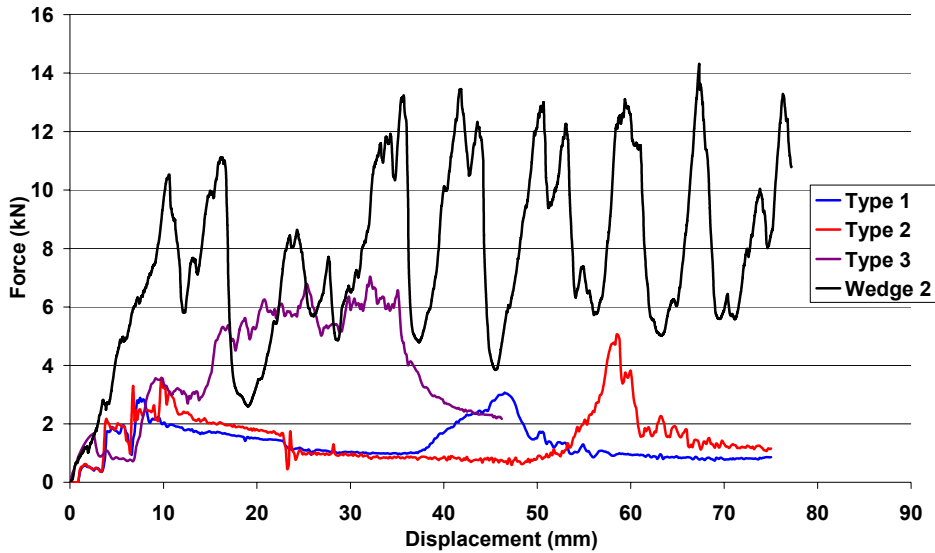
Figure 5-47: Comparison between standard PAM-CRASH^{TM} sandwich modelling and test results for 4-ply oblique specimens
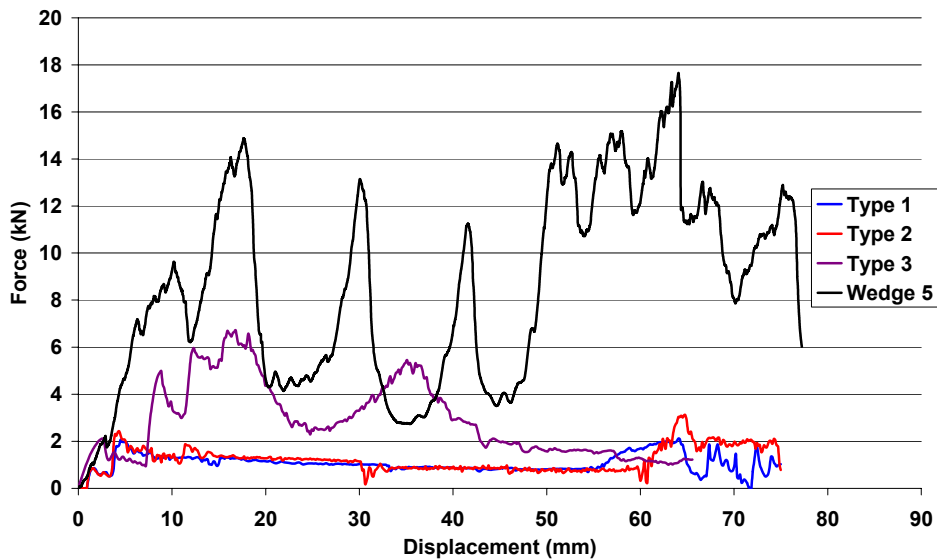
Figure 5-48: Comparison between standard PAM-CRASH^{TM} sandwich modelling and test results for 5-ply oblique specimens

The methods applied have been found to generate an inaccurate global failure mode as the composite shell element does not contain the required adjustment in properties to account for the effect of localised damage at the impact surface. The off-axis wedge is forced to hinge about a point near the secured base, thus the energy absorption of the sandwich is lower and dependent on the hinging mechanism as shown in Figure 5-49. It is believed that a corrected failure criterion for the composite shells to initiate and propagate local failure at the tip of the specimen would have corrected this problem.
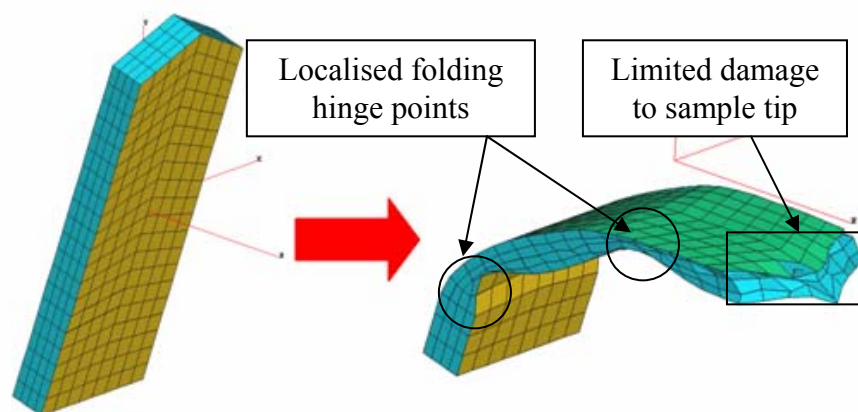
Figure 5-49: Folding of wedge FE model due to oblique loading

This degradation in composite properties cannot be determined from the experimental investigations conducted during this thesis. To achieve this, a further investigation is required to determine the onset of localised damage at the wall front. This will need to be followed by an additional modification to the constitutive material code in PAM-CRASH^{TM}.

Wedge Modelling using a Shell Element Based Core

Replacing the macro-solid element core with the meso-shell method, as shown in Figure 5-50, introduces the effect of individually folding cell walls. The numerical model represents half of the sample in order to reduce the computation time. A centreline boundary condition is applied to restrict movement in the X direction. To represent the separation of the skins, a central tied interface is provided between the two sets of composite skins, tied together using the tied contact interface calibrated in Section

5.3.2. The base skin, shown as light blue shell elements in Figure 5-50, represents a single ply of the composite material.
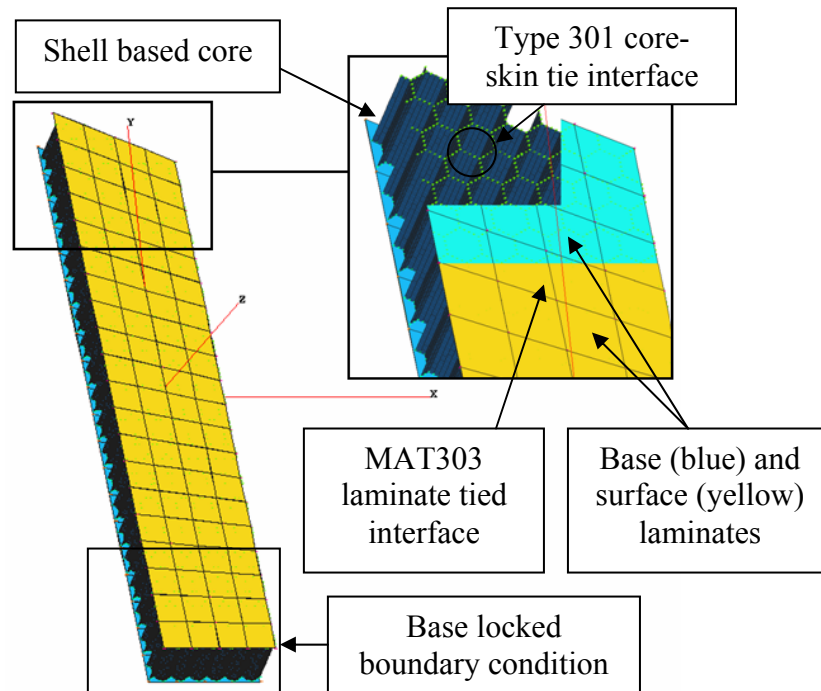
Figure 5-50: Description of wedge model with meso-shell core

The force-displacement curves are presented in Figure 5-51 for the axial loading condition and Figure 5-52 for the oblique loading condition. The model does not accurately reproduce the energy absorbing mechanisms observed during experimental tests. In both cases, the model produces a Mode-4 failure mechanism where the sample hinges at points along the length of the sample and reduces the structural strength of the sample as shown in Figure 5-53.
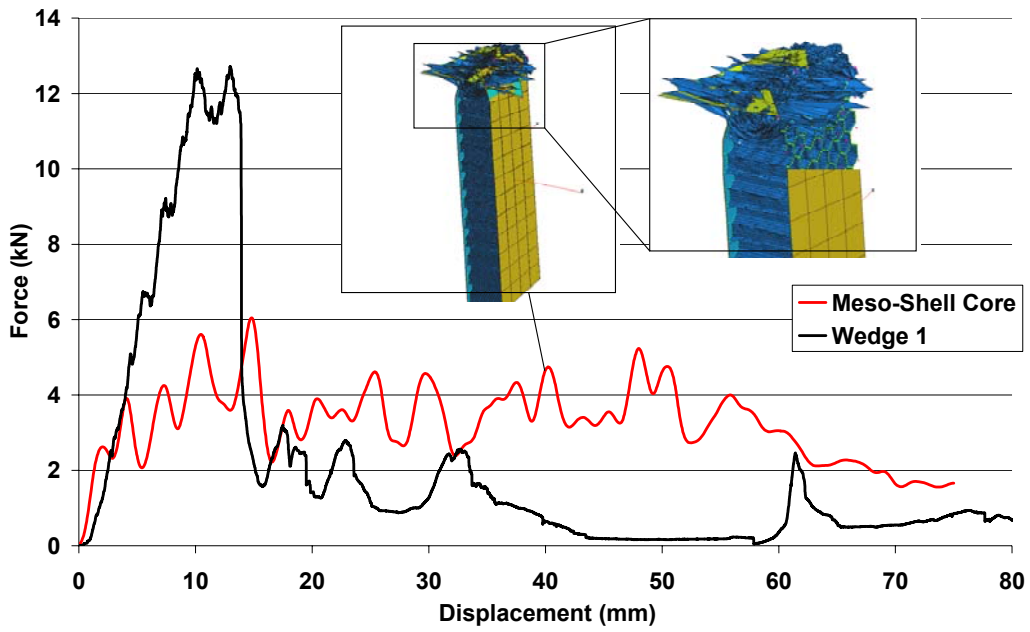
Figure 5-51: Comparison between meso-shell core wedges and 4-ply axial test
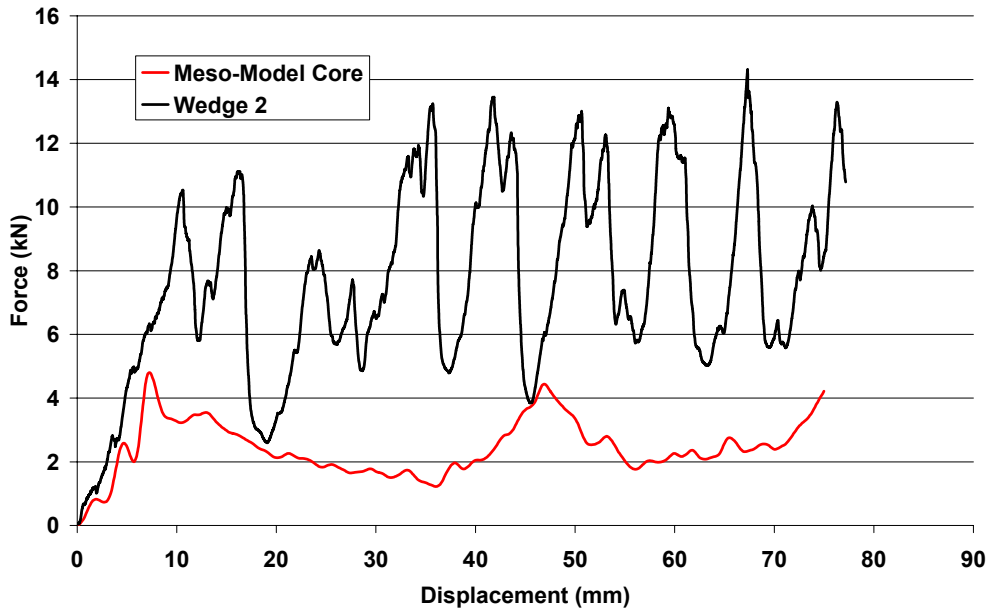
Figure 5-52: Comparison between meso-shell core wedges and 4-ply oblique test
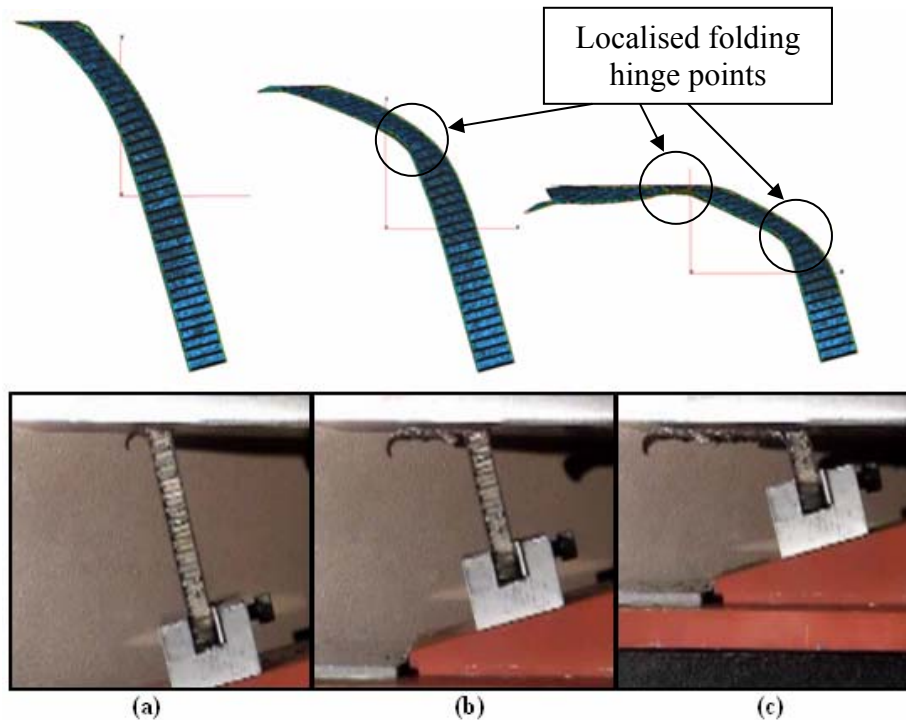
Figure 5-53: Meso-shell core wedge model compared with experimental observations

This study has established that the current methods of modelling composite sandwich structures using the standard version of PAM-CRASH^{TM} are not adequate; even with the introduction of additional improvements to the honeycomb and skin material codes introduced in Sections 5.1.1 and 5.2. The investigation using the meso-shell core approach did improve accuracy of modelling the core but with little success to improve the overall structure behaviour. It is likely that further improvements are required to the composite shell damage model to improve the overall sandwich crushing behaviour.

5.4   Considerations towards Nosecone Modelling

The previous sections of this Chapter have investigated the methods and suitability of PAM-CRASH^{TM} with regards to modelling the sandwich structure. Although this investigation has suggested PAM-CRASH^{TM} still requires further improvements to accurately represent these materials it was felt to be a valuable exercise to attempt crash modelling of the formula 1 nosecone structure.

For this study, the geometry of the 006 Bar-Honda Formula 1 nosecone has been supplied by Honda Racing F1. The nosecone FE model was produced from an IGES file and is shown in Figure 5-54. In this study, the core is represented using solid elements, utilising PAM-CRASH^{TM} MAT41 model and composite skins using MAT131. Representing the core with the meso-shell element method would is not feasible due to the excessive computational requirements and so has not been investigated here.
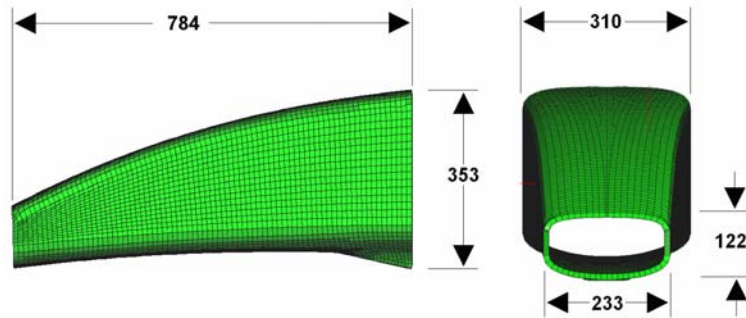
Figure 5-54: BAR-Honda 006 nosecone geometry (all dimensions in mm)

The mesh must be prepared so that the principal local element directions of both the honeycomb core and the composite laminate skin are consistent throughout the model. To achieve this, a Fortran program was written to re-arrange the sequence of nodes in each element has reference system defined in [50] and shown in Figure 5-55. The program rearranges the elements so that the local directions are pointing in approximately the same direction; due to the complex geometry of the nosecone, the shapes of these solid elements are not perfectly consistent, thus there will always be some level of variance in the local directions. Given the low stiffness properties in the in-plane directions and that this variance will not apply to the 'T' direction, this approximation is considered acceptable.
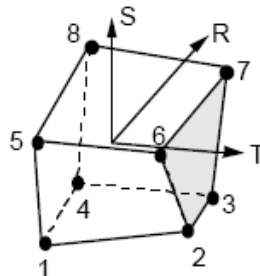
Figure 5-55: Solid element local frame system [50]

To simplify the model and reduce the computational requirements only one half of the model is generated and analysed. The centre line of the model is constrained using a displacement boundary condition to prevent any movement in the Y direction. The rear of the structure is locked using a displacement boundary condition to prevent any movement and represent the secure fixing of the structure to the chassis; this assumes that the chassis does not deform or move during impact, which is not strictly correct but for the purposes of this evaluation is acceptable. A rigid wall is then directed toward the structure with a mass of 390kg, equal to half the total mesh due to symmetry, and having an impact velocity of 14m/s; this represents the test conditions specified by the for FIA frontal impact test [3]. The simulation setup is summarised in Figure 5-56.
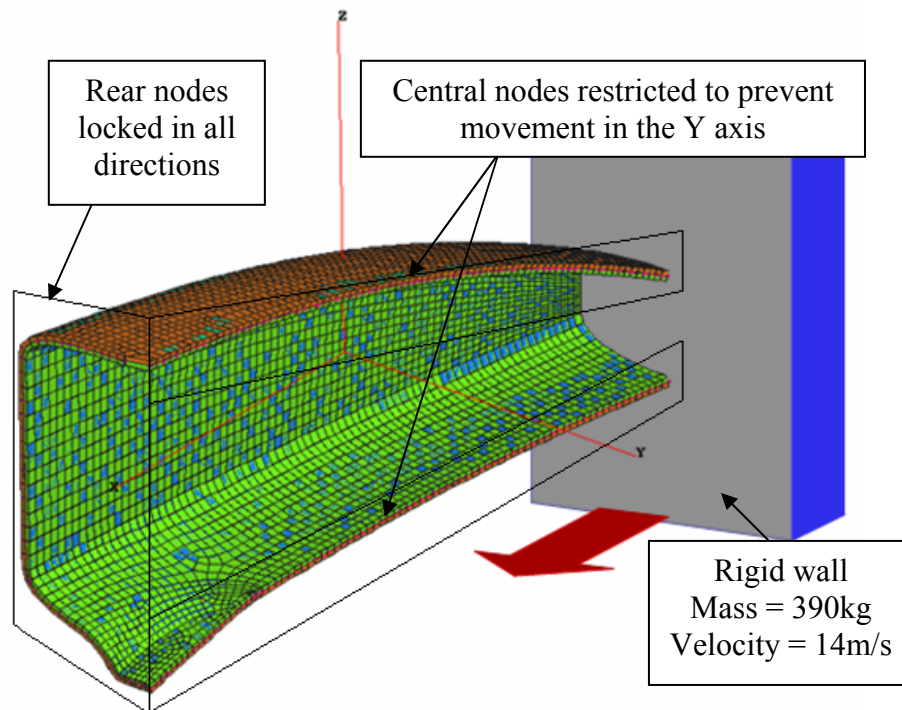
Figure 5-56: Nosecone boundary conditions and rigid wall settings

Considering these boundary condition requirements, the method of bonding the laminate with the core is addressed. The simplest bonding method is to assemble the shell and solid elements together as shown in Figure 5-57, identical to the Type 1 method presented earlier during the 3PB and wedge impact modelling investigations.

Core and skins assembled to share nodes
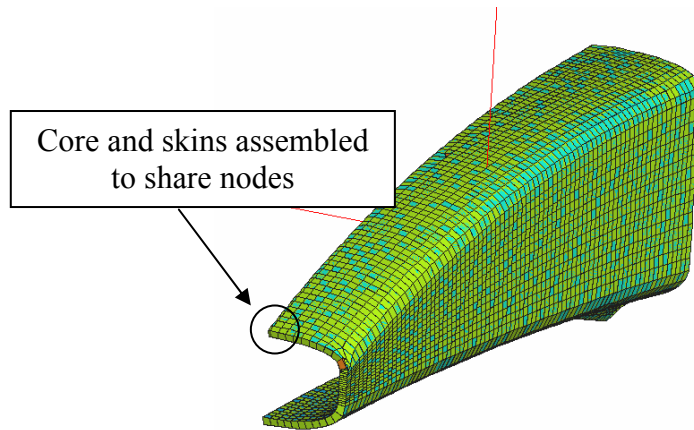
Figure 5-57: Assembled nosecone variant

An investigation using the central core delamination method has also been conducted, identical to the Type 3 modelling method used in the CSB and impact wedge modelling investigations. The model, shown in Figure 5-58, has the laminate and core materials assembled together so that they share nodes in the same manner as the fully assembled nosecone. This image has been mirrored to give the impression of a full nosecone.

Two honeycomb core solid models with tied interface
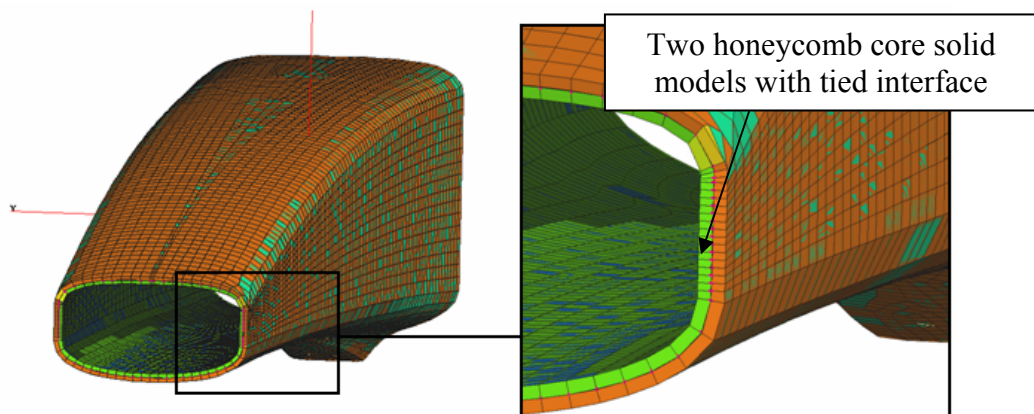
Figure 5-58: Type 3 nosecone model

The numerical simulation shows that the nosecone model folds and absorbs energy in very much the same manner as an actual experiment shown in Figure 5-59. A detailed observation of the crushing mechanisms during the test is difficult since the high-speed photography by composite dust and debris during the impact. The assessment of this model is based on comparing the final test sample with the fully deformed numerical model.
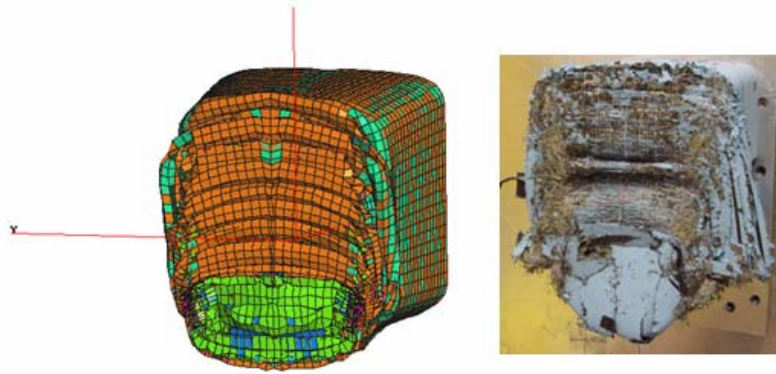
Figure 5-59: Post collapse model compared with nosecone test

One benefit of the computational model is identification of localised premature failure in the composite skin material. Figure 5-60 shows damage analysis of the nosecone during the crushing process. The blue region is undamaged composite and it is seen that the majority of damage is localised at the impact front, whilst a small region on the underside of the structure has undergone a significant amount of damage that leads to element elimination in this region even before the impact front has reached this point. The high-speed video recording from impact testing may not reveal this region of failure due to its low visibility.
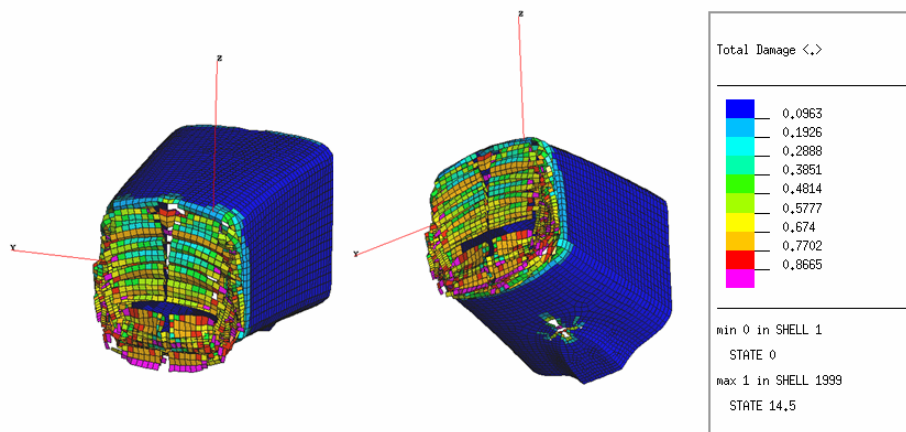
Figure 5-60: Damage analysis of nosecone skin

The numerical model results are shown in Figure 5-61 and are compliant with the FIA test regulations. In this figure, the comparison is made with a tests result from a regulation meeting structure from the same year as the investigated structure.
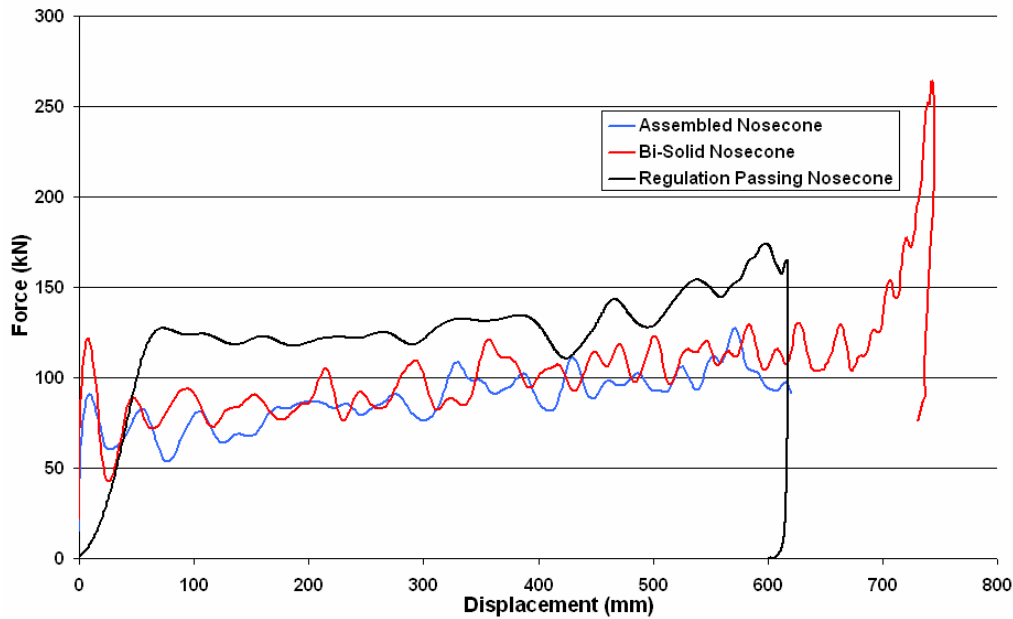
Figure 5-61: Comparison of nosecone models with regulation passing structure [93]

Article 16 of the FIA crash testing regulations [3] states the average deceleration must not exceed 25g, which equates to 190kN assuming conservation of mass. The regulation meeting structure and the simulation model are both below this average. Both methods of representing the nosecone have yielded approximately the same result despite the fact that investigation into the wedge modelling suggest both methods yielded differing results for an edgewise compression loading. This similarity in results suggests that the general shape of the nosecone controls the strength of the structure as the square frusta produces a stiff structure that does not undergo premature buckling or delamination.

5.5 Section Summary

A variety of computational representations of the composite skin and honeycomb core have been investigated using the FE package PAM-CRASH^TM. The objective of this investigation was to determine the accuracy of these methods when compared to experimental results and the suitability of these methods when applied to the modelling of sandwich structures. Limitations have been identified in both commercial composite and honeycomb modelling methods. Proposed improvements have also been presented and implemented into the constitutive material code.

The methods investigated to represent the core material have included an orthotropic macro-solid element approach and a geometrically accurate meso-shell element method. Comparisons were made with the low-density honeycomb used in a Formula 1 nosecone structure. The macro-solid element model, MAT41, discards a number of direction dependent properties which were addressed in this work. The findings from the honeycomb experimental investigation have successfully been implemented into the constitutive model and have been shown to improve representation of some of the direction dependent properties. An automated method for calculating the loading angle could not be implemented in the code and limited the further sandwich investigation using the honeycomb model developed for mixed shear-compression modelling.

An investigation to represent the core using shell elements was conducted. A variety of modelling methods to represent the thicknesses of the cell wall at the interface between cells have been investigated using the experimental results from 'T' direction compression test. It was found that using a consistent single wall thickness throughout the model produced a suitable representation. Under a variety of loading conditions, the meso-shell method produced adequate comparisons with experimental results.

The composite material has been modelled using the Ladevéze damage shell model, MAT131. This approach has been shown to represent tensile properties of a woven fabric composite material accurately; however, the in-plane shear representation used in the standard code has been shown to be inadequate. The constitutive material code has therefore undergone improvement by implementing a non-linear damage progression law for shear determined from experimental testing.

A variety of modelling methods have been investigated to access the current version of PAM-CRASH^{TM} suitability to represent composite sandwich structures using MAT41 for the core and MAT131 for the skins. To represent Mode-I delamination failure observed in the core during CSB testing, a numerical model of the CSB sample was produced using a pair of solid element beams to represent the central core crack propagation. The beams were bonded using a delamination tied interface with the G_{IC}

value obtained from CSB testing. This method produced an accurate fit between the numerical and experimental force-displacement curves.

This Chapter also presented two other methods of modelling the sandwich using the solid element core material model. These were:

- Core and skins sharing nodes preventing delamination.
- Core and skins tied using the tied contact calibrated from the CSB model.

These modelling methods were compared with the 3PB tests presented in Chapter 4. The methods did not reproduce the force-displacement trends observed from testing; however, the deformation mechanisms and energy absorption for complete failure were found to be similar. The improved models for in-plane pre-deformation honeycomb and woven composite skin were also found to be insufficient. The honeycomb core meso-shell model was found to improve the 3PB representation, but still requires some further improvements.

The three solid element core modelling methods were also compared with the wedge impact samples. These models were found to inadequately represent the deformation mechanisms in the sandwich due to oblique loading. The meso-shell core was also investigated here and showed similar inaccuracies. Therefore, the Ladevéze skin material requires further development.

This Chapter has also investigated the modelling of a complex Formula 1 nosecone structure. A mesh conditioning program was developed to assure the solid element local frame directions were consistent throughout the model. The boundary and loading conditions were representative of the regulations specified by the FIA. The nosecone models were observed to fold and deform in a similar progressive manner to that expected during a frontal impact test. The resultant force-displacement curves produced from the impact modelling conformed to the FIA crashworthiness regulations. The modelling methods investigated produced encouraging agreement with the test force-displacement curve.

6 Discussion

The numerical crash representation of composite-honeycomb sandwich structures is problematic due to the complex failure and energy absorbing mechanisms that occur in the skin and core materials and their interactions. This thesis has presented experimental research to investigate the energy absorbing mechanisms in the individual honeycomb core and composite skin materials before examining the full sandwich structure. This experimental work has been used to assess and improve the constitutive material models used in a commercial FE code to improve representation of both the core and skin materials. The energy absorbing properties of the sandwich structure has been examined and used to validate a variety of modelling methods available in the commercial FE code PAM-CRASH^{TM} to represent these structures. This Chapter discusses the investigation and findings presented in this research thesis. The limitations of the experimental and numerical work are highlighted.

6.1 Honeycomb Experimental and Numerical Investigation

The energy absorbing properties of honeycomb materials are well established for the principal loading directions and were presented in Section 2.2.1. There have been studies, both experimental and numerical, to increase knowledge of these materials when subjected to complex loading conditions, such as mixed shear-compression loading by Mohr and Doyoyo [24] [25] and biaxial in-plane loading conditions by Zhang and Ashby [29]. The findings of such research show that material properties in the principal honeycomb directions depend on deformations in the cellular structure and the loading direction.

The current commercially available honeycomb models are generally based on constitutive material models that consider the material to be a homogeneous solid, as opposed to a series of cells. The commercial FE code PAM-CRASH^{TM} utilises such a model as a computationally robust and efficient representation of honeycomb. This model considers deformations in the principal material directions to be independent and so cannot treat complex loading conditions properly when load interactions occur.

One objective of this thesis has been to equip the current constitutive model with coupled properties for sandwich applications. Experimental investigations have been conducted to acquire the variations in these properties with complex loading conditions. This Section discusses the experimental results and the improvements made to the numerical model.

6.1.1 Experimental Limitations of Honeycomb Testing

The honeycomb experimental investigation has been performed on the honeycomb core material used in the nosecone structure of a Formula 1 car. The nosecone utilises two honeycomb types in the nosecone; namely, a high-density and low-density core. Due to the amount of low-density core and the location of the high-density core, the assumption has been made here that only the low-density honeycomb material is used throughout the nosecone.

The experimental investigation was conducted to investigate and introduce new constitutive material laws for use in the current honeycomb model in PAM-CRASH^{TM}. The investigation was limited to proportional loading cases which it is believed are reasonably representative of the deformation mechanisms in the nosecone structure during a frontal impact test. These loading cases were considered quasi-static to build the material laws and is possible that these laws will vary when high-loading rates are applied; for instance [109] shows that 'T' direction crushing strengths of honeycomb increase as loading rates increase. Considerations towards dynamic variations in constitutive property laws would be a valuable study for future work.

The 'T' direction compressive properties of the honeycomb material were investigated to provide the basic PAM-CRASH^{TM} MAT41 model inputs and essential data for model improvements. This investigation was conducted with the use of the optical strain measuring equipment to measure sample deformations. The compressive strength properties of the material were found to be consistent with the manufacturer's specifications. However, the elastic compression modulus was found to be lower than

the manufacturer's specifications. This was observed in both honeycomb types and in the out-of-plane compressive loading of the sandwich material. It was suggested that the upper and lower loading blocks are deforming around the sample and increasing the measured displacement. To overcome this, the compression plates must be reduced in size to reduce deformation and rotations about the sample during out-of-plane compression; this deformation mechanism was described in Section 4.3.1.

The standardised method of measuring 'T' direction compression properties is with the use of a mechanical displacement device, shown in Figure 6-1. The device can potentially interfere with the folding mechanism occurring in both the bare and sandwich samples, as shown in Figure 6-2. In the case of the sandwich sample, a hole must be drilled through the skins to accommodate the device. It is possible that this may introduce a reduction in the compression strength of the sandwich as the drilling process may damage the skin-core interface; which was shown in Section 4.5.1 to change the out-of-plane compression strength of the sample.
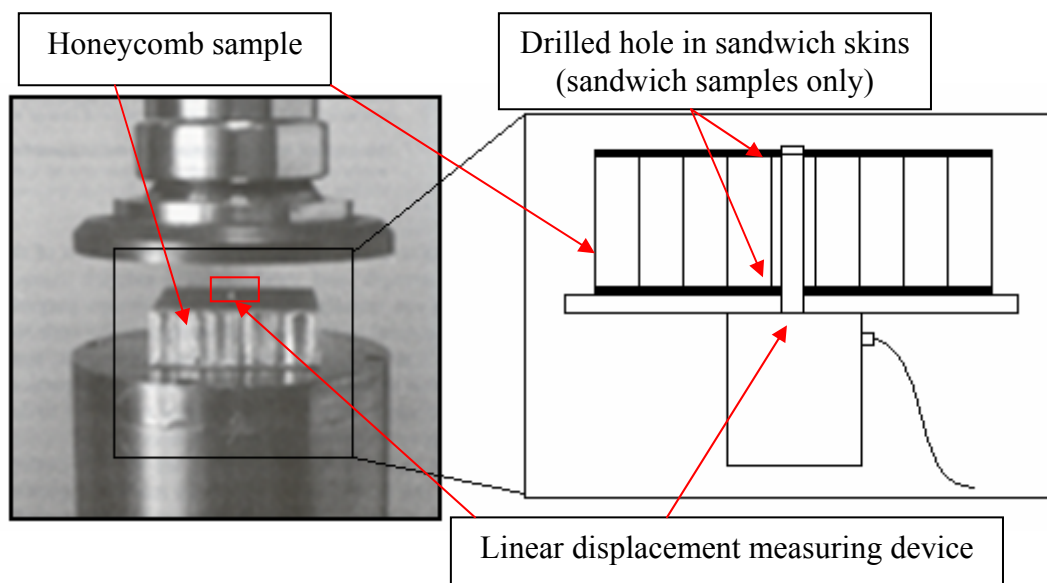
Figure 6-1: Linear displacement device used in ASTM C365-03 [19]
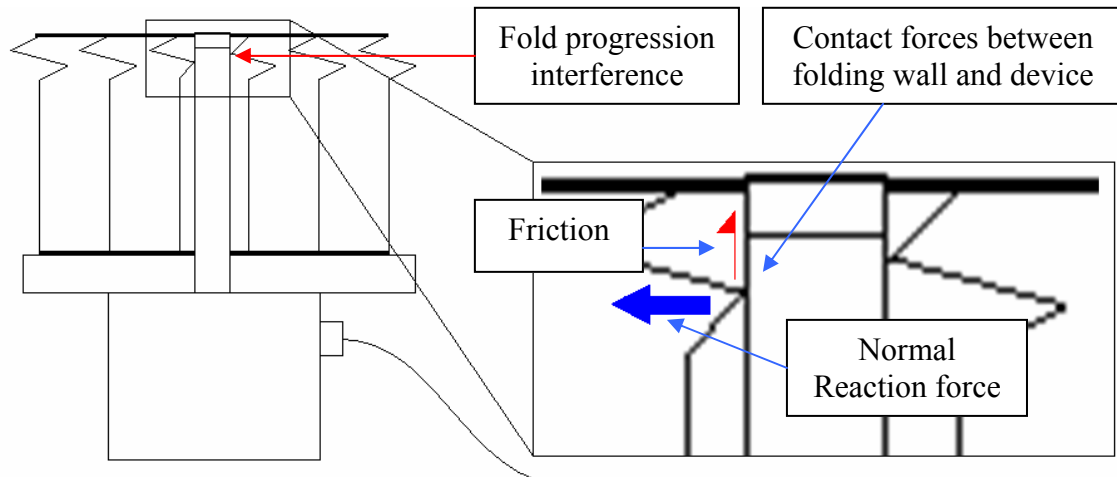
Figure 6-2: Potential folding interference caused by mechanical displacement measuring device

Therefore, the optical measurement method presented in this thesis can potentially provide increased accuracy when measuring the out-of-plane compression properties of honeycomb materials.

Honeycomb Mixed Shear-Compression Investigation

An Arcan apparatus has been developed to load a honeycomb sample in mixed out-of-plane shear-compression condition. The orientation of the in-plane direction was varied to investigate 'T-TW' and 'T-TL' mixed shear-compression loading. This research has suggested that the 'T-TL' relationships had greater dependency on the consistency and quality of the hexagonal cell arrangement than the 'T-TW' arrangement. This can only be confirmed with further testing in the 'T-TL' direction to assess the scatter of results.

The investigation of 'T-TW' properties produced a similar trends in peak crushing normal and shear strengths to that found by Mohr and Doyoyo [24] [25]. The variations between plateau strengths presented here and those by Mohr and Doyoyo [25] are possibly due to the stiffness of the Arcan apparatus. The sample grips used in [25] imposes greater restrictions to the horizontal direction and rotation of the specimen and produced a specific folding mechanism. The Arcan apparatus presented in this work imposes less restraint; however, it is still adequate to prevent localisation of buckling that can influence the folding mechanism of the cells. A further in-depth study of the

device is required to examine the precise movement of both sample grips during the loading process; this could influence the direction dependent property laws presented in this work.

Despite the above limitation, the property laws derived from the Arcan investigation are valid. The objective of this study was to determine the general trends in these loading directions to improve the honeycomb material model MAT41. The current apparatus can be applied to other cellular solids and it is likely that honeycombs with a similar cellular geometry, such as Nomex, will display similar trends. However, it would have to be verified if the properties of novel geometry cores, such as Chiral [79] or Flex-core [18], will display similar trends and should be considered as a potential follow-on study.

In-Plane Pre-Deformation Influences on 'T' Direction Compression Properties
The effects of pre-crushing in the 'W' and 'L' directions on the 'T' direction compressive properties have been investigated. Pre-deformations to the cellular geometry were introduced due to constraints imposed in the transverse direction. These samples were observed to maintain the 'T' direction crushing strength by resisting the development of large folding mechanisms. Pre-deformation in the 'W' direction without restrictions in the 'L' direction transforms the hexagonal geometry into a series of flat plates as the transverse direction expands. These plates provide less resistance to the production of large folds and thus a reduction in crushing strength is observed.

The in-plane crushing strengths of the material were established without restrictions imposed on the transverse in-plane direction. This research did not determine the in-plane compressive strengths of the core with a restriction on the transverse expansion. The in-plane strength of the material will increase and reach compaction earlier with the addition of these imposed constraints. This can be investigated using the proposed test apparatus in Figure 6-3. The apparatus is designed to impose a restriction to the transverse direction whilst undergoing in-plane compression. The coefficient of friction in the transverse restriction walls must be established as friction acting at the honeycomb sample edges will be included in the vertical force measurement. Horizontal

load measurements are required to calculate the vertical friction force. Thus the compression properties can be calculated using;

$$\sigma_i = \frac{\left(F_V + 2\mu F_H\right)}{A}, \qquad\qquad [6\text{-}1]$$

where, F_V is the measured vertical force, F_H is the measured horizontal force, μ is the coefficient of friction in the transverse walls, A is the cross-sectional area of the sample and σ_i is the compression stress in the loaded in-plane direction. Alternatively, the apparatus can be simplified to include only the vertical force measuring device by lubricating the transverse walls and reducing frictional forces until they are negligible.
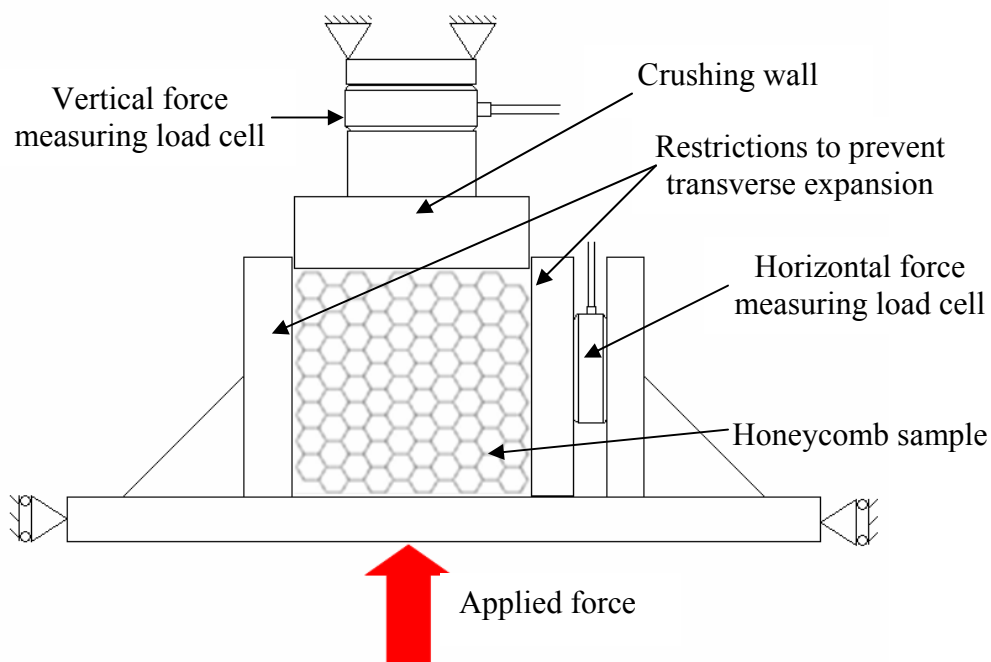
Figure 6-3: Proposed in-plane compression apparatus with transverse restrictions

6.1.2 Limitations of the Investigated Honeycomb Modelling

Macro-Solid Element Modelling

The honeycomb solid element material model, MAT 41, has been the main focus of this research. One objective of this aspect of work was to improve the current model to represent further loading conditions using material laws developed from testing. There are alternative material models, such as considering the kinematics of folding walls [74] which are based on the cellular geometry to predict folding wall mechanisms. Introducing such constitutive material modelling methods into PAM-CRASH™ was not

the object here as this would require the development of a new material model, rather than the modification of an existing one.

Mixed Shear-Compression Property Coupling

The current model does not contain coupled properties that relate loading direction with the principal direction properties. The introduction of these coupled laws has been implemented into the constitutive material model. This method was effective at improving the solid element properties for mixed shear-compression modelling with a single element case. Further coupled properties can be applied to include variations in average plateau shear and normal stresses to increase the accuracy of the element. The commercial version of this method would require these laws to be applied using a function law; this would require extensive access to the code which was not possible. Alternatively, further material testing may find that the hexagonal core materials adhere to specific trends. A future code may implement a general trend for all honeycomb models based on 'T' direction compression and out-of-plane shear properties.

The limitations of this method include the lack of an automated direction calculation system due to restrictions in the available code. Currently, the improved code requires the user to specify the loading angle and so cannot be used in a structure, such as a 3PB sample, where a variable mixed shear-compression condition is applied. A strain based loading angle calculation method may provide a potential solution. The deformation due to mixed shear-compression loading is shown in Figure 6-4.
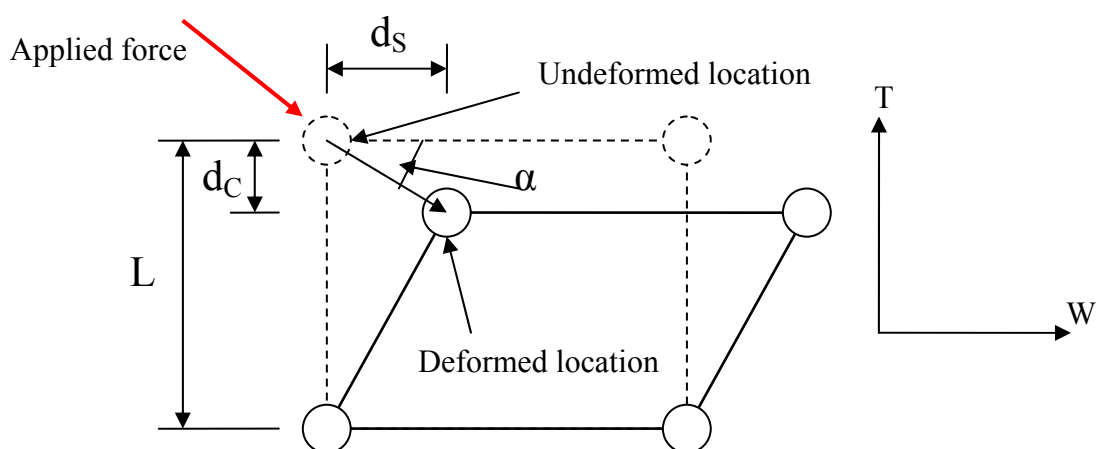
Figure 6-4: Deformation of solid element during mixed shear-compression loading

To calculate the loading direction using displacement measurements, shear displacement, d_S, and compression displacement, d_C, are required. The available material code does not specify these displacements. However, shear strain and compression strain in the principal directions are specified in the material code and these can be used to calculate normal displacement, equation 6-2, and shear displacement, equation 6-3.

$$\varepsilon_T = \ln\left(\frac{L - d_C}{L}\right) \Rightarrow d_C = L - Le\varepsilon_T \,, \qquad\qquad [6\text{-}2]$$

$$\varepsilon_{TW} = \frac{d_S}{L} \Rightarrow d_S = L\varepsilon_{TW} \,, \qquad\qquad [6\text{-}3]$$

where, L is the original length of the element in the T direction, ε_T is the compression strain and ε_{TW} is the shear strain. These can be used to specify the loading angle, α, using equation 6-4.

$$ATAN\left(\frac{d_C}{d_S}\right) = ATAN\left(\frac{(L - Le\varepsilon_T)}{L\varepsilon_{TW}}\right) = ATAN\left(\frac{(1 - e\varepsilon_T)}{\varepsilon_{TW}}\right) = \alpha \qquad [6\text{-}4]$$

This solution may overcome the limitation with the mixed shear-compression enhancement to the material model and requires an investigation to validate the method.

Coupling In-Plane Deformations with 'T' Direction Properties

The current commercial model does not couple deformation in the in-plane principal directions with 'T' direction properties; also, it does not account for change in area in the calculation of compression 'T' stress; this progressively lowers the amount of force required to crush the element in the 'T' direction. The relationships between in-plane deformation and out-of-plane compression properties have been introduced to the material model.

The improvements do not account for Poisson's ratio of the material. The model requires this property, especially in the in-plane direction as the experimental research found that removing the transverse restriction during pre-deformation had a direct effect on the crushing properties. A relationship between the extent of transverse deformation and the change in crushing properties can be identified either experimentally, or could be determined numerically, using the meso-shell honeycomb model. The further

improvement to include Poisson's ratio and extend the stiffness matrix is required to take advantage of these new relationships.

Future of the Improved Honeycomb Material Models

This research has shown that improvements can be readily introduced into the constitutive honeycomb material model to represent complex loading cases. The model still requires further improvements for increased non-proportional loading and improvements to exploit the benefits of the mixed shear-compression modelling. In addition, there are other loading conditions, such as bi-axial loading [77], not considered during this research simply due to time and experimental complexity. It is unlikely that a single solid element model will encompass all energy absorbing mechanisms in the honeycomb structure due to the complexity of the code required. It is possible that a future honeycomb solid element model will include these relationships and provide operators with an improved material model for development of sandwich structures.

Meso-Shell Element Modelling

Representing the honeycomb material using a geometrically accurate shell model has been presented as a potential extension to the experimental investigation of honeycomb. The folding and deformation of the cellular geometry is similar to that observed during the various experimental investigations conducted during this research. The predicted strength of the modelling has also been shown to produce an adequate comparison for 'T' directional compressive strengths, even with variations in loading direction and deformation in the in-plane directions prior to 'T' direction loading. The only case where the model failed to produce an adequate representation was with the Series 3 in-plane pre-deformation in which the 'W' direction was loaded with no restrictions in the 'L' direction; however, the cellular geometry was not identical to that tested and therefore is not a fair comparison.

The manufacturing methods used to produce the structure will introduce imperfections to the foil walls. The numerical representation was produced with a perfectly consistent hexagonal cell and with a homogeneous base material definition. With codes such as

PAM-FORM^{TM}, it would be possible to build into the material the variation in properties due to deformation at the foil wall edges by recreating the manufacturing process.

Another difference between the honeycomb sample and the investigated meso-model is the representation of the bonded walls. Comparisons were made between the methods used to represent this region and it was found that the simplest modelling method; namely the single wall thickness shell and material model, provided an appropriate level of accuracy when compared with 'T' direction compressive loading tests. This accuracy was not maintained throughout the investigation, such as the out-of-plane mixed shear-compression investigation, but did suggest general trends in properties when subjected to a variety of loading conditions.

6.2   Composite Material Testing and Numerical Modelling Investigation

The composite material used for the skins of the composite-honeycomb sandwich structure in the BAR-Honda 006 nosecone has been investigated. The investigative study was to obtain input data for the Ladevéze damage model used in PAM-CRASH^{TM} and to establish accurate damage progression laws. This Section discusses the findings from this experimental testing and limitations of the current numerical material model.

6.2.1 Experimental Investigation of the Woven Composite Material

The composite material properties have been examined using standardised testing methods for tension and in-plane shear properties. The optical measuring system was used to examine the strain and deformation of the sample for each test. This method proved effective as the location of failure varied between samples, especially with shear samples. The use of traditional mechanical strain gauge devices would have provided an inaccurate indication of damage. The results from the tensile tests showed a large scatter of results which were lower than the manufacturer's datasheet. This is possibly due to the sample preparation and the number of tests conducted. Further tests are required to

reduce this scatter; however, the tensile properties were used for further model calibration.

During the in-plane shear test examination, the effectiveness of the optical measuring system was compromised as the paint and speckle pattern were lost due to large deformation of the sample, however the system was capable of analysing the region undergoing the largest deformation close to the eventual loss in strength. The deformation measured by the DIC system is only representative of surface deformation. Variations in strain between each ply in the composite sample, leading to inter-ply failure mechanisms, cannot be measured with the DIC system.

The cyclic load tests were used to establish an improved damage progression law for the 2x2 twill woven fabric composite. The damage progression law was found to be non-linear for this material. UD composite materials were found to produce linear damage progression laws. Woven and braided materials have been shown here, and in [51], to produce non-linear damage progression laws. The damage progression law proposed here will most likely be unique to this particular composite type.

The compression study was conducted using a new non-standard experimental testing apparatus to increase the gauge length of the composite sample. This was devised to reduce grip effects and also permit the usage of optical measuring system which has proven effective in other material tests. Although the modulus of the composite material was found to be in agreement with the manufacturer's datasheet, the maximum compressive strength was found to be approximately 65% lower than the specified failure strength. The failure strength is likely to represent the buckling strength and not the compressive strength. To overcome this, the dimensions of the sample can be increased, specifically the thickness of the sample due to the cubic function in the moment of inertia formula. The buckling force for pin ended beam compression samples is given by;

$$P_{CR} = \frac{\pi^2 EI}{L^2},$$
[6-5]

where P_{CR} is the buckling force, E is the elastic modulus of the material and L is the length of the sample. I is the second moment of inertia which is calculated using;

$$I = \frac{bt^3}{12},$$ [6-6]

where b is the width of the sample and t is the thickness.

To accommodate this test apparatus, the width of the sample must be 25mm. Thus, the minimum thickness required to prevent Euler buckling is 6mm. This solution is not applicable for a number of reasons. The thickness of the sample must not exceed 10% of the minimum width to maintain plane strain conditions. Furthermore, the apparatus cannot accommodate a 6mm thickness sample; also, the failure stress off this sample would be 120kN which exceeds the load cell used in the Instron test machine. Therefore, the apparatus must be redesigned to further prevent the buckling process before further investigation with this apparatus is conducted.

6.2.2 Composite Numerical Limitations

The woven composite material has been represented by a shell element with orthotropic damage properties. The original Ladevéze damage model was developed around the damage parameters observed during the testing of UD composite materials. As stated in this work, the damage progression for composite materials varies greatly, especially between UD and woven fabrics. The damage progression law identified here for the woven composite has been introduced into the constitutive material model. This research, and that of Fouinneteau [51], suggests that future commercial versions of PAM-CRASH™, and other FE codes using the Ladevéze damage model, would be improved by using a general non-linear function for shear damage.

There are limitations with the usage of this modelling method. The model only accounts for intra-laminar failure mechanisms, the effects of potential inter-laminar delamination have yet to be introduced. It is likely that the deformation processes in the nosecone structure will include some inter-laminar delamination. The individual shell element cannot recreate these failure mechanisms as it is not capable of separating. The

degradation in strength due to inter-laminar failure mechanisms can be introduced to represent the effects of an impact on the surface of the composite. A series of experimental tests are required to assess the influence of damage on the in-plane shear and compression properties, in-plane tensile properties are unlikely to be reduced unless there is significant damage to the fibrous material.

Alternatively, the introduction of the tied interface between two or more shell elements can be considered, such as [88]. The tied interface in PAM-CRASH^{TM} is designed for Mode-I, -II and mixed Mode-I/II loading conditions [89]. This would require an extensive investigation including DCB and mixed mode beam (MMB) testing.

6.3 Sandwich Structure Testing and Numerical Modelling Investigation

A series of experimental studies have been conducted to investigate numerical methods to represent the composite-honeycomb sandwich material used in the nosecone structure of the BAR-Honda 006. The potential folding mechanisms in the nosecone were identified and used to determine the required experimental testing for model validation. This limited the potential number of tests to only those required to build the necessary failure mechanism database to represent the nosecone folding mechanism. It is likely that other failure mechanisms exist and contribute to the strength and crashworthiness of the nosecone structure. To determine these mechanisms, and the relevant tests to establish the energy absorbency, the nosecone deformation during impact testing must be inspected in closer detail. This Section discusses findings from the experimental research and limitations with the numerical models.

6.3.1 Experimental Investigation of the Sandwich Structure

Out-of-Plane Compressive Testing

The experimental research began with an investigation on the out-of-plane compressive properties of the sandwich structure. The objective was to establish the effects of the adhesive glue-line constraints on the elastic buckling and crushing properties of the core

material. This area of research has not previously been examined and so these effects have yet to be established. The experimental test was conducted using the same methods used during the honeycomb 'T' direction compressive tests. The elastic yield (Peak) strength of the sandwich was predicted to be greater than the core alone as the end constraints are changed from a mixed free/fixed assumption by Gibson and Ashby [17] to a fixed dominated end condition. This work showed that the end constraint factor is increased from 4 to approximately 5.2 for this particular sandwich structure. It is likely that a variation in adhesive properties, such as fillet size and strength, will vary the end constraint factor and should be considered as a potential future area of study as the choice of adhesive has been shown to influence sandwich properties [57][58].

In addition to this increase in peak strength, the plateau crushing strength was observed to change due to end constraints. This was an unforeseen effect as previous mathematical methods to predict the crushing strength of honeycomb are based on the plastic work per unit length of the cell wall required to continue folding [17] [33]. Thus, the plateau strength should remain constant regardless of end constraints. However, this research has shown the crushing strength to be increased. In addition, the folds observed during the core alone tests produced a distinct wavelength in the force-displacement curve. The sandwich compression displayed no wavelength, despite the observed creation of folds and, instead, produced a consistent growth in crushing strength. The potential reason for this is that the adhesive glue line introduces an imbalance to the folding mechanisms which prevent some folds from developing. This change in plateau strength was observed through two compressive tests to be identical, further tests will show how consistent this effect is.

Mode-I Crack Propagation Testing

Crack propagation through the composite sandwich material has been of interest to this research. The wedge impact and Mode-I testing of the low-density core material showed that crack propagation will not occur at the skin/core interface, but continue through the aluminium core material. The Mode-I crack propagation was investigated using a CSB test and it was found that the crack tends to stabilise centrally through the core during quasi-static loading. This stabilisation simplifies the calculation of G_{IC}, for a variety of

methods, including the modified beam theory and compliance calibration methods. The maximum variation between methods was found to be approximately 11.5% for Sample-9 and 20% for Sample-11. Both samples were found to produce consistent values of G_{IC} through corresponding methods.

Mode-I testing of the high-density core material was not investigated; however, given the increased strength of the material, shown in high-density wedge impact testing, it is possible that the crack will propagate through the adhesive glue-line. When compared with other CSB experimental research, such as [60] and [104], the value of G_{IC} found during this research is high, [63] presented research with a similar G_{IC} to that recorded here. These published works vary in sandwich materials, such as foams and adhesion type, and thus direct comparisons are not possible. The research does show how the choice of in sandwich base materials influences crack propagation structural properties.

An experimental Mode-I test apparatus to introduce higher loading rates to the CSB was also evaluated. The crack propagation was again stable but tended to be nearer to one skin as opposed to stabilising centrally. The calculated strain energy release rate, G_{IC}, was found to increase with loading speed. However, the difference between the 1mm/min quasi-static test and the 1.3m/sec dynamic test is relatively small. Traditionally, aluminium is considered to be strain-rate insensitive and thus the strain energy release rate should remain constant with an increase in loading rate. An increase in failure strain with loading rate has been observed by Smerd et al. [115] and suggested that the phenomena may be due to inertia stabilisation which delays the onset of final fracture. This delay in reaching final fracture will increase the amount of energy required to continue crack propagation through the honeycomb material. Further testing is required at higher loading rates to establish the change in G_{IC} through the honeycomb core.

Three-Point Bend Testing
3PB tests were conducted to establish the flexural properties of the sandwich construction. The tests found consistent failure mechanisms between the 4 and 5-ply specimens. The flexural properties of the sandwich were also found to be very similar

between specimens having the two skin thicknesses. It is established that flexural properties of sandwich materials are influenced by the core; the high-density core material sandwich will likely have increased flexural strength. This was not investigated due to time constraints encountered during this research. The failure mechanisms in the composite skin and core materials will likely be identical to those observed during low-density core testing. A further investigation to establish the variance of failure mechanisms and flexural properties with a change in the core thickness would be of potential benefit to further sandwich structure development.

The 4-ply specimens consistently separated at the end of the test, whilst the 5-ply specimens held together. It is possible to surmise that the lower skin in the 5-ply samples does not completely split; also, upon inspection of the force-displacement curve, the material displayed a less sudden drop in strength at the end of the test than the 4-ply samples. It follows that the drop in strength signals a progressive failure through the lower skin plies whereas the 4-ply samples display a complete skin failure and produce the near instantaneous drop in strength.

In-Plane Edgewise Wedge Compression Testing

In order to investigate the in-plane edgewise loading properties of the sandwich, wedge samples have been manufactured and subjected to quasi-static and dynamic edgewise loading. This research found a mixture of failure mechanisms occurring in the core and skin materials. The failure mechanisms and, ultimately, the strength of the wedge was dependent on the core material. The strength and resistance of the core against crack propagation affects the stability of the sandwich during in-plane loading. In the case of the axial tests on the low-density core samples, crack propagations were frequently observed in the core material. The 4-ply skins did not resist bending and thus these samples displayed sandwich separation and low energy absorption. The 5-ply skins resisted bending and contained the majority of deformation at the impact wall, cracks were observed to propagate through the core and reduce structural stiffness. The high-density core samples resisted crack propagation and folding mechanisms for both 4 and 5-ply specimens. In these cases, the failure mechanisms were localised at the crushing wall.

As stated by Mamalis et al. [10], samples which maintain deformation at the impact wall front, Mode-1 end progression failure, maintain a consistent crushing strength. These investigations displayed a mixture of folding and fountain end progression failure processes occurring in the samples. The composite skins undergo a damage process at the impact front, such as cracking in the resin and debonding of the fibres, which localise the damage at the impact wall and prevent folding mechanisms further down the length of the sample. During higher-rate loading, these mechanisms were observed along with a reduction in energy absorbency. The reduction in strength is observed due to the propagation of larger cracks between the skin and core materials than those observed in low-rate compressive tests.

The samples were also subjected to an oblique loading condition which was shown to produce a higher specific absorption of the material during quasi-static loading. In this loading case the loading conditions did not produce crack propagation through the core. The samples were observed to resist large folding mechanisms and produced a folding failure mechanism isolated at the impact wall. This isolation is likely to be caused by damage propagating through the composite skin material and reducing their strength.

Dynamic oblique impact testing was not investigated here due to limitations of the test apparatus. The sample was consistently dislodged from the apparatus at the start of the impact process and tightening the bolt grip mechanism was found to be ineffective. In future, samples will need to be locked in position with use of a bolt through the sample base to hold it firmly. Alternatively, lower oblique angles, i.e. 5^0, could be investigated with a change in the wedge base.

To date there is little research into the in-plane sandwich impact deformation; the majority of academic interest is with the crashworthiness of structural components made entirely from composite materials. Thus it is difficult to compare the energy absorbing mechanisms observed here with other sandwich structures. This research has presented the effects of varying the core and skin materials. It is likely that the deformation processes observed and recorded here are representative of many other variations in the

sandwich constructions. This work has provided an insight into the deformation mechanisms involved in an enclosed sandwich structure, such as the nosecone, which are difficult to observe experimentally, especially during dynamic impact loading.

6.3.2 Limitations of Investigated Numerical Sandwich Modelling

Representing the sandwich structure using material models available in PAM-CRASH^{TM} has yet to be established or recommended, although a previous investigation by Aktay et al. [90] did use options available in PAM-CRASH^{TM} to represent a sandwich structure. This study has investigated three modelling methods using the solid element MAT41 for the honeycomb core and the shell element MAT131 for the composite skin material. The models included variations in representing the skin core adhesive and crack propagation properties.

The modelling of the 3PB and wedge samples showed that, in general, the simplest of these methods which used a fully assembled model in which the skin and core share common nodes produced the best overall representation. However, these investigated methods are currently not capable of accurately representing the failure and energy absorbing behaviour of these materials. The improved material models developed in this work had limited influence on the 3PB models; it is likely that the deficiency with this model is with the mixed shear-compression representation of the core as this loading condition was observed during testing. The 3PB model using the meso-shell core model represented the failure mechanisms observed in the experimental sample more accurately than the macro-solid element core models. This method displayed a mixed shear-compression mechanism around the deformed region, thus the inclusion of the improved solid element model to reproduce mixed shear-compression properties will most likely improve the solid element representation of the core and the overall sandwich behaviour.

The modelling of the wedge impact samples was less successful as the failure mode in these models differed considerably from the experimental tests. The experimental investigation displayed a contained Mode-1a and Mode-1b, depending on load direction

and failure in the composite skin material was localised at the impact wall for both axial and oblique loading cases. However, the numerical models displayed a Mode-4 failure mechanism where the wedge samples created hinge points down the length of the sample. The degradation in material properties due to isolated cracking in the composite material at the impact front cannot be modelled using the current damage model and requires further improvements. This assessment is also supported by the honeycomb meso-shell core models which produced a similar hinging mechanism.

6.4   Current and Future Crashworthiness Modelling of Sandwich Structures

This work has presented findings which suggest that the FE code PAM-CRASH^{TM} requires further development to represent composite-honeycomb sandwich structures accurately. A numerical model of the 006 BAR-Honda nosecone structure has suggested that the current tool is capable of determining if the structure will definitely pass or fail the crashworthiness requirements. The nosecone model did produce a similar force-displacement curve to a regulation passing structure and recreated a similar crushing process to that observed during testing. The detailed examination of the wedge impact samples highlighted limitations of the code to model certain failure mechanism in the skin material accurately, such as degradation in material properties due to cracks in the resin and fibre fragmentation at the impact wall. The nosecone shape introduces a structural support to the sandwich structure which prevents the Mode-4 buckling and helps localise deformation to the impact front.

The nosecone model cannot account for degradation at the impact front and so is missing important failure criteria. Thus, optimising a nosecone design with PAM-CRASH^{TM}, or any other commercial explicit FE code, is not yet possible. In addition, this work has been built on the assumption that the core and skin materials are consistent throughout the nosecone. In reality, deformation produced during the nosecone manufacture, especially at the edges, will influence the material properties of the sandwich in those areas.

It is likely that explicit computational codes will become accurate and efficient enough to determine the crashworthiness of components made from these materials. The constitutive material codes will continue to improve as more information concerning the energy absorbing properties of cores, skins and sandwich structures become available. FE companies must improve their software to represent these structures as manufacturers are introducing composites into further more complex and critical applications in order to remain competitive.

7 Conclusions

The following summarises the main contributions and conclusions of this work.

Contributions to the knowledge of honeycomb material properties during mixed loading conditions

1. The variations in out-of-plane compression and shear when subjected to mixed shear-compression loading have been experimentally investigated and presented. An improved Arcan apparatus has been developed and used in conjunction with digital image correlation to produce a series of mixed shear-compression laws. These laws were then used to calculate compression and shear material properties depending on loading direction.

2. The variation in mixed shear-compression properties, depending on in-plane orientation angle, has also been studied in both the 'TW' and 'TL' directions. Experimental work showed the 'T-TL' normal compression and shear properties to be 60% higher than the 'T-TW' loading case for the low-density honeycomb material presented in this thesis.

3. The influence of in-plane deformation on out-of-plane compression properties is important in edgewise loading of these materials and has therefore been investigated. The variation in out-of-plane compression properties was shown to be dependent on transverse boundary conditions during the initial in-plane deformation process and on the extent of pre-deformation. Relationships between the increase of in-plane deformation with the increase in plateau strength and decrease in compaction strain have been established. These relationships have been shown to be relevant to limited experimental testing which was undertaken with the high-density honeycomb material.

Contributions to the numerical modelling of honeycomb materials

1. The solid element material model available in PAM-CRASH^{TM} has been improved to include the mixed shear-compression response observed during testing. The mixed shear-compression relationships derived from the experimental investigation were applied directly into the material model. The improved material model has

been shown to accurately reproduce the mixed shear-compression properties of the honeycomb material.

2. A further improvement has been successfully implemented to vary the out-of-plane compression properties depending on the amount of in-plane pre-crushing. The relationships between in-plane deformation with plateau crushing strength and compaction strain, derived from the experimental investigations, have been successfully introduced into the PAM-CRASH^{TM} material model.

3. This thesis has shown that relationships between loading conditions and variations in principal direction properties can be introduced directly into the material code and have shown improved representation for the crushing behaviour of the honeycomb material.

4. A geometrically accurate shell based model of the honeycomb has been investigated and presented. The model was found to replicate many of the trends observed during mixed shear-compression loading and pre-crushing in the in-plane directions.

5. The shell based model of the honeycomb has been shown to improve the representation of the composite-honeycomb sandwich material during edgewise, oblique and flexural loading.

Contributions towards woven composite material testing and modelling

1. The woven composite skin material has been experimentally investigated using the digital image correlation technique. This method provided many benefits over the use of traditional strain gauge measuring devices, such as full-field strain measurement and the measurement of strains over 5%. Tensile, shear and compression deformation and failure strains were successfully monitored using this technique.

2. The digital image correlation technique was used to derive damage evolution properties using cyclic shear testing. Damage progression was found to be non-linear for this woven fabric, from which new damage and failure laws were established and validated specifically for this woven composite material.

3. The improved non-linear damage progression law was successfully introduced into the composite material model in PAM-CRASH^{TM}. The new model was shown to correctly represent in-plane shear response of the woven composite material.

Contributions to the knowledge of composite-honeycomb deformation and energy absorption mechanisms

1. The composite-honeycomb sandwich material has been experimentally tested under static and dynamic edgewise loading. A variety of failure mechanisms have been observed and documented for cases that covered pure edgewise through to oblique (15°) edgewise loading.

2. The influence of the adhesive interface between the core and skins has been shown to increase the out-of-plane compression properties of the core. The restrictions imposed by the adhesive fillets at the interface increase end constraints and thus increase the initial peak load and plateau compression strength of the honeycomb.

3. Cracked sandwich beam investigations were conducted to determine crack propagation properties through the composite sandwich when subjected to transverse (Mode I) loading. This investigation revealed that stable crack growth initiates from the bond line and then propagates through the central portion of the aluminium honeycomb. Strain energy release rate through the core was found to be between 15.1-16.5kJ/m^2.

4. The change in fracture toughness in aluminium honeycomb due to higher loading rates was investigated and presented. This investigation was conducted using a new test apparatus specifically designed for DCB sample testing. The results showed there was an increase in fracture toughness of 50% for loading velocities of 1.3m/sec.

5. The flexural properties of the sandwich were examined using three-point bend testing. The failure and deformation mechanisms occurring in the skins and core materials were consistently shown to involve initial failure of the upper skin giving a sudden drop in flexural strength; this was followed by failure of the lower skin. A mixed shear-compression deformation in the core was observed throughout each test.

6. The edgewise compression properties of the sandwich material have been investigated and presented. The failure mechanisms and energy absorption were found to be highly dependent on the properties of the core. Furthermore, the use of

the low-density core was shown to be responsible for lack of overall stability of the composite honeycomb sandwich.

7. Oblique edgewise testing has also been investigated and presented. This investigation found an increase in energy absorption of 50% for the 5 ply skin thickness samples and 120% increase in the 4 ply skin thickness samples. A change in failure mechanisms were also observed during oblique loading tests. A series of folding mechanisms isolated near the crushing wall were observed which produced a consistent fluctuation in loading strength from 5kN to 13kN for the 4ply skin thickness sandwich and 4kN to 15kN for the 5 ply skin thickness sandwich. The specific energy absorption was found to be similar for both skin thickness samples during oblique loading.

8. Impact testing of the wedge samples revealed a reduction in energy absorption of 25-35% depending on the number of plies in the skin material. Crack propagation between core and skins was found to extend beyond the impact front and was greater than that observed in quasi-static testing, thus reducing the overall structural energy absorption properties of the sandwich.

Contributions to the modelling of composite-sandwich structures

1. This work has concluded that the currently available models in PAM-CRASH^{TM} are not yet fully capable of replicating the energy absorbent behaviour and deformation mechanism observed during edgewise impact testing of composite- honeycomb materials.

2. A variety of modelling methods to represent the sandwich using composite shell elements attached either directly, or using a tied contact interface elements, to a honeycomb solid element have been evaluated and presented. These models failed to reproduce well the experimental force-displacement curves.

3. Improvements to constitutive modelling of the core material to include in-plane pre-crushing effects on the out-of-plane compression properties have shown marginal improvement to the energy absorption of the three-point bend numerical model. Further improvements are required as the force-displacement curves produced by the numerical model did not adequately reproduce experimental observations. These improvements include the automated mixed shear-compression core model.

4. The use of a geometrically accurate shell based core model has been shown to improve correlation with the experimental force-displacement curve and reproduce the observed deformation mechanisms.

5. The numerical models of the wedge samples were evaluated: Edgewise and oblique loading conditions were applied to correspond to the experimental studies. However, unrealistic folding mechanisms were observed in these numerical models for both loading cases, which reduced the structural strength of the numerical model compared to tests. A meso-shell core model was also investigated, but produced similar unrealistic folding mechanisms.

6. Deficiencies in the composite skin material model were identified as the main source of inaccuracy in these models. The reduction of strength in the composite skin material is due to debonding between the fibre and resin. The composite skin shell elements are too strong and thus the edgewise compression force exceeds the buckling strength of the sandwich. This produced the unrealistic folding mechanisms observed in the wedge sandwich modelling.

7. Despite these limitations in the skin and core material models, this thesis has shown that useful crashworthiness evaluations can be conducted. A numerical model of the nosecone structure of the 2004 BAR-Honda racing car was developed and presented here. The force-displacement recordings from the numerical model were found to be compatible with the FIA regulations.

8. This work has concluded that crashworthiness analysis of a nosecone structure is possible; however, the identified problems are likely to limit possibilities to optimise the structure.

8   Future Research

This Chapter presents possible directions of future research that could build upon the results of this research. Some of the limitations encountered during this research and suggestions for further work are discussed below.

8.1.1   Addressing Investigation Limitations

This research has identified a number of limitations with the modelling of composite-honeycomb sandwich structures. Further experimental and numerical investigations to follow this work include;

- *Improved constitutive modelling to represent the degradation of composite materials due to a frontal impact:* The numerical models of the wedge impact specimens provided an inaccurate representation of the failure modes. This inaccuracy is caused by the constitutive model for the composite material. An investigative study is required to determine the progressive degradation in composite material properties when loaded in this manner.

- *Loading rate dependency on the mixed shear-compression properties of honeycomb:* This thesis has presented the mixed shear-compression properties of the aluminium honeycomb core at low rates of loading. The out-of-plane compression properties are known to vary at higher rates of loading and thus the mixed shear-compression properties are likely to be loading rate dependent. The findings from this investigation will improve the numerical honeycomb model.

8.1.2   Further Crashworthiness Evaluation

The frontal impact crashworthiness evaluation has been the focus of this research and investigated to develop a nosecone model. A truly valid computational model for crashworthiness evaluation will be capable of representing the component under a variety of loading conditions, such as the side impact test. A further series of experimental studies are required to establish the energy absorbing properties of

sandwich materials, such as the effects of impact loading on the surface of the sample similar to that of Schubel et al. [68].

8.1.3 Extended Material Investigation

A potential future application of this work is to predict the crashworthiness of a new structure constructed from composite and sandwich materials. Modern motorsport and aerospace vehicles are developed using an increasing variety of composite and core materials. This work has also suggested multiple avenues of research to further understand the properties of composite and honeycomb materials. These potential studies include:

- *Inter-laminar damage of the composite skin material:* The current composite material model does not account for inter-laminar delamination. An investigation of inter-laminar failure mechanisms introduced through manufactured, or impact loading, on the in-plane compression and shear properties could be beneficial for future model development. Modelling methods to represent this delamination could include the use of a tied interface between plies, such as that presented by Greve [105] and Pickett et al. [89].

- *Combined mixed shear-compression with pre-deformation of the honeycomb material:* In this work, mixed shear-compression and pre-deformation loading conditions were investigated and implemented separately. In an impact structure application, it is likely that a mixture of these loading conditions will take place. The Arcan apparatus developed in this work could also be applied to samples having pre-deformation. Another method is the use of the apparatus developed by Hong et al. [28] which would be easier to use. The use of the numerical shell representation of the honeycomb developed in this research could be used to save materials and determine general property trends.

- *Extended Material Databases:* The methods and techniques presented in this work can be applied to other core and skin materials. It is useful to extend the material database for comparisons and produce further constitutive property laws for the material models used in FE codes.

9 References

1. New McLaren may not race now until Monza. Edited by Smith D. Autosport. pp. 8. June 26th. 2003.

2. Treymayne D. The Science of Safety – The Battle against Unacceptable Risk in Motor Racing. Haynes Publishing. Somerset, England. 2000.

3. FIA, 2005 Technical Regulations. Articles 16, 17 and 18. 30th October 2004.

4. Savage G. Composite Materials in Formula 1 Racing. Metals and Materials 7(10). pp. 617-624. 1991.

5. MP4/1 Image. The McLaren Group. www.McLaren.com/technical. 2006.

6. Savage G. Safety and Survivability in Formula One Motor Racing. Metals and Materials 3. pp. 147-153. 1992.

7. Savage G., Bomphray I., and Oxley M. Exploiting the Fracture Properties of Carbon Fibre Composites to Design Lightweight Energy Absorbing Structures. Engineering Failure Analysis 11. pp. 677-694. 2004.

8. 006 BAR-Honda F1 car. Honda Racing F1. www.hondaracingf1.com. 2006.

9. Sigalas I, Kumosa M. and Hull D. Trigger Mechanisms in Energy Absorbing Glass Cloth/Epoxy Tube. Composites Science and Technology 40. pp. 265-287. 1991.

10. Mamalis A.G., Manolakos D.E., Demosthenous G.A. and Ioannidis M.B. Crashworthiness of Composite Thin-Walled Structural Components. Technomic Publishing co. Lancaster. pp. 177-198. 1998.

11. Mamalis A.G., Manolakos D.E., Demosthenous G.A. and Ioannidis M.B. Energy Absorption Capability of Fibreglass Composite Square Frusta Subjected to Static and Dynamic Axial Collapse. Thin-Walled Structures 25 (4). pp. 269-295. 1996.

12. Hull D. A Unified Approach to Progressive Crushing of Fibre-Reinforced Composite Tubes. Composites Science and Technology 40. pp. 377-421. 1991.

13. Bisagni C., Di Pietro G., Fraschini L. and Terletti D. Progressive Crushing of Fibre-reinforced Composite Structural Components of a Formula One Racing Car. Composite Structures 68. pp. 491-503. 2005.

14. Marsh G. Airframers Exploit Composites in Battle for Supremacy. Reinforced Plastics 49(3). pp. 26-32. March 2005.

15. Marsh G. Duelling with Composites. Reinforced Plastics 50(6). pp. 18-23. June 2006.

16. Wilson S. A New Face of Aerospace Honeycomb. Technical Report. Materials & Design 11(6). pp. 323-326. 1990.

17. Gibson L.J. and Ashby M.F. Cellular Solids – Structure and Properties. Pergamon Press. 1988.

18. HexWeb Honeycomb Attributes and Properties – A Comprehensive Guide to Standard HEXCEL Honeycomb Materials, Configurations, and Mechanical Properties. HEXCEL^{TM} Composites. 1999.

19. ASTM C365-03. Standard Test Method for Flatwise Compressive Properties of Sandwich Cores. Annual Book of ASTM Standards 2005. ASTM International. pp. 25-27. 2005.

20. Mohr D. and Doyoyo M. Large Plastic Deformation of Metallic Honeycomb: Orthotropic Rate-Independent Constitutive Model. International Journal of Solids and Structures 41. pp. 4435-4456. 2004.

21. ASTM C273-00. Standard Test Method for Shear Properties of Sandwich Cores. Annual Book of ASTM Standards 2005. ASTM International. pp. 8-11. 2005.

22. Kelsey S., Gellatly R.A. and Clark B.W. The Shear Modulus of Foil Honeycomb Cores – A Theoretical and Experimental Investigation on the Cores Used in Sandwich Construction. Aircraft Engineering 30. pp. 294-302. 1958.

23. Mohr D. and Doyoyo M. Analysis of the Arcan Apparatus in the Clamped Configuration. Journal of Composite Materials 36(22). pp. 2583-2594. 2002.

24. Doyoyo M. and Mohr D. Microstructural Response of Aluminium Honeycomb to Combined Out-of-Plane Loading. Mechanics of Materials 35. pp. 865-876. 2003.

25. Mohr D. and Doyoyo M. Experimental Investigation on the Plasticity of Hexagonal Aluminium Honeycomb under Multiaxial Loading. Journal of Applied Mechanics 71. pp. 375-385. 2004.

26. Arcan M., Hashin Z. and Voloshin A. A Method to Produce Uniform Plane-Stress States with Application to Fibre-reinforced Materials. Experimental Mechanics. pp. 141-284. 1978.

27. Doyoyo M. and Wierzbicki T. Experimental studies on the yield behaviour of ductile and brittle aluminium foams. International Journal of Plasticity 19. pp. 1195-1214. 2003.

28. Hong S.T., Pan J., Tyan T. and Prasad P. Quasi-static crush behaviour of Aluminium honeycomb specimens under compression dominant combined loads. International Journal of Plasticity 22. pp. 73-109. 2006.

29. Zhang J. and Ashby M.F. Buckling of Honeycombs under In-plane Biaxial Stresses. International Journal of Mechanical Science 34(6). pp. 491-509. 1992.

30. Mohr D. and Doyoyo M. Nucleation and propagation of plastic collapse bands in Aluminium honeycomb. Journal of Applied Science 94(4). pp. 2262-2270. 2003.

31. Alexander J.M. An Approximate Analysis of the Collapse of Thin Cylindrical Shells under Axial Loading. Quarterly Journal of Mechanical and Applied Mathematics 13. pp. 10-15. 1960.

32. McFarland R.K. Hexagonal Cell Structures under Post-Buckling Axial Load. AIAA Journal 1(6). pp. 1380- 1385. 1963.

33. Wierzbicki T. Crushing Analysis of Metal Honeycombs. International Journal of Impact Engineering 1(2). pp. 157-174. 1983.

34. Fielding J.P. Introduction to Aircraft Design. Chapter 5. What's under the skin? – Structure and propulsion. Cambridge University Press. UK. 1999.

35. SP Guide to Composites. SP Systems. www.spsystems.com

36. McLaren SLR. McLaren Automotive. www.mclarenautomotive.com. 2006.

37. Rudd C.D., Long A.C., Kendall K.N. and Mangin C.G.E. Liquid Moulding Technologies: Resin Transfer Moulding, Structural Reaction Injection Moulding, and Related Processing Techniques. Society of Automotive Engineers. 1997.

38. Magnamite Carbon Fibre Selector Guide. HEXCEL^{TM} Composites. 2002.

39. Cycom 2035 Epoxy Prepreg. Cytec Engineering Materials. September 2003.

40. McBeath S. Competition Car Composites - A Practical Handbook. Haynes Publishing. 2000.

41. Savage G. Enhancing the Exploitation and Efficiency of Fibre-Reinforced Composite Structures by Improvement of Inter-laminar Fracture Toughness. Engineering Failure Analysis 13. pp. 198-209. 2006.

42. Daniel I.M. and Ishai O. Engineering Mechanics of Composite Materials. Oxford University Press. England. 1994.

43. Hull D. and Clyne T.W. An Introduction to Composite Materials, 2nd Edition. Cambridge University Press. 1996.

44. Anderson T. Fracture Mechanics – Fundamentals and Application, 2nd Edition. CRC Press LLC, Boca Raton, Florida. 1995.

45. Onck P.R., Andrews E.W. and Gibson L.J. Size Effects on Ductile Cellular Solids. Part 1: Modelling. International Journal of Mechanical Science 43. pp. 681-699. 2001.

46. Williams J.G. On the Calculation of Energy Release Rates for Cracked Laminates. International Journal of Fracture 36(2). pp. 101-119. 1988.

47. ASTM D5528-01. Standard Test Method for Mode-I Inter-laminar Fracture Toughness of Unidirectional Fibre-Reinforced Polymer Matrix Composites. Annual Book of ASTM Standards 2005. ASTM International. pp. 252-263. 2005.

48. Hinton M.J., Kaddour A.S. and Soden P.D. A Comparison of the Predictive Capabilities of Current Failure Theories for Composite Laminates, Judged Against Experimental Evidence. Composites Science and Technology 62. pp. 1725-1797. 2002.

49. Ladevéze P. and Le Dantec E. Damage Modelling of the Elementary Ply for Laminated Composites. Composites Science and Technology 43. pp. 257-267. 1992.

50. PAM-CRASH^{TM} Solver Notes Manual 2005. Engineering System International. ESI-Group.

51. Fouinneteau M.R.C. Damage and Failure Modelling of Carbon and Glass 2D Braided Composites. PhD Thesis. Cranfield University. 2006.

52. Pickett A.K. and Fouinneteau M.R.C. Material Characterisation and Calibration of a Meso-Mechanical Damage Model for Braided Reinforced Composites. Composites: Part A 37. pp. 368-377. 2006.

53. HexWeb – Honeycomb Sandwich Design Technology. HEXCEL^{TM} Composites. 2000.

54. Styles M., Compston P. and Kalyanasundaram S. The Effect of Core Thickness on the Flexural Behaviour of Aluminium Foam Sandwich Structures. Composite Structures (2006), doi:10.1016/j.com. pstruct. 2006.07.002.

55. ASTM C393-00. Standard Test Method for Flexural Properties of Sandwich Constructions. Annual Book of ASTM Standards 2005. ASTM International. pp. 32-35. 2005.

56. Lingaiah K. and Suryanarayana B.G. Strength and Stiffness of Sandwich Beams in Bending. Experimental Mechanics 31(1). pp. 1-7. 1991.

57. Okada R. and Kortschot M.T. The Role of the Resin Fillet in the Delamination of Honeycomb Sandwich Structures. Composite Science and Technology 62. pp. 1811-1819. 2002.

58. Grove S.M., Popham E. and Miles M.E. An Investigation of the Skin/Core in Honeycomb Structures using Statistical Experimentation Techniques. Composites: Part A. 37. pp. 804-812. 2006.

59. Han T.S., Ural A., Chen C.S., Zehnder A.T., Ingraffea A.R. and Billington S.L. Delamination Buckling and Propagation Analysis of Honeycomb Panels using a Cohesive Element Approach. International Journal of Fracture 115. pp. 101-123. 2002.

60. Shivakumar K.N. and Smith S.A. In Situ Fracture Toughness Testing of Core Materials in Sandwich Panels. Journal of Composite Materials 38 (8). pp. 655-668. 2004.

61. Carlsson L.A., Matteson R.C., Aviles F. and Loup D.C. Crack Path in Foam Cored DCB Sandwich Fracture Specimens. Composite Science and Technology 65. pp. 2612-2621. 2005.

62. Shivakumar K., Chen H. and Smith S.A. An Evaluation of Data Reduction Methods for Opening Mode Fracture Toughness of Sandwich Panels. Journal of Sandwich Structures and Materials 7. pp. 77-90. 2005.

63. Ural A., Zehnder A.T. and Ingraffea A.R. Fracture mechanics approach to facesheet delamination in honeycomb: measurement of energy release rate of adhesive bond. Engineering Fracture Mechanics 70. pp. 93-103. 2003.

64. HEXCEL – Prepreg Technology. HEXCEL^{TM} Composites. 2005.

65. Lacy T.E. and Hwang Y. Numerical Modelling of Impact-Damaged Sandwich Composites Subjected to Compression-after-Impact Loading. Composite Structures 61. pp. 115-128. 2003.

66. Kosza P. and Sayir M.B. Failure Patterns in the Core of Sandwich Structures under Impact Loading. International Journal of Impact Engineering 15(4). pp. 501-517. 1994.

67. Dear J.P., Lee H. and Brown S.A. Impact Damage Processes I Composite Sheet and Sandwich Honeycomb Materials. International Journal of Impact Engineering 32. pp. 130-154. 2005.

68. Schubel P.M., Luo J.J. and Daniel I.M. Impact and Post-Impact Behaviour of Composite Sandwich Panels. Composites: Part A. 2006, doi:10.1016/j.compositesa.2006.06.022.

69. Mouritz A.P. and Thomson R.S. Compression, Flexure and Shear Properties of a Sandwich Composite Containing Defects. Composite Structures 44. pp. 263-278. 1999.

70. Burnett D.S. Finite Element Analysis, From Concepts to Applications. AT&T Bell Industries. Addison-Wesley Publishing. 1987.

71. PAM-SCL (Solid Core Library) Version 2000. Theory Notes Manual. PAM SYSTEM INTERNATIONAL. 2000.

72. ESI Group. www.esi-group.com. 2006.

73. Schreyer H.L., Zuo Q.H. and Maji A.K. Anisotropic Plasticity Model for Foams and Honeycombs. Journal of Engineering Mechanics 120(9). pp. 1913-1930. 1994.

74. Mohr D. and Doyoyo M. Deformation-Induced Folding Systems in Thin-Walled Monolithic Hexagonal Metallic Honeycomb. International Journal of Solids and Structures 41. pp. 3353-3377. 2004.

75. ANSYS LS-DYNA User's Guide. ANSYS Release 10.0. ANSYS, INC. 2005.

76. Yamashita M. and Gotoh M. Impact Behaviour of Honeycomb Structures with Various Cell Specifications – Numerical Simulation and Experiment. International Journal of Impact Engineering 32. pp. 618-630. 2005.

77. Papka S.D. and Kyriakides S. In-plane biaxial crushing of honeycombs – Part 2: Analysis. International Journal of Solids and Structures 36. pp. 4397-4423. 1999.

78. Papka S.D. and Kyriakides S. Experiments and full-scale numerical simulations of in-plane crushing of a honeycomb. Acta Mater 46(8). pp. 2765-2776. 1998.

79. Scarpa F., Blain S., Lew T., Perrott D., Ruzzene M. and Yates J.R. Elastic Buckling of Hexagonal Chiral Cell Honeycombs. Composites: Part A 38. pp. 280-289. 2007.

80. Tang X., Whitcomb J.D., Kelkar A.D. and Tate J. Progressive Failure Analysis of 2x2 Braided Composites Exhibiting Multicale Heterogeneity. Composite Science and Technology 66. pp. 2580-2590. 2006.

81. Tang X., Whitcomb J.D., Li Y. and Sue H.J. Micromechanics Modelling of Moisture Diffusion in Woven Composites. Composites Science and Technology 65. pp. 817-826. 2005.

82. D'Amato E. Finite Element Modelling of Textile Composites. Composite Structures 54. pp. 467-475. 2001.

83. Woo K. and Whitcomb J.D. Effects of Fibre Tow Misalignment on the Engineering Properties of Plain Weave Textile Composites. Composite Structures 37 (3/4). pp. 343-355. 1997.

84. Woo K. and Whitcomb J.D. A Post-Processor Approach for Stress Analysis of Woven Textile Composites. Composites Science and Technology 60. pp. 693-704. 2000.

85. Iannucci L. and Willows M.L. An Energy Based Damage Mechanics Approach to Modelling Impact onto Woven Composite Materials: Part I. Numerical Models. Composites: Part A 37. pp. 2041-2056. 2006.

86. Iannucci L. and Willows M.L. An Energy Based Damage Mechanics Approach to Modelling Impact onto Woven Composite Materials: Part II. Experimental and Numerical Results. Composites: Part A 38. pp. 540-554. 2007.

87. Boutaous A., Peseux B., Gornet L. and Belaidi A. A New Model of Plasticity Coupled with the Damage and Identification of Carbon Fibre Composite Laminates. Composite Structures 74. pp. 1-9. 2006.

88. Greve L. and Pickett A.K. Delamination Testing and Modelling for the Composite Crash Simulation. Composite Science and Technology 66. pp. 816-826. 2006.

89. Pickett A.K., Johnson A.F. and Rozicky P. Computational Methods for Predicting Impact in Composite Structures. Composites Science and Technology 61. pp. 2183-2192. 2001.

90. Aktay L., Johnson A.F. and Holzapfel M. Prediction of Impact Damage on Sandwich Composite Panels. Computational Materials Science 32. pp. 252-260. 2005.

91. Foo C.C., Chai G.B. and Seah L.K. Quasi-Static and Low-Velocity Impact Failure of Aluminium Honeycomb Sandwich Panels. Proc. IMechE. 220 Part 1: Journal of Materials: Design and Applications. pp. 53-66. 2006.

92. Askeland D.P. The Science and Engineering of Materials. Third S.I. Edition. Chapman & Hall, UK. 1996.

93. Temple M. Numerical Simulation of F1 Nosecone Impact Testing. MSc Thesis. Cranfield University. 2003.

94. LIMESS GmbH. www.limess.com. 2006.

95. TML. Precise & Flexible Strain Gauges. TML Tokyo Sokki Kenkyujo Co. Ltd. Japan. 2006.

96. ASTM D3039M-00. Standard Test Method for Tensile Properties of Polymer Matrix Composite Materials. Annual Book of ASTM Standards 2005. ASTM International. pp. 64-76. 2005.

97. ASTM D3518M-94. Standard Test Method for In-Plane Shear Response of Polymer Matrix Composite Materials by Tensile Test of a $\pm 45^0$ Laminate. Annual Book of ASTM Standards 2005. ASTM International. pp. 109-115. 2005.

98. ASTM D3410M-03. Standard Test Method for Compressive Properties of Polymer Matrix Composite Materials with Unsupported Gage Section by Shear Loading. Annual Book of ASTM Standards 2005. ASTM International. pp. 109-115. 2005.

99. Adams D.F. and Lewis E.Q. Influence of Specimen Gage Length and Loading Method on the Axial Compressive Strength of a Unidirectional Composite Material. Experimental Methods 31(1). pp. 14-20. 1991.

100. Andrews E.W, Gioux G, Onck P.R. and Gibson L.J. Size Effects on Ductile Cellular Solids. Part 2: Experimental Results. International Journal of Mechanical Science 43. pp. 701-713. 2001.

101. Silbermann V. Mode 1 Dynamic Delamination Testing for Advanced Composite Materials. MSc Thesis. Cranfield University. 2003

102. May M. The Effect of Tufting on the Mechanical Properties of 2D Textile Composites. Diploma Thesis. University of Sttutgart. 2006.

103. MATWEB. Material Property Data. www.matweb.com. Designed and maintained by Automation Creations, Inc. 2006.

104. Prasad S. and Carlsson L.A. Debonding and Crack Kinking in Foam Core Sandwich Beams-II. Experimental Investigation. Engineering Fracture Mechanics 47(6). pp. 825-841. 1994.

105. Greve L. Damage and Failure Modelling of carbon/epoxy Non Crimp Fabric Composites. PhD Thesis. Cranfield University. 2005.

106. Pickett A.K. Review of Finite Element Simulation Methods Applied to Manufacturing and Failure Prediction in Composites Structures. Applied Composite Materials 9. pp. 43-58. 2002

107. Lourenco N.F.S. Predictive Finite Element Method for Axial Crush of Composite Tubes. PhD Research Thesis. University of Nottingham. 2002.

108. CADEC. Computer Aided Design Environment for Composites software. West Virginia University. www.mae.wvu.edu/~barbero/cadec.html.

109. HexWeb – Honeycomb Absorption Systems. HEXCEL^{TM} Composites. 2005.

110. Warrior N.A., Turner T.A., Robitaille F. and Rudd C.D. The Effect of Inter-laminar Toughening Strategies on the Energy Absorption of Composite Tubes. Composites: Part A 35. pp. 431-437. 2004.

111. ASTM C364-99. Standard Test Method for the Edgewise Compressive Strength of Flat Sandwich Constructions. Annual Book of ASTM Standards Vol. 15.03. ASTM International. 2000.

112. Mamalis A.G., Manolakos D.E., Ioannidis M.B. and Papapsotolou D.P. On the Crushing Response of Composite Sandwich Panels Subjected to Edgewise Compression: Experimental. Composite Structures 71. pp. 246-257. 2005.

113. Lichtenburger R. and Schreier H. Contactless and Fullfield 3D-Deformation Measurement for Impact and Crash Tests. LIMESS GmbH. www.limess.de. 2004.

114. Ambur D.R., Jaunky N. and Hilburger M.W. Progressive Failure Studies of Stiffened Panels Subjected to Shear Loading. Composite Structures 65. pp. 129-142. 2004.

115. Smerd R., Winkler S., Salisbury C.P., Worswick M.J., Lloyd D. and Finn M. High Strain Rate Tensile Testing of Automotive Aluminium Alloy Sheet. International Journal of Impact Engineering 32. pp. 541-560. 2005.

10 Appendices

This Chapter presents work to compliment the experimental and numerical research presented in this PhD thesis.

Appendix A - Summary of the FIA Frontal Impact Test Requirements

Appendix B - Explicit Solution Method

Appendix C - Modified Arcan Design for Cellular Solids

Appendix A – Summary of the FIA Frontal Impact Test Requirements

To establish the crashworthiness of an energy-absorbing structure, a prototype structure is manufactured and tested according to the FIA regulations.

Article 16 of the 2004 FIA Technical Regulations [3] specifies the test requirements for frontal impact. The criteria for preparing this test are as follows:

- all parts, i.e. the nosecone, which could affect the outcome of the test, are to be fitted to the monocoque. The monocoque itself must be solidly fixed to the impact trolley via the engine mounting points in a way that does not increase the impact resistance,
- a fuel tank must be fitted and filled with water,
- a dummy weighing at least 75kg must be included with safety belts fastened,
- fire extinguishers must be fitted,
- the mass of the trolley and test structure, including dummy, must weight 780kg and have an impact velocity of 14m/s.

The frontal impact structure must absorb 76.4 kJ of energy during the test. Furthermore, the regulations also stipulate load profile requirements created by the structure during test, these are:

- average deceleration over the first 150mm must not exceed 5g,
- average deceleration of the trolley must not exceed 40g throughout the test,
- peak deceleration in the dummy chest cavity must not exceed 60g for more than a cumulative 3ms.

In addition, the safety belts and fire extinguisher mountings must be undamaged and no liquid may be spilled from the fuel tank.

Appendix B – Explicit Solution Method

The explicit solution performs a finite difference solution in the time domain [71]. Consider the simple one degree of freedom (1 DOF) spring mass system in Figure 1.
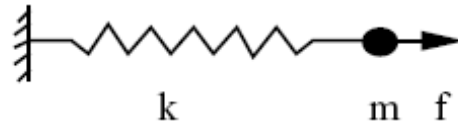

Figure 1: Spring-mass system [71]

In order to describe this system, the dynamic equation of motion is applied, thus,

$$m\frac{d^2x}{dt^2} + kx = f,$$ [C-1]

where m is the mass, k is the spring stiffness, f is the applied force, x is the displacement and t is time. In order to calculate the position, velocity and acceleration of the mass at a point in time, the explicit solution routine determines velocities at half time intervals, i.e. $t_{n-1/2}$, $t_{n+1/2}$, and displacements and accelerations at full time intervals where n is the time increment number; this is shown schematically in Figure 2.
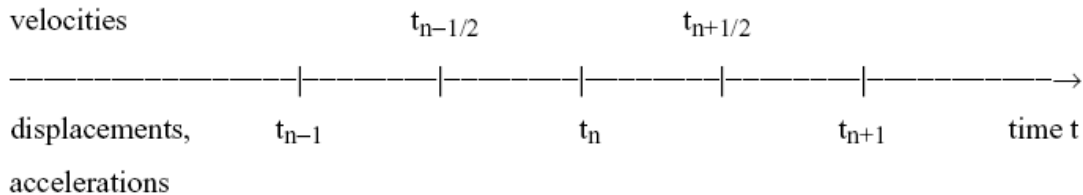

Figure 2: Velocity, displacement and acceleration at time increments using explicit routine [71]

In order to progress from the current time t_n, the solution is required to calculate the displacement at t_{n+1}, velocity at $t_{n+1/2}$ and acceleration at t_n using the known quantities of displacement at t_n and velocity at $t_{n-1/2}$. The equation of motion is stated at t_n,

$$m\frac{d^2x_n}{dt^2} + kx_n = f_n.$$ [C-2]

Rearranging equation C-2 gives acceleration at t_n as,

$$\frac{d^2x_n}{dt^2} = \frac{(f_n - kx_n)}{m}.$$ [C-3]

Using the newly acquired acceleration and central finite difference time integration the velocities and displacements for the next increments can be determined using equations C-4 and C-5,

$$\frac{dx_{n+1/2}}{dt} = \frac{dx_{n-1/2}}{dt} + \frac{d^2 x_n}{dt^2} \Delta t_n ,$$ [C-4]

$$x_{n+1} = x_n + \frac{dx_{n+1/2}}{dt} \Delta t_{n+1/2} .$$ [C-5]

This algorithm does have an apparent disadvantage when compared with implicit methods. The limit for time step Δt so that the solution remains stable is based on element size and properties given by equation C-6,

$$\Delta t \leq \sqrt{\frac{2m}{k}} = \frac{L}{C} ,$$ [C-6]

where L is the length of the element and C is the acoustic wave speed or the speed of sound through a material. The implicit method is independent of properties concerning the mesh and is described as 'unconditionally stable'.
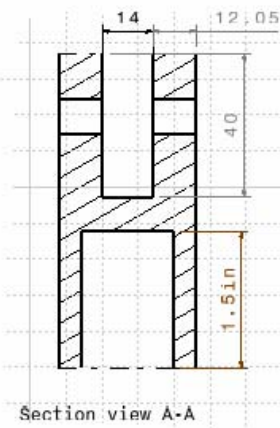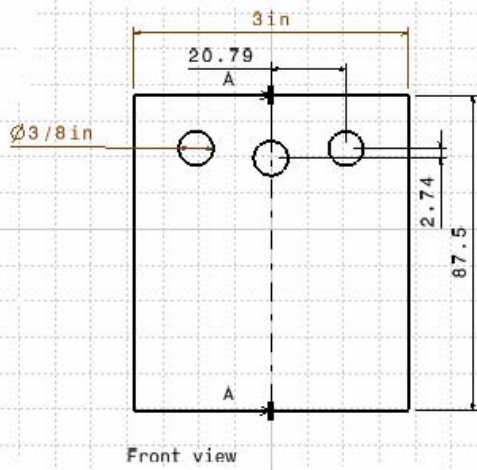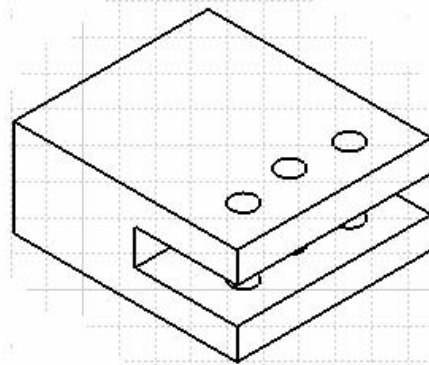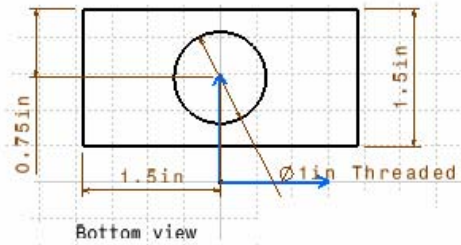
Appendix C – Modified Arcan Design for Cellular Solids

Arcan Circular Section Modifications
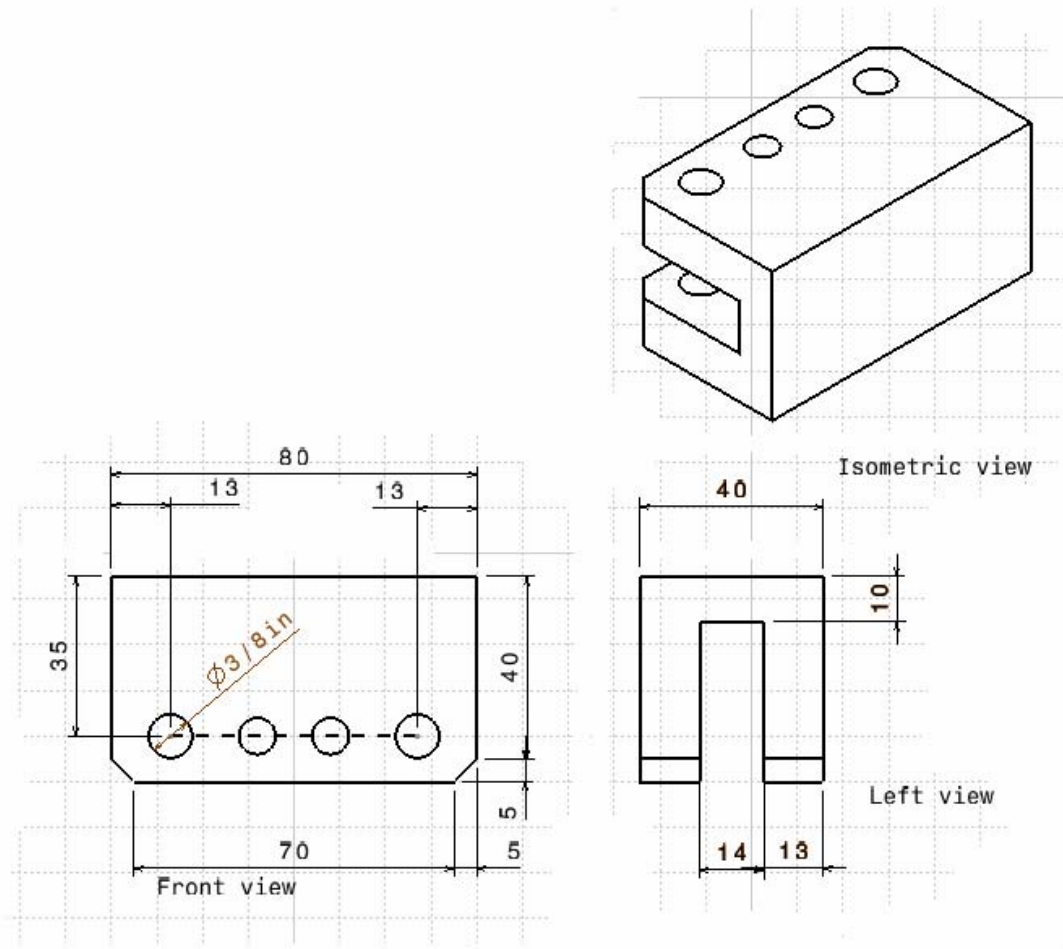

Front view
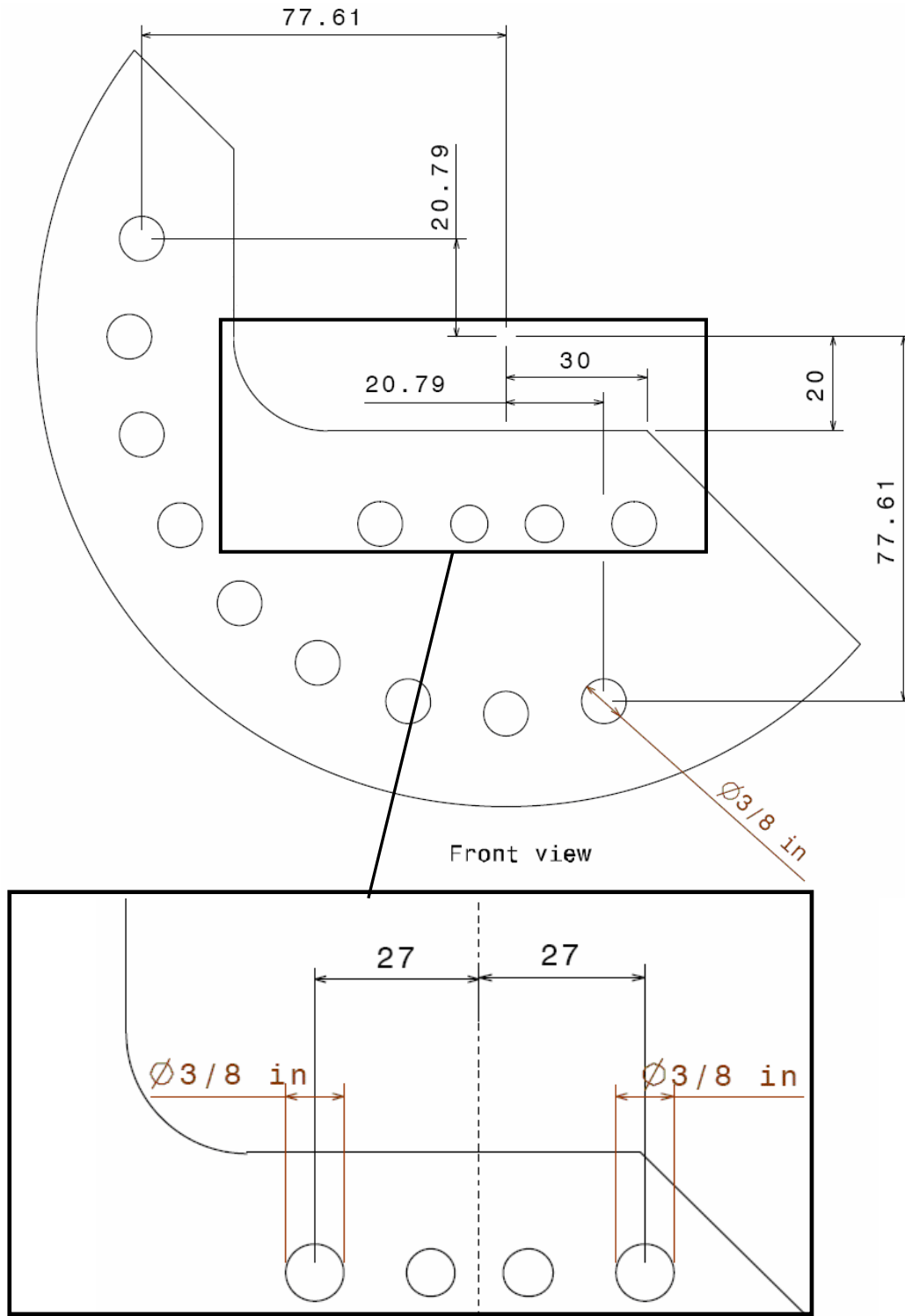
Not to Scale - All Dimensions in mm unless otherwise stated

Base Clamp Units

Not to Scale - All Dimensions in mm unless otherwise stated

Honeycomb Sample Grips

Not to Scale - All Dimensions in mm unless otherwise stated